Introduction

According to the Quantum-Chromo Dynamics, for temperatures higher than the critical value $T_c \sim 150 - 180\,MeV$ and energy densities greater than $1 - 3\,GeV/fm^3$, nuclear matter should undergo a phase transition towards a new state of matter, where quarks and gluons are no more confined into hadrons but behave as free particles. This state of matter is called Quark-Gluon Plasma (QGP).

It is thought that the inverse transition (from QGP to ordinary nuclear matter) has occured in the first instants of the Universe, when the extreme conditions of temperature and density required for the QGP formation were reached, and that the QGP still characterize today the evolution of the collapsing neutron stars.

Experimentally, ultra–relativistic heavy–ion collisions are a powerful tool to investigate the transition from ordinary nuclear matter to QGP.

Over the past 15 years, an extensive program of high energy nuclear collisions was carried out at the CERN SPS and at the BNL AGS in order to study the quark–gluon plasma formation in heavy ion collisions.

CERN started the program with the acceleration of light ions (^{16}O and ^{32}S) at 200 GeV/nucleon on heavy targets, while from 1994 a ^{208}Pb beam of 158 GeV/c per nucleon has become available. At the AGS ^{28}Si beams of 15 GeV/nucleon were followed by ^{200}Au beams of 12 GeV/nucleon. Nowadays at the BNL RHIC collider Au–Au collisions are studied at center of mass energies 10 times higher than the SPS ones.

In February 2000, on the basis of the results coming from all the heavy–ion program experiments (NA44, NA45/CERES, NA49, NA50, NA52/NEWMASS, WA97/NA57 and WA98), CERN claimed that "we now have a compelling evidence that a new state of matter has indeed been created... The new state of matter found... features many of the characteristics of the theoretically predicted quark–gluon plasma."

The experiments involved in this heavy ion program were intended to detect the signals proposed as signatures of the formation of this new state of deconfined matter. In particular, the NA50 experiment is aimed to study, by means of Pb-Pb collisions at 158 GeV/c per nucleon, the suppression of the charmonium state production, expected in a QGP environment, where the Debye screening prevents the $c\bar{c}$ pair from binding in a J/ψ meson.

The suppression of the charmonium states indeed represents one of the most clearly observable signatures of plasma formation in nuclear collisions, since they are produced in the early stages of the collision, when the energy available is higher, and are too tightly bound to be destroyed already in interactions with the hadronic medium.

Since the J/ψ suppression is expected to be more important in central collisions, where the conditions for the QGP formation can be more likely achieved, the determination of the centrality of the collision becomes a crucial point in the NA50 experiment. For this reason, three different centrality detectors are used: an electromagnetic calorimeter, devoted to the detection of the neutral tranverse energy released in the interaction, a multiplicity detector, which counts the number of charged particles produced in the collision, and a Zero Degree Calorimeter (ZDC), which measures the energy carried by the projectile spectators of the interaction.

The data collected by the NA38, NA51 and NA50 experiments in collisions from p–p up to S–U, has shown a continuous and monotonic J/ψ suppression pattern, which can be understood in terms of ordinary nuclear absorption of the $c\bar{c}$ pair before it forms a J/ψ state.

The measurements with proton and light ions are useful to establish a reference baseline (the "normal" charmonium absorption by nuclear matter) with respect to which the heavy ion specific features can be identified.

The previous results obtained by NA50 in Pb–Pb collisions at 158 AGeV/c have indicated a decreasing pattern of the J/ψ production yield from peripheral to central Pb–Pb collisions, with a clear departure from the "normal" nuclear absorption curve. This suppression pattern can be understood in a deconfinement scenario, as due to the disappearance first of the χ_c mesons, responsible for about 30–40% of the indirect J/ψs, and then of the more tightly bound and directly produced J/ψs.

The purpose of the year 2000 data taking was to extend the previous knowledge about the suppression mechanism of the charmonium states to very peripheral Pb–Pb interactions. For this reason, a vacuum system has been designed for the target region, in order to reduce the contamination from Pb–air interactions, which affects expecially the peripheral events. Moreover, a thin target was used to reduce the probability to have reinteractions of the secondary particles produced in the collision, which can bias the results relative to the most central collisions.

The results obtained in the analysis of these new data as a function of different centrality estimators, have confirmed the suppression pattern observed in the past and have provided a complete description of the J/ψ suppression, ranging from peripheral to central Pb–Pb collisions, showing that the most peripheral $J/\psi/DY$ points are consistent with the "normal" nuclear absorption curve, more precisely determined by new high statistics p-A data, together with previous p–p, p–d, p–A and S–U results from NA38, NA51 and NA50.

In particular, the subject of this thesis is to analyse the year 2000 data, using the information provided by the zero–degree calorimeter to estimate the centrality of the collision.

In the first chapter, I will introduce the basic elements of the QGP physics and, after a brief description of the dynamics of the interactions among ultra–relativistic heavy ions, I will discuss the experimental "signatures" that allow to identify the plasma and, in particular, those studied by the NA50 experiment.

In chapter 2, I will briefly describe the elements that compose the NA50 experimental apparatus and, in chapter 3, I will concentrate on the techniques adopted for the operations of calibration, pedestal subtraction and beam pile–up correction of the ZDC signal, before starting the data analysis.

Chapter 4 is devoted to the description of the selection and cleaning cuts imposed to the reconstructed muon pairs in order to obtain a clean data sample to be analysed.

In Chapter 5 the different steps of the standard analysis technique are described and the final $\sigma_{J/\psi}/\sigma_{DY}$ results of the 2000 data taking are presented and compared to the results of the analysis of the same data performed as a function of E_T and to the previous NA50 results. Moreover, the consequence of systematic effects on the $\sigma_{J/\psi}/\sigma_{DY}$ ratios will be taken into account.

In parallel with the study of the J/ψ and ψ' suppression as a probe of Quark Gluon Plasma formation, the NA50 Collaboration has investigated the fission of Pb projectiles at 40 and 158 GeV/c per nucleon on different targets.

For this purpose, a Cerenkov detector has been added to the standard NA50 set–up to measure the charge of the spectator fragments emitted by the projectile after its interaction in the target.

In heavy–ion collisions at ultra–relativistic energies, fission can be due both to electromagnetic and nuclear processes. The first mechanism plays a role only in collisions at large impact parameter (greater than the sum of the projectile and target nuclear radii), while for smaller impact parameters the interaction is dominated by the strong nuclear force.

Measurements on different target nuclei and at different incident energies can allow to disentangle these two contributions from the measured fission cross–sections, since the dependence of the fission cross–section as a function of the incident energy and of the target nucleus mass (or charge) are different for the two mechanisms.

In Chapter 6, the results obtained from these data will be presented and the contributions of the electromagnetic fission mechanism, extracted from the experimental fission cross–sections, will be compared to the Weizsäcker–Williams model predictions.

According to this model, the electromagnetic interaction between two nuclei is expressed in terms of the interaction of the projectile nucleus with a virtual photon emitted by the target nucleus, which may induce the fission of the projectile.

Proving the validity of the WW description of the electromagnetic processes is very important, since, at the LHC heavy ion collider, they will constitute the major beam loss mechanism. In particular, the cross–section for the electromagnetic dissociation in Pb–Pb interaction at LHC energies is expected to be of the order of 220 barn, and hence represents the main contribution to the total cross–section.

Therefore, an accurate description of the electromagnetic interactions is necessary, in order to give a correct prediction of the beam lifetime for operations with heavy ions and to measure the beam luminosity.

Even if the heavy–ion fission represents only a few percent of the EM processes at ultra–relativistic energies, it is a useful tool to test the WW model, which can then be applied to all the EM processes.

Introduzione

La Quanto–Chromo Dinamica prevede, per temperature piú alte del valore critico $T_c \sim 150-180\,MeV$ e densitá di energia maggiori di $1-3\,GeV/fm^3$, una transizione di fase della materia adronica verso un nuovo stato in cui quark e gluoni non sono piú confinati negli adroni, ma si comportano particelle come libere. Questo stato della materia é chiamato Quark–Gluon Plasma (QGP).

Si pensa che la transizione inversa (da QGP a materia ordinaria) possa essere avvenuta nei primi istanti di vita dell'Universo, quando é probabile che siano state raggiunte le condizioni estreme di temperatura e di densitá richieste per la formazione del QGP e che il QGP caratterizzi ancora oggi l'evoluzione delle stelle di neutroni che stanno collassando.

Sperimentalmente le collisioni tra ioni pesanti ultra–relativistici possono essere un valido strumento per indagare il passaggio da materia nucleare ordinaria a QGP. Negli ultimi 15 anni, un esteso programma di collisioni nucleari ad alte energie é stato messo a punto all'SPS del CERN e all'AGS del BNL al fine di studiare la formazione del quark–gluon plasma in urti di ioni pesanti.

In particolare, il CERN ha avviato un programma per l'accelerazione di ioni leggeri (^{16}O e ^{32}S) a 200 GeV/c per nucleone su bersagli pesanti, mentre dal 1994 ha avuto a disposizione un fascio di ^{208}Pb a 158 GeV/c per nucleone. All'AGS a fasci di ^{28}Si di 15 GeV/nucleone si sono susseguiti fasci di ^{200}Au a 12 GeV/nucleone. Oggigiorno il collider RHIC del BNL studia urti Au–Au ad energie nel centro di massa 10 volte piú alte di quelle dell'SPS.

Nel Febbraio del 2000, sulla base dei risultati di diversi esperimenti con ioni pesanti dell'SPS (NA44, NA45/CERES, NA49, NA50, NA52/NEWMASS, WA97/NA57 e WA98), il CERN ha dichiarato di aver ottenuto prove inconfondibili dell'avvenuta creazione del Quark–Gluon Plasma.

Gli esperimenti coinvolti in questo programma per lo studio degli ioni pesanti sono stati progettati per rivelare i segnali proposti come prove della formazione di questo nuovo stato di materia deconfinata. In particolare, l'esperimento NA50 é mirato a studiare, per mezzo di collisioni Pb-Pb a 158 GeV/c per nucleone, la soppressione della produzione degli stati del charmonio, attesa nel caso di formazione del QGP, quando la schermatura di Debye dovrebbe impedire alle coppie $c\bar{c}$ di legarsi a formare i mesoni J/ψ .

La soppressione degli stati del charmonio infatti rappresenta una delle prove piú evidenti della formazione del QGP in collisioni nucleari, poiché essi sono prodotti negli stadi iniziali della collisione, quando l'energia disponibile é piú alta, e sono troppo saldamente legati per essere distrutti giá in interazioni con la materia adronica ordinaria.

Poiché ci si aspetta che la soppressione della J/ψ sia piú importante nelle collisioni centrali, dove le condizioni per la formazione del QGP possono essere piú probabilmente raggiunte, la determinazione della centralitá della collisione diventa un punto cruciale nell'esperimento NA50. Per questa ragione, sono utilizzati tre diversi rivelatori di centralitá: un calorimetro elettromagnetico, che rivela l'energia neutra trasversa rilasciata nell'interazione, un rivelatore di molteplicitá, che conta il numero di particelle cariche prodotte nella collisione e un calorimetro a zero–gradi (ZDC), che misura l'energia trasportata dai nucleoni spettatori dell'interazione.

I dati raccolti dagli esperimenti NA38, NA51 e NA50 in collisioni da p–p a S–U, hanno mostrato una soppressione continua e monotòna della J/ψ , che puó essere compresa in termini dell'assorbimento nucleare "normale" della coppia $c\bar{c}$ prima che formi uno stato J/ψ . Le misure con protoni e ioni leggeri sono utili per stabilire un riferimento (l'assorbimento "normale" del charmonio nella materia nucleare) rispetto al quale possano essere identificate le caratteristiche specifiche della soppressione della J/ψ in collisioni tra ioni pesanti.

I risultati precedentemente ottenuti da NA50 in collisioni Pb–Pb a 158 AGeV/c per nucleone, hanno mostrato una crescente soppressione della J/ψ passando da collisioni Pb–Pb piú periferiche a collisioni piú centrali, con una chiara deviazione dalla curva di assorbimento nucleare "normale". Questo pattern di soppressione puó essere compreso, nel caso di formazione del QGP, come causa della scomparsa prima del mesone χ_c, responsabile per almeno il 30–40% delle J/ψ totali, e poi delle J/ψ prodotte direttamente (che sono piú saldamente legate).

Lo scopo dei dati del 2000 é quello di estendere le precedenti conoscenze sul meccanismo di soppressione degli stati del charmonio a interazioni Pb–Pb estremamemente periferiche. Per questa ragione, un sistema di vuoto é stato progettato per la regione del bersaglio per ridurre la contaminazione delle interazioni Pb–aria, che influiscono specialmente sugli eventi piú periferici. Inoltre, é stato utilizzato un bersaglio sottile per ridurre la probabilitá di avere reinterazioni delle particelle secondarie prodotte nella collisione, che puó influire soprattutto nella regione degli urti piú centrali.

I risultati ottenuti nell'analisi di questi nuovi dati in funzione di diversi "stimatori" di centralitá, hanno confermato il pattern di soppressione osservato in passato e hanno fornito una descrizione completa della soppressione della J/ψ , in un range che va da collisioni Pb–Pb estremamente periferiche a collisioni centrali. In particolare, i punti di $J/\psi/DY$ piú periferici giacciono sulla curva di assorbimento nucleare "normale", piú precisamente determinata dai nuovi dati p-A ad alta statistica, insieme ai risultati precedenti di NA38, NA51 e NA50 ottenuti con collisioni p–d, p–p, p–A e S–U.

Il soggetto di questa tesi é l'analisi dei dati raccolti nel 2000, utilizzando le informazioni fornite dal calorimetro a zero gradi per stimare la centralitá della collisione.

Nel primo capitolo, sono introdotti gli elementi di base della fisica del QGP e, dopo una breve descrizione della dinamica delle interazioni tra ioni pesanti relativistici, vengono considerate le possibili "prove" sperimentali che permettono di identificare il QGP (in particolare, quelle studiate dall'esperimento NA50).

Nel capitolo 2, sono descritti brevemente gli elementi che compongono l'apparato sperimentale di NA50, mentre il capitolo 3 é dedicato alle tecniche adottate per le operazioni di calibrazione, sottrazione piedistalli e correzione degli eventi di pile–up applicate al segnale dello ZDC prima dell'analisi dei dati. Nel Capitolo 4 sono descritti i tagli imposti alle coppie di dimuoni ricostruiti per ottenere un campione di dati pulito da analizzare.

Nel Capitolo 5 sono quindi considerati i vari passi della tecnica di analisi "standard" e sono presentati i risultati finali del rapporto $\sigma_{J/\psi}/\sigma_{DY}$ per il 2000, paragonati ai risultati dell'analisi degli stessi dati eseguita in funzione di E_T e ai risultati di NA50 precedentemente pubblicati. Inoltre, sono stati considerati gli effetti sistematici sul rapporto $\sigma_{J/\psi}/\sigma_{DY}$.

In parallelo allo studio della soppressione della J/ψ e della ψ' , la Collaborazione di NA50 si é occupata dello studio della fissione di proiettili Pb a 40 e a 158 GeV/c per nucleone su vari bersagli.

A questo scopo, un rivelatore Cerenkov é stato aggiunto al setup standard di NA50 per misurare la carica dei frammenti emessi dal proiettile dopo la sua interazione nel bersaglio.

Negli urti di ioni pesanti ad energie ultra–relativistiche, la fissione puó essere dovuta sia a processi elettromagnetici che nucleari. Il primo meccanismo gioca un ruolo fondamentale nelle collisioni ad alto parametro di impatto (maggiore della somma dei raggi nucleari del bersaglio e del proiettile), mentre per parametri di impatto piú piccoli l'interazione é dominata da processi nucleari.

Le misure su vari nuclei bersaglio e a diverse energie possono permettere di separare questi due contributi a partire dalla sezione d'urto di fissione misurata sperimentalmente, dal momento che la dipendenza dall'energia incidente e dalla massa del proiettile (o del bersaglio) é diversa per i due meccanismi.

Nel Capitolo 6 saranno presentati i risultati ottenuti da questi dati e i contributi elettromagnetici alla sezione d'urto di fissione, estratti dai risultati sperimentali, saranno paragonati alle predizioni del modello di Weizsäcker–Williams. Secondo questo modello, l'interazione elettromagnetica tra due nuclei puó essere espressa in termini dell'interazione del nucleo proiettile con un fotone virtuale emesso dal nucleo bersaglio, che puó portare alla fissione del proiettile.

Provare la validitá della descrizione di Weizsäcker–Williams dei processi elettromagnetici é molto importante, dal momento che, alle energie dell'LHC, essi costituiranno il principale meccanismo di perdita dei fasci. In particolare, ci si aspetta che la sezione d'urto per la dissociazione elettromagnetica in interazioni Pb–Pb alle energie dell'LHC sia dell'ordine di 220 barn (e che perció rappresenti il contributo principale alla sezione d'urto totale). Quindi, una descrizione precisa delle interazioni elettromagnetiche é necessaria per dare una stima corretta della vita media dei fasci durante le operazioni con ioni pesanti ultra–relativistici e misurare la luminositá dei fasci. Anche se la fissione rappresenta solo una piccola percentuale dei processi EM ad energie ultra–relativistiche, essa é un utile strumento per provare la validitá del modello di Weizsäcker–Williams, che potrá essere poi applicato a tutti i processi EM.

Contents

Chapter 1

The Quark–Gluon Plasma and the ultra–relativistic heavy ions collisions physics

1.1 Introduction

In conditions of sufficiently high density and temperature, the short range forces between nucleons could be overcome and the compressed nucleons could merge into one another, producing a new state of matter.

The theory of strong interactions, the Quantum Chromodynamics (QCD), predicts that this new state should be a "deconfined" state of unbound quarks and gluons, the Quark–Gluon Plasma (QGP). The inverse transition, from QGP to ordinary hadronic matter, is believed to have occurred in the first instants of our Universe, about 10 μs after the Big–Bang, and to characterize today the evolution of the collapsing neutron stars [1].

Important information on the nature of the mechanisms responsible for the confinement of quarks in hadrons and for the spontaneous chiral symmetry breaking could be provided by the QGP study, together with cosmological and astrophysical issues.

The thermodynamic conditions necessary for the QGP formation are deduced from lattice QCD calculations: deconfinement could occur in a medium at a temperature of about $140 \div 180\ MeV$, hence for energy densities of $1 \div 3\ GeV/fm^3$ [2].

Experimentally these extreme conditions could be obtained in ultra–relativistic heavy ions collisions. Over the past 15 years, an extensive program of high energy nuclear collisions was carried out at the CERN SPS and at the BNL AGS in order to study the quark–gluon plasma formation in heavy ion collisions. CERN started the program with the acceleration of light ions (^{16}O and ^{32}S) at 200 GeV/nucleon on heavy targets; in 1994 the ^{208}Pb beam of 158 GeV/nucleon became available. At the AGS ^{28}Si beams of 15 GeV/nucleon were followed by ^{200}Au of 12 GeV/nucleon.

In February 2000, on the basis of the results coming from all the heavy–ion program experiments (NA44, NA45/CERES, NA49, NA50, NA52/NEWMASS, WA97/NA57 and WA98), CERN stated that "we now have a compelling evidence that a new state of matter has indeed been created... The new state of matter found... features many of the characteristics of the theoretically predicted quark–gluon plasma"

High energy heavy–ion physics is actually studied at the BNL RHIC, which started its experimental program in 2000, studying Au–Au collisions at center of mass energies 10 times higher than the SPS ones.

In the future, ultra–relavivistic heavy–ion physics will be studied at the CERN LHC at a centre–of–mass energy of 5.4 TeV/nucleon by means of the heavy-ion detector ALICE.

I am going to introduce in this chapter the basic elements of the QGP physics. After a brief description of the dynamics of the interactions among ultra–relativistic heavy ions, I am going to discuss the experimental "signatures" that allow to identify the plasma and, in particular, those studied by the NA50 experiment.

1.2 The phase transition: theoretical aspects

Quantum Chromodynamics (QCD), the fundamental theory of strong interactions, describes hadronic matter as an ensemble of quarks and anti–quarks confined inside hadrons and interacting through gluons exchange. Gluons own null mass and a colour charge, and are associated to the local colour symmetry $SU(3)_c$.

The interaction among two coloured particles is characterized by the coupling constant for strong interactions

$$\alpha_s(Q^2) = \frac{12\pi}{(33 - 2f) \cdot ln(\frac{Q^2}{\Lambda^2_{QCD}})} \tag{1.1}$$

where f is the number of flavours and $\Lambda_{QCD} \sim 200\,MeV$ is the scale of the QCD. The coupling constant increases with growing transferred momentum Q (inversely proportional to the distance between the constituent quarks $r \sim \frac{1}{Q}$). For this reason, in ordinary matter quarks are confined inside hadrons (infrared slavery). By contrast, at very short distances, quarks and gluons act as nearly free particles (asymptotic freedom).

At high energy density, i.e. at high temperature and/or high nuclear matter density, we can have a transition of ordinary matter toward a deconfinement phase, where gluons shield the colour forces among quarks, which can thus move freely. This phenomenon is analogous to the Debye screening of the Coulomb potential between two electric charges, which at sufficiently high density of negative charges becomes:

$$V(r) = \frac{e}{r} \longrightarrow \frac{e}{r}\, e^{-\frac{r}{r_d}} \tag{1.2}$$

where r is the distance between the two electric charges, $r_d \sim \frac{1}{\rho}$ is the Debye radius and ρ is the matter density. For high densities (low r_d values) the material turns from insulator into conductor.

Colour deconfinement is the QCD version of insulator–conductor transition studied in atomic physics. The colour potential among quarks in vacuum can be expressed by

$$V(r) = \sigma r - \frac{\alpha}{r} \tag{1.3}$$

with the long–range confining part of the strong interaction and a short–distance Coulombian part. r is the separation distance between quarks, σ is the string tension and α is the Coulomb coupling constant.

In a dense medium, the potential is screened by the presence of other colour charges and turns into

$$V(r) = \sigma r \; (\frac{1 - e^{-\mu r}}{\mu r}) - \frac{\alpha}{r}\; e^{-\mu r} \tag{1.4}$$

where $\mu(T) = \frac{1}{r_c}$ is the screening mass (inverse of the screening radius), which is related to the system temperature ($\mu \sim \sqrt{T}$).

In a deconfined medium the string tension σ is equal to zero, while the second term is weakened by the different density of quarks and gluons in the QGP, which implies:

$$V(r) = -\frac{\alpha}{r}\; e^{-\mu r} \tag{1.5}$$

where μ increases with T. The potential has a finite interaction range of the order of $r_c = \frac{1}{\mu}$. Therefore beyond a critical value of the system temperature, μ becomes so large that the screening radius r_c is negligible and the binding potential vanishes. The temperature predicted for this effect is $T_c \simeq 150 - 180\ MeV$ [3]. Hence, in presence of QGP, colour screening shortens the range of the force among quarks.

Quarks confined inside hadrons have a non–zero mass, due to their interaction with other quarks and gluons. In the QGP, the quark effective mass is reduced to zero and quarks assume their "bare" masses: $m_u \simeq 1 \div 5$ MeV, $m_d \simeq 3 \div 9$ MeV and $m_s \simeq 75 \div 170$ MeV [4]. The vanishing of the quark masses determine the chiral symmetry restoration [5] of the QCD Lagrangian:

$$\mathcal{L}_{QCD} = -\frac{1}{4} F^a_{\mu\nu} F^{\mu\nu}_a - \sum_f \overline{\Psi}^f_\alpha (i\gamma^\mu \delta_\mu + m_f - g\gamma^\mu A_\mu)^{\alpha\beta} \Psi^f_\beta \tag{1.6}$$

$\mathcal{L}_{QCD}$ satisfies many symmetry properties [6], but not the chiral symmetry, because the mass term $\overline{\Psi}\Psi$ is not invariant under the chiral rotation of the quark four–spinor

$$\Psi \;\rightarrow\; \Psi' = e^{i\alpha\gamma_5}\Psi \tag{1.7}$$

In a QGP environment, with small (in comparison with the $\Lambda_{QCD} \sim 200$ MeV scale of the QCD) and almost equal quark masses, a partial chiral symmetry restoration is expected [5]. From this, we can conclude that deconfinement, at least approximately, leads to chiral symmetry restoration.

In Fig. 1.1 one of the results of lattice QCD calculations is reported [7, 8, 9].

$< L > \sim e^{-\frac{V(\infty)}{T}}$, where $V(\infty)$ is the potential of a static quark–antiquark system at infinite mutual distance, gives an idea of the binding between q and $\overline{q}$: in a confined medium (low T) $V(\infty)$ diverges and therefore $< L >$ becomes negligible; the colour screening acting in deconfined matter (T $\geq$ 150 GeV in the picture) makes

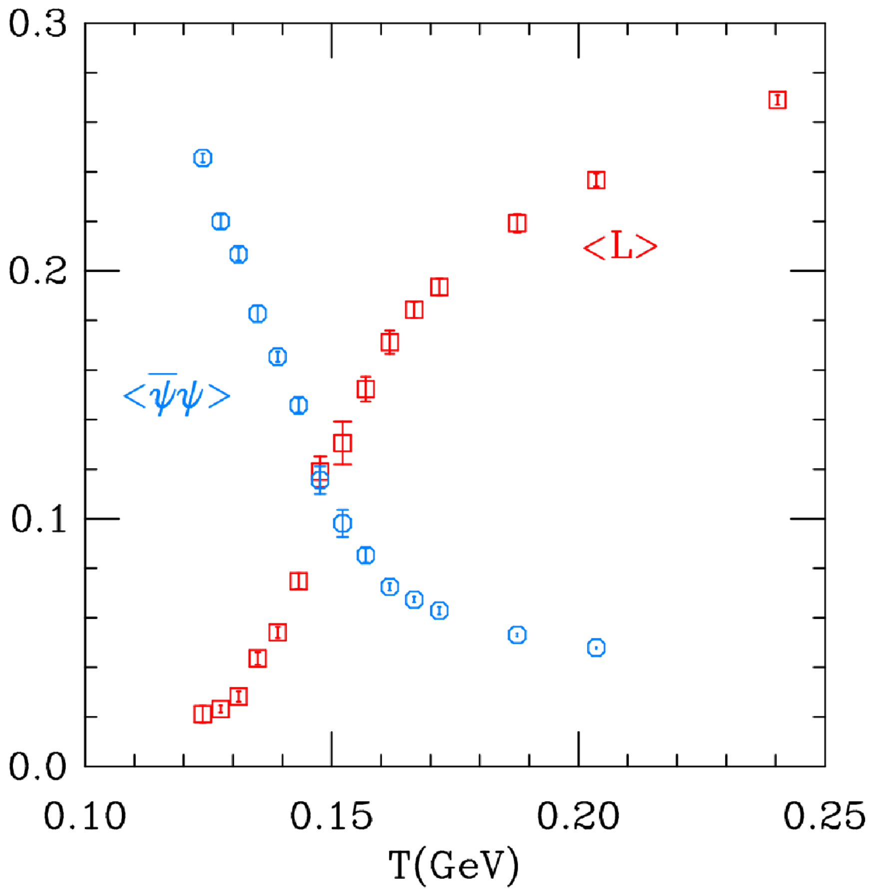

Figure 1.1: *Deconfinement and chiral symmetry restoration in two–flavours QCD [10].*

$V(\infty)$ and hence also $< L >$ finite.

The transition from ordinary hadronic matter to QGP for $< L >$ coincides with the decreasing of the effective quark mass, represented by $< \Psi\overline{\Psi} >$, up to the negligible value of the u and d "bare" masses (these calculations are performed in two–flavour QCD [10]). Therefore in a plasma of quarks and gluons the chiral symmetry is partially restored.

1.3 Creation and evolution of QGP

The way on Earth to reach the energy densities needed for the QGP formation, is through ultra–relativistic heavy ions collisions.

This is or will be realized by different accelerators, whose characteristics are reported in Table 1.1.

Site	Accelerator	Type	Start	p (AGeV/c)	beam	$\sqrt{s}$ (GeV/A)
BNL	AGS	fixed target	1986	14.5	Si	5.4
			1992	1.8–11.5	Au	2.3–4.8
CERN	SPS	fixed target	1986	200	S,O	19
			1994	158	Pb	17
BNL	RHIC	collider	2000	30–100	Au	60–200
CERN	LHC	collider	2007	2700	Pb	5400

Table 1.1: *Table of different accelerators of ultra–relativistic heavy ions and of their characteristics: p is the momentum of a nucleon inside a nucleus (in the laboratory frame), $\sqrt{s}$ is the energy per nucleon in the centre–of–mass frame of the nucleus–nucleus collision.*

1.3.1 Conditions for plasma formation

The plasma of deconfined quarks and gluons requires, to be produced, particularly high energy densities and temperatures. Lattice QCD calculations give values for the transition temperature between 150 and 180 MeV [2, 3] and energy densities of about 1 GeV/fm^3 (seven times that of ordinary nuclear matter) and to a density of about $(5 \div 10)\rho_o$, where $\rho_o = 0.17$ nucleons/fm^3 is the density of nuclear matter in normal conditions.

In order to describe ultra–relativistic heavy ions collisions by means of methods and theories typical of thermodynamics, the following requests must be satisfied.

- The volume of the created system must be "large": its dimensions must be bigger than 1 fm (which is the order of magnitude of the strong interactions) and, inside it, a "high" enough number of participant nucleons must be involved.

- The number of collisions among particles has to be "high" in order to guarantee the equilibrium achievement. For this purpose, the system lifetime must be greater than 1 fm/c.
- The beam energy must allow to reach the critical energy density for the phase transition, at least in the most central collisions.

More favorable conditions for the QGP formation are obtained in collisions at low impact parameter [1], where a big amount of energy is involved, since almost all the nucleons of the two colliding nuclei interact ("participant" nucleons). By contrast, in peripheral collisions most of the nucleons are "spectators", which do not take part in the interaction and continue along their original direction with modest perturbation.

1.3.2 Ultra–relativistic heavy–ion collisions: the Bjorken model

The ions used for the QGP search are ultra–relativistic objects, hence they are strongly subjected to the Lorentz contraction, as shown in Fig. 1.2 (the contraction factor is about 10 at 200 GeV/c per nucleon).

According to the Bjorken calculations [11], at ultra–relativistic energies, ions are partially transparent and they cross each other mutually. Immediately after the collision, we can distinguish two so–called "fragmentation" regions, one corresponding to the target, the other one to the projectile (Fig. 1.2).

These two regions surround a central rapidity [2] region, very excited, where many of the particles produced in the collision (basically mesons) are emitted from. It is inside this region that the plasma of quarks and gluons can more likely appear.

The space–time evolution of the collision has been studied by Bjorken [11]. This description makes use of an hydrodynamic model with the following assumptions:

- the energy of the collision is high enough to generate a "plateau" in the rapidity distribution of the produced particles in the "central rapidity" region: $\frac{dN}{dy} = constant$;

[1] The impact parameter b is defined as the minimum distance between the two colliding nuclei.

[2] For a given particle, the rapidity y is defined by

$$y = \frac{1}{2} ln(\frac{E + p_z}{E - p_z}) \tag{1.8}$$

where E is the total energy of the particle and p_z is its longitudinal momentum. This kinematic variable allows to estimate the longitudinal evolution of the particle motion after the collision. This variable is additive for Lorentz transformations.
If the particle mass is negligible with respect to its total energy, we use the pseudo–rapidity:

$$\eta = -\frac{1}{2} ln(tg\frac{\theta}{2}) \tag{1.9}$$

which needs the measure of only a variable, the emission angle θ with respect to the beam axis.

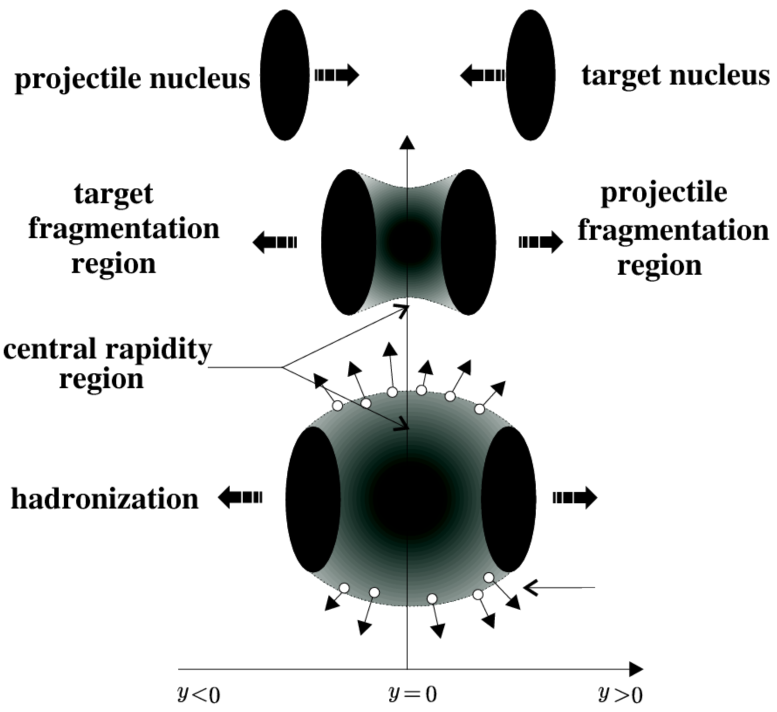

Figure 1.2: *Schematic representation of a ultra–relativistic nucleus–nucleus collision, in the center–of–mass frame as a function of rapidity.*

- the baryonic number is zero in this "central rapidity" region, i.e. the totality of baryonic number is concentrated in the "fragmentation" regions.

According to the Bjorken model, the initial energy density released during the collision is estimated by [11]:

$$\epsilon_{Bj} = \frac{1}{S_{\perp}\tau_o}\left(\frac{dE_T}{dy}\right)_{y=0} \tag{1.10}$$

where $S_{\perp}$ is the transverse intersecting area of the two nuclei in the collision, $\tau_o \approx 1$ fm/c is the proper time of the plasma formation, $(\frac{dE_T}{dy})_{y=0}$ is the total transverse energy (see Chapter 2) of the particles produced per rapidity unit around $y_{cm} = 0$. The energy density, estimated in this way, for central Pb–Pb collisions at 158 AGeV/c is 3.2 $\pm$ 0.3 GeV/fm^3 [12]. This value is comparable to the one determined by QCD calculations for the plasma existence conditions [2]. A compatible result is reported in [13].

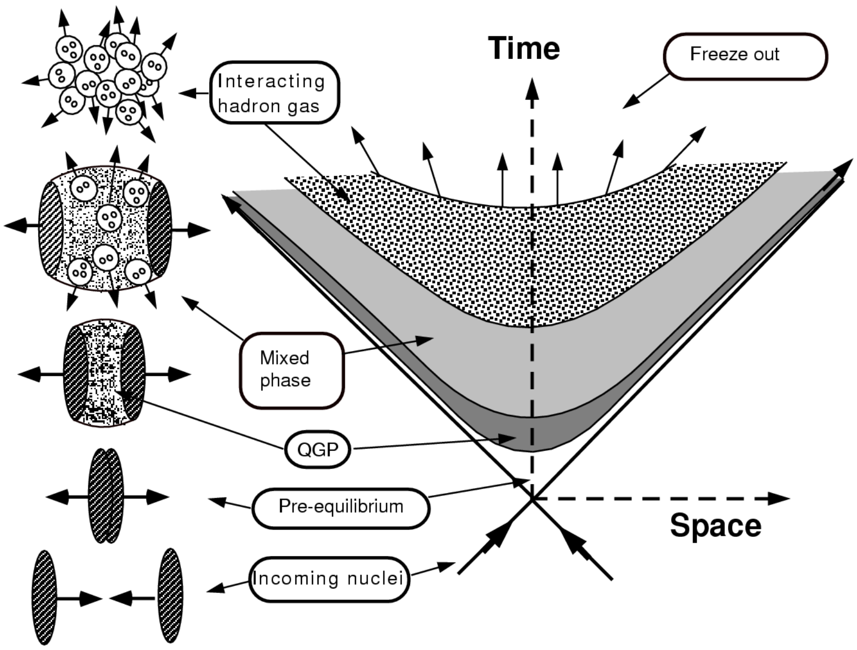

Figure 1.3: *Space–time diagram for a central nucleus–nucleus collision according to the Bjorken model [11].*

1.3.3 Plasma evolution

If the experimental conditions guarantee the phase transition, the evolution of a central nucleus–nucleus collision is described by the space–time diagram of Fig. 1.3, according to the model proposed by Bjorken [11]. The collision occur at t=0, z=0 in the center–of–mass frame and we limit only to the longitudinal expansion of the system. Starting from the instant when the two nuclei collide, the collision evolves through the following steps [14].

1. In the first instants ($\tau \leq 1\, fm/c$) a lot of collisions among partons give rise of a big number of quarks and gluons.

2. This gas of quarks and gluons evolves to the point of thermodynamic equilibrium: this is the QGP phase (its duration is estimated to be of the order of some fm/c).

3. In the "mixed" phase the system expands, because of the high plasma pressure, with the consequent temperature drop: some quarks combine again and form hadrons. Plasma of quarks and gluons and hadronic gas coexist in this phase, which last about 10 fm/c.

4. As the temperature decreases, the hadron formation prevails once more (phase of interacting hadronic gas).

5. At the "freezout" point hadrons decouple and, as free particles, leave the collision region ($\tau \sim 20$–30 fm/c).

1.4 QGP signatures

Even if the QGP is produced in a laboratory experiment, its positive identification is difficult because of its very short lifetime (of some $10^{-23}s$).

It would be interesting to directly access to the thermodynamic variables of the system during the collision, but this is experimentally impossible. Hence we must turn to indirect measurements of QGP formation.

A clear signature of the transition from ordinary matter to a deconfined medium must allow to establish if the medium is deconfined or not. Furthermore it must be present in the early phase of the transition and keep unvaried throughout the system evolution, until its detection.

Many probes have been proposed to provide information about different stages of the QGP evolution [15, 16]:

- soft probes, related to signals produced in physical processes with small momentum transfer (soft processes). They appear when the density of the medium has dropped enough to allow the existence of hadrons, that is in the hadronic final state of the system evolution. Nevertheless they can also provide indirect information on the earlier (deconfined) stages of the collision. Among the proposed soft probes there are the enhancement of the strange particle production [17, 18], the transverse momentum broadening and flow, and the in–medium modifications of the resonance properties (mass and/or width) observable in their dilepton decays [19, 20].

- hard probes, which are created early in the collision, during hard processes, so that the associated length scale is much less than the confinement scale $\Lambda_{QCD}^{-1} \sim 1\ fm$. These probes can be used to study directly the short distance features of a hot deconfined medium and to probe the very early stage of the collision. They include hard thermal photons and dileptons [21, 22], whose spectrum should serve as a thermometer of the thermal medium that has emitted them, charmonium suppression [23], due to the colour screening in a deconfined medium, and jet quenching [24, 25].

A brief summary of these probes, in particular of those studied by the NA50 experiment, is reported in the following sections.

1.4.1 Strangeness enhancement

The increase of the strange particles production was proposed in 1982 [17] as a possible signature of QGP formation.

In a QGP environment, the production of a $s\bar{s}$ couple requires only $2m_s c^2 \sim$ 300 MeV of energy, which corresponds to the "bare" mass owned by quarks when the chiral symmetry is restored.

By contrast, in a hadron gas the strangeness production threshold for the reactions

$$\pi + \pi \to K\overline{K} \qquad p + p \to p + \Lambda + K^+ \tag{1.11}$$

is about 700 MeV. Therefore the production of s quarks is energetically favorite in the QGP through the processes:

$$gg \;\to\; s\bar{s} \quad \sim 90\% \text{ of cases} \tag{1.12}$$

$$q\bar{q} \;\to\; s\bar{s} \tag{1.13}$$

The first process is more likely and quicker in a plasma of quarks and gluons, thanks to the great abundance of gluons.

The experiment WA97/NA57 [26, 27, 28] studies the production of the strange baryons $\Lambda(uds)$, $\overline{\Lambda}(\overline{u}\overline{d}\overline{s})$, $\Xi^-(dss)$, $\overline{\Xi}^+(\bar{d}\bar{s}\bar{s})$, $\Omega^-(sss)$ and $\overline{\Omega}^+(\bar{s}\bar{s}\bar{s})$ in p–A and Pb–Pb collisions at the CERN SPS.

From Fig. 1.4 it emerges that the enhancement in the production of these particles is more pronounced if they contain more than one strange quark. Actually in a

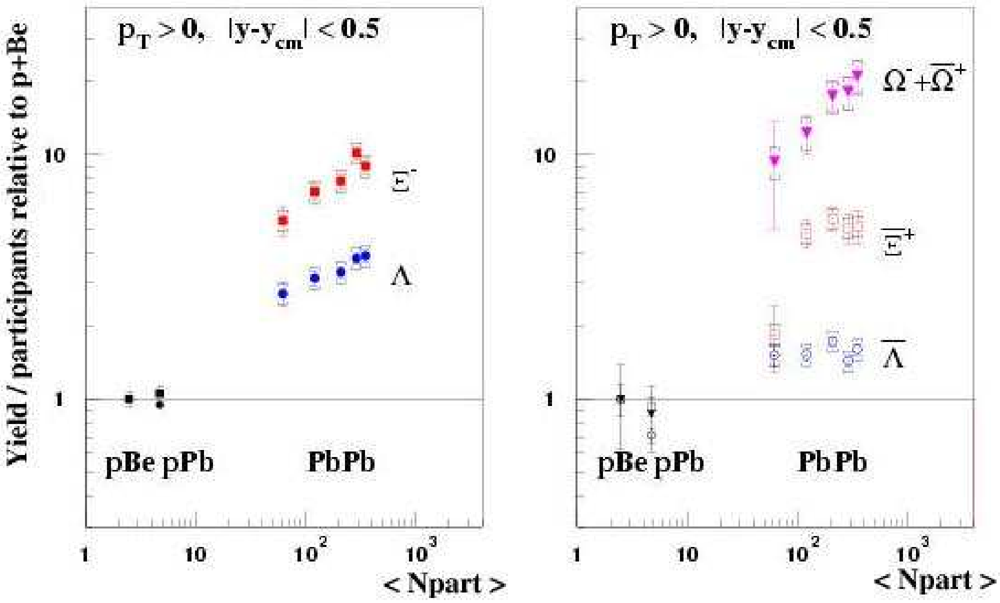

Figure 1.4: *Yields of produced baryons and anti–baryons as a function of the number of participants, normalized to p–Be results (WA97/NA57).*

deconfined medium with a strangeness content enhanced by a factor E_s, hadrons containing N strange quarks should be enhanced by a factor E_s^N, explaining the enhancement hierarchy $E_{\Omega(s=3)} > E_{\Xi(s=2)} > E_{\Lambda(s=1)}$. As it can be seen in Fig. 1.4, the experimental results show that the expected hierarchy, which is the opposite of what should happen in absence of deconfinement, is indeed observed at the SPS. The production of strange baryons has increased up to 10 times and more, in comparison to the rates measured in p–p collisions.

An other way to obtain an evidence of the strangeness enhancement is to study the ratios $< K > / < \pi >$ or $E_S = (< \Lambda > + < K + \overline{K} >)/ < \pi >$. Results from the SIS (GSI), the AGS (BNL) and the SPS (CERN) show that these ratios increase as a function of the number of charged particles produced in nucleon–nucleon collisions and as a function of the centrality in nucleus–nucleus collisions. Furthermore these ratios regularly increase with the beam energy for nucleon–nucleon collisions [29, 30], while they lose this monotonic behaviour for nucleus–nucleus collisions at energies larger than the AGS one (Fig. 1.5)

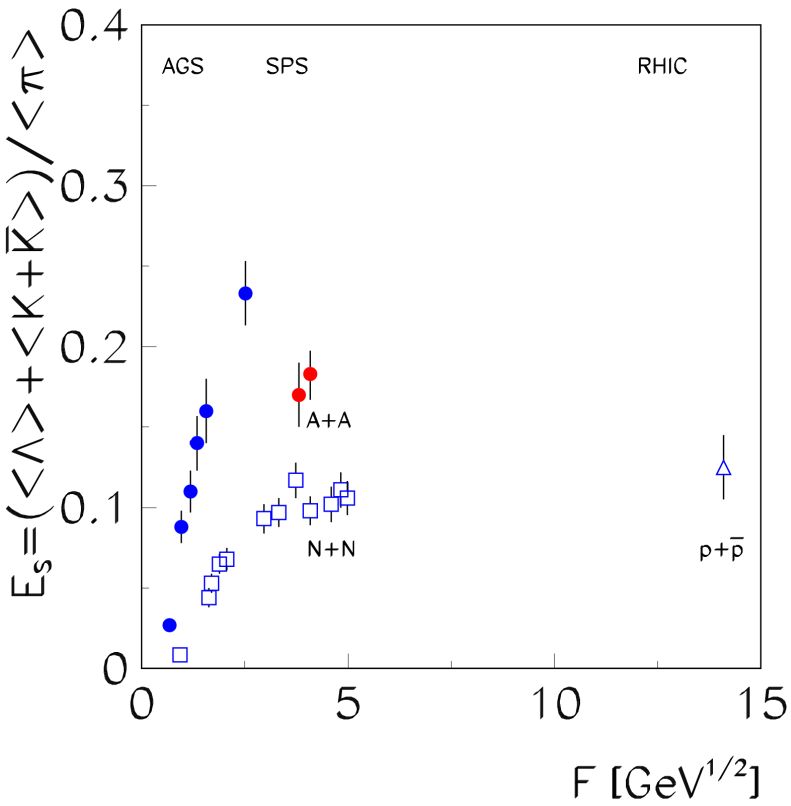

Figure 1.5: E_S *as a function of the beam energy* $F \approx s^{1/4}$ *for nucleon–nucleon and nucleus–nucleus collisions.*

The increasing yield of the $\phi(s\overline{s})$ production with respect to that of ρ and ω

(which are $u\overline{u}$ and $d\overline{d}$ combinations and keep unaffected in a deconfined medium) was proposed in 1985 [31, 32] as a signature of QGP formation. The NA50 experiment has studied the ϕ, ρ and ω production in p–A, d–U, S–U and Pb–Pb collisions, since the ratio $\phi/(\rho+\omega)$ can provide information on the ratio $s\overline{s}/(u\overline{u}+d\overline{d})$ [33, 34].

The measured ratios $\frac{\Phi}{\rho+\omega}$ for Pb–Pb collisions at 158 AGeV/c is reported in Fig. 1.6 as a function of the number of participant nucleons. These ratios are evaluated for invariant masses $1.5 \leq M_T \leq 3.2$ GeV/c^2 in the $\mu^+\mu^-$ channel [35, 36]. A 10% systematic uncertainty has to be added to the statistical errors plotted in the figure. The ratio exhibits a 70% increase when going from the most peripheral to the most central collisions and flattens for $N_{part} \geq 250$.

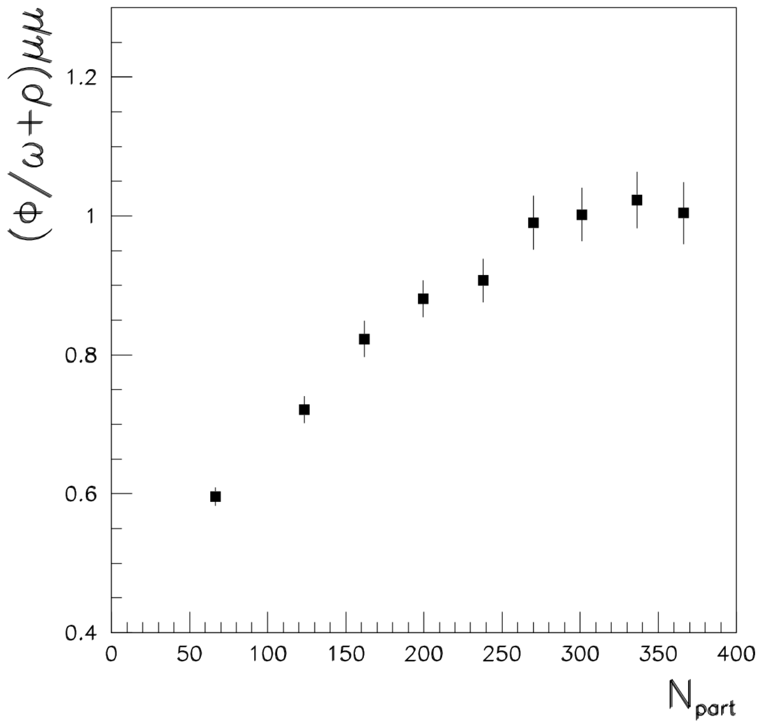

Figure 1.6: *The* $(\frac{\Phi}{\rho+\omega})_{\mu^+\mu^-}$ *ratio as a function of the number of participant nucleons* N_{part}*, in the domain* $M_T \geq 1.5$ *GeV/*c^2*.*

1.4.2 Thermal photons and dileptons

Photons and dileptons are interesting signals to study the dynamics of ultra–relativistic heavy ion collisions. They are abundantly produced in the early stages of the collisions, when temperature and density reach their highest values.

Due to their large mean free path, dimuons, which interact only electromagnetically, can leave the collision region without perturbation and they can preserve information about the properties and the conditions of the matter where they have been produced.

The interesting point is to identify the thermal dilepton radiations emitted when the system has come to the equilibrium. They can provide indications about the QGP or the hadronic gas phase. The involved elementary processes are the $\pi^+\pi^-$ annihilation in the hadron gas (this contributes to the mass spectrum with the $\rho \rightarrow \pi^+\pi^-$ peak) and the $q\overline{q}$ annihilation in the QGP phase. This second contribution is shifted toward the low masses, below the ρ region, as indication of the chiral symmetry restoration [37].

The dilepton mass spectrum is usually divided into tree regions:

- the low mass region (LMR from the threshold $2m_\mu$ to 1.5 GeV/c^2), which has a complex structure, resulting from many resonances decays, above which the ϕ and $\rho + \omega$ peaks emerge;

- the intermediate mass region (IMR about $1.5 < M < 2.5$ GeV/c^2), which is characterized by the continuum between the ϕ and the J/ψ peaks, and includes contributions from Drell–Yan and from decays of charmed mesons (D and $\overline{D}$);

- the high mass region (HMR), starting from 2.5 GeV/c^2, where the J/ψ and the ψ' resonances are visible on the Drell–Yan continuum generated by the reaction $q\overline{q} \rightarrow \gamma^* \rightarrow \mu^+\mu^-$.

Low mass dielectrons have been extensively studied by the CERES/NA45 collaboration [38]. The mass spectrum of dielectrons produced in p–A collisions is fairly well accounted for by the expected sources in the LMR: the ρ, ω and Φ resonances and the light meson Dalitz decays. In S–Au [39] and Pb–Au [40, 41] collisions, a significant enhancement of electron pairs is observed for masses lower than the ρ mass. This enhancement amounts to about a factor 3, with respect to the contributions expected from p–A collisions.

The NA38/NA50 experiment has dealt with muon pairs produced in the LMR during p–U collisions, in the restricted region $P_T > 1$ GeV/c. An increase of 40%, in comparison with the expectations, has been observed in the invariant mass region below the ρ and ω resonances. By extending the $q\bar{q}$ annihilations to low masses, the p–U mass distribution is well reproduced. This does not mean that there is not compatibility with the CERES results, since the NA38/NA50 results refer only to high momentum muon pairs and the $q\bar{q}$ annihilations are important only in this p_T region.

The NA38 and NA50 experiments have studied also the dimuons produced in the IMR, where the HELIOS3 experiment has already observed a dimuon excess in S–W collisions [42]. In the IMR, after the combinatorial background subtraction, the dimuons are mainly due to Drell–Yan annihilations and to semi–leptonic decays of two simultaneous D and $\overline{D}$ mesons. The p–A data are perfectly reproduced by the superposition of these two contributions [43, 44]. By contrast, the number of dimuons produced in Pb–Pb collisions is clearly underestimated by the previous superposition, extrapolated from proton induced reactions [45, 46]. This excess of dimuons in Pb–Pb grows as a function of the number of participants.

The study of direct (not virtual) photons is one of the first signatures proposed to identify the formation of the QGP [21]. In a plasma of quarks and gluons, the direct photons are produced through Compton scattering, $q\bar{q}$ annihilation ($q\bar{q} \rightarrow g\gamma$) and bremsstrahlung ($gq(\bar{q}) \rightarrow \gamma q(\bar{q})$). Since their interaction length is much bigger than the colliding system size (unlike hadrons), they can carry information about their source for the whole duration of the collision.

The direct photons were the subject of intensive experimental studies at the CERN SPS, by the WA80 experiment [47] in collisions with O and S beams and then by the WA98 experiment [48] with Pb beams. WA80 has not observed remarkable excesses of the photon production rate, with respect to the background due to π° and η decays. Instead, for central Pb–Pb collisions, an excess of 10% has been observed for transverse momenta greater than 1.5 GeV/c, in comparison with p–A collisions. This result seems to imply a different process of photon production in nucleus–nucleus collisions, compared to proton–nucleus systems.

1.4.3 Charmonium suppression

Sixteen years ago, T. Matsui and H. Satz [23] proposed the J/ψ suppression in nuclear collisions as an unambiguous and experimentally accessible probe of quark–gluon plasma formation.

The J/ψ meson is a bound state of a charm quark c and its antiquark $\bar{c}$ in a colour–singlet state with angular momentum quantum numbers 1^3S_1 . The J/ψ is the lowest mass resonance among the charmonium states, reported in Table 1.2 together with their main decay modes. For the J/ψ there is a huge indirect contribution from the decays of excited charmonium states. In hadronic collisions about 32% of the measured J/ψs originates from χ_c decays into J/ψ, while about 8% comes from ψ' decays. Only 60% are directly produced J/ψs [7, 49, 50].

If high energy heavy ion collisions lead to the formation of a hot quark–gluon plasma, then colour screening dissolves the binding energy between the c and the $\bar{c}$ quarks that form the J/ψ mesons. Thus, in a deconfined environment, the J/ψ constituents separate and, during the hadronization phase, they combine with light quarks to form a D and a $\overline{D}$ instead of a J/ψ.

The J/ψ suppression in nuclear collisions indeed represents one of the clearly observable signatures of plasma formation, thanks also to the relatively easy experimental detection of the J/ψ in its leptonic decay into $\mu^+\mu^-$. In fact, muons are not affected by strong interactions and therefore bring to the detectors an undistorted image of the earliest stages of the collision. Since the J/ψs are created in the first instants of the collision, when the energy available is higher, and they retain

Resonance	Mass (MeV)	Full width (MeV)	Decays	Branching ratios (%)
$J/\psi(1\,^3S_1)$	3096.87 ± 0.04	0.087 ± 0.005	hadrons	87.7 ± 0.5
			e^+e^-	5.93 ± 0.10
			$\mu^+\mu^-$	5.88 ± 0.10
$\psi'(2\,^3S_1)$	3685.96 ± 0.09	0.300 ± 0.025	hadrons	98.10 ± 0.30
			e^+e^-	0.73 ± 0.04
			$\mu^+\mu^-$	0.70 ± 0.09
			J/ψ+X	55.7 ± 2.6
$\chi_{c0}(1\,^3P_0)$	3415.0 ± 0.8	14.9 ± 2.6	$J/\psi+\gamma$	0.66 ± 0.18
$\chi_{c1}(1\,^3P_1)$	3510.51 ± 0.12	0.92 ± 0.13	$J/\psi+\gamma$	31.6 ± 3.2
$\chi_{c2}(1\,^3P_2)$	3556.18 ± 0.13	2.08 ± 0.17	$J/\psi+\gamma$	18.7 ± 2.0

Table 1.2: Characteristics of the charmonium bound states and their main decay modes [4]. The quantum numbers are given in the form $n^{2S+1}L_J$ where n is the radial quantum number and S, L and J define respectively spin, orbital and total angular momentum.

memory of their origin, they make it possible to investigate the initial conditions of the colliding matter.

In Sec. 1.5 and 1.6 I will discuss more in details the characteristics of the J/ψ production and suppression.

1.5 Charmonium production

The charmonium production in high energy nucleon–nucleon collisions begins with the creation of a $c\bar{c}$ pair, due to the fusion of a target and a projectile gluon or to the annihilation of a quark with a sea anti–quark [7], as shown in Fig. 1.7.

Because of the high mass of the charm quark, this process requires a very short time, of the order of 0.07 fm ($\tau_\circ \simeq \frac{1}{2m_c}$ where $m_c = 1500\ MeV/c^2$ is the charm mass) [51]. The created $c\bar{c}$ is in general in a colour octet state and has a small relative momentum (if it is much larger than $m_c v$ the c and the $\bar{c}$ will unlikely bind and will instead fly apart and form D and $\overline{D}$ mesons).

The second step of the charmonium production consists in the colour neutralization of the $c\bar{c}$ colour octet state by emission or absorption of gluons to produce a physical resonance, such as J/ψ, ψ' or χ_c. Different models have been proposed to explain this process [52]. The colour singlet model [53, 54, 55, 56] is based on a perturbative treatment of this colour neutralization but it has been ruled out by high energy results from the FNAL experiment [57]. According to this model, the charmonium states are considered as non–relativistic bound states of a c and a $\bar{c}$

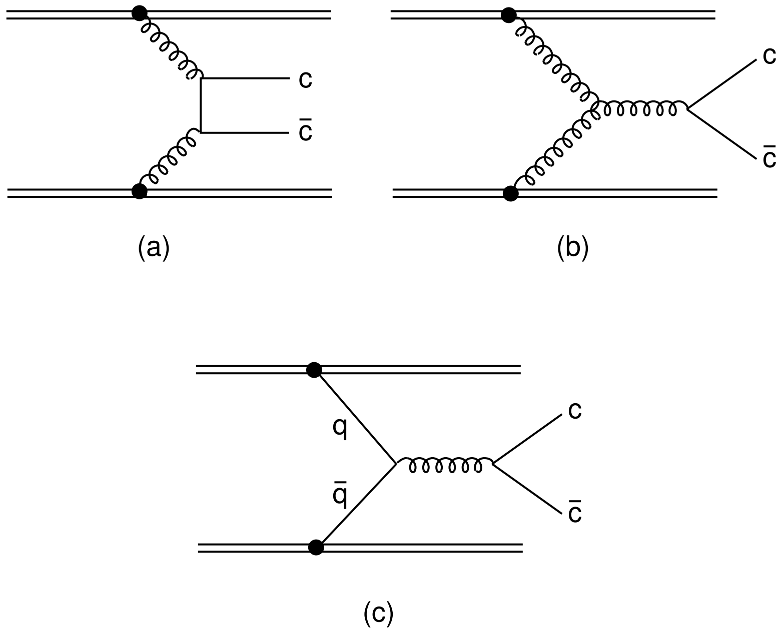

Figure 1.7: *Diagrams (at the lowest order) of the $c\bar{c}$ production in hadronic collisions: through gluon fusion (a e b) and $q\bar{q}$ annihilation (c).*

through a confining potential. This model assumes that a $c\bar{c}$ pair produced in high energy collisions can bind to form a charmonium state only if it has been created in a colour–singlet state with the angular momentum quantum numbers that match those of the bound state. For example, in order to form a J/ψ, the $c\bar{c}$ pair must be produced in a colour–singlet $^3S_1$ state.

The CDF collaboration at the Tevatron $p\bar{p}$ collider found out that the cross–sections for the direct J/ψ and ψ' production at large transverse momentum were larger than the prediction of the colour singlet model by about a factor of 30 [57, 58]. This put an end to the colour singlet model, now replaced by the colour octet formalism [51, 59]. This model describes the J/ψ (like every meson) as the superposition of several states in the Fock space:

$$|J/\psi >= a_0|(c\overline{c})_1 > +a_1|(c\overline{c})_8 g > +a_2|(c\overline{c})_1 gg > +a_2'|(c\overline{c})_8 gg > +... \tag{1.14}$$

i.e. a pure $c\bar{c}$ colour singlet component ($^3S_1$), a $c\bar{c}$ colour octet ($^1S_0$ or ^3P_J) plus a gluon, and so on.

Analogous Fock space decompositions hold for the other charmonium states [51, 59]. In all cases, the first higher state consists of a colour octet $c\bar{c}$ plus a gluon. For the ψ', the next–to–leading terms again contain a colour octet (^3P_J or $^1S_0$) plus a gluon; for the χ a $^3S_1$ colour octet $c\bar{c}$ is combined with a gluon.

In most mesons $a_0 \gg a_1 \gg a_2, a_2'$ and the colour singlet $(c\overline{c})_1$ becomes the dominant term, while in the J/ψ production at high energy the second term prevails.

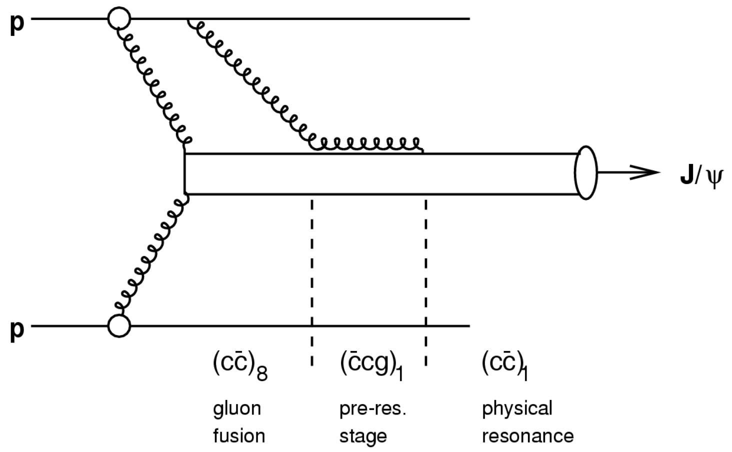

Figure 1.8: *The J/ψ production in p–p collisions.*

The $(c\bar{c})_8$ crosses the nuclear matter together with an additional collinear gluon that neutralizes its colour (Fig. 1.8). This pre–resonant charmonium state $c\bar{c}g$ can either be absorbed by the surrounding matter or, after a "relaxation time" $\tau_8 \simeq (2m_c\Lambda_{QCD})^{-1/2} \simeq 0.3\ fm$, the $(c\bar{c})_8$ can absorb the accompanying gluon thus becoming a colour singlet $(c\bar{c})_1$ and subsequently a J/ψ meson.

We have only considered those $c\bar{c}$ pairs that will later on form charmonia, but the $(c\bar{c})_8$ could as well neutralize its colour by combining with a light quark–antiquark pair, resulting in open charm production.

1.6 Charmonium dissociation

The suppression of the J/ψ yield in ultra–relativistic heavy–ion collisions is a possible signature for the formation of the quark–gluon plasma because the J/ψ should dissolve in the QGP, due to the colour screening, as discussed in section 1.2. This suggestion has stimulated the experimental research to measure the J/ψ production in the heavy–ion collisions and various theoretical models have been proposed to interpret the experimental results.

Once the $c\bar{c}$ pair is produced, it may be absorbed by nucleons in the target [60] and/or interact with secondary particles produced in the collision and comoving with the pair, the so–called "comovers" [61, 62].

In a deconfined medium an "anomalous" suppression is observed [63, 64], which cannot be explained only by the previously cited mechanisms. The charmonium suppression due to colour deconfinement was already predicted by [23]. To verify this prediction, one has to exclude what are generally called "conventional" mechanisms, covering all the possible ways to suppress the J/ψ production without invoking deconfinement. Together with the absorption in nuclear matter and by hadronic comovers mentioned above, other possible sources of the J/ψ suppression can be the nuclear shadowing of the parton distribution functions [65], the medium–induced energy loss of the incident partons leading to the $c\bar{c}$ production [66] or, more in general, the in–medium modifications of the $c\bar{c}$ production process [67]. In a realistic model of the J/ψ production in p–A and A–B collisions, all these effects should be included. For a complete review see [68, 69].

In the following sections, I will focus on the nuclear absorption, the comover scattering and the charmonium dissociation by deconfined media.

1.6.1 Nuclear absorption

In section 1.5 we have seen that the J/ψ production passes through the three–step process $gg(q\bar{q}) \to (c\bar{c})_8 \to (c\bar{c})_1 g \to J/\psi$. The pre–resonant state $(c\bar{c})_1 g$ takes a time $\tau_8 \simeq 0.3\ fm$ to convert to a fully formed J/ψ, by absorbing the collinear gluon. It may happen that this pre–meson state interacts with the nucleons of the target and of the projectile and it is absorbed before becoming a physical resonance. This nuclear absorption is taken into account by all the models proposed to explain the J/ψ suppression in collisions from p–A to A–B. In p–A collisions this pre–resonance absorption allows to completely understand the experimental results, while in A–B collisions other additional mechanisms are required [70, 71].

The cross–section for the nuclear absorption of the $c\bar{c}g$ state in nuclear matter can be theoretically estimated [72], but also derived from experimental p–A data, as I will explain in section 1.8. In A–B collisions, the probability that a $c\bar{c}$ pair survives the interactions with the nuclear matter is the product of the survival probabilities for interactions with the target and the projectile nucleons [7, 71]

$$S^{abs}_{J/\psi}(b) \sim exp\left\{-\int_{z_A}^{\infty} dz \rho_A(z) \sigma^{abs}_{J/\psi-N} \int_{z_B}^{\infty} dz \rho_B(z) \sigma^{abs}_{J/\psi-N}\right\} \tag{1.15}$$

where ρ is the nuclear density, b the impact parameter and $\sigma^{abs}_{J/\psi-N}$ is the absorption cross–section for the J/ψ-nucleon interactions. Here z_A represents the formation point of the pre-resonance within the projectile nucleus A, z_B within the target nucleus B. Note that $S^{abs}_{J/\psi}$=1 for $\sigma^{abs}_{J/\psi-N}$=0. In p–A collision only the first probability is considered.

Since the J/ψ travels through the surrounding nucleons, an appropriate variable to parametrize the measured J/ψ yield is the number of nucleons which the J/ψ can potentially interact with. This number can be calculated as the product ρL, where ρ is the average nuclear density and L is the mean length of nuclear matter crossed by the $c\bar{c}$ pair, while escaping from the interaction region [73]. As a first approximation, the charmonium survival probability can be parametrized as $exp(-\rho\sigma_{abs}L)$ [74].

In section 1.8 I will deal with the experimental results from the NA38 and NA50 experiments for p–p, p–A and A–B collisions. In these experiments the produced J/ψs have momenta of the order of 50 GeV/c or more (in the target rest frame).

Therefore, the transition $c\bar{c}g \rightarrow J/\psi,\ \psi'$ or χ_c occurs outside the target nucleus and the nuclear medium sees only the passage of the pre–resonance states, which have nearly the same life–time and size for all the charmonium states. Hence the same amount of suppression is expected for $J/\psi,\ \psi'$ and χ_c.

1.6.2 Charmonium absorption by hadronic comovers

In nucleon–nucleon collisions the hadrons produced along with the $c\bar{c}$ pair are called "comovers". These comoving secondaries, formed after $\tau \sim 1-2\ fm$ (greater than the typical formation time of the J/ψ, $\tau_8 \sim 0.3\ fm$) from the collision time, can scatter with the final charmonium state and destroy it, via the inelastic reaction

$$J/\psi + h \rightarrow D\overline{D} + X \tag{1.16}$$

This produces an additional suppression of the produced J/ψ, which was studied to explain the experimental J/ψ suppression without requiring deconfinement [69, 75, 76, 77].

The probability that the J/ψ survives an interaction with comovers is [61]:

$$S^{com}_{J/\psi} \sim exp\left\{-\int d\tau < \sigma_{J/\psi-com} \cdot v > \rho_{com}(\tau)\right\} \tag{1.17}$$

where $\rho_{com}(\tau)$ is the comover density at time τ, $\sigma_{J/\psi-com}$ is the J/ψ absorption cross–section in the comover medium and $v \sim 0.6$ is the J/ψ velocity relative to the comovers. Note that, if $\sigma_{J/\psi-com} = 0$, the survival probability $S^{com}_{J/\psi}$ becomes equal to 1. The product $\sigma_{J/\psi-com} \cdot v$ is averaged over all the possible comovers [3] and their relative energy [69]. $\sigma_{J/\psi-com}$ is treated as an adjustable parameter by different models, which include also the nuclear absorption [69]. In these calculations the values found for $\sigma_{J/\psi-com}$ range from 0.4 mb to 3 mb . All these different approaches [78, 79, 80, 81] lead to a monotonic increase of the J/ψ suppression with increasing centrality and comover density. This can reproduce the J/ψ suppression observed in data from p–A to central S–U collisions, where no deconfinement is expected, but fails in the description of central Pb–Pb data [82].

1.6.3 Charmonium dissociation in Quark–Gluon Plasma

The basic mechanism for the deconfinement in dense matter is the Debye screening of the quark colour charge [83], as already seen in section 1.2. If a charmonium state is placed into a hot medium of deconfined quarks and gluons, colour screening will dissolve the binding between the c and the $\bar{c}$ quarks. Actually, because of the large

[3]The composition of the comoving hadrons for central Pb–Pb collisions is: π (37%), ρ(42%), ω (13%) and η (8%).

mass of the charm quarks, the charmonium states in vacuum can be described by the Schrödinger equation [84]:

$$[2m_c + \frac{1}{m_c}\nabla^2 + V(r)]\Psi_{n,l} = M_{n,l}\Psi_{n,l} \tag{1.18}$$

where the potential is given by Eq. 1.3 and (n,l) are the quantum numbers of the different charmonium states (J/ψ, χ, ψ'). In a dense medium the binding forces between the quarks inside hadrons are screened by the presence of other colour charges, which shorten the range of the potential (Eq. 1.4). If the medium is deconfined, the potential is given by Eq. 1.5 and has a finite interaction range of the order of $r_c = \frac{1}{\mu}$, where μ is the screening mass ($\mu \sim \sqrt{T}$). Once μ becomes sufficiently large (with the increase of the temperature), the bound states start to disappear and only separated c and $\bar{c}$ are present. For each bound state, there is a critical screening mass μ_c above which that state dissociates. In Table 1.3 the μ_c values (determined by finite temperature lattice QCD) for the most important charmonium states are summarized, together with the Debye critical temperatures and the energy densities [71]. Also the binding energies are reported, calculated as the energy difference between the charmonium mass and the open charm threshold.

State	μ_c (GeV)	T_D	ϵ_D	ΔE (GeV)
J/ψ	0.68	$1.2T_c$	$2\epsilon_c$	0.64
ψ'	0.35	T_c	ϵ_c	0.06
χ	0.35	T_c	ϵ_c	0.24

Table 1.3: *Debye critical screening masses, temperatures, energy densities and binding energies for the charmonium states (referred to* $T_c = 0.17\ GeV$*, and* $\epsilon_c = 1.3 - 2.1\ GeV/fm^3$ *[69]).*

In Fig. 1.9 the Debye radius r_D is plotted as a function of T/T_c, where T_c is the critical temperature. The intersection of the curve with the lines corresponding to the critical r_c for each charmonium state, individuates the corresponding critical temperature, listed in Table 1.3.

Both the ψ' and the χ_c melt at the critical deconfinement point, while the J/ψ, smaller and more tightly bound, survives up to $1.2T_c$ and hence about twice the critical energy density. Therefore, when the critical temperature is exceeded, the melting of the different charmonium states begins at different steps [85, 86]. This hierarchy of suppression for the charmonium states can be used to measure the temperature of deconfining media.

This explanation of the charmonium suppression in terms of colour screening is based on “macroscopic” features of the medium. However, the suppression can also be interpreted by considering the dissociation of the charmonium bound states as

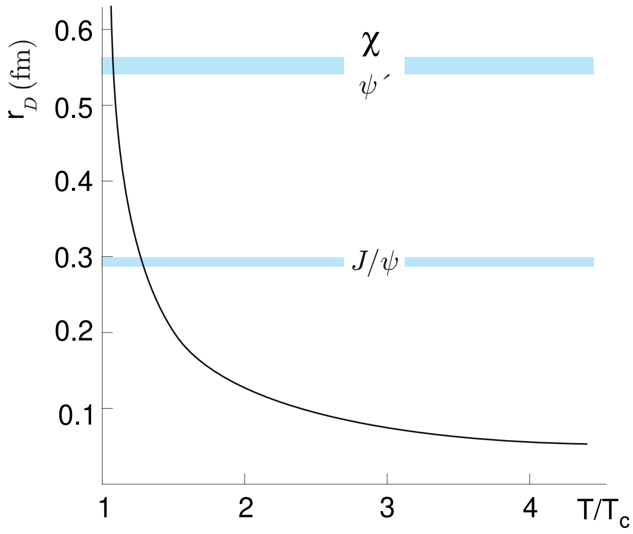

Figure 1.9: *Debye radius r_D as a function of T/T_c, where T_c is the critical temperature. The lines correspond to the critical Debye radius (r_c) for the different charmonium states.*

a consequence of microscopic collisions with the constituents of the medium [7]. In this alternative approach, it is the interaction of the J/ψ with hard gluons during the deconfined phase that causes their disappearance. The high bindind energy of the J/ψ makes it resistant to possible interactions with gluons confined into hadrons, which have too low transverse momenta to dissociate the J/ψ. Actually, in a pion gas (which represents a confined medium [4]) at temperature T, the average momenta of gluons confined into pions is $\sim 0.6T$ and therefore not hard enough to dissolve the $c\bar{c}$ binding inside the J/ψ [7, 71].

By contrast, in a deconfined medium, the gluons have an average momentum $\sim 3T$ and can more easily achieve the 0.64 GeV necessary to break the J/ψ.

The J/ψ production can thus be used to probe the in–medium gluon hardness and hence the confinement status of the medium.

The situation for the χ is quite similar, except for the earlier gluon dissociation threshold, due to the lower χ binding energy (see Table 1.3). This fact is at the basis of the two–step suppression pattern of the charmonium states.

Since the ψ' has an almost negligible binding energy of 0.06 GeV (Table 1.3), its suppression does not differ in confined or deconfined media.

In conclusion, deconfinement, however is treated, in terms of colour screening or gluon dissociation, is characterized by a multi–step suppression pattern for the charmonium states. The suppression starts with a sharp onset, when a certain deconfinement critical temperature is reached.

[4] the same considerations are also valid for heavier mesons or nucleons [87]

1.7 The Drell–Yan reference

As I will discuss in Chapter 2, the J/ψ mesons are identified in the NA50 experiment through their decays into two opposite sign muons. The process used as a reference, in the J/ψ suppression study, is the Drell–Yan, which produces opposite sign muon pairs in the same invariant mass range of the J/ψ. It consists in the electromagnetic annihilation of a valence quark and a sea antiquark with the same flavour [88]. In the annihilation a lepton pair is created through the emission of a virtual photon. Fig. 1.10 is a representation of the Drell-Yan process at the leading order.

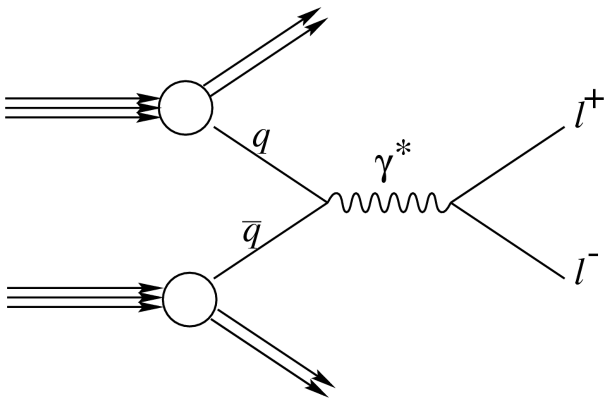

Figure 1.10: *Leading order diagram of the Drell–Yan process.*

The elementary cross–section of the quark–antiquark annihilation in a lepton pair can be expressed as

$$\sigma_i(q_i\overline{q_i} \to \gamma^* \to l^+l^-) = \frac{4\pi\alpha^2}{3M^2}e_i^2 \qquad (1.19)$$

where e_i is the electric charge of the quark with flavour i, M is the mass of the virtual photon (or the invariant mass of the lepton pair produced by its decay) and α is the fine structure constant.

For a hadron–hadron collision, this cross–section can be evaluated at the leading order by convoluting the cross–section of Eq. 1.19 with the probabilities of finding respectively a quark and an antiquark of flavour i in the two colliding hadrons:

$$\frac{d^2\sigma}{dx_1dx_2} = \frac{1}{3}\frac{4\pi\alpha^2}{3M^2}\sum_i e_i^2[f_i^A(x_1)\overline{f_i^B}(x_2) + \overline{f_i^A}(x_1)f_i^B(x_2)] \qquad (1.20)$$

where $f_i^A(x_j)$ and $f_i^B(x_j)$ are the parton distribution functions of the projectile (A) and of the target (B), i.e. the probabilities of finding a quark with flavour i in A or in B, carrying a longitudinal momentum fraction x_j of the total hadron momentum. The factor 1/3 forces to consider only parton-antiparton annihilation between partons of the same flavour.

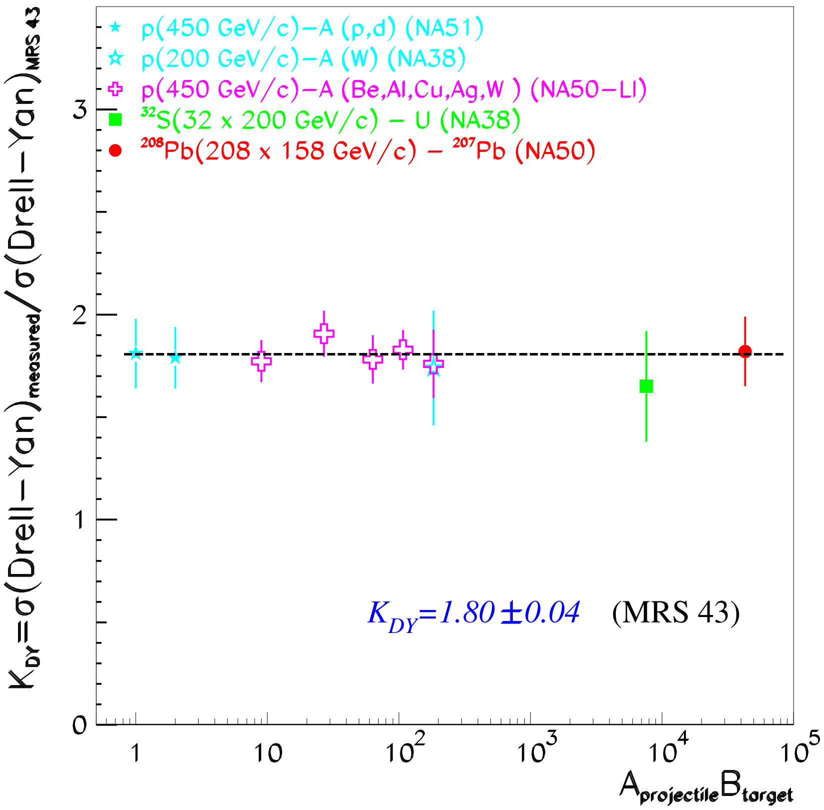

Figure 1.11: *Ratio between measured and computed Drell–Yan cross–sections. The experimental data have been obtained by the NA51, NA38 and NA50 experiments. The PDF's set for the calculation of theoretical Drell–Yan is MRS A (set n.43) [94, 95].*

A systematic study of the Drell–Yan behaviour, ranging from p–p and some p–A systems to S–U and Pb–Pb collisions, is shown in Fig. 1.11, which displays the ratio between the measured Drell–Yan cross–sections (from the NA51 [89], NA38 [90, 73] and NA50 [91, 92, 93] experiments) and the lowest order Drell–Yan cross–sections computed by means of Eq. 1.20, using the MRS A (set 43) parton distribution functions [94, 95]. The ratio (called K–factor) is plotted as a function of the product AB of the target and the projectile atomic mass numbers. Its constant value proves that the Drell–Yan cross–section is proportional to the number of nucleon–nucleon collisions and can be written as

$$\sigma_{AB}^{DY} = \sigma_{NN}^{DY}(AB)^{\alpha} \tag{1.21}$$

where σ_{NN}^{DY} is the averaged DY cross–section in nucleon-nucleon collisions. The α exponent is equal to 1, which indicates that no nuclear absorption is present. In particular, the Pb–Pb cross–section exhibits a behaviour fully compatible with lighter systems and do not suffer from any further suppression mechanism. Hence the Drell–Yan mechanism provides a good reference for studying the J/ψ production and the ratio $B_{\mu\mu}\sigma_{J/\psi}/\sigma_{DY}$ can be used to study the centrality dependence of the J/ψ suppression [96]. This has the advantage that systematic errors related to detector inefficiencies and flux uncertainties cancel out in the ratio between the experimentally measured quantities $\sigma_{J/\psi}/\sigma_{DY}$.

The K_{DY} factor is found to be of the order of ≈ 2. This means that the the Drell–Yan cross–sections, calculated at the leading order, underestimate the experimental ones. The perturbative QCD corrections at higher orders allow to obtain a better agreement between theoretical predictions and experimental data.

The K_{DY} factor can depend, to a certain extent, on the particular set of parton distribution functions chosen for its calculation. I will get back on this subject in Section 5.6.7.

Since the Drell–Yan production in nucleon–nucleon collisions depends on the nucleon isospin, the Drell–Yan cross–sections in pp, pn, np, nn collisions are different. Therefore, to compare the Drell–Yan yields produced in systems characterized by a different proton to neutron ratios, the measured Drell–Yan cross–sections must be corrected for the "isospin effect" and replaced by [63]

$$\sigma^{DY}_{corr} = \sigma^{DY}_{meas} \frac{AB \cdot (\sigma^{DY}_{th})_{pp}}{(\sigma^{DY}_{th})_{AB}} \tag{1.22}$$

which is equivalent to the Drell–Yan cross–section we would have measured for the same two nuclei made only of protons. The theoretical cross–sections $(\sigma^{DY}_{th})_{AB}$ and $(\sigma^{DY}_{th})_{pp}$ must be evaluated with the same set of parton distribution functions. The set GRVLO [97] gives for the isospin correction factor a value of 1.30 [63], while if we use the MRS A (set n.43) [94, 95] distribution functions, we obtain a factor equal to 1.01.

1.8 Published experimental results

The production of the J/ψ and ψ' charmonium states has been studied for 10 years by the NA38 experiment [98], using proton [99], oxygen and sulfur beams [100, 101, 90, 73] delivered by the CERN SPS. The proton data were collected with beams of 200 and 450 GeV/c, while the ion beams had an energy of 200 GeV/c per incident nucleon.

The NA51 experiment [102, 89] was performed in 1992 with the aim of studying pp and pd collisions at 450 GeV/c. From the collected high statistics sample, information on the J/ψ and ψ' production cross–sections can be deduced.

The NA38 and NA51 experiments have observed a J/ψ suppression that increases continuously and monotonically from pp to S–U reactions. The same behaviour has been observed as a function of the centrality of the collision in S–U interactions.

The increasing pattern exhibited by the J/ψ suppression is fully described by the absorption of the pre–resonance states ($c\bar{c}g$) by the nucleons of the interacting nuclei. The measurements with proton and light ions are useful to establish a reference baseline (the "normal" charmonium absorption by nuclear matter) with respect to which the heavy ion specific features can be identified.

Since 1995 the NA50 experiment has started to collect data with lead beams at 158 GeV/c per nucleon. The J/ψ suppression measured in Pb–Pb collisions exhibits a clear departure from the smooth trend observed with lighter projectiles. The discovery of this anomalous J/ψ suppression represents a striking indication of the transition from nuclear matter to QGP.

1.8.1 From pp to S–U collisions

As already said, the study of proton–proton, proton–deuterium and proton–nucleus collisions, where only the nuclear absorption of the charmonium states is predicted to play a role, provides a reference for the study of the J/ψ and ψ' suppression in nucleus–nucleus collisions.

Actually, in p–A and light nucleus–nucleus collisions the behaviour of the J/ψ production cross–section can be understood in terms of the absorption of the pre–resonant $c\bar{c}$ state by the surrounding nuclear matter. As for Drell-Yan events, the number of produced $c\bar{c}$ pairs is proportional to the number of nucleon–nucleon collisions, but the pre–resonant object can be destroyed before becoming a fully formed J/ψ state, through its strong interaction in the surrounding medium. Therefore the observed yield of final charmonium states is suppressed with respect to the linear A–dependence expected for the Drell–Yan mechanism (Eq. 1.21 with $\alpha = 1$).

In this framework, the J/ψ production cross–section can be parametrized, as a function of the target and the projectile mass numbers, in the following way:

$$\sigma(AB \to J/\psi + X) \ \propto \ AB \ exp(-\rho_0 \ \sigma_{abs} \ \overline{L}) \tag{1.23}$$

where the product AB accounts for the $c\bar{c}$ production, being proportional to the number of nucleon–nucleon collisions (hard process). The exponential term represents the probability for the break–up of the $c\bar{c}$ pair, with cross–section σ_{abs}. The parameter $\rho_0 = 0.17$ nucleons/fm^{-3} is the average nuclear matter density, $\overline{L}$ is the mean length that the $c\bar{c}$ traverses in the nuclear matter before being absorbed [73]. The ρL product corresponds to the number of nucleons the $c\bar{c}$ pair can potentially interact with. It takes into account the interaction of the charmonium state both with the target and the projectile nucleons and can be computed by means of a Monte Carlo program based on the Glauber formalism [64].

In order to use the charmonium suppression as a probe of QGP formation in nucleus–nucleus collisions, it is very important to study the charmonium production yields as a function of the centrality of the collision. For this purpose, the production of Drell–Yan dileptons is considered as a reference, because it is not affected by a deconfined medium.

Since the DY production cross–section is proportional to the number of nucleon–nucleon collisions AB, the ratio $\sigma(J/\psi)/\sigma(DY)$ represents the J/ψ cross–section per nucleon–nucleon collision. The J/ψ production cross–section can be described, as a first approximation, by Eq. 1.23 and therefore the $\sigma(J/\psi)/\sigma(DY)$ ratio can be parametrized as

$$\sigma(J/\psi)/\sigma(DY) \propto exp(-\rho_0 \sigma_{abs} \overline{L}) \tag{1.24}$$

The ratio $\sigma(J/\psi)/\sigma(DY)$ is reported in Fig. 1.12 as a function of $\overline{L}$, for data measured by NA51 [89] in pp and pd collisions and by NA50 [73] in p–A collisions, at 450 GeV/c, together with NA38 data [73] for p–W, p–U and S–U systems at 200 GeV/c per nucleon. The most recent high statistics p–A data collected by the NA50 experiment are also reported in the picture [92]. The Drell–Yan cross–sections have been estimated in the invariant mass interval 2.9–4.5 GeV/c^2. The ratio $\sigma(J/\psi)/\sigma(DY)$ allows to cancel the systematic errors that are equal for the J/ψ and the DY sample of events, such as detector inefficiencies and flux uncertainties.

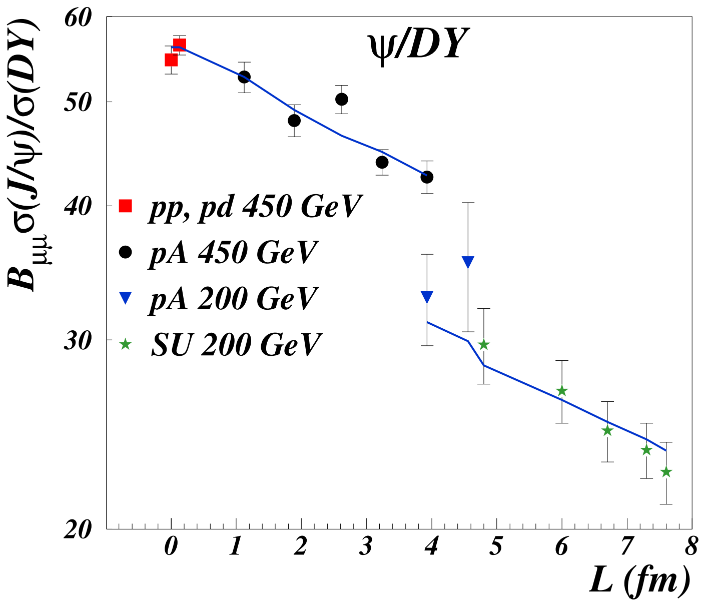

Figure 1.12: *Ratio $\sigma(J/\psi)/\sigma(DY)$ as a function of $\overline{L}$ at 450 and 200 GeV/c (in different kinematic domains), from NA38, NA51 and NA50. The continuous line is the simultaneous fit to the 450 and 200 GeV/c points with the $exp(-\rho_0 \sigma_{abs} \overline{L})$ dependence.*

The NA38, NA51 and NA50 experiments used different incident beams and targets, but always the same basic apparatus. Due to the different energies and kinematic domains, a significant difference between the absolute normalizations of the data sets at the two energies is visible. To compare the different cross–section values we need to convert all the results in the same kinematic domain: all the values are rescaled to a 200 GeV/c incident momentum and recomputed, if necessary, in the kinematic domain $0 \leq y^* \leq 1$, $|cos\ \theta_{CS}| < 0.5$. In order to find the rescaling factor, the two sets of data at different energies are fitted independently by means of Eq. 1.24, with a common nuclear dependence and a scaling factor.

The good compatibility between the $\sigma_{abs}^{J/\psi}$ values obtained for data at 450 and 200 GeV/c [92] justifies a simultaneous fit to the data at the two different energies, imposing the same value of σ_{abs} and letting free the normalizations of the two data sets. The curve resulting from this fit is reported on Fig. 1.12. The corresponding absorption cross–section is $4.4 \pm 0.5\ mb$, while the rescaling factor between the two data sets is 0.75 ± 0.04 [91].

The two sets of data at different energies are well described by a single value of the absorption cross–section. This implies that the J/ψ suppression observed from p–p to S–U collisions can be explained by the nuclear absorption model, without requiring a new absorption mechanism.

The NA50 results published before the recent high statistics p–A data referred to an absorption cross–section of $5.4 \pm 0.4\ mb$, given, as a first approximation, by

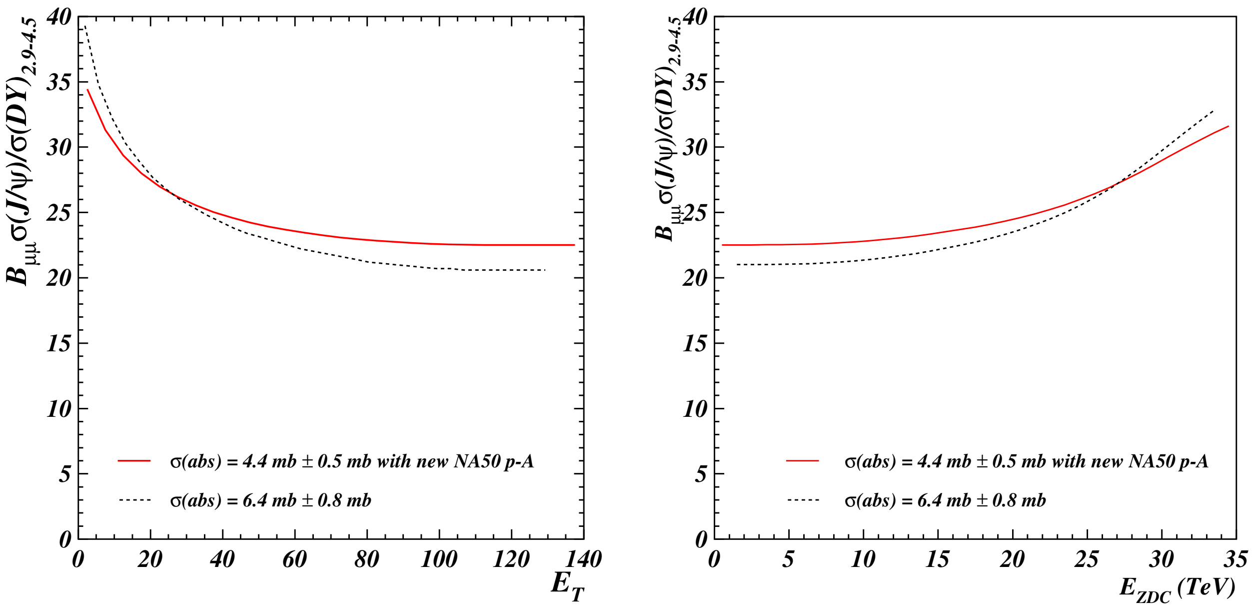

Figure 1.13: *Comparison between the "normal" absorption curves evaluated with the Glauber model using* $\sigma_{abs} = 4.4 \pm 0.5\ mb$ *or* $\sigma_{abs} = 6.4 \pm 0.8\ mb$*, as a function of* E_T *(left) and* E_{ZDC} *(right).*

the exponential fit or, better, to $\sigma_{abs} = 6.4 \pm 0.8$ mb provided by a full Glauber calculation [103].

In Fig. 1.13 the "normal" nuclear absorption curves, evaluated by means of the Glauber model using $\sigma_{abs} = 4.4 \pm 0.5$ mb or $\sigma_{abs} = 6.4 \pm 0.8$ mb are compared. The normalization of the curves has been obtained by rescaling to 158 AGeV/c the $\sigma_{J/\psi}/\sigma_{DY}$ values relative to p–p, p–d, p–A and S–U collisions at 200 and 450 AGeV/c. In the figure the new and old estimates of the Pb–Pb nuclear absorption curve are presented as a function of the neutral transverse energy E_T and the forward energy E_{ZDC}.

In spite of the different values of the absorption cross–sections obtained if the new p–A data are included or not in the calculation, the nuclear absorption curves do not differ very much in the region corresponding to the semi–peripheral collisions. This is essentially due to the normalization constraints imposed by the S–U points. Therefore the conclusions drawn on the J/ψ suppression pattern as a function of centrality will be the same, independently from the used nuclear absorption curve.

In the following section, showing the published Pb–Pb results, I will always refer to the old $\sigma_{abs} = 6.4 \pm 0.8$ mb value (contemporaneous to the $J/\psi/DY$ results), while the new $\sigma_{J/\psi}/\sigma_{DY}$ results that are the subject of this thesis will be compared in Section 5.5 to the new and more refined nuclear absorption curve (corresponding to $\sigma_{abs} = 4.4 \pm 0.5$ mb).

1.8.2 Pb–Pb collisions

I will consider now the results of the NA50 experiment with a Pb beam sent on a Pb target and I will compare them with the reference provided by hadron–induced collisions and light ion interactions. As already seen in the previous section, the nuclear absorption model reproduces quite well all the $J/\psi/DY$ points from p–p up to S–U collisions.

Two strategies can be adopted in order to search for an "anomalous" behaviour of the charmonium production rates in Pb–Pb interactions:

1. to study different systems of projectiles and targets and compare the charmonium cross–sections in proton and ion induced reactions. In order to compare the charmonium production yield in these experimental systems, resulting from different beam and target combinations, it is useful to calculate the "cross–section per nucleon–nucleon collisions". This quantity is obtained by dividing the measured charmonium cross–sections by the product AB of the projectile and the target atomic mass numbers.

2. to study the charmonium states suppression in a given heavy ion system as a function of the centrality of the collision. In this case, a reference is needed. The NA50 experiment uses, as a reference, the well known Drell–Yan mecha-

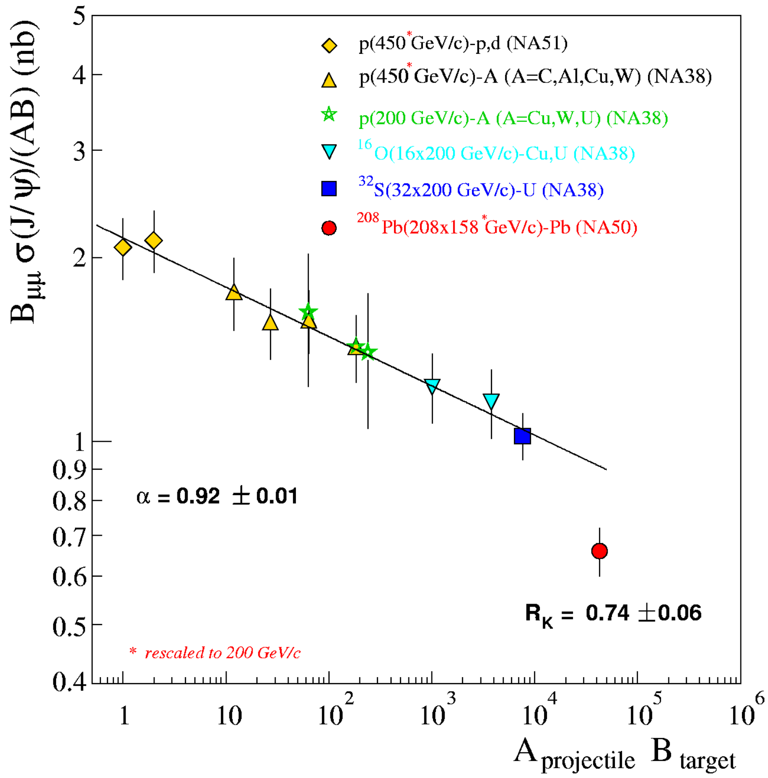

Figure 1.14: *The J/ψ cross–sections per nucleon–nucleon collisions (times the branching ratio into dimuons, $B_{\mu^+\mu^-}$) as a function of the product AB of the projectile and the target atomic mass numbers. The simultaneous fit to the 450 GeV/c and 200 GeV/c points is also reported.*

nism (see section 1.7), which is insensitive to strong interactions and is not perturbed by the evolution of the system after hadronisation [104].

In Fig. 1.14 the J/ψ cross–sections per nucleon–nucleon collisions are plotted as a function of the product AB of the projectile and the target atomic mass numbers [89, 73, 103]. Since the data are collected at different energies and in different kinematic domains, they have been rescaled to 200 GeV/c incident momentum and recomputed, if necessary, in the same kinematic domain. In order to find the rescaling factor between the two sets of data at 450 and 200 GeV/c, the corresponding $\sigma(J/\psi)/AB$ values have been fitted independently with a common nuclear dependence and a normalization term. The charmonium production cross–section is parametrized as $\sigma_0 A^\alpha$ for p–A collisions and as $\sigma_0 (AB)^\alpha$ for nucleus–nucleus collisions. The α exponent implicitly contains information about all the nuclear effects, both in the final state (absorption or dissociation) and in the initial state (nuclear modifications of the parton distribution functions, due for example to QGP formation).

The 450 and 200 GeV/c results have a compatible nuclear dependence for the J/ψ

production cross–section, i.e. consistent α values [73], confirming the AB dependence of the J/ψ production cross–section, whatever the energy and the kinematic domain are. This good compatibility justifies a simultaneous fit to the data at the two different energies, imposing the same value of α for the two samples. This fit gives $\alpha = 0.92 \pm 0.01$, in agreement with previous p–A results [63].

The fact that the found α values for p-A and light nucleus–nucleus collisions are smaller than one can be attributed to the final state interaction between the produced charmonium states and the surrounding medium. This is not true for muon pairs produced through the Drell–Yan mechanism, which is a hard process too (quark–antiquark annihilation instead of gluon fusion), but do not suffer of final state interactions and has a linear A–dependence ($\alpha = 1$).

The rescaling factor obtained from the simultaneous fit to the data at 450 and 200 GeV/c is 0.38 ± 0.04, which is compatible with the value 0.418 ± 0.083 that results from the x_F and $\sqrt{s}$ dependence of the J/ψ cross–section according to the Schuler parametrization [105].

The rescaled 450 GeV/c data are plotted in Fig. 1.14 together with the 200 GeV/c data and the result of the simultaneous fit. The Pb–Pb point, measured at 158 GeV/c per nucleon [63], has been rescaled to 200 GeV/c by means of the Schuler parametrization and also reported in Fig. 1.14. In this figure it can be seen that all the data from p–p up to S–U collisions exhibits a continuous and monotonic J/ψ suppression pattern from the lighter to the heavier interacting nuclei, while the Pb–Pb point is about 5 standard deviations off the fitted function and lies below the expected value (extrapolated from the fit) by a factor 0.74 ± 0.06. This observation indicates that a new mechanism, besides the nuclear absorption, is required to explain the Pb–Pb collision results.

In order to perform a study of the charmonium production as a function of the centrality of the collision, the ratio $\sigma(J/\psi)/\sigma(DY)$ is considered. In Fig. 1.15 the $\sigma(J/\psi)/\sigma(DY)$ ratios for p–p, p–d [89], p–A [73, 106], S–U [73] and Pb–Pb [107] collisions are shown as a function of the L variable, which allows to compare different systems, characterized by different kinematic domains. The most recent high statistics p–A data collected by the NA50 experiment [92] are not reported in the picture. All the 450 GeV/c, 400 GeV/c and 200 GeV/c data presented in the figure have been rescaled to 158 GeV/c using the Schuler parametrization [105] and the Drell-Yan cross–section have been corrected for isospin effects, according to the procedure explained in [63].

The full line reported on Fig. 1.15 is the exponential fit $exp(-\rho_0 \sigma_{abs} \overline{L})$ to the data from p–p to S–U, which is compatible with the nuclear absorption of a pre–resonant $c\bar{c}$ state [72]. This simple exponential fit leads to the nuclear absorption cross–section $\sigma_{abs} = 5.4 \pm 0.4$ mb, while a full Glauber calculation provides $\sigma_{abs} = 6.4 \pm 0.8$ mb. It is important to underline that the set of experimental data considered here does not include the recent p–A data at high statistics, which, on the contrary, are taken into account in the fit reported in Fig. 1.12.

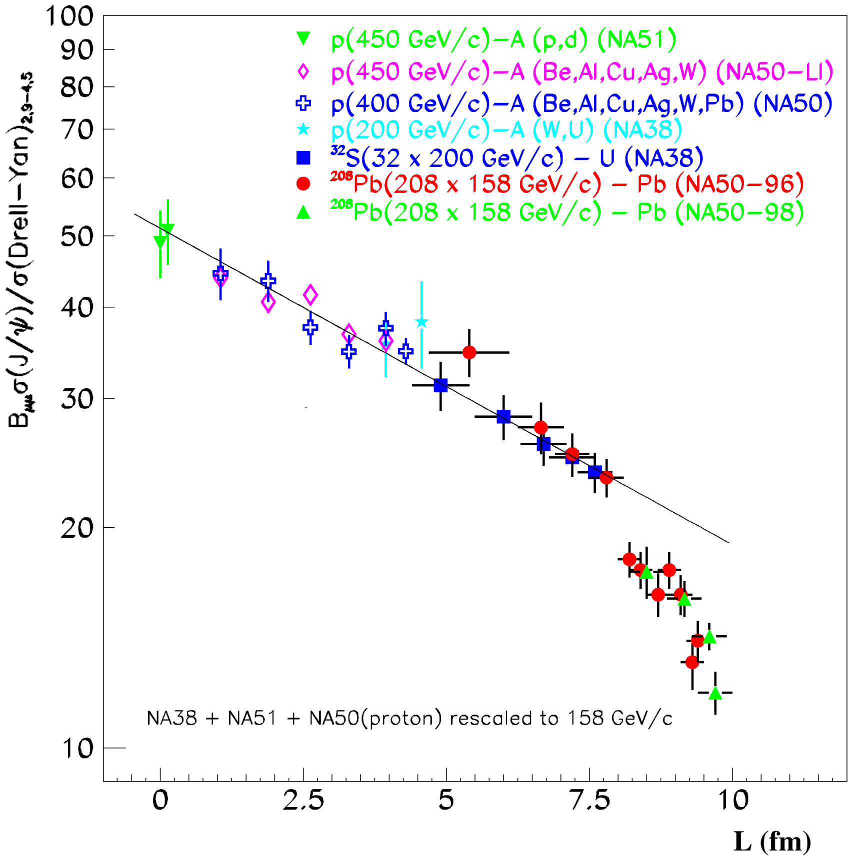

Figure 1.15: *Ratio $\sigma(J/\psi)/\sigma(DY)$ as a function of $\overline{L}$. The results obtained at 450 GeV/c, 400 GeV/c and 200 GeV/c are rescaled to 158 GeV/c. The dotted line is a fit to data from p–p to S–U.*

Fig. 1.15 confirms that all the results from p–p to peripheral Pb–Pb collisions can be described with the same absorption behaviour. By contrast, the most central Pb–Pb points (corresponding to $L > 8\ fm$, i.e. $b < 8\ fm$) show a clear departure from this trend, indicating the onset of an anomalous J/ψ suppression.

The ratio of J/ψ to Drell–Yan cross–sections has also been studied by the NA50 experiment as a function of two independent centrality estimators: the transverse energy E_T detected by the NA50 electromagnetic calorimeter and the forward hadronic energy E_{ZDC} released in the zero–degree calorimeter [103, 108].

Two different analysis techniques have been used to evaluate the ratio $\sigma(J/\psi)/\sigma(DY)$: the standard and the minimum bias analyses. In the first analysis method the numbers of J/ψ and Drell–Yan events are extracted from the fit to the invariant mass spectrum above 2.9 GeV/c^2, taking into account the different processes that contribute to the spectrum. For a detailed description of this procedure, see Section 5.4. In the second method, developed to overcome the problem of the statistical fluctuations in the Drell–Yan sample, the Drell–Yan spectrum is extracted from the huge sample of minimum bias events. This sample is collected by means of a trigger that fires whenever a minimum amount of energy is measured by the zero–degree calorimeter. For a complete description of the two analyses see [64].

The transverse energy spectrum (or the forward energy spectrum when E_{ZDC} is used to estimate the collision centrality) is divided into bins: in each of these bins the J/ψ over Drell–Yan ratio is calculated. Because of the bigger size of the minimum bias sample, the minimum bias analysis is less affected by statistical fluctuations and a finer binning is possible.

The results obtained by NA50 in Pb–Pb collisions at 158 GeV/c per nucleon as a function of E_T and E_{ZDC} are shown for the standard analysis in Fig. 1.16 [103, 108]. The solid line represents the "ordinary" nuclear absorption of the $c\bar{c}$ pair with a cross–section $\sigma_{abs} = 6.4 \pm 0.8$ mb, which accounts for the J/ψ yield measured in collisions from p–p to S–U. While for the most peripheral Pb–Pb collisions (at low E_T or high E_{ZDC} values) the J/ψ suppression can be described by the nuclear absorption, a clear departure from this "normal" trend can be seen at around $E_T \sim$ 40 GeV (or $E_{ZDC} \sim$ 27 TeV), corresponding to an impact parameter $b \sim$ 8 fm. Moreover, no visible saturation is present in the more central collisions (high E_T or low E_{ZDC} values), but a second change of behaviour can be seen at $E_T \sim$ 90 GeV ($E_{ZDC} \sim$ 10 TeV).

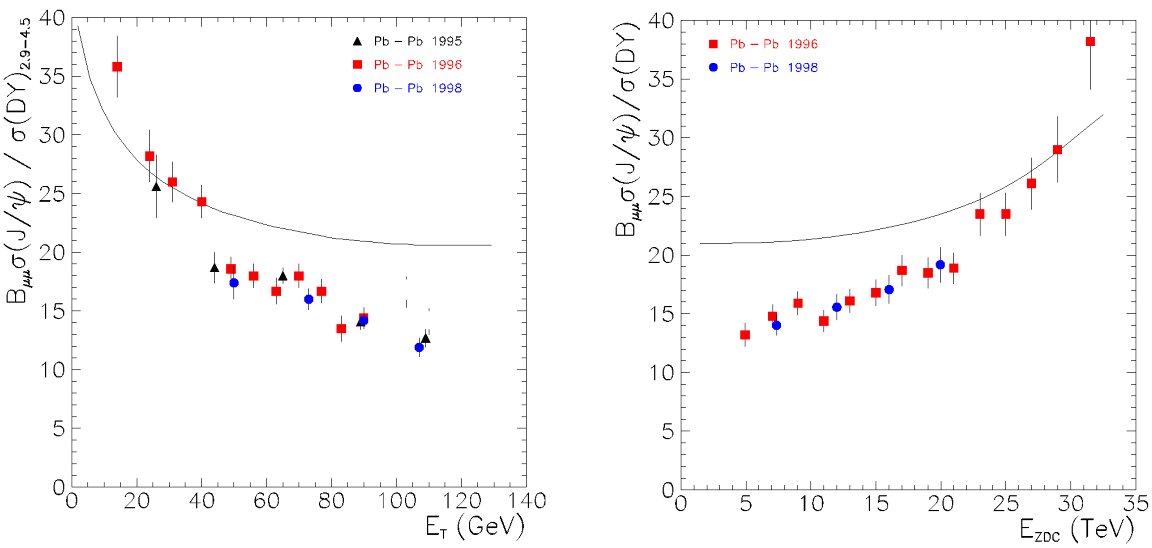

Figure 1.16: $\sigma(J/\psi)/\sigma(DY)$ *ratios in Pb–Pb collisions at 158 AGeV/c as a function of* E_T *(left) and* E_{ZDC} *(right) obtained with the standard analysis method. The solid line is the nuclear absorption with* $\sigma_{abs} = 6.4 \pm 0.8$ *mb.*

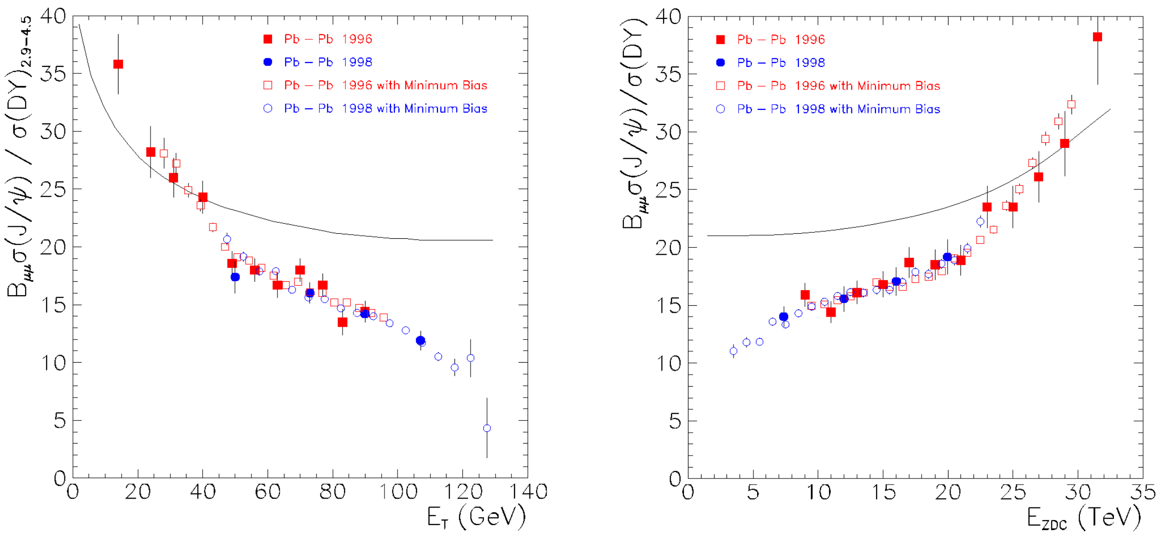

Figure 1.17: *$\sigma(J/\psi)/\sigma(DY)$ ratios in Pb–Pb collisions at 158 AGeV/c as a function of E_T (left) and E_{ZDC} (right) obtained in the minimum bias (open symbols) and the standard (closed symbols) analyses. The solid line is the nuclear absorption with $\sigma_{abs} = 6.4 \pm 0.8$ mb.*

As already explained, this suppression pattern can be understood in a deconfinement scenario, as due to the disappearance first of the χ_c mesons, responsible for about 30–40% of the indirect J/ψs (first drop), and then of the more tightly bound and directly produced J/ψs (second inflection). The two independent analyses, using E_T and E_{ZDC} as centrality variable, are fully consistent and confirm the same charmonium suppression pattern.

In Fig. 1.17 the results of the minimum bias analysis are compared to those obtained with the previously discussed standard method, for the same NA50 data taking periods [103, 108]. Again the $\sigma(J/\psi)/\sigma(DY)$ ratios are plotted as a function of E_T (left) or E_{ZDC} (right). A good agreement is visible between results from different analysis procedure: in both cases a significative departure from the nuclear absorption reference is observed at $E_T \sim 40$ GeV ($E_{ZDC} \sim 27$ TeV), whereas there is no saturation of the J/ψ suppression for the most central Pb–Pb collisions and at around $E_T \sim 90$ GeV ($E_{ZDC} \sim 10$ TeV) a change of behaviour is seen. Hence it can be concluded that the J/ψ suppression observed by the NA50 experiment, in two independent analyses and by means of two different detectors as centrality estimators, provides a significant evidence for deconfinement of quarks and gluons in Pb–Pb collisions.

In order to describe more quantitatively the observed suppression pattern, it has been studied as a function of the energy density ϵ reached during the collision. Besides, the energy density variable could allow to compare the results obtained by

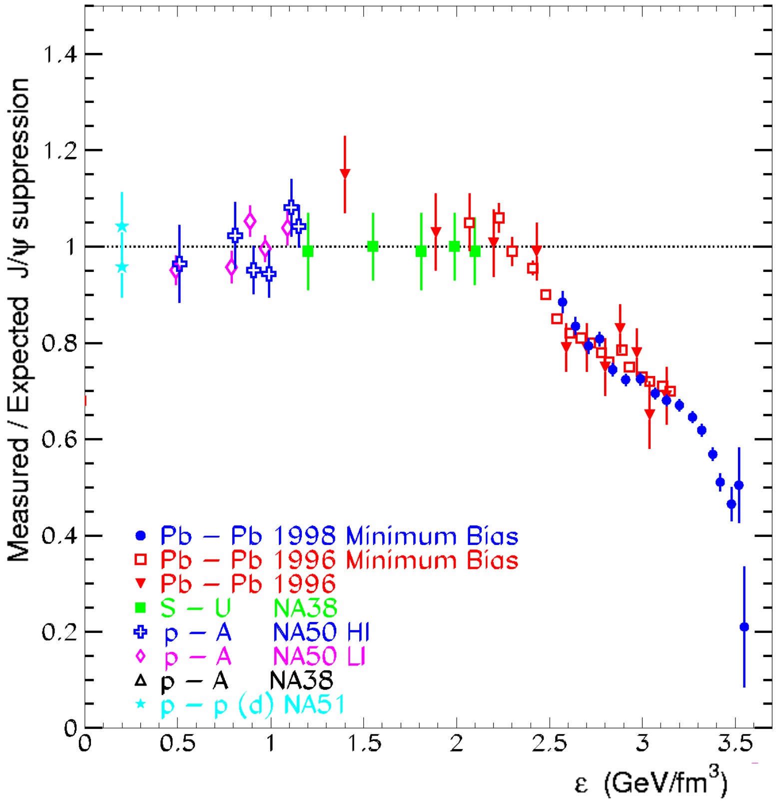

Figure 1.18: *Measured J/ψ suppression yields, normalized to the yields expected in case of normal nuclear absorption ($\sigma_{abs} = 6.4 \pm 0.8$ mb). The results are plotted as a function of the energy density ϵ reached in different colliding systems.*

NA50 and NA38 with future results from other experiments.

The energy density is computed according to the Bjorken's model [11], as already discussed in Section 1.3.2. In Fig. 1.18 the ratio between the observed J/ψ suppression pattern and the normal nuclear absorption curve is shown as a function of ϵ for different colliding systems. Whereas the more peripheral Pb–Pb points lie on the absorption curve, the more central ones show a sudden drop of 20% at $\epsilon \sim 2.3\ GeV/fm^3$, followed by an inflection point at $\epsilon \sim 3.1\ GeV/fm^3$. This charmonium suppression pattern confirms the conclusions we have already reached studying the J/ψ production as a function of E_T or E_{ZDC}.

Different theoretical models have been proposed in order to interpret these NA50 observations. Some of them are based on conventional assumptions [109, 110, 111, 112, 113], which are not invoking the QGP formation; other models introduce the possibility of having a deconfined state of quarks and gluons [114, 115]. None of the conventional models can describe simultaneously both the $J/\psi/DY$ results obtained with proton and sulfur induced reactions and the pattern of $J/\psi/DY$ as a function

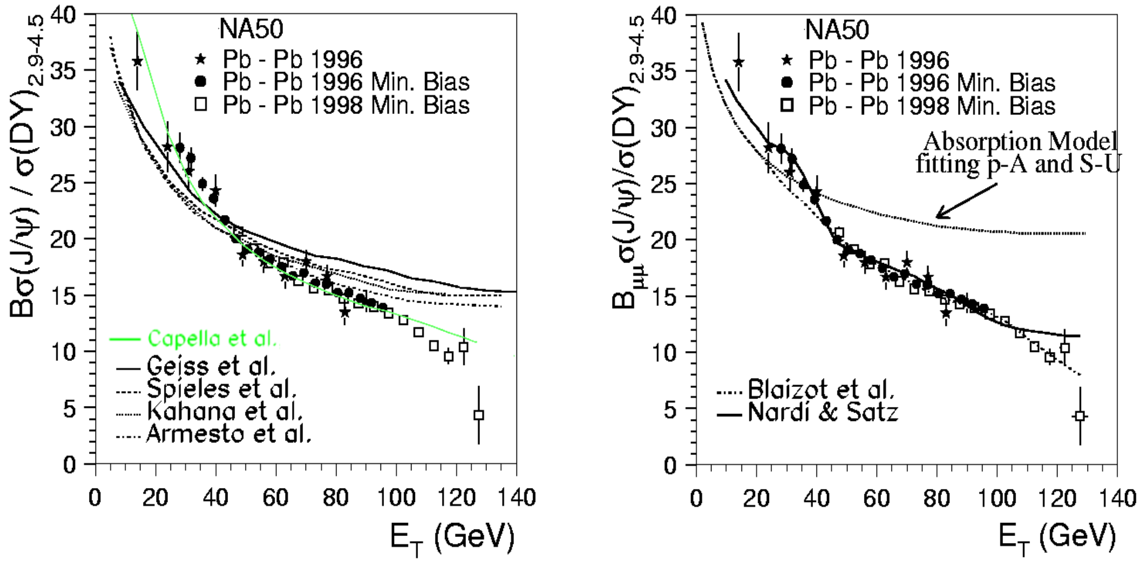

Figure 1.19: *Experimental $\sigma(J/\psi)/\sigma(DY)$ ratios obtained by NA50 in Pb–Pb collisions at 158 AGeV, as a function of E_T, compared to different conventional theoretical models [109, 110, 111, 112, 113] (on the left), and to models that include deconfinement [114, 115] (on the right).*

of centrality observed in Pb–Pb collisions. This can be clearly seen in Fig. 1.19 (left), where the ratios $\sigma(J/\psi)/\sigma(DY)$ as a function of E_T, measured in Pb–Pb collisions at 158 AGeV/c, are compared to the curves calculated by models assuming the absorption of charmonium states by interactions with the nuclear medium and with comoving hadrons. A first incompatibility between the experimental results and the predictions of these models is the sharp onset of the J/ψ anomalous suppression, observed at $E_T \sim 40$ GeV, while all the models predict a smooth decrease of the J/ψ production yield with increasing centrality. Moreover, the data show a second drop of the J/ψ production yield at $E_T \sim 90$ GeV, while the hadronic models predict a saturation of its steady decrease.

The NA50 measurements seem more in agreement with the patterns predicted by other models [114, 115], which assume a phase transition to a deconfined state of quarks and gluons with two thresholds, corresponding respectively to the χ_c and the J/ψ melting points (Fig. 1.19 right).

Bibliography

[1] I.Bombaci, Proceedings of the Third Catania Relativistic Ion Studies Conference, Acicastello, Italy, May 22–26, 2000.

[2] F. Karsch, Nucl. Phys. B (Proc. Suppl.) 83–84 (2000) 14.

[3] F. Karsch, Nucl. Phys. A 698 (2002) 199c.

[4] Review of particle physics, Phys. Rev. D 66 (2002) 010001.

[5] V.Bernard, Phys. Lett. B 227 (1989) 465.

[6] V.Koch, "Introduction to chiral symmetry", presented at the 3rd TAPS Workshop, Bosen, Germany, 10–15 Sep 1995; nucl-th/9512029; LBL-38000.

[7] H. Satz, Proceeding of The International School of Subnuclear Physics, Erice/Sicily, 26 August–4 September 1997, hep–ph/9711289.

[8] E. Laermann, Nucl. Phys. A610 (1996) 1c.

[9] F. Karsch, Nucl. Phys. A590 (1995) 367c.

[10] T. Blum et al., Phys. Rev. D51 (1995) 5153.

[11] J.D. Bjorken, Phys. Rev. D27 (1983) 140.

[12] T. Alber et al., NA49 Coll., Phys. Rev. Lett. 75,21 (1995) 3814.

[13] U. Heinz, "Hunting down the quark–gluon plasma in relativistic heavy–ion collisions", presented at the "Workshop on Strong and Electroweak Matter", Copenhagen, Denmark, 2–5 Dec 1998 , hep–ph/9902424.

[14] B.Muller, Rept. Prog. Phys. 58 (1995) 611.

[15] H.Satz, Nucl. Phys. B (Proc. Suppl.) 94 (2001) 389.

[16] H.Satz, hep–ph/0209181.

[17] J.Rafelski and B.Müller, Phys. Rev. Lett. 48 (1982) 1066.

[18] J.Rafelski, Phys. Lett. B 262 (1991) 153.

[19] R.Pisarski, Phys. Lett. B 110 (1982) 155.

[20] G.E.Brown et al., Phys. Rev. C 43 (1991) 1881.

[21] E.V.Shuryak, Phys. Lett. B 78 (1978) 150.

[22] K.Kajantie and H.I.Miettinen, Z. Phys. C 9 (1981) 341.

[23] T.Matsui and H.Satz, Phys. Lett. B178 (1986) 416.

[24] J.D.Bjorken, Fermilab–Pub–82/59–THY (1982) and Erratum.

[25] R.Baier, D.Schiff and B.G.Zakharov, Annu. Rev. Nucl. Part. Sci. 50 (2000) 37.

[26] R. Lietava et al., WA97 Coll., J. Phys. G25 (1999) 181.

[27] F. Antinori et al., WA97 Coll., Nucl. Phys. A661 (1999) 130c–139c.

[28] K.Fanebust et al., NA57 Coll., J. Phys. G 28 (2002) 1607.

[29] M.Gazdzicki, M.I. Gorenstein and D.Röhrich, Comment on "Comparison of strangeness production between A–A and p–p reactions from 2 to 160 AGeV", by J.C.Dunlop and C.A.Ogilvie, hep-ph/0006236.

[30] S.V. Afanasiev et al., NA49 Coll., "Study of the onset of deconfinement in nucleus- nucleus collisions at low SPS energies",CERN/SPS 2000-035, CERN/SPSLC/P264 Add. 7.

[31] A. Shor, Phys. Rev. Lett. 54 (1985) 1122.

[32] P.Koch, B.Muller and J.Rafelski, Phys. Rep. 142 (1986) 167.

[33] M.C.Abreu et al. (NA50 coll.), Nucl. Phys. A 663-664 (2000) 721.

[34] L.Villatte et al, (NA50 Coll.), 38th International Winter Meeting on Nuclear Physics, Bormio, Italy, 24–29 Jan 2000, Ric. Sci. Educ. Perm., Suppl. 116 (2000) 241-248.

[35] J. Astruc, PhD Thesis, July 1997, Université de Paris 6.

[36] L. Villatte, PhD Thesis, March 2001, Université de Paris 7.

[37] G.E. Brown and M. Rho, Phys. Rev. Lett. 66 (1991) 2720.

[38] B. Lenkeit, for the CERES Coll., Nucl. Phys. A 661(1999) 23c.

[39] G. Agakichiev et al., CERES Coll., Phys. Rev. Lett. 75 (1995) 1272.

[40] I. Ravinovic, for the CERES Coll., Nucl. Phys. A638 (1998) 159c.

[41] G. Agakichiev et al., CERES Coll., Phys. Lett. B422 (1998) 405.

[42] A.L.S.Angelis et al., HELIOS/3 Coll., Eur. Phys. J. C 13 (2000) 433.

[43] C.Soave, PhD thesis, December 1998, Universitá di Torino.

[44] L.Capelli (NA50 Coll.), Nucl. Phys. A 698 (2002) 539c.

[45] L.Kluberg (NA50 Coll.), Nucl. Phys. A 661 (1999) 300c.

[46] M.C.Abreu et al., NA50 Coll, J. Phys. G 25 (1999) no.2, pp.235-45.

[47] R.Albrecht et al., WA80 Coll., Phys. Rev. Lett. 76 (1996) 3506.

[48] T.Peitzmann for the WA98 Coll., Nucl. Phys. A 685 (2000) 399c.

[49] S.Digal, P.Petreczky and H.Satz, Phys. Rev. D 64 (2001) 094015.

[50] R.V.Gavai et al. (Hard Probe Collab.), Int. J. Mod. Phys. A 10 (1995) 3043.

[51] G.T.Bodwin, E.Braaten and G.P.Lepage, Phys. Rev. D 51 (1995) 1125.

[52] E.Braaten, Annu. Rev. Nucl. Part. Sci. 46 (1996) 197–235.

[53] C.H.Chang, Nucl. Phys. B 172 (1980) 425.

[54] E.L.Berger and D.Jones, Phys. Rev. D 23 (1981) 1521.

[55] R.Baier and R.Rückl, Phys. Lett. B 102 (1981) 364 and Z. Phys C 19 (1983) 251.

[56] E.Braaten, Nucl. Phys. B (Prod. Suppl.) 71 (1999) 441.

[57] F.Abe et al. (CDF), Phys. Rev. Lett. 79 (1997) 572 and 578.

[58] A.Sansoni (CDF), Nuovo Cim. 109 A (1996) 827.

[59] E.Braaten and S.Fleming, Phys. Rev. Lett. 74 (1995) 3327.

[60] C.Gerschel and J.Hüfner, Annu. Rev. Nucl. Part. Sci. 49 (1999) 255–301.

[61] S.Gavin and R.Vogt, Nucl. Phys. B 345 (1990) 104.

[62] S.J.Brodsky and A.H.Mueller, Phys. Lett. B 206 (1988) 685.

[63] M.C.Abreu et al. (NA50 coll.), Phys. Lett. B 410 (1997) 337.

[64] M.C.Abreu et al. (NA50 Coll.), Phys. Lett. B 450 (1999) 456.

[65] S.Gupta and H.Satz, Z. Phys. C 55 (1992) 391.

[66] R.C.Hwa and J.Pisut, Phys. Rev. C 58 (1998) 434.

[67] J.Qiu, J.P.Vary and X.Zhang, hep-ph/9809442, 1998.

[68] B.Mueller nucl–th/9806023 (1998).

[69] R.Vogt, Phys. Rep. 310 (1999) 197.

[70] D.Kharzeev et al., Z. Phys. C 74 (1997) 307.

[71] H.Satz, Rep. Prog. Phys. 63 (2000) 1511.

[72] D.Kharzeev and H.Satz, Phys. Lett. B 366 (1996) 316.

[73] M.C.Abreu et al. (NA38 coll.), Phys. Lett. B 466 (1999) 408.

[74] C.Gerschel and J.Hüfner, Z. Phys. C 56 (1992) 171.

[75] J.Ftacnik et al., Phys. Lett. B 207 (1988) 194.

[76] S.Gavin et al., Phys. Lett. B 207 (1988) 257.

[77] R.Vogt et al., Phys. Lett. B 207 (1988) 263.

[78] R.Vogt, Phys. Lett. B 430 (1998) 15.

[79] S.Gavin and R.Vogt, Nucl. Phys. A 610 (1996) 442c.

[80] J.P.Blaizot and J.Y.Ollitrault, Phys. Rev. D 39 (1989) 232.

[81] J.Geiss, Phys. Lett. B 447 (1999) 31.

[82] M.C.Abreu et al., Nucl. Phys. A 661 (1999) 93c.

[83] H.Satz, Nucl. Phys. A 418 (1984) 447c.

[84] S.Jacobs et al., Phys. Rev. D 33 (1986) 3338.

[85] F. Karsch, M.T.Mehr and H.Satz, Z. Phys. C 37 (1988) 617.

[86] F. Karsch and H.Satz, Z. Phys. C 51 (1991) 209.

[87] D.Kharzeev, Proceeding of the International School of Physics "Enrico Fermi", Varenna, Italy, 6–17 Jun 1995, nucl-th/9601029 ; CERN-TH-95-342 ; BI-TP-95-41.

[88] C.Y.Wong, Introduction to High Energy Ion Collisions, World Scientific, Singapore, 1994.

[89] M.C.Abreu et al. (NA51 coll.), Phys. Lett. B 438 (1998) 35.

[90] M.C.Abreu et al. (NA38 coll.), Phys. Lett. B 449 (1999) 128.

[91] M.C.Abreu et al. (NA50 coll.), Phys. Lett. B 553 (2003) 167.

[92] M.C.Abreu et al. (NA50 coll.), Proceeding of Quark Matter 2002, Nantes submitted to Nucl. Phys. A (2002)

[93] P.Cortese, PhD Thesis, Dec. 2000, Universitá di Torino.

[94] A.D.Martin et al., hep–hp/9409257.

[95] A.D.Martin et al., Phys. Rev. D 51 (1995) 4856.

[96] M.C.Abreu et al. (NA50 coll.), Phys. Lett. B 410 (1997) 327.

[97] M.Gluck et al., Z. Phys. C 53 (1992) 127.

[98] L. Anderson et at., Nucl. Instrum. Methods 223 (1984) 26.

[99] M.C.Abreu et al. (NA38 coll.), Phys. Lett. B 444 (1998) 516 and references therein.

[100] C.Baglin et al. (NA38 coll.), Phys. Lett. B 220 (1989) 471.

[101] C.Baglin et al. (NA38 coll.), Phys. Lett. B 255 (1991) 459.

[102] A.Baldit et al. (NA51 coll.), Phys. Lett. B 332 (1994) 244.

[103] M.C.Abreu et al. (NA50 coll.), Phys. Lett. B 477 (2000) 28.

[104] S.Gavin et al. (Hard Probe coll.), Int. J. Mod. Phys. A 10 (1995) 2961.

[105] G.A. Schuler, CERN-TH/94-7170 (1994)

[106] E.Scomparin (NA50 Coll.), Nucl. Phys. A 698 (2002) 543c.

[107] P.Bordalo (NA50 Coll.), Nucl. Phys. A 698 (2002) 127c.

[108] M.C.Abreu et al. (NA50 coll.), Phys. Lett. B 521 (2001) 195.

[109] J.Geiss, Phys. Lett. B 117 (1999) 31.

[110] C.Spieles et al., Phys. Rev. C 60 (1999) 54901.

[111] D.E.Kahana et al., P. P. Nucl. Phys. 42 (1999) 269.

[112] N.Armesto et al., Phys. Rev. C 59 (1999) 395.

[113] A.Capella et al., Phys. Rev. Lett. 85 (2000) 2080.

[114] M.Nardi and H.Satz, Phys. Lett. B 442 (1998) 14.

[115] J.P.Blaizot et al., Phys. Rev. Lett. 85 (2000) 4012.

Chapter 2

The experimental apparatus

2.1 Introduction

The NA50 experiment was proposed in 1991 [1] with the aim of studying the muon pairs and the vector mesons produced in the interactions of ultra–relativistic Pb ions or protons on fixed targets. The experimental apparatus meant for these observations is located in the North area of the SPS accelerator at CERN.

The central element of the NA38/NA50 experimental set–up derives from the old NA10 spectrometer [2]. The NA50 apparatus has been upgraded with respect to the NA38 experiment [3, 4] (which took data from 1986 to 1992 with $^{16}_{8}O$ and $^{32}_{16}S$ projectiles), with the addition of two new centrality detectors (the multiplicity detector and the zero–degree calorimeter). A picture of this experimental set–up is shown in Fig. 2.1.

The detectors placed before the target region allow to count the number of incident particles, to select the interactions inside the target and to reject pile–up events.

The target is followed by a hadron absorber where the beam, as well as the hadrons produced in the collision, are stopped. The absorber is passed through by muons, which are detected by the muon spectrometer, based on an air–core toroidal magnet equipped with hexagonal multiwire proportional chambers and scintillator hodoscopes.

Since the J/ψ and ψ' suppression is related to the centrality of the collision, special care has been taken to measure the impact parameter b. For this purpose the experiment makes use of three centrality detectors: an electromagnetic calorimeter, which detects the electromagnetic transverse energy released in the interaction, a

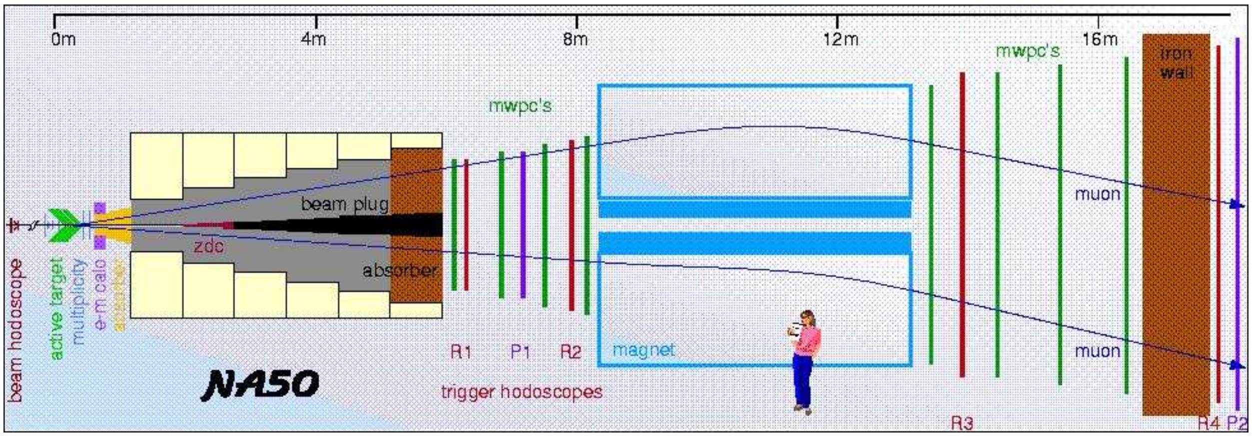

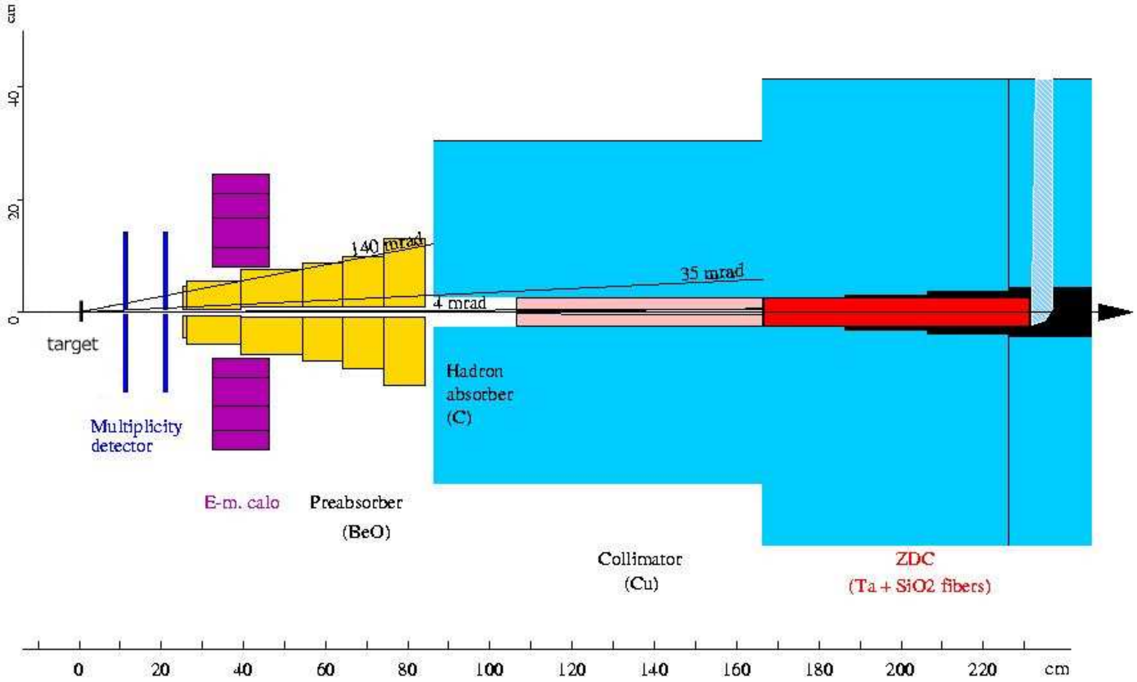

Figure 2.1: *The NA50 experimental apparatus (on the top). Details of the detectors in the target area are reported in the bottom.*

silicon microstrip multiplicity detector, which counts the number of charged particles produced in the collision, and a zero–degree calorimeter, which measures the forward energy carried by the projectile spectator nucleons.

In the following sections I will briefly describe the elements that compose this experimental apparatus.

2.2 The beam and the beam detectors

2.2.1 The beam

The NA50 experimental apparatus is placed on the ECN3 line of the CERN SPS, where a high intensity beam is extracted. To achieve the NA50 experimental purposes, two kinds of beam are required:

- a proton beam with a momentum of 450 GeV/c and an intensity of 10^{11} particles per burst (beam cycle of 20 s, effective spill of 5 s)
- a $^{208}_{82}Pb$ beam of 158 GeV/c per nucleon at an intensity of about $6 - 7 \cdot 10^7$ particles per burst (burst of 14 s, 2.5 s of effective spill). Data at 40 AGeV/c have also been taken for fission (see chapter 6) and multiplicity measurements [5, 6].

The choice of the beam intensity during the ion–ion data taking periods is a compromise between the requirement of collecting a high statistics sample of events for low cross–section processes and of containing the pile–up problems and the radiation damage risk of the detectors.

In the p–A runs the centrality is not measured and, therefore, the beam intensity is not limited by the operations of the centrality detectors and can be raised to values of about $10^8 - 10^9$ protons per burst.

The momentum distribution of the Pb beam can be approximated by a gaussian with $\Delta p/p = 0.1\%$. The beam dimensions are checked by a multiwire chamber; typical values are $\sigma_x = 0.5$ mm and $\sigma_y = 0.45$ mm.

2.2.2 The beam Hodoscope

The Beam Hodoscope (BH) is used for counting the number of incoming ions during the ion–ion data taking periods [7]. It is placed 22 m before the target, where the beam spot is large enough ($\sigma_x \sim 0.8$ mm and $\sigma_y \sim 6$ mm) for the detector to tag each single incident ion and it consists of a plane of sixteen 0.7 mm thick quartz blades. The transverse size of the blades is adapted to the beam intensity profile so that each blade detects about 1/16 of the total beam intensity. The signal produced by Cerenkov effect in the quartz blades is sent to the photomultipliers (one for each blade) through optical fibres.

Standard TDCs record the arrival time of the Pb ions within a 20 ns window, appropriately timed with respect to the ion that has triggered the apparatus. This way the BH information allows to reject in the analysis all the events where more than one ion crosses the BH in this time window (pile–up events). For a detailed description of the beam pile–up correction see Section 3.4.4.

This quartz detector resists counting rates up to 10^8 particles per burst and its detection efficiency is better than 99%.

Moreover, the BH signal is used for timing precisely the trigger signal with less than 1 ns jitter with respect to the Pb ion time of arrival (see Section 2.6.1).

During the proton beam runs, the BH cannot be used because of the large number of incoming particles and is replaced by three ionization chambers filled with argon, which allow to monitor the beam intensity.

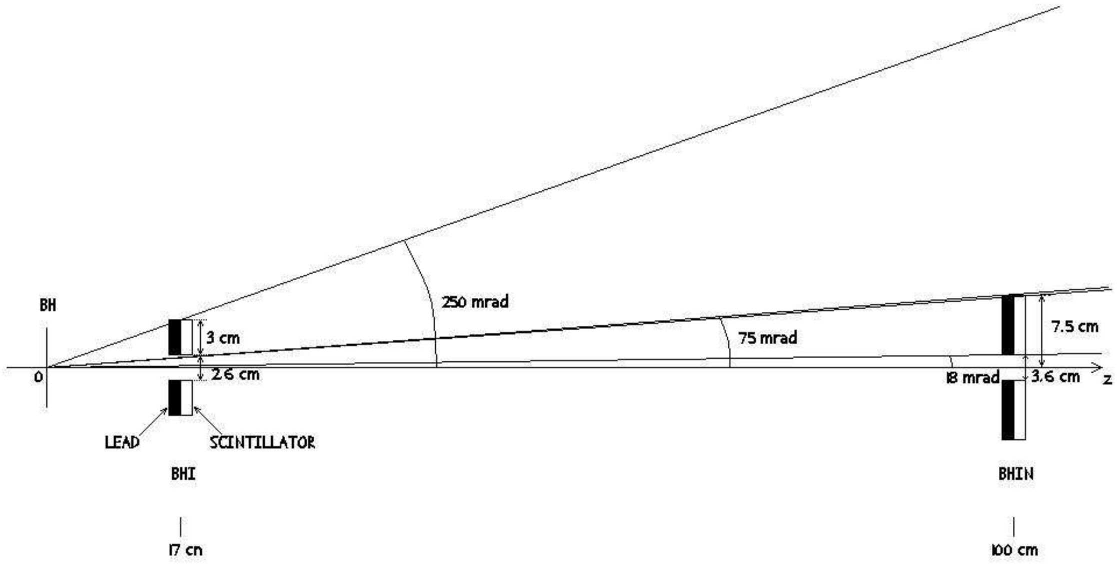

Figure 2.2: *Geometry of the Beam Hodoscope and of the interaction detectors (the BHI and the BHIN). The z axis corresponds to the beam axis and the origin of the abscissae coincides with the BH position.*

2.2.3 Other beam detectors

Two detectors are placed just after the BH and outside the beam line in order to detect possible interactions of the incoming particles inside the BH itself: the BHI (Beam Hodoscope Interactions) and the BHIN (or BHI new) [7] (Fig. 2.2). It is very important to detect these parasite interactions, since the produced fragments could pollute the beam and interact in the target. Moreover, these fragments have a Z/A ratio different from the Pb ions and, consequently, are not correctly focused.

The BHI consists of two scintillator blades of $1 \times 3 \times 8\ cm^3$ (in z, x and y respectively), covering a pseudo–rapidity interval of $2 < \eta < 3.1$.

The BHI new complements the BHI, being placed $1\ m$ after it and covering the pseudo–rapidity domain $3.3 < \eta < 5.1$. It is made up of four scintillator blades of $1 \times 3 \times 9\ cm^3$ arranged around a central hole so that the ions that have crossed the BH do not interact with the BHIN blades.

Two detectors, named "anti–halo" counter (AH) and Beam Anti–Halo (BAH), are located on the beam axis, respectively 8 cm and immediately before the target system. The AH is made up of a quartz blade with a central hole of 3 mm diameter and it allows to reject particles not crossing the central hole: both fragments coming from projectile interactions before the target and Pb ions distant more than 1.5 mm from the beam axis.

The BAH consists of 6 scintillating elements, covering a $15\pi^2\ cm^2$ surface around a 15 mm diameter hole, and allows to detect the residual light fragments due to interactions before to the target.

Two pairs of small wire proportional chambers (called GANIL chambers) are placed 50 cm before the target position in order to monitor the horizontal and vertical beam profile, during the beam tuning operations.

Three scintillator telescopes (called "Jura", "Saleve" and "Vertical") check the beam stability during the proton–nucleus runs, when no scintillating counters can be placed on the beam axis, because of the high beam intensity. The "J" and "S" telescopes lie on the target horizontal plane, while the "V" telescope is vertical. All these telescopes receive only a small amount of the interaction products, being out of the beam axis, and their counting rate depends on the beam impact point on the target.

2.3 The target

Since the probability of producing a muon pair due to the decay of a J/ψ resonance is very low [1], a thick target and a high beam intensity are needed in order to increase the number of nucleus–nucleus collisions per second.

[1] The charmonium production cross–section is $\sigma_{J/\psi}$/nucleon $\sim 30\ nb$ and the branching ratio for the J/ψ in the $\mu^+\mu^-$ channel is $\sim 6\%$.

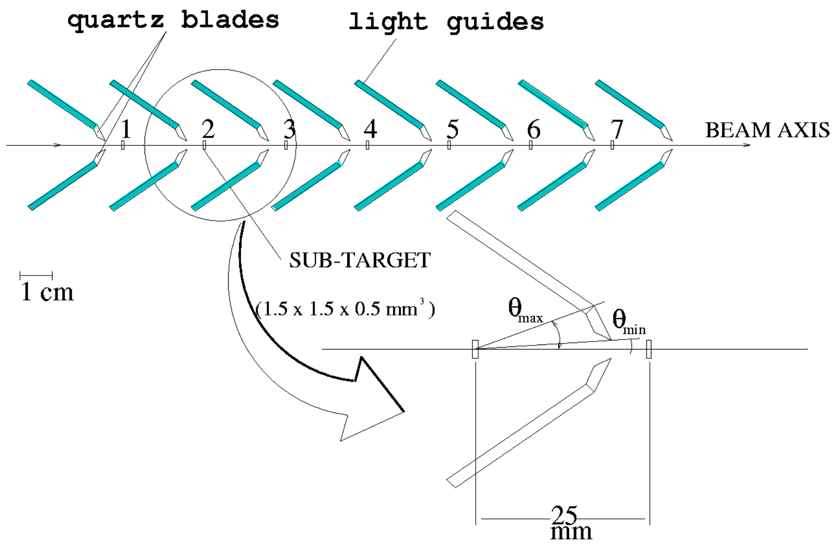

Figure 2.3: *The "active target" system used in the 1995 and 1996 data taking periods.*

However, a thick target has the disadvantage to cause a not negligible rate of reinteractions (inside the target) of the projectile fragments and of the secondary particles produced in a first Pb–Pb interaction. These reinteractions produce a bias on the centrality measurements of the Electromagnetic and the Zero–Degree calorimeters. Therefore eliminating this kind of events becomes of essential importance.

During the 1995 and 1996 Pb–Pb data takings a segmented Pb target was used, made up of 7 subtargets thin enough to minimize reinteractions (Fig. 2.3). Each subtarget is equipped with 2 quartz blades (placed off the beam axis respectively on the left and on the right of the subtarget) [8], allowing the vertex position identification both for a primary interaction and for a reinteraction of the produced fragments.

The quartz material has been chosen for its radiation resistance properties, suitable in a high radiation environment such as that of NA50.

An interaction inside one subtarget produces charged particles ($\pi^{\pm}, K^{\pm}$) that release a signal by Cerenkov effect in the subsequent quartz blades [8, 9]. The geometry of the quartz blades system and the angular properties of the Cerenkov light lead to a signal amplitude strongly correlated to the subtarget that has produced the interaction, allowing the identification of the event vertex and of a possible reinteraction after the primary interaction.

Immediately before the first subtarget, two quartz blades count the interactions in the air before the target system.

The 7 targets are disposed on the beam line at a distance of 25 mm from each other. In the 1995 run, each subtarget was 1 mm thick, for a total length corresponding to

17.5% λ_I. They had a circular transverse area of 2.5 mm diameter, except for the first one, which had a 5 mm diameter in order to intercept the whole beam.

The 1996 target system was modified in order to collect larger statistics: the first and the last subtargets were 1 mm thick, while the other five were thicker (2 mm), for a total length of 12 mm, corresponding to 30% λ_I.

To reduce the probability of fragment reinteractions, in 1998 only one thin Pb target (3 mm of thickness, corresponding to 7% λ_I) was placed on the fourth mechanical target support. The disadvantage of using a thin target is linked to the increase of beam–air interactions, which affect especially the most peripheral events.

In order to eliminate the contamination of these Pb–air interactions, a new target system has been realized for the 1999 (Pb beam at 40 AGeV/c on different targets, interesting for fission studies, as discussed in Chapter 6) and the 2000 data takings.

In the 1999 setup a vacuum system including the target region was realized. The target system in the vacuum consists of a vacuum box containing three different targets, which can rotate in order to have one (and only one) of them on the beam line (Fig. 2.4).

For the 2000 data taking, the beam vacuum tube has been extended up to the multiplicity detector, thus reducing the distance that the incoming particles cover in air, before reaching the centrality detectors. The target vacuum box has been equipped with an appendix crossing the central hole of the MD detectors to extend the vacuum as far as the BeO absorber. In this way there is no background coming from δ rays in air and in the box end cap.

Two quartz blades are placed outside the beam axis respectively on the left and on the right of the used target (among the 3 available ones). They allow the identification of the interaction vertex, by measuring the Cerenkov light produced by the crossing particles.

During the proton–nucleus runs, different targets are used, by placing only a single thin target at a time on the beam line. In 2000, during the acquisition runs with Pb ion beams, a 4 mm thick target was used, corresponding to 10% λ_I.

2.4 The centrality detectors

Since the transition from ordinary nuclear matter to QGP is expected to occur under particularly high conditions of temperatures and baryon densities, it becomes very important to be able to distinguish central collisions, where the high energy density that is reached is more favorable to the phase transition.

The centrality of a collision is defined by the impact parameter b, which cannot be directly measured [2].

In NA50 the centrality is inferred from the measurements of three independent detectors:

[2] b is defined as the minimum distance between the centers of the two colliding nuclei.

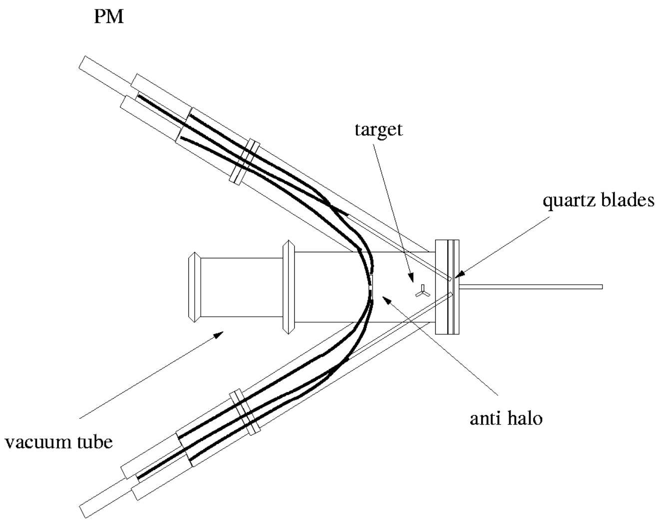

Figure 2.4: *The target vacuum system used in the 1999 and 2000 data takings.*

- the Electromagnetic Calorimeter (EMC) which measures the transverse energy E_T of the neutral particles emitted during the collision (essentially γ particles coming from π° decays)
- the Zero–Degree Calorimeter (ZDC) which measures the energy (E_{ZDC}) released by the projectile nucleons that have not taken part to the collision
- the Multiplicity Detector (MD) which counts the total number (N_{ch}) of charged secondary particles produced in the interaction

All the quantities measured by these detectors are related to the centrality of the collision.

In Fig 2.5 the geometry of a central and of a peripheral collision is plotted. Almost all the nucleons of the projectile and of the target are involved during a central collision, where high densities and temperatures are reached in the central "hot" region of the collision (Fig. 2.5a). Most of these participant nucleons and of the produced secondary particles will hit the MD and the EMC; E_T and N_{ch} will grow with centrality, being themselves approximately proportional to the number of participant nucleons.

In the case of a peripheral collision (high b), most of the nucleons are not involved in the interaction (spectator nucleons, Fig. 2.5b) and leave the target region with nearly the same energy as the beam. They reach the ZDC, which measures a quantity (E_{ZDC}) proportional to the number of the projectile spectator nucleons, i.e. anti–correlated to the centrality of the collision.

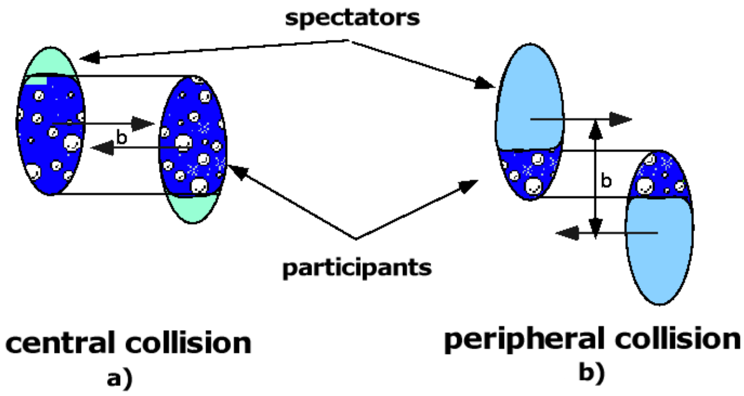

Figure 2.5: *Collision between two ions: a) central and b) peripheral collision.*

The three detectors provide three different and complementary measurements of the centrality. Moreover, the correlations between these three measured quantities are a useful tool to clean the data sample, allowing to reject events that have originated upstream or downstream the target region (see Section 4.3.4).

2.4.1 The Electromagnetic calorimeter

The Electromagnetic Calorimeter (EMC) measures the transverse energy of the neutral particles emitted in the collision (mainly direct γs or γs coming from π° decays) in the pseudo–rapidity interval $\Delta\eta = 1.1 - 2.3$.

As seen before, E_T is one of the essential parameters for the determination of the centrality of the collision and of the reached energy density ϵ.

The EMC is located on the beam axis about 32 cm downstream the target and it consists of polystyrene scintillating fibres (of 2 mm diameter), placed parallelly to the beam direction and arranged into a 14 cm long lead and bismuth alloy converter (see Fig. 2.6).

The ratio between the fibre volume and the passive volume is 1:2 and the thickness of the converter corresponds to about 15 radiation lengths ($X_o = 0.95$ cm).

The EMC has the same hexagonal shape as the muon spectrometer and is placed outside its acceptance in order to reduce the deterioration of the mass resolution of the spectrometer. A central hole with a 2.4 cm radius allows the passage of the beam particles that have not interacted inside the target.

The detector is divided into six azimuthal sectors and each of them is further subdivided into four radial rings which cover roughly equal pseudo–rapidity bins. The division makes it possible to study the transverse energy as a function of the pseudo–rapidity.

The light produced in the scintillating fibres is collected by optical fibres to the 24 (6 sextants $\times$ 4 rings) photomultipliers, which are radially disposed around the calorimeter, out of the charged particles flux in order to avoid radiation damage.

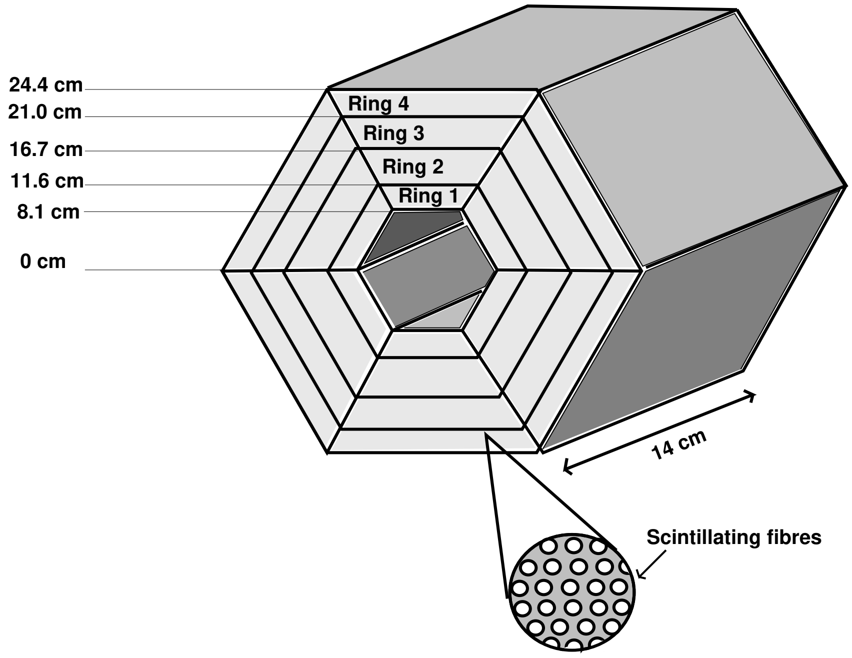

Figure 2.6: *The NA50 electromagnetic calorimeter.*

The calibration of the calorimeter has been performed by means of electron beams of 10, 20 and 30 GeV/c. The stability of the photomultiplier gain is continuously monitored by sending a laser pulse to each photomultiplier.

The total neutral transverse energy is obtained as the sum of the contributions from all the units (rings and sextants) of the calorimeter

$$E_T = \sum_i \alpha(i)\ E_i\ sin\theta_i \tag{2.1}$$

where E_i is the energy measured in the unit i, θ_i is the mean angle formed by the unit i with respect to the target, $\alpha(i)$ is the correction factor for the charged particles contribution, depending on the target position.

The resolution of the detector is

$$\frac{\sigma(E_T)}{E_T} \approx \frac{0.72}{\sqrt{E_T}} \tag{2.2}$$

where E_T is measured in GeV. For central Pb–Pb collisions the resolution is about 7%.

The contribution from charged particles is of the order of 50% of the raw transverse energy measured by the calorimeter. This contamination is estimated through a GEANT simulation and then subtracted from the raw transverse energy in order to have a clean measurement of E_T to be used in the further analysis [10].

2.4.2 The Zero–Degree calorimeter

The next chapter is entirely devoted to a detailed description of this detector.

2.4.3 The Multiplicity Detector

The Multiplicity Detector (MD) measures the angular distribution and the multiplicity of the charged particles produced during the collision, in the pseudo–rapidity window $\Delta\eta = 1.5 - 3.9$ [11, 12].

Since it is placed 10 cm after the target region and before the preabsorber, the MD is subject to high counting rates and has to opearte in a very radioactive environment (characterized by a dose of the order of 10 Mrad for the most irradiated part of the detector and by particle fluxes of 10^{14} particles/cm^2 and more). Therefore it is required to be very fast (dead time below 50 ns), radiation resistant and, to provide a good estimation of the particle multiplicity, of high granularity.

The MD is made up of two identical dicks (MD1 and MD2) of about 7000 silicon strips each [12]. One of these two planes is shown in Fig. 2.7.

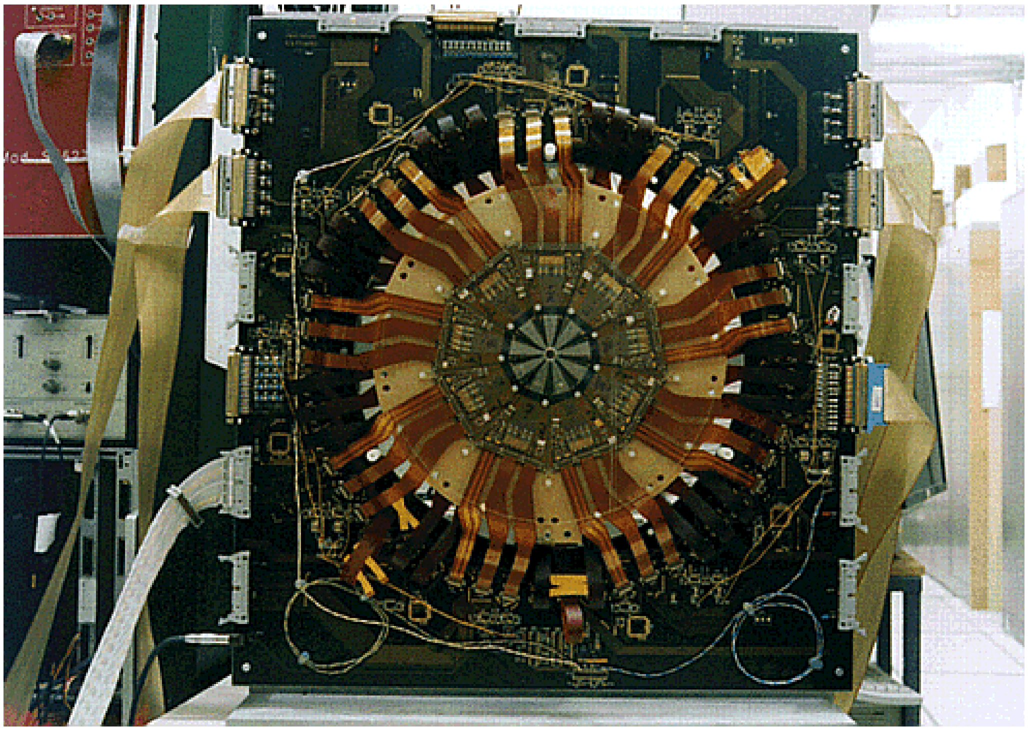

Figure 2.7: *One of the two MD planes.*

The two disks have an inner radius of 6.5 mm and an outer radius of 88.5 mm and are azimuthally and radially segmented, so that each element covers a region of $\Delta\eta \sim 0.02$ and $\Delta\phi \sim 10°$. The first disk allows to count the charged particles produced in the Pb–Pb interactions in the first subtargets; the second one plays a role for interactions with vertex localized in the second part of the target system.

The MD gives information on the $dN/d\eta$ distribution and, in the runs where different subtargets are used (1995 and 1996 data takings), the angular distribution of charged particles is measured thanks to information on the position of the interaction vertex provided by the active target. This measurement is affected by uncertainties due to the beam size and to the multiple scattering inside the target.

From 1998 an alternative method of target recognition (besides that based on the quartz blades located downstream each subtarget), based on the MD, has been developed (see section 4.3.4). The interaction vertex is reconstructed by means of an algorithm that evaluates the probability of having a couple of strips on the two detectors hit by a particle coming from one of the 7 subtargets [13].

2.5 The muon spectrometer

The NA50 spectrometer derives, with some small modifications, from the NA10 muon spectrometer [2], realized to measure the production of high mass muon pairs with good mass resolution.

The spectrometer has hexagonal symmetry around the beam direction and consists of (see Fig. 2.8):

1. a hadron absorber which stops all the secondary particles produced in the interaction, except for the muons;
2. a toroidal field magnet which bends the muon tracks;
3. eight multiwire proportional chambers for the reconstruction of the muon tracks before and after the magnet;
4. four planes of plastic scintillator hodoscopes used for the trigger.

The spectrometer extends over 18 metres along the beam axis and detects dimuons in the pseudo–rapidity interval $2.8 < \eta < 4.0$. Dimuon events can come from different sources: the decay of hadronic resonances (ϕ, ρ, ω, J/ψ, ψ'), the decay of pions and kaons produced during the interaction, the decay of charmed mesons and from hard scattering processes.

The resulting J/ψ mass resolution is 3.1% (r.m.s.) and the acceptance for muon pairs is of the order of 15% for invariant masses above 3 GeV/c^2.

2.5.1 The hadron absorber

An hadron absorber has been placed between the target and the muon spectrometer with a double role:

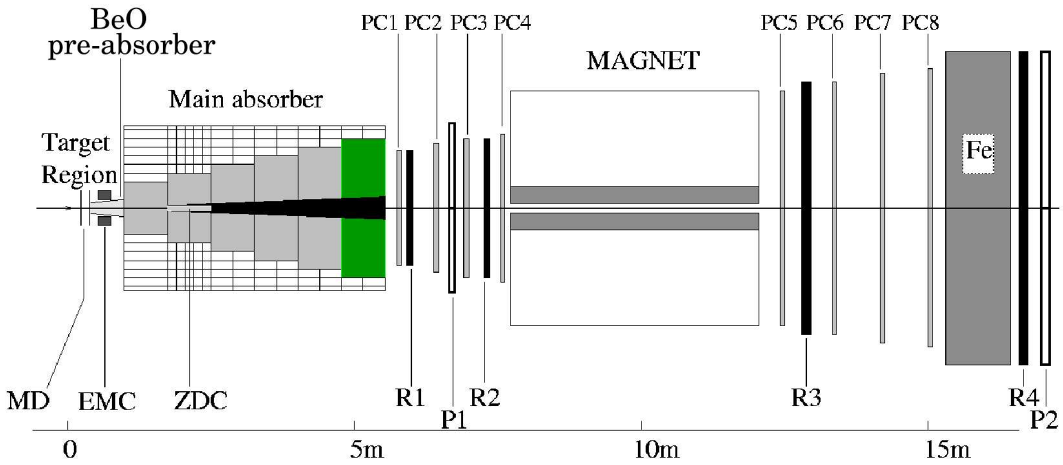

Figure 2.8: *The NA50 muon spectrometer.*

1. to stop the particles of the hadron showers (mostly π and K mesons), generated in the Pb–Pb interactions, before they decay into muons; this filters only the dimuons coming from the decay of hadronic resonances (ϕ, ρ, ω, J/ψ, ψ');

2. to absorb the beam particles that have not interacted in the target and that have not been stopped in the ZDC.

A material with a short interaction length λ_I (high mass number A) must be chosen to contain the hadronic showers. However, the absorber must not affect the momentum of muons that are not stopped by the absorber itself and that reach the magnet region. In order to minimize the multiple scattering, which can produce a deterioration of the mass resolution of the spectrometer (causing problems for a correct identification of the resonances), materials with long radiation length $X_\circ$ (small atomic number Z) are needed. A compromise between the requests of a small

Material	Aim	Length (cm)	λ_I (g/cm^2)	ρ (g/cm^3)	X_0 (g/cm^2)
BeO	Pre-abs.	59.1	84.90	2.81	41.30
C	Main-abs.	400.0	86.30	1.93	42.70
Fe	Main-abs.	80.0	131.90	7.20	13.84
Air	Main-abs.	80.0	84.40	$1.29\ 10^{-}3$	36.66
Ta	ZDC(Main-abs.)	65.0	197.95	16.6	6.83
W	Main-abs.	80.0	185.00	17.80	6.76
U	Main-abs.	320.0	199.00	18.95	6.00

Table 2.1: *Characteristics of the absorber and pre-absorber materials.*

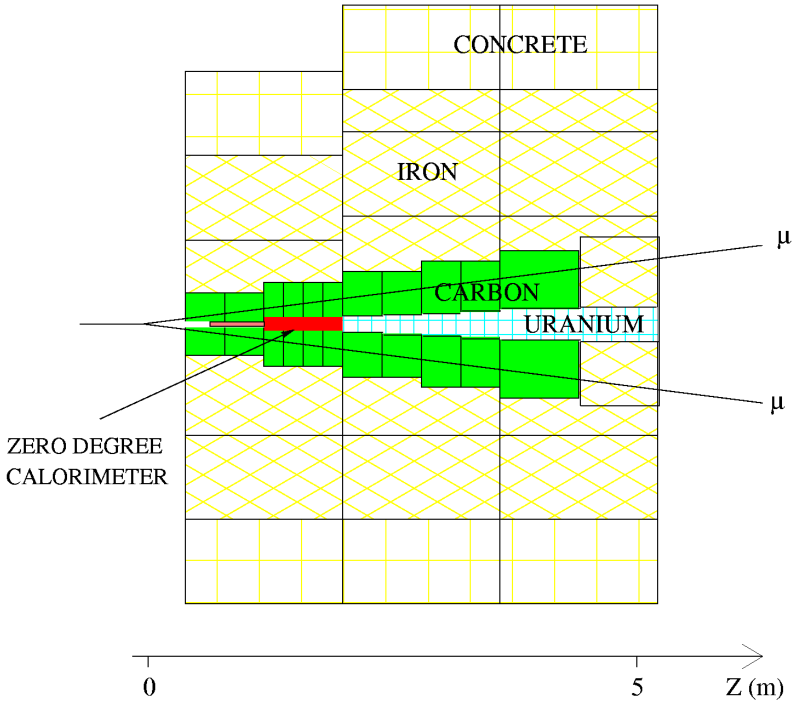

Figure 2.9: *The main absorber.*

λ_I and of a high $X_\circ$ values can be reached by an hadron absorber composed of different layers of materials, which minimize the $\lambda_I/X_\circ$ ratio (see Table 2.1). It is made up of three elements:

1. the BeO preabsorber, which is the first element of the absorber, formed by a 60 cm long conical block and placed 25 cm downstream the target center (Fig. 2.8). The covered pseudo–rapidity interval is $2.42 < \eta < 4.43$. A central hole along the beam axis lets the ions that have not interacted inside the target or the projectile fragments pass through and reach the ZDC.

2. The main absorber, placed immediately after the preabsorber and 4.8 m long (Fig. 2.8), stops the residual beam ions, the fragments produced in the collision and the very forward hadrons. The central part has a conical shape around the beam axis and is made up of 80 cm of air followed by the ZDC, then by 15 cm of air, and finally by a 3.2 m long block of Uranium. This central cone is surrounded by cylinders of Carbon for the first 4 metres and of Iron for the remaining 80 cm. Finally, Iron and concrete blocks are placed all around the Carbon cylinders to stop the particles produced at high angles.

   All these elements cover completely the spectrometer acceptance. The muon tracks are affected by a small angular deflection due to the multiple scattering in the Carbon and Iron cylinders [3].

3. A final 1.2 m long iron wall is arranged between the last MWPC and the last hodoscope (R4) to stop the hadrons that have been able to escape from the previous absorbers and that could give fake triggers (Fig. 2.8). Being placed after the MWPCs, this last part of the absorber does not affect the spectrometer resolution and guarantees that the particles crossing the R_4 hodoscope are muons.

2.5.2 The magnet

The muon transverse momentum is deduced from the deviation of the muon trajectories induced by a toroidal field magnet. The magnet constitutes the central element of the muon spectrometer and it is placed at about 10.5 m from the target (Fig. 2.8). It has a length of 4.8 m and an hexagonal symmetry around the beam axis (Fig. 2.10).

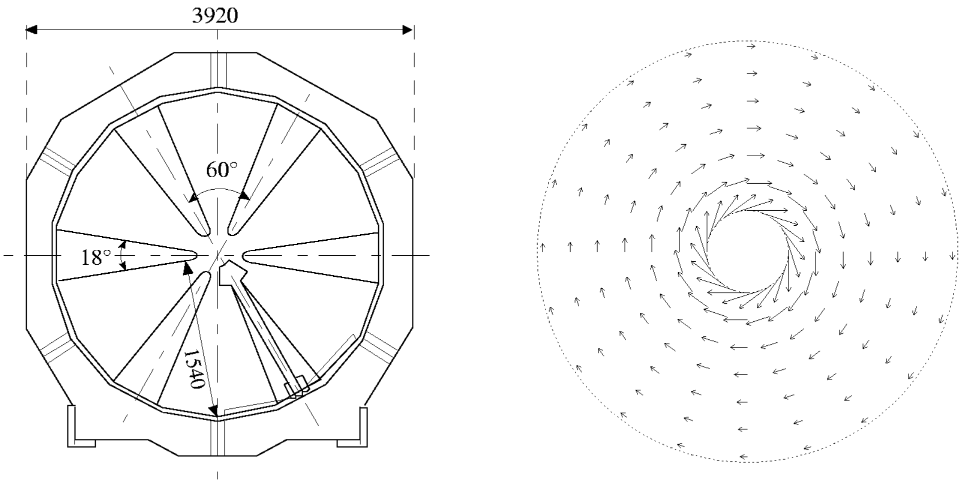

Figure 2.10: *View of the front face of the NA50 magnet (on the left); shape of the magnetic field in a plane orthogonal to the beam axis (on the right).*

The total radius of the magnet is 2.05 m, but the angular acceptance (between $\sim$ 35 mrad and $\sim$ 115 mrad, corresponding to the pseudo–rapidity interval $2.6 < \eta <$

[3]The angular deflection of the muon tracks is of the order of $\Delta\theta_\mu \simeq 64$ mrad/p (GeV) in Carbon and $\Delta\theta_\mu \simeq 101$ mrad/p (GeV) in Iron [14].
The muon angle is defined, in the Gaussian angular distribution approximation,as

$$\theta_\mu = tan^{-1}(\frac{p_t}{p_l}) \tag{2.3}$$

where p_t and p_l are respectively the transverse and the longitudinal muon momenta in the laboratory frame.

4.26) is limited to the space between the 29.5 cm internal radius and the 1.54 m external radius.

The magnetic field is produced by six bobines mounted on six iron supports, each of them occupying an azimuthal angle of 18°. The pulsed current (of 7000 A) is synchronized with the SPS cycle and generates a magnetic field that is essentially toroidal (see Fig. 2.10) in the azimuthal direction and with an intensity inversely proportional to the distance r from the beam axis:

$$\overrightarrow{B}(r) = \frac{B_o}{r}\ \overrightarrow{u_\varphi} \tag{2.4}$$

where $\overrightarrow{u_\varphi}$ is the azimuthal versor, B_o is a constant depending on the current intensity ($B_o = 0.383\, T \cdot m$ for I = 7000 m typically used in NA50). A current value of 7000 A has been chosen in order to eliminate the soft muon background and to get a J/ψ mass resolution of $\simeq 3\%$.

This current in the magnet provides a pure toroidal field $B_\phi = 0.51$ T at the mean radius r = 75 cm with $\int Bdl = 2.1\ T \cdot m$. In such a magnetic field, a charged particle emitted from the target remains on the same azimuthal plane and is deflected only along the polar direction by an angle inversely proportional to its transverse momentum [15]:

$$\Delta\theta \simeq \frac{qB_o}{p_T} ln(\frac{z_2}{z_1}) \propto \frac{1}{p_T} \tag{2.5}$$

where z_1 and z_2 are the distances of the beginning and of the end of the magnet from the target position.

In order to avoid systematic effects related to the sign of the magnetic field, the polarity of the magnet has been reversed every few hours during the data taking period, so that half of the total statistics has been collected with one polarity, half with the opposite one. The amplitude of the magnetic field is continuously checked by means of a Hall–probe.

During the off–line analysis, events where at least one of the two muons passed through one of the Iron supports (and so underwent a severe multiple scattering) are rejected.

2.5.3 The tracking chambers

The reconstruction of the muon tracks is performed by means of the measurements provided by 8 Multi–Wire Proportional Chambers (MWPCs), shown in Fig. 2.1. Four chambers ($PC_{1,2,3,4}$) are placed before the magnet, immediately after the absorber, in order to reconstruct the first part of the muon track, pointing to the interaction vertex. A second set of chambers ($PC_{5,6,7,8}$) is disposed after the magnet for the reconstruction of the track after the deflection inside the magnetic field.

The chambers have an hexagonal geometry and each of them is equipped with 3 independent planes of anode wires rotated respectively by 0, 60 and 120 degrees with respect to the vertical axis, as it can be seen in Fig. 2.11. This way, the spatial coordinates of the muon tracks can be determined in the three directions (u,v,w).

The anodes are made up of gold–plated tungsten wires, 20 μm in diameter and 3 mm spaced. The upstream chambers have a radius of 1.3 m and consist of 749 wires each, while the downstream ones are bigger (3 m radius) and equipped with 1229 wires each.

The MWPCs are fluxed with a gas mixture of Argon (80%), Isobutane (19.8%) and Freon (0.2%).

The three planes of each chamber are placed 2.2 cm from each other.

The chamber system provides a measurement of the muon angle with an uncertainty of some tenth of mrad.

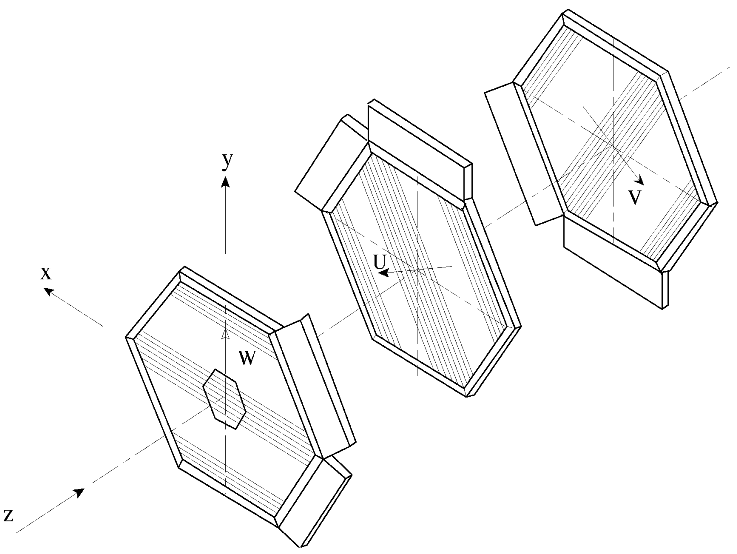

Figure 2.11: *The NA50 MWPC system.*

2.5.4 The trigger hodoscopes

The signal that triggers the data acquisition system is provided by the four hodoscopes R_1, R_2, R_3 and R_4, which allow a first determination of the muon trajectory too. They have an hexagonal symmetry, like the rest of the apparatus, and are divided into six sextants of 30 (for R_1 and R_2, 24 for R_3 and 32 for R_4) scintillator blades each, placed parallelly to the outer border and perpendicularly to the symmetry axis (Fig. 2.12).

The light produced in each scintillator by the crossing particles is collected by plastic light–guides and read by a single photomultiplier.

The R_1 and R_2 planes are placed between the main absorber and the magnet and R_2 is the homothetic copy of R_1 with respect to the central subtarget position. For

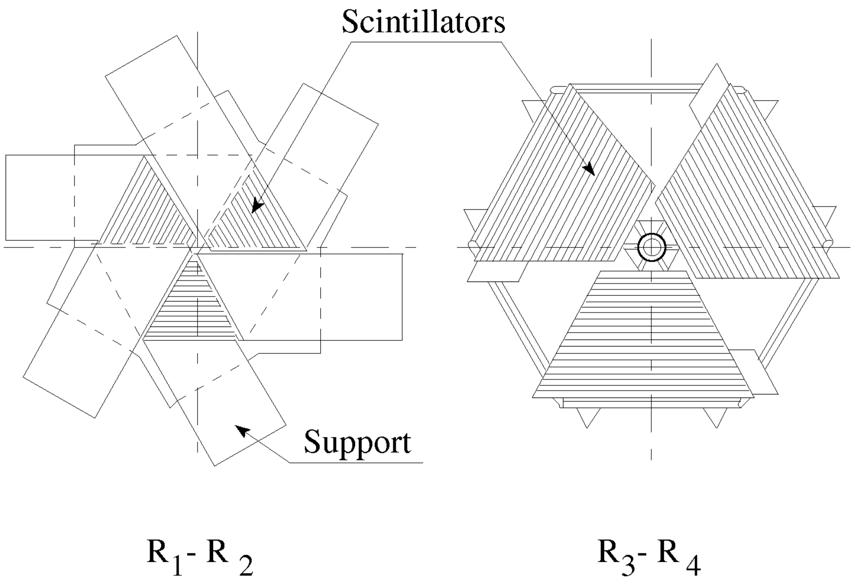

Figure 2.12: *The NA50 electromagnetic calorimeter.*

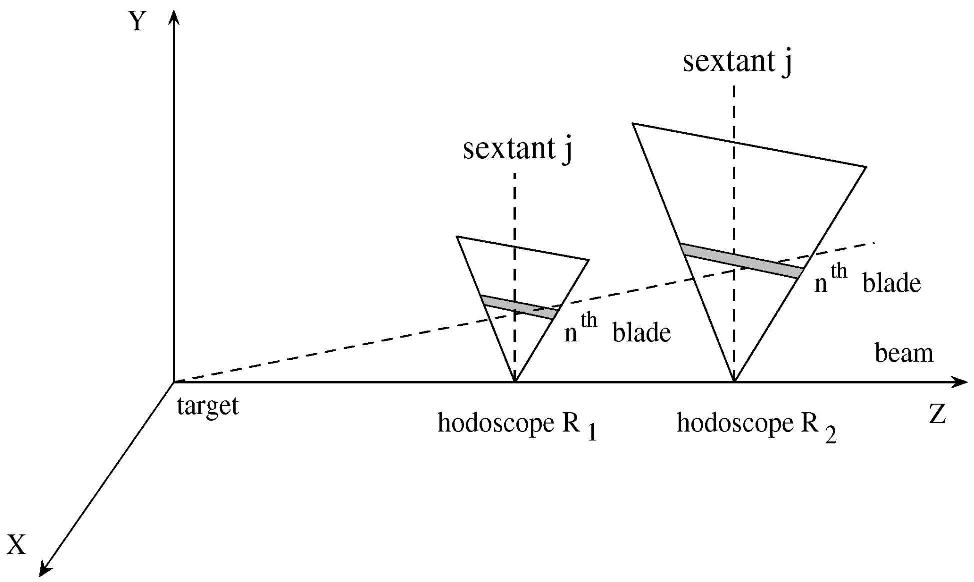

Figure 2.13: *Coincidence* $V = R_1^i \times R_2^i$.

this reason and since for these 2 hodoscopes the dimensions of the plastic blades increase gradually with the distance from the beam axis, the trajectory of a particle crossing the blades R_1^i and R_2^i comes directly from the interaction vertex, as it is visible in Fig. 2.13.

The coincidence $V = R_1^i \times R_2^{i-1}$ is also accepted to take into account the multiple scattering in the absorbers.

The hodoscopes R_3 and R_4 are placed after the magnet, one before and the other after the iron wall. Thus R_4 allows to ensure that the detected particles are muons. All their scintillating blades have the same width (5.5 cm) and provide a first estimation of the trajectory of the particles after their deflection inside the magnet. Together with the signal coming from R_1 and R_2, they contribute to form the dimuon trigger signal and allow also to estimate the transverse momentum of the muons from the measure of the deflection angle through the magnet.

Two other hodoscopes named P_1 and P_2 are placed respectively before the magnet and after the iron wall [16]. Each P_1 scintillator is connected to a photomultiplier placed on the outside edge, while P_2 is connected to two photomultipliers whose signals reach a *mean timer*. During special periods of the data taking, the magnetic field is set to zero and these two telescopes are used to trigger on straight tracks. They provide an independent trigger, which allows to evaluate the efficiency of the dimuon trigger system, which ranges from 86 to 90%.

2.6 The trigger system

In the NA50 experiment three different kinds of trigger are used for selecting events to be acquired and recorded by the data acquisition system.

2.6.1 The dimuon trigger

This is the main trigger of the experiment and it was thought to select muon pairs (dimuon) originated in the Pb–Pb interactions and to reject muons produced by K and π decays or in interactions inside the absorber. The trigger is based on the information provided by the four hodoscopes and is a two–level trigger. The first level selects events where two tracks coming directly from the target region have crossed the spectrometer in two different sextants, satisfying the coincidence $V_i = R_1^i \times (R_2^i + R_2^{i-1})$, which defines the first half of the muon track (as already explained in Section 2.5.4). If the $V_i \times R_4$ coincidence is satisfied, a particle has crossed the whole apparatus. The R_4 hodoscopes, placed after the iron wall, ensures that the detected particle is really a muon. The $V_i \times R_4$ coincidence is validated by the R_3 hodoscope in order to reduce the rate of fake triggers, due to accidental tracks before and after the magnet.

The system provides also a rough estimation of the deflection angle of each muon and of its transverse momentum p_T. Single muons are grouped into four categories ,on the basis of their p_T, and sent to a logical system called "Magic box" which produces an output signal whenever two muons cross different sextants of the hodoscopes. The coincidence of the V and of the "Magic box" signals gives the trigger of the experiment, the so–called TSJ (Trigger Sans Jitter), which has a time instability of about 1 ns. This time fluctuations ("jitter") can be reduced thanks to the information provided by the BH, which supplies the time reference of the experiment (the time when a Pb ion hits one of the BH blades). The coincidence between the TSJ and the signal of the 16 BH blades allows the stabilization of the trigger and reduces its "jitter" to 0.5 ns. The resulting trigger is called T0J (Trigger Zero Jitter) and it is the basic trigger of the apparatus. In case the synchronization between the TSJ and the BH is not achieved, the TSJ is considered and it is defined TSJ SOS.

2.6.2 The Minimum Bias triggers

A Minimum Bias (MB) trigger is generated whenever the signal of the ZDC overcomes a threshold corresponding to the minimum signal detectable by the ZDC [17]. A very low value has been fixed for this threshold (of the order of 50 mV), in order to have a trigger every time a particle hits the ZDC and to avoid any trigger bias. Most of these triggers correspond to Pb ions that have not interacted in the target and have released all their energy ($\simeq$ 33 TeV) inside the ZDC.

This trigger is downscaled to keep its rate at a reasonable level and it is collected through the data taking, together with the dimuon trigger.

In the 2000 data taking an other MB trigger has been used: the BH minimum bias trigger. It is based on information provided by one central blade of the BH. As already said, the BH blades are placed 22 m before the target, where the beam spot is large enough that the detector can tag each single incident ion. The Pb ions of the projectile hit the BH before interacting in the target and therefore they produce signals proportional to the beam incident energy. The choice of the minimum threshold is easier with the BH trigger than with the ZDC one, since the MB BH spectrum consists of the clear peak of the non-interacting Pb ions (while in the MB ZDC spectrum also events corresponding to interactions in the target are present).

2.6.3 The Laser trigger

The so–called laser trigger is generated by means of a pulse generator, which sends a laser pulse to the photomultipliers of the EM calorimeter. This trigger is useful to study the gain stability for these PMs, but also to estimate the pedestal values [4] for other detectors, whose PMs are not connected to this laser.

[4] The pedestal is the answer of an ADC when there are no inputs to the detector.

2.7 Data acquisition and running conditions

The data acquisition of the NA50 experiment started in 1994 with a "technical run", aimed at the tuning of the detectors. In 1995 the first run devoted to real physics purposes was performed, while during 1996 a higher statistics sample was collected, in particular to better understand the peripheral collisions with lower statistical errors. For this reason a higher beam intensity and a thicker target were used. To solve the problems of the reinteractions due to the thick target, the 1998 data taking tried to shed more light on the most central Pb–Pb collisions, by using a thinner target. Finally, in the year 2000 a latest acquisition run with a target vacuum system was devoted to the study of the peripheral events, where the interactions of the Pb ions with the air around the target are more probable.

The characteristics of these data taking periods are summed up in Table 2.2.

Data taking period	1995	1996	1998	2000
Number of subtargets	7	7	1	1
Total target thickness	7 mm ($17\%\ \lambda_I$)	12 mm ($30\%\ \lambda_I$)	3 mm ($7\%\ \lambda_I$)	4 mm ($10\%\ \lambda_I$)
Target environment	air	air	air	vacuum
Beam Intensity (Pb/burst)	3.2×10^7	5.4×10^7	5.5×10^7	6.5×10^7
Weeks of run	5	6	8	6
Number of triggers	58×10^6	170×10^6	80×10^6	195×10^6
Number of J/ψ events	53400	190000	40000	99850
Number of Drell-Yan ($M_{\mu\mu} > 4.2 GeV/c^2$)	630	2100	500	1170

Table 2.2: *Comparison of some characteristics of the NA50 data taking periods.*

For each event that fulfills the trigger requirements, the information about all the detectors is stored into temporary memories, which are able to contain data of the whole 2.5 s effective spill of the burst (up to 5000 events, corresponding to about 17 Mbytes [18]). At the end of the spill, the relative data are transferred via transputer links (10-20 Mbits/s) to the final acquisition memories, connected to the tape recording system. In parallel, the same information is sent to the "spy" crate, which allows a continuous on–line monitoring of the detector operations, without interfering with the acquisition. More details on the acquisition procedure can be found in [19].

Bibliography

[1] M.Abreu et al. (NA50 coll.), CERN/SPSLC 91-55/SPSLC/P 265 (1991).

[2] L. Anderson et at., Nucl. Instrum. Methods 223 (1984) 26.

[3] C.Baglin et al. (NA38 coll.), Phys. Lett. B 220 (1989) 471.

[4] M.C.Abreu et al. (NA50 coll.), Phys. Lett. B 449 (1999) 128.

[5] M.C.Abreu et al. (NA50 coll.), Phys. Lett. B 530 (2002) 33.

[6] M.C.Abreu et al. (NA50 coll.), Phys. Lett. B 530 (2002) 43.

[7] L.Villatte, PhD Thesis, Université de Paris 7, 2001.

[8] F.Bellaiche et al., Nucl. Instrum. and Meth. in Phys. Res. A398 (1997) 180.

[9] F.Bellaiche, PhD Thesis, Apr. 1997, Université de Lyon.

[10] M.C. Abreu et al. (NA50 coll.), Phys. Lett. B 410 (1997) 327.

[11] B.Alessandro et al., Nucl. Instr. Meth. A 360 (1995) 189.

[12] S.Beolé, PhD Thesis, February 1998, Universitá di Torino.

[13] F.Prino, PhD Thesis, December 2001, Universitá di Torino.

[14] Review of particle physics, Phys. Rev. D 66 (2002) 010001.

[15] F.Fleuret, PhD Thesis, Apr. 1997, E. P., Paris.

[16] A.De Falco, PhD Thesis, Feb. 1997, Universitá di Cagliari.

[17] R.Arnaldi, PhD Thesis, December 2000, Universitá di Torino.

[18] M.C. Abreu et al. (NA50 coll.), Phys. Lett. B 410 (1997) 337.

[19] V.Capony, PhD Thesis, July 1996, Université de Savoie.

Chapter 3

The Zero Degree Calorimeter

3.1 Introduction

The Zero Degree Calorimeter (ZDC) gives a measure of the energy of the projectile nucleons that have not interacted in the target (projectile spectators) and that have continued to travel forward with the same energy per nucleon as the incident beam. Depending on the impact parameter, a different number of nucleons is affected by the interaction inside the target. The more peripheral the collision is, the larger is the number of the spectator nucleons and projectile fragments (emitted at very small angles) that arrives in the ZDC. From the measurement of the energy released in the ZDC it is possible to deduce the number of participant nucleons and therefore an estimation of the centrality of the collision [1].

In this chapter I will describe the requirements that the NA50 ZDC has to fulfill in order to be inserted in the pre–existing NA38 experimental setup. The pedestal subtraction and the calibration of the ZDC will be performed for the 2000 data taking. Finally, I will provide an estimation of the radiation damage of the detector during the entire period of data acquisition.

3.2 Characteristics of the NA50 ZDC

Since the NA50 ZDC, as an estimator of the centrality of the collision, was introduced in the pre–existing NA38 setup, it had to satisfy some experimental requirements, which imposed strict limits on its technical features [2]. The ZDC is placed inside the

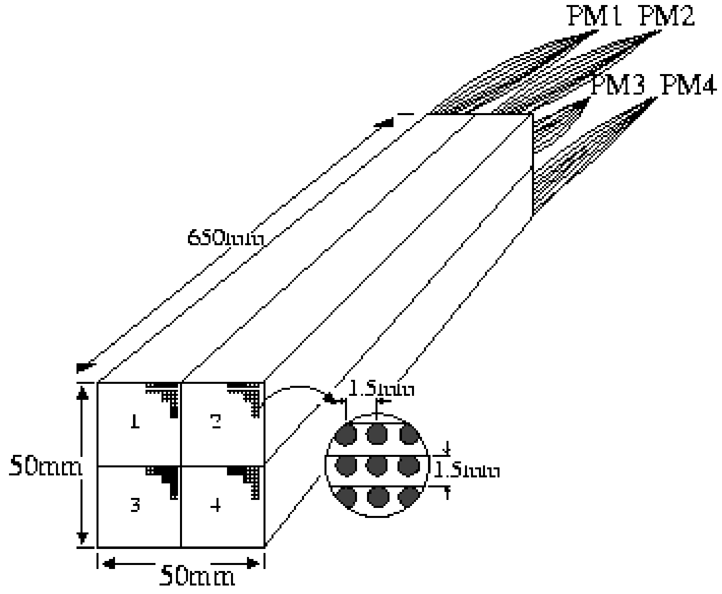

Figure 3.1: *The NA50 Zero Degree Calorimeter.*

hadron absorber, on the beam axis, at 165 cm from the target center (see Fig. 2.1). It is the first element of the beam dump, made up of high density and high Z material. Hence it has to lie outside the spectrometer angular acceptance in order to minimize the multiple scattering of the detected muons. This limits the transverse size of the ZDC to $5 \times 5\ cm^2$. Also its longitudinal size is limited to 65 cm, due to practical reasons linked to the structure of the absorber.

An other important requirement for the NA50 ZDC is the radiation hardness. Actually it is disposed on the beam trajectory, and therefore exposed to a high level of radiation. As I will explain in Section 3.4.3, it has been estimated that, in the six weeks of the 2000 data taking period, at a beam intensity of $6 \div 7 \cdot 10^7$ ions/burst, the dose released in the calorimeter central zone is of the order of 5.5 Grad. Such a value is much higher than the dose tolerated by plastic scintillators as active material of the calorimeter. Therefore the NA50 calorimeter makes use of quartz fibres [3, 4, 5] as active material, where the charged particles of the showers, generated in the absorber, produce light for Cerenkov effect.

As a consequence of the high intensity used, the signal duration has to be very short ($\leq\ 10\ ns$) to reduce pile–up problems. The advantage of the chosen detection technique is that the intrinsic speed of the Cerenkov effect makes the detector suitable for experimental triggering purposes.

The ZDC is also required to be position sensitive, in order to provide a continuous monitoring of the beam position and of the beam spot size during the data taking.

The response to all these requirements is a quartz fiber spaghetti calorimeter (shown in Fig. 3.1), characterized by a high Z passive absorber, where the charged particles produce electromagnetic and hadronic showers, and by a sensitive material (the quartz fibres), meant for measuring the energy of the shower particles. The passive material is made up of 30 Tantalum slabs (each of them 1.5 mm thick), grooved to host 900 quartz fibres uniformly distributed and parallel to the beam line. The quartz to Tantalum volume ratio is 1/17. Tantalum as passive element of the calorimeter has the advantage of having a small interaction length ($\lambda_I \sim 11.9\ cm$) and of being easier to machine than other materials with similar interaction lengths, such as Tungsten.

The fibres have a pure silica core (365 μm diameter) which allows the light production by Cerenkov effect, a silica fluorinate cladding (400 μm diameter) which guarantees the total reflection of the light inside the fibre itself and which is much more radiation resistant than polymer claddings, and a hard polymer coat (430 μm diameter) which protects the fibre from abrasions or chemical agents. The numerical aperture for the fibre is $NA = \sqrt{n^2_{core} - n^2_{cladding}} = 0.22$ [3]. The total length of the fibres is 180 cm, of which 65 cm are inside the Tantalum matrix, while the rest is bent at 90° with respect to the ZDC axis and acts as a light guide toward the photomultipliers, located at about 1 m from the beam line, in order to reduce the background of the shower particles crossing the PM window. The four fibres closest to the beam axis start 10 cm downstream from the ZDC front face and these initial 10 cm of grooves are filled with Tungsten rods. This way we can reduce the radiation damage in the central fibres (much more hit by the beam particles) and to avoid channeling of heavy nuclear fragments in the fibres, which can bias the centrality measurement. This solution produces a slightly worse energy resolution, but is technically simpler than fibre tilting.

This disposition of the fibres inside the calorimeter reduces of 50% the Cerenkov light production, which would be maximized by the fibre orientation at 45° with respect to the beam direction. The choice of disposing the fibres parallel to the beam axis is imposed by mechanical and technical constraints connected to the need to introduce the calorimeter into the hadron absorber. Nevertheless even if this configuration lowers the produced light yield, it does not affect the ZDC energy resolution, which is independent of the photoelectrons statistics, in the energy regime we work at [2].

The ZDC is divided into four towers. The fibres are grouped into four bunches and arrive at four different photomultipliers (6–stages Philips XP2242B, operating with a gain of about $5 \cdot 10^3$, corresponding to a mean anode current of 30 μA when the ZDC is exposed to the full–intensity Pb beam). The choice of the PMs is dictated by the need to keep the anode current under 100 μA, in order to reduce instability problems.

The division of the ZDC into four towers makes the calibration procedure easier (for details see Section 3.4.2) and makes the detector position sensitive. Actually

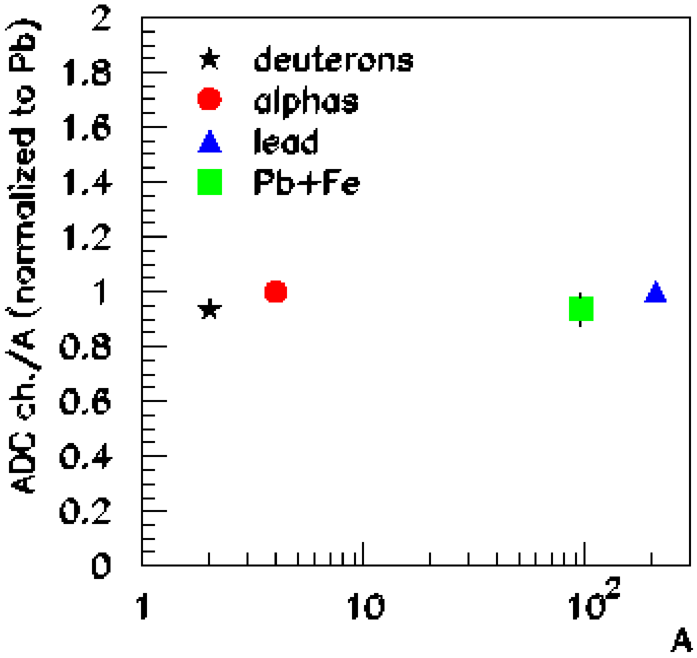

Figure 3.2: *Response of the ZDC to different nuclear beams of 158 AGeV/c: ratio between the ADC channel corresponding to the Pb peak observed for each projectile and its mass number A. All the ratios are normalized to that of Pb.*

the coordinates of a given Pb ion entering the ZDC are estimated by evaluating the centroid of the shower

$$x_{ZDC} = \frac{\sum_{i=1}^{4} Q_i^{\alpha} x_i}{\sum_{i=1}^{4} Q_i^{\alpha}} \tag{3.1}$$

where Q_i is the ADC signal of the ith tower, x_i is the x coordinate of its center and $\alpha = 0.46$ was tuned to the data to minimize the experimental spatial resolution [6]. The y coordinate can be analogously evaluated, thanks to the symmetry of the detector. The ZDC spatial resolution is found to be of the order of few hundreds μm (that is the order of magnitude of the beam spot size on the calorimeter front face). Therefore the ZDC can be used to check continuously the beam position and its spot size during the data taking.

A 60 cm long copper cylindrical collimator is arranged in front of the ZDC, to reduce the background due to pions and participant nucleons. The ZDC acceptance is limited by the conical aperture of the collimator (35 $mrad$, corresponding to a 7 mm radius hole on the ZDC front face) to the pseudorapidity region $\eta \geq 6.3$.

The ZDC measures essentially the energy carried by nucleons that have not participated in the collision and that have left the interaction point with the same energy as the incident beam. From the measurement of E_{ZDC} we can deduce the number of spectator nucleons and hence the centrality of the collision. Nevertheless, in order to use the ZDC as a centrality detector, it is important to check that its response is linear as a function of the number of spectator nucleons. This has been tested by means of ion beams of different mass numbers but with the same energy per nucleon (158 AGeV/c) [2]. The results of this test are reported in Fig. 3.2. For each nuclear beam, the ratio between the ADC channel corresponding to the Pb peak observed for that projectile and the projectile mass number remains constant as a function of the mass number. This indicates a linear behaviour of the detector, in the region $A = 2 - 208$.

An other important characteristic of the ZDC is its energy resolution, which can be parametrized by

$$\frac{\sigma}{E} = \frac{a}{\sqrt{E}} \oplus b \oplus \frac{c}{E} \tag{3.2}$$

where the three independent terms are respectively:

1. $a/\sqrt{E}$ is the fluctuation due to statistical processes (i.e. the production of ionization charge, of Cerenkov photons...), on which the detection of the shower particles is based. The resolution improves with the increase in energy, proportionally to $1/\sqrt{E}$. But other factors affect the energy resolution, causing a deviation from $1/\sqrt{E}$.

2. b is a constant term linked to non–gaussian fluctuations on the energy that leaks from the calorimeter (essentially π°), to errors in the calibration or in the pedestal subtraction, to the non–uniformity in the signal production and collection.

3. the term c/E represents the influence on $\sigma(E)/E$ of the electronics noise and of possible particles, stranger to the measurement, that enter the ZDC and contribute to the signal.

The energy resolution of the ZDC has been experimentally measured by means of protons, deuterons, alphas and Pb nuclei with the same energy per nucleon (158 GeV/c) [2]. The resolution $\sigma(E)/E$ is obtained from the gaussian fit to the peak corresponding to the total energy released by the projectile. The results are reported versus $1/\sqrt{A}$ in Fig. 3.3. The full/open symbols refer to data obtained respectively with a 20 ns and 12 ns (standard NA50 run condition) gate. The behaviour of $\sigma(E)/E$ is linear as a function of $1/\sqrt{A}$ and can be fitted as

$$\frac{\sigma(E)}{E} = \frac{a_1}{\sqrt{A}} + a_2 \tag{3.3}$$

The parameter values given by the fit to the open symbol points (full line) are $a_1 = 26.8\%$ and $a_2 = 6.2\%$. For Pb–Pb collisions at 158 AGeV/c we expect an energy resolution of the order of 8%.

From the fit to the full symbols (20 ns gate) we get $a_1 = 27.9\%$ and $a_2 = 3.1\%$ (dashed line). The slopes of the two lines are basically the same, while the constant

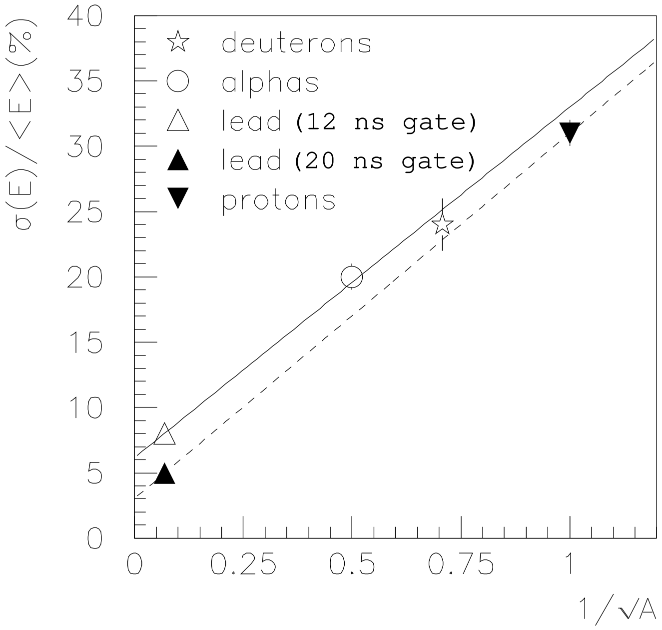

Figure 3.3: *Energy resolution of the ZDC for projectile nuclei of different mass number A, but with the same energy per nucleon (158 AGeV/c), as a function of* $1/\sqrt{A}$*. The full symbols refer to a 20 ns gate, the open ones to a 12 ns gate.*

term is smaller by using a larger gate (more favorable condition). In conclusion, it can be deduced from both sets of data that the energy resolution improves by increasing the energy released in the calorimeter (i.e. the number of nucleons of the projectiles, which have all the same energy per nucleon).

3.3 Data acquisition

The electronic chain for the NA50 ZDC and the related data acquisition system are sketched in Fig. 3.4.

As already said, the ZDC is divided into four towers, whose signals are sent to four Philips XP2242B photomultipliers. The signal of each PMT, after 43 m of coaxial cable, is amplified (by a factor 10) by a fast linear amplifier, which provides two output signals. The analogical sum of the four amplified signals is discriminated with a very low threshold (of the order of 50 mV), to get the ZDC minimum bias trigger. The second output is delayed through 157 m long coaxial cable, amplified again (by a factor 10) and strobed by the trigger signal in linear gate modules [7]. These linear modules provide a slow output which is sent to a charge to digital converter module (QDC).

The gate is 12 ns wide, while the signal at the entrance of the linear gate is about 10 ns. Pile-up effects, due to the high beam intensity, are reduced thanks to the

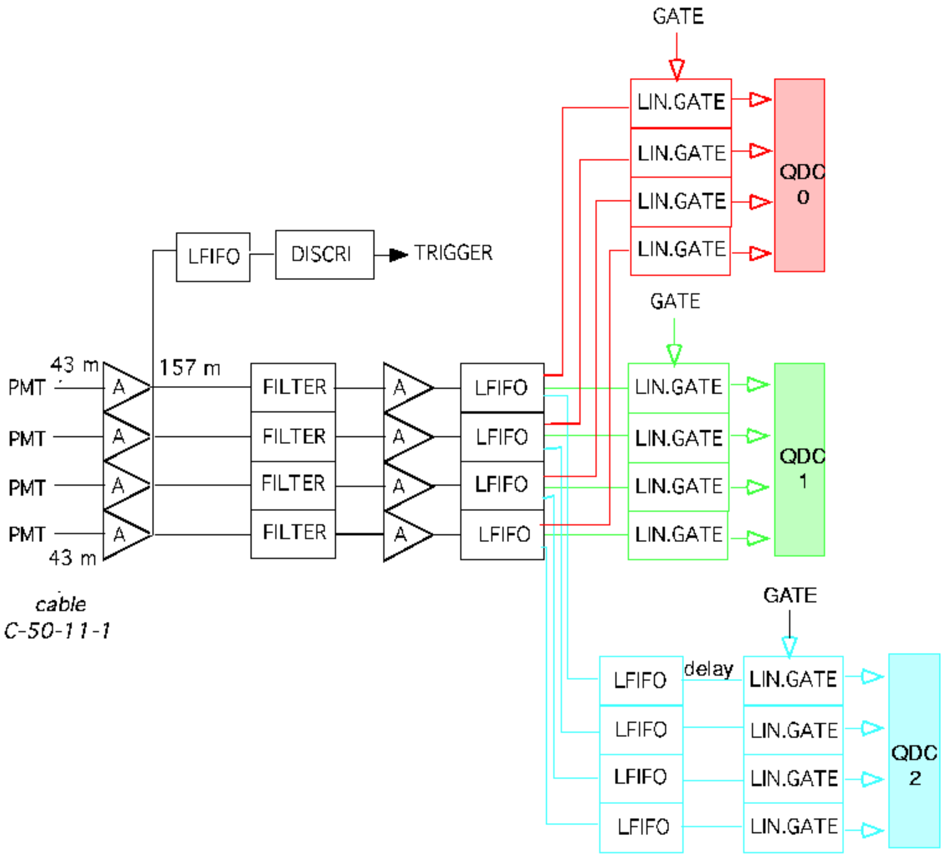

Figure 3.4: *ZDC electronic circuit and data acquisition system for the main and the parallel acquisition.*

very short time duration of the signal. In Fig. 3.5 the signals produced in one of the ZDC towers by one incident Pb ion and by two incident Pb ions close in time (pile-up event) are shown.

On-line information on the behaviour of each detector of the experimental apparatus is provided by the general monitoring of the experiment. However, a dedicated data acquisition system has been set up in order to check on–line the behaviour of the different detectors, independently of the main acquisition, and to intervene in case of anomalies or problems. It is based on the SPIDER code, running on a VME front-end processor, and it can work in two alternative ways. The first option (spy mode) consists in copying the buffer containing all the events of each burst from the main acquisition to the front-end processor. This way the spy acquisition is run in the same conditions as the main one. In the second option (parallel mode), four independent additional QDC channels are directly read–out by the processor. In this case a trigger and a gate widths different from those of the main acquisition can be used. In Fig. 3.4 the electronic chain for the main and the parallel acquisition

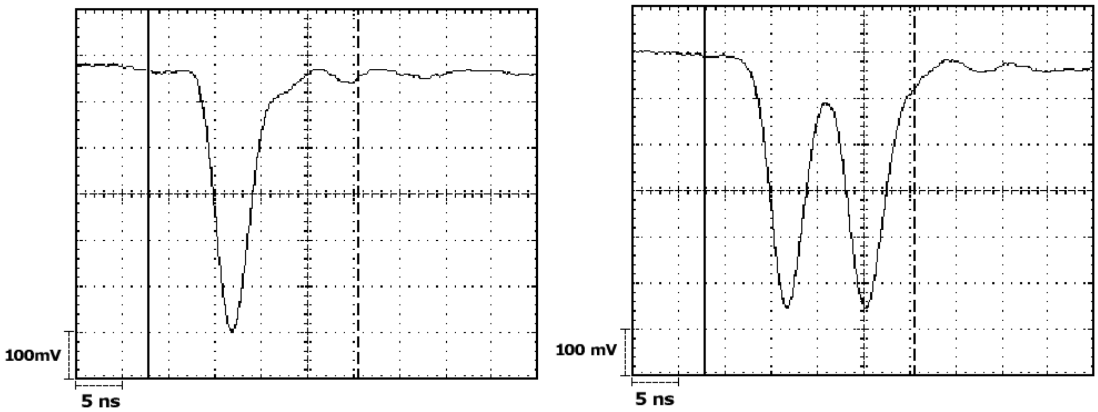

Figure 3.5: *Signal of one of the ZDC tower at the input of the linear gate, due to a single incident Pb ion (a) and to two Pb ions separated in time by a few ns (b).*

is represented. The linear gate modules give several outputs. One of them reaches a QCD read by the main acquisition (QDC 1), while another one arrives at a QCD read by the parallel acquisition (QDC 0). QDC 2 is used to estimate the pedestal contribution (see Section 3.4.1).

3.4 Data analysis

The early stage of data analysis, as for the ZDC, consists of:

- pedestal subtraction and detector calibration
- study of the ZDC response as a function of time, in order to recover the signal decreases, due to the radiation damage
- evaluation of the dose deposited in the calorimeter
- correction of beam pile–up effects, due to the high beam intensity that has been used

After this preliminary analysis, raw data have been compressed into μDST (Micro Data Summary Tapes). These tapes are analyzed by means of a specific program, DIMUREC, which provides higher level information, reconstructing the kinematic variables of μ mesons, the interaction vertex, the transverse momentum p_T and the invariant mass $M_{\mu\mu}$ of a dimuon event ($\mu^+\mu^-$).

In the next sections I will consider in details the four steps of the pre–analysis of the ZDC data. All the operations described in the following refer to events collected in 2000 with the MB trigger given by the ZDC. Only T0J triggers are taken into account, while the TSJ S0S triggers are neglected.

3.4.1 Pedestal subtraction

The analogical signal coming from each ZDC photomultiplier is sent to an ADC module, where its charge is converted into a digital signal. Even if no signal is produced by the incoming particles, in any case the ZDC ADCs receive an amount of charge that represents the pedestal contribution to the signal. It can be due to the background noise of the electronic modules present in the electronic chain and to the baseline oscillations. This latter contribution to the pedestal depends mainly on the signal shape and on the high beam intensity we work at. The ZDC signal has a short time duration (of the order of 10 ns), but a long "tail" (see Fig. 3.5a), which can overlap with a following signal, causing a lowering of the baseline. As the baseline oscillations can change in time, we do not simply subtract a fixed pedestal contribution, but we apply a more complete method, estimating the pedestal values event by event during the burst. For this purpose we integrate the signal of each ZDC tower in four gates, delayed with respect to the main one (Fig. 3.6). As the signals and the gates are not synchronized, in this four gates no Pb signals are detected, but only the pedestal contribution is acquired. For technical reasons in the NA50 electronic chain it has been chosen to delay the signals instead of the gates, but I will continue to refer to delayed gates and not to delayed signals.

In order to avoid pile–up effects, four delayed gates are considered. In the offline analysis the pedestal contribution is evaluated from the cleanest configuration, that is the one that has the lowest pedestal contribution, as I will explain in the following.

This method allows to evaluate the pedestal whatever the beam intensity is, and to take into account intensity fluctuations during the burst.

Because of the low frequency of the oscillations due to the electronic noise and the baseline fluctuations, the signal in the delayed gates ("out of time" pedestal) is

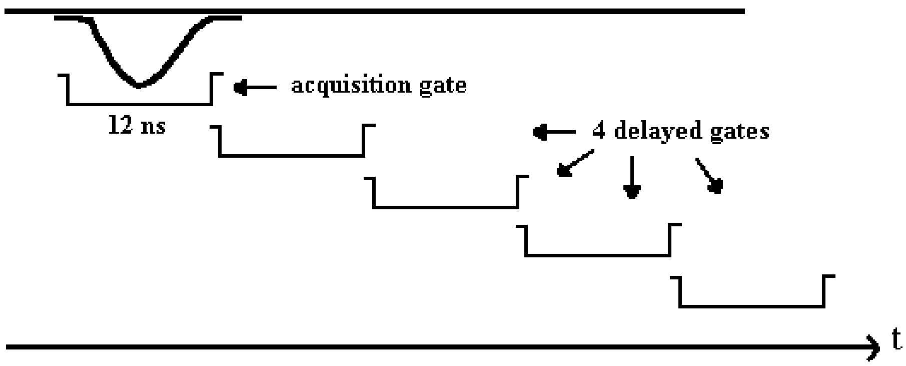

Figure 3.6: *Four gates delayed with respect to the acquisition gate.*

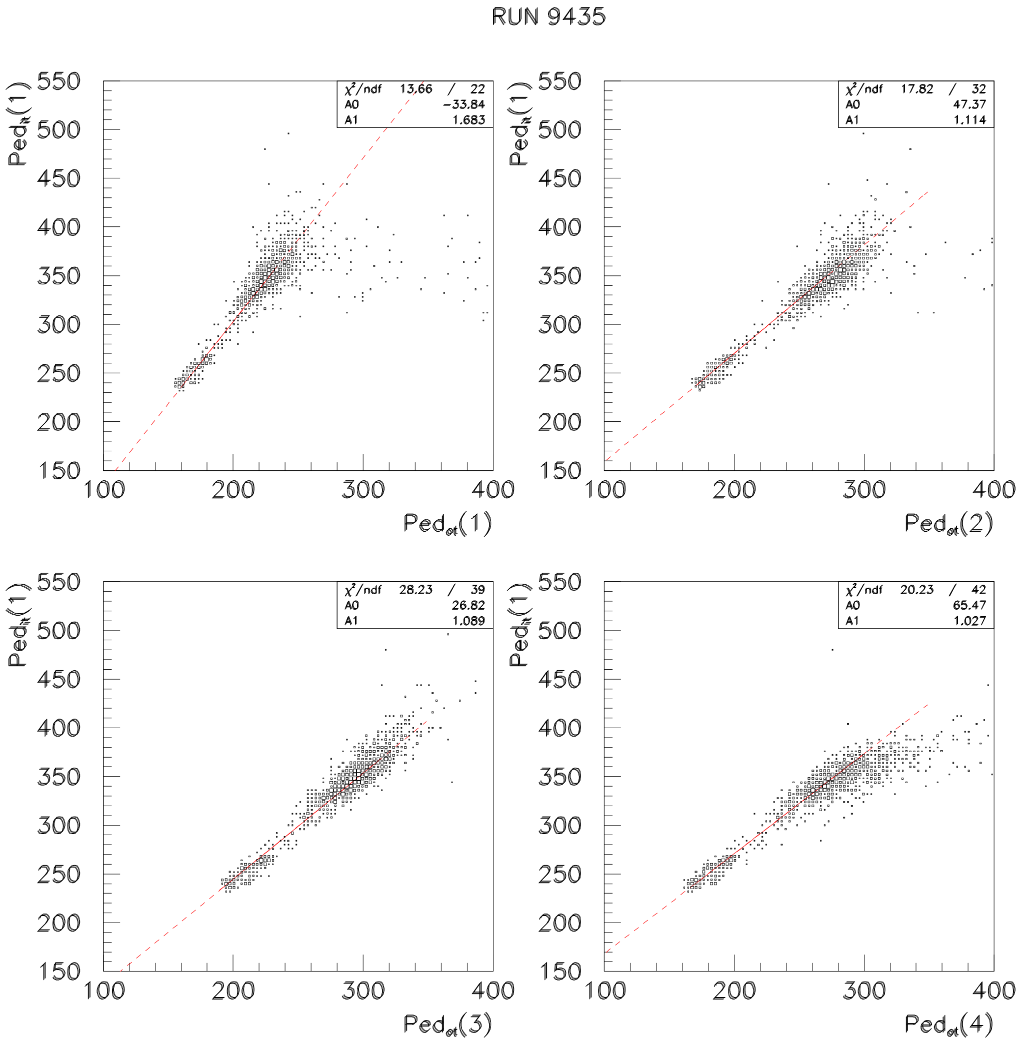

Figure 3.7: *Correlations between $Ped_{ot}(i)$with i=1,4 and $Ped_{it}(1)$ in laser trigger for a certain run.*

proportional, event by event, to the pedestal in the in-time gate (that is the real pedestal contribution which lies below the Pb signal). The correlations between the "in time" and the "out of time" pedestals have been studied in laser trigger, when both signals do not refer to Pb ions impinging on the detector. These correlations, established in laser trigger, are assumed to be the same in dimuon or MB trigger.

Therefore 16 correlations between the "in time" (Ped_{it}(i) with i=1,4 for each photomultiplier) and the "out of time" pedestals (Ped_{ot}(j) with j=1,4 for each delayed gate) are produced. In Fig. 3.7 an example of these correlations in laser trigger is reported for a certain run.

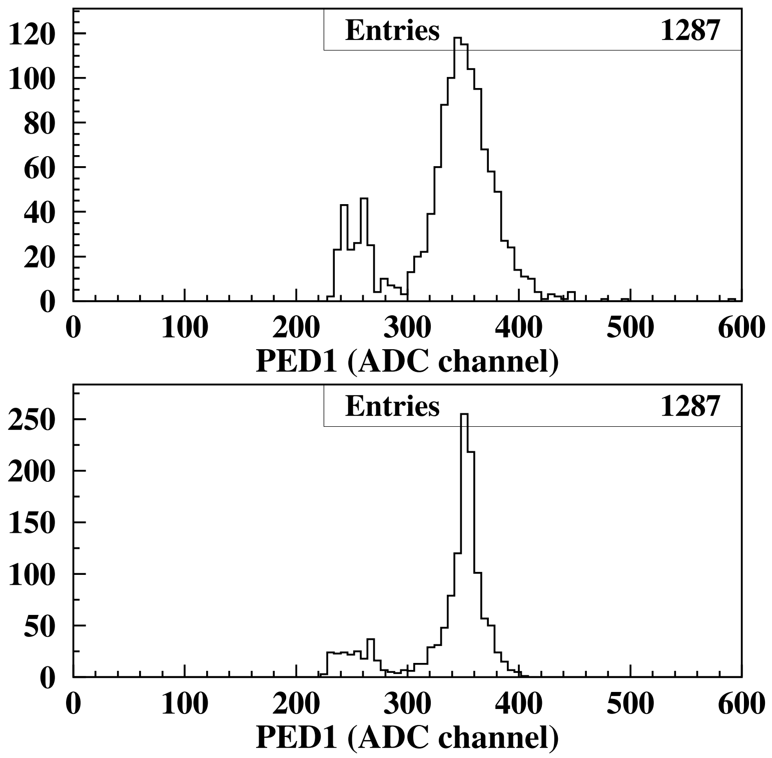

Figure 3.8: *Ped_{it} contribution to the first ZDC tower signal, evaluated in laser trigger before and after the application of the pedestal estimation method based on the Ped_{it} vs Ped_{ot} correlations.*

The Ped_{it} vs Ped_{ot} correlations in laser trigger are fitted by means of straight lines:

$$Ped_{it}(i) = a + b * Ped_{ot}(j) \quad \text{i=1,4} \quad \text{j=1,4} \tag{3.4}$$

Event by event, for each $Ped_{it}(i)$, the correlation where $Ped_{ot}(j)$ better approximates the mean value $< Ped_{ot}(j) >$ of its distribution is chosen. This way, the "cleanest" pedestal is considered.

In Fig. 3.8 the "in time" pedestal contribution to one of the ZDC tower signal is shown in laser trigger before (top) and after (bottom) the application of this method, based on the fit to the Ped_{it} vs Ped_{ot} correlations. This procedure allows to estimate a cleaner and narrower pedestal contribution.

These correlations are then used in dimuon or MB trigger to determine the "in time" pedestal that must be subtracted from the Pb signal. Therefore, the ZDC signal in MB or dimuon trigger in each of the four electronic channels, subtracted

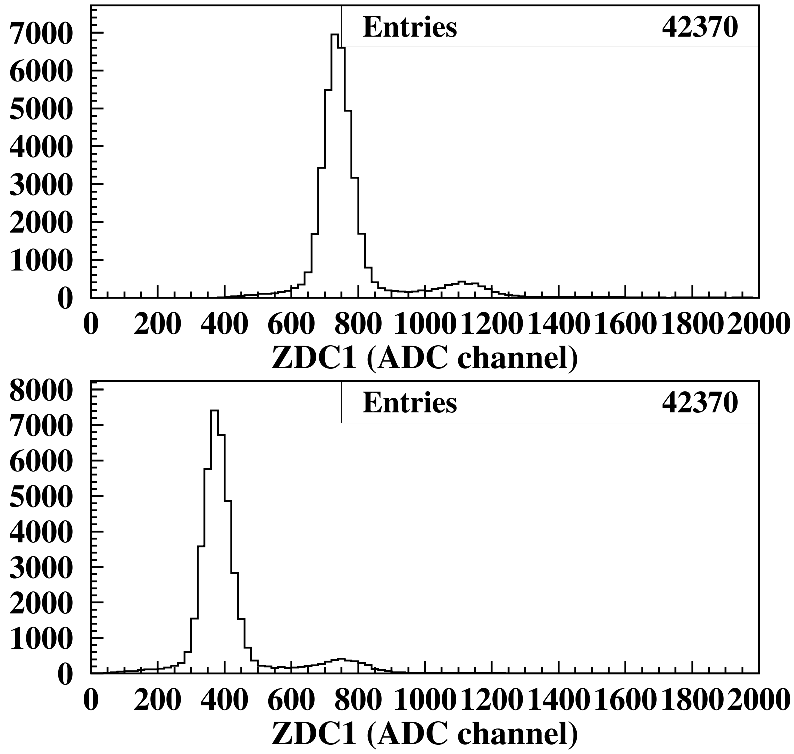

Figure 3.9: *ADC spectrum for one of the ZDC towers, before (top) and after (bottom) the pedestal subtraction, for a selected run.*

of the pedestal, is:

$$ZDC(i) = ZDC_{raw}(i) - (a + b * Ped_{ot}(j)) = ZDC_{raw}(i) - Ped_{it}(i) \qquad \text{i=1,4}$$

where $ZDC_{raw}(i)$ is the raw signal of the i–tower of the detector before the pedestal subtraction and $Ped_{it}(i)$ is the corresponding pedestal contribution (in MB or dimuon trigger), evaluated, event by event, from the $Ped_{ot}(j)$ value (Eq. 3.4).

The signal of one of the ZDC towers, before and after the pedestal subtraction, is shown in Fig. 3.9.

This procedure is used only if at least one of the four $Ped_{ot}(j)$ differs from its $< Ped_{ot}(j) >$ mean value by less than 2σ. This happens when the baseline measured by Ped_{ot} is not affected by the tail of a ZDC signal. Otherwise Ped_{it} is evaluated from the fit to the correlation, using $< Ped_{ot}(j) >$.

The correlation $Ped_{it}(i)$ versus $Ped_{ot}(j)$ changes in time during the data taking period because the electronic noise and the baseline oscillations change in time. For this reason the fit to the correlation has been periodically repeated. A total of 100 runs has been selected ($\sim$ 3 runs a day, at a temporal distance of about 8 hours).

3.4.2 ZDC calibration

After the pedestal subtraction, the ZDC must be calibrated. The signal coming from the four towers must be equalized, so that the detector response is independent of the beam impact point. A first on–line calibration is completed by an off-line correction, which takes into account the signal loss due to the radiation damage.

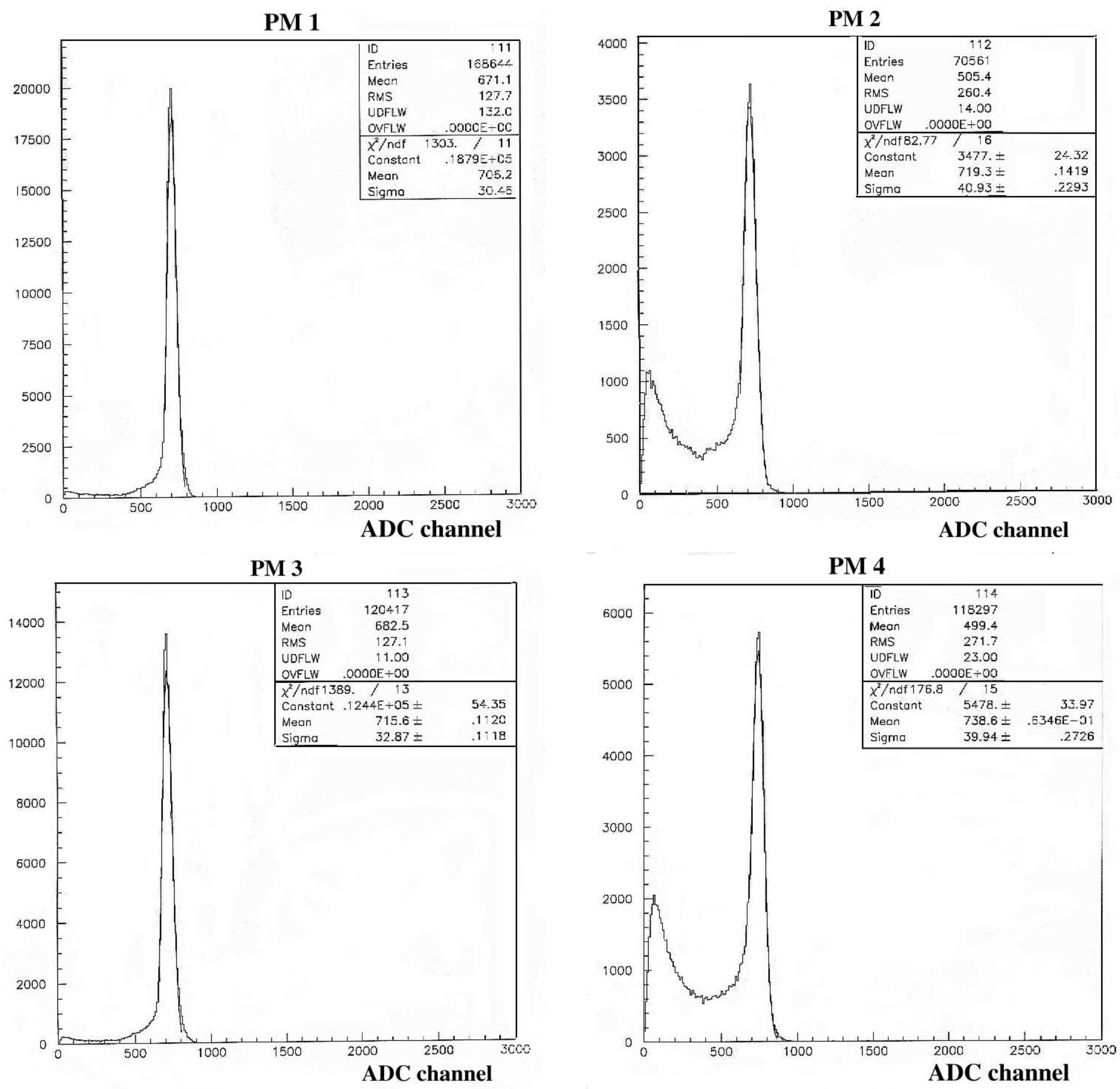

Figure 3.10: *Signals obtained with the beam in the center of each tower, after the on–line calibration (MB trigger).*

On–line calibration

The on–line calibration consists in setting the photomultiplier HV values so that the responses of the four towers are similar. At the beginning of the data taking, some runs have been performed sending a low intensity beam (about 10^2 Pb ions/burst) to the center of each ZDC tower with the target off; a trigger gate of 25 ns has been adopted instead of the 12 ns used in the standard NA50 runs. The photomultiplier high voltages have been adjusted in order to have the ADC Pb peak at the same channel for all the four photomultipliers, as shown in Fig. 3.10. This way, if the beam is sent to the center of the calorimeter, the signals coming from the four towers are equal. In Fig. 3.11 the signal obtained summing upon all the four photomultipliers, with the beam in the ZDC center, is reported. Comparing this spectrum with one of the spectra in Fig. 3.10, we observe that, when the beam hits the center of the ZDC instead of the center of a tower, the Pb peak resolution is slightly worse (7% instead of 5%). This difference can be ascribed to the fact that, in the NA50 standard runs, the trigger gate is shorter (12 ns) than in the initial runs devoted to the calibration.

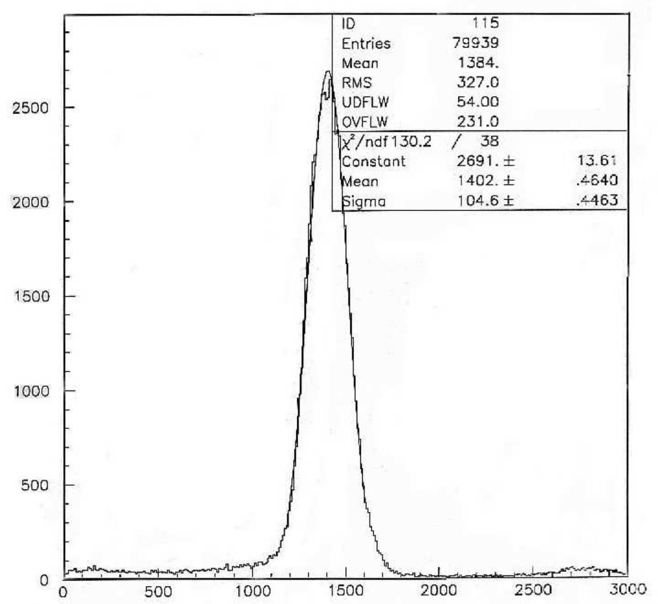

Figure 3.11: *Total ZDC signal, obtained with the beam hitting the center of the calorimeter front face, after the on–line calibration (MB trigger).*

This increases the energy resolution of the calorimeter. Moreover, a worsening of the resolution can be due to the fact that the four central fibres of the calorimeter start 10 cm downstream the ZDC front face, as described in Section 3.2.

During the data taking period, the ZDC response has been continuously checked, looking at the Pb peak position of the ADC spectrum in MB trigger. The high voltages of the photomultipliers have been increased twice, in order to recover the signal reduction due to the radiation damage of the detector. The on–line calibration is completed off-line, taking these changes into account.

At last, the gain stability of the four photomultipliers can be monitored out of the burst by means of a laser diode, optically connected to each photomultiplier by means of a quartz fibre and pulsed by a CAEN 529 Led Driver module.

Off-line calibration

The ZDC calibration has been checked and eventually corrected during the data analysis. The off-line calibration considers a sample of about 100 runs ($\sim$ 3 runs a day, at a distance of about 8 hours) with the beam in the center of the calorimeter front face.

The first step is to study the behaviour of the Pb peak position as a function of time, separately for the four towers. The Pb peak position is deduced from the gaussian fit to the ADC spectrum in MB trigger. In Fig. 3.12 the signals measured in ADC channels during all the data taking period are reported for each tower. Due to the radiation damage, the signal decreases as a function of time (represented by the increasing run number). The HV changes, performed to recover the signal losses for radiation damage, are clearly visible in two deep jumps of the Pb peak position. Other discontinuities can be attributed to beam movements during the beam tuning operations. In such a situation, if the beam is moved up, for example, toward the upper part of the calorimeter, the upper towers will produce signals greater than those of the lower towers, but the total signal of the calorimeter will be nearly the same. An other leap in the correlation between the Pb peak position and the run number is due to the insertion of a quartz blade after the run 9699, during which the ZDC has been displaced. The hole visible from run 9714 to run 9757 corresponds to the not considered low intensity runs, performed with a quartz blade placed inside the hadron absorber, just in front of the ZDC. This detector allows to study fission phenomena at lower beam intensity ($I \simeq 4 \cdot 10^6$ Pb ions/burst), by measuring the charge of the projectile fragments produced in the collision (see Chapter 6). After the run 9757 the quartz blade has been removed and the beam intensity has been restored to $6 \div 7 \cdot 10^7$ Pb ions/burst. In the standard NA50 analysis these low intensity runs will be left out.

At the beginning of the data taking period, immediately after the on–line calibration, the signals coming from the four towers are not equal in the “general” acquisition (that is the main acquisition of the experiment), because this first cali-

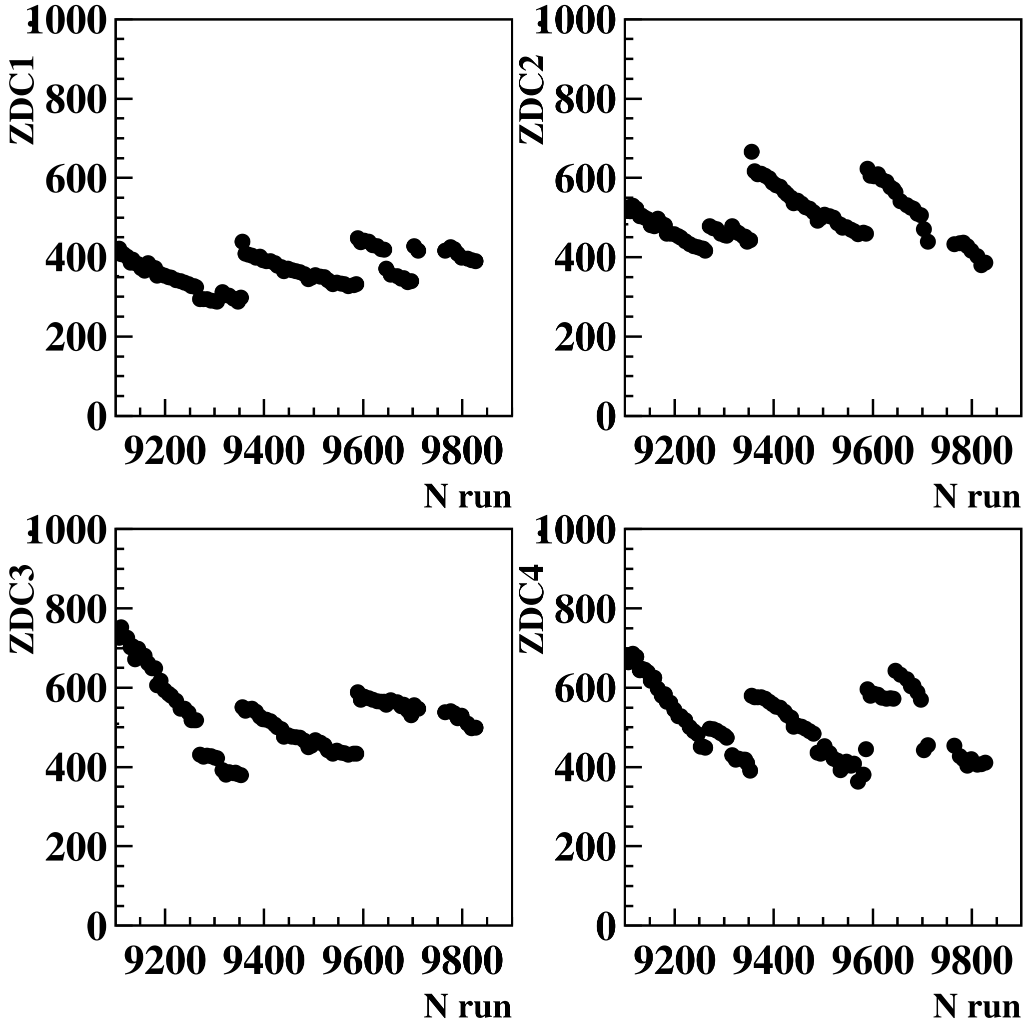

Figure 3.12: *Pb peak position (in ADC channels) in the spectra of the four ZDC towers during the 2000 data taking period.*

bration has been performed in the "parallel" acquisition. In the more refined off–line calibration I have found the coefficients to refer the four tower signals to the values they had at the beginning of the data taking in the "parallel" acquisition.

The correlation between the Pb peak position and the run number can be divided into three regions with the same trend, which are fitted as straight lines.

For each tower, run by run, the ZDC signal, corrected for the signal loss, is:

$$ZDC_{correct}(i) = \frac{ZDC(i)}{ZDC^{gen}_{fit}(i)} * ZDC^{gen}_{fit}(1) * \frac{ZDC^{par}(1)}{ZDC^{gen}_{fit}(1)} \tag{3.5}$$

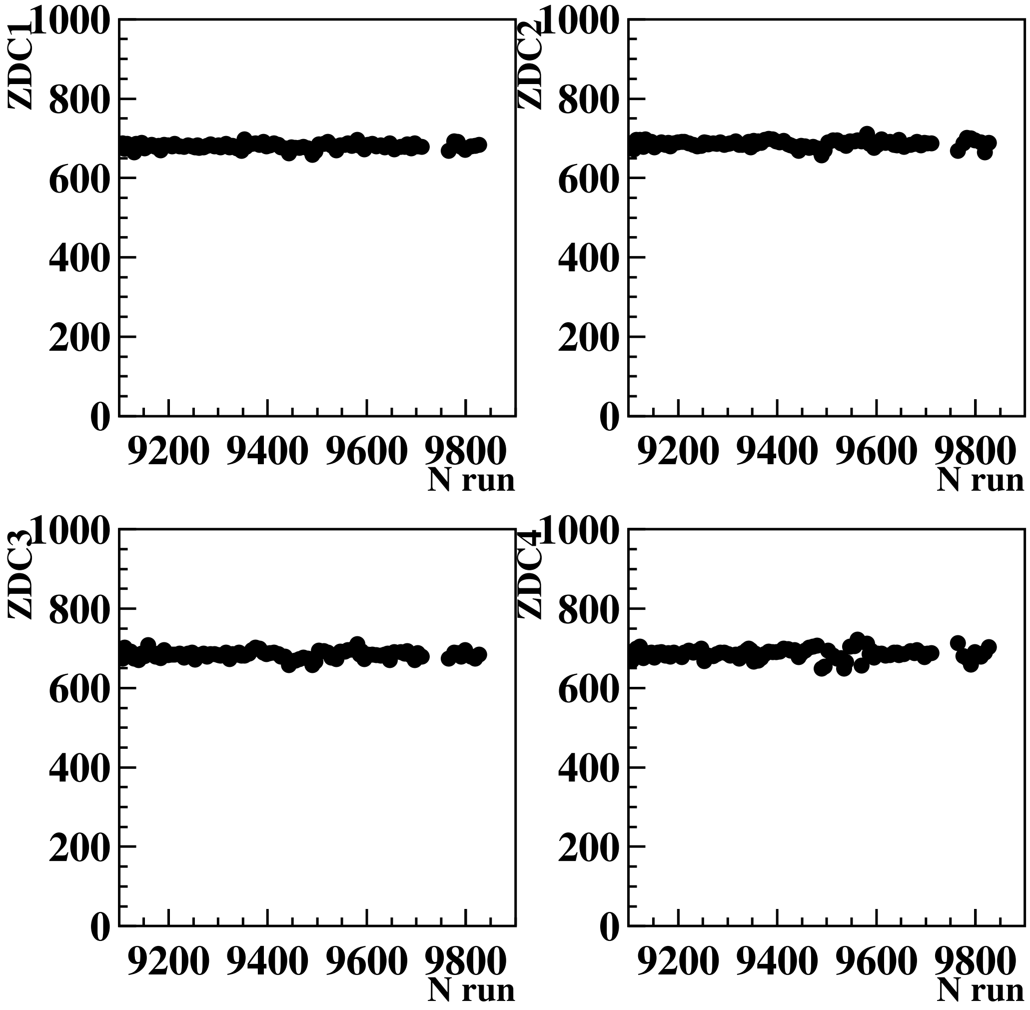

Figure 3.13: *Pb peak position (in ADC channels).in the four ZDC towers, after the calibration, as a function of the run number.*

where *ZDC(i)* is the ZDC signal, for a given tower, in the run i, after the pedestal subtraction; $ZDC^{gen}_{fit}(i)$ is the corresponding ZDC signal for that run, deduced from the linear fit; $ZDC^{gen}_{fit}(1)$ is the ZDC value determined from the fit for the first run of the "general" acquisition (run 9107).

The first product recovers the signal loss for radiation damage, by referring the ZDC signal produced in a tower in the run i to the value it had in the first run of the data taking period. The resulting signal is multiplied by a third term which allows to compare "parallel" and "general" acquisition. $ZDC^{par}(1)$ is the Pb peak

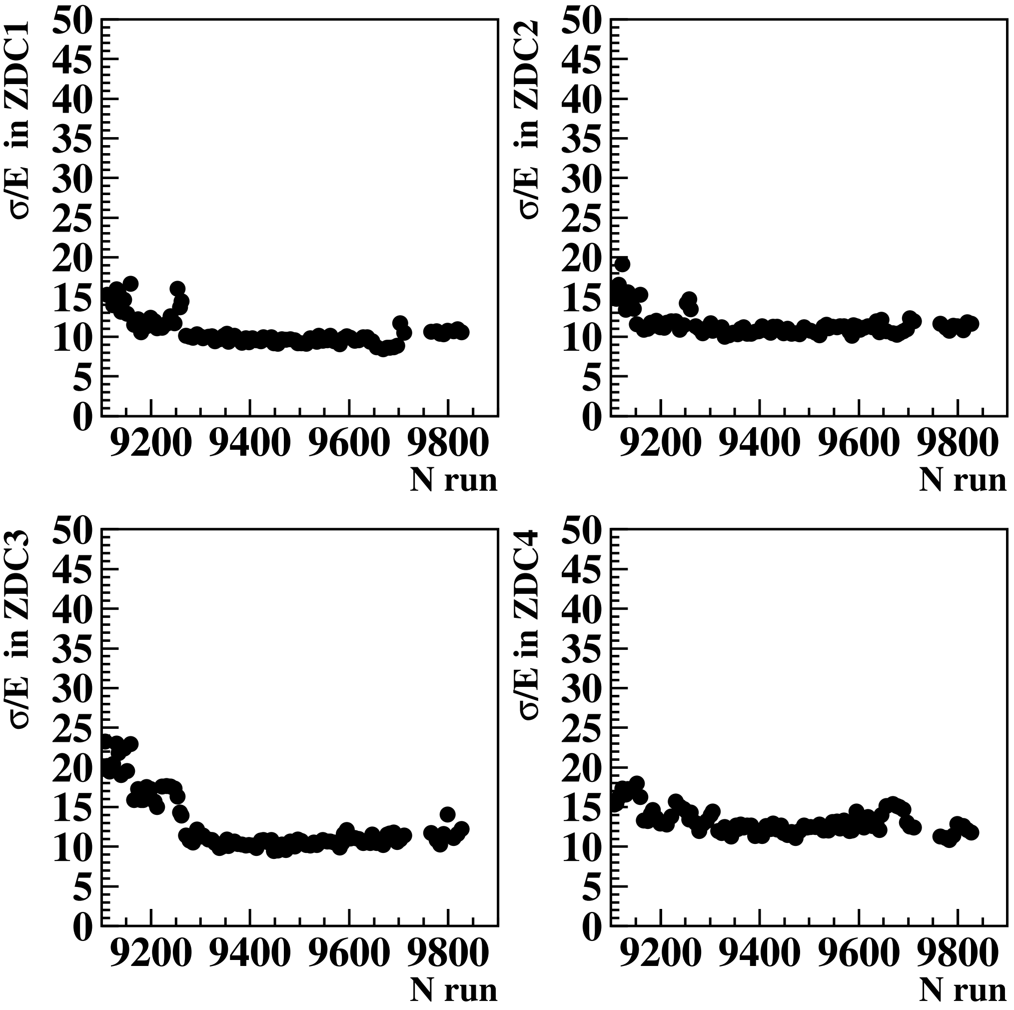

Figure 3.14: *Pb peak resolution (in %) in the four ZDC towers, after the calibration, as a function of the run number.*

position, for a given tower, in the first run with the beam sent to the center of the ZDC front face, after the on–line calibration, in "parallel" acquisition.

By simplifying Eq. 3.5, the calibrated ZDC signal, for a given tower, in the run i, becomes:

$$ZDC_{correct}(i) = \frac{ZDC(i)}{ZDC^{gen}_{fit}(i)} * ZDC^{par}(1) \qquad (3.6)$$

In Fig. 3.13 the result of the calibration, performed separately for the four ZDC towers, is reported. The Pb peak position in the four towers (deduced from the

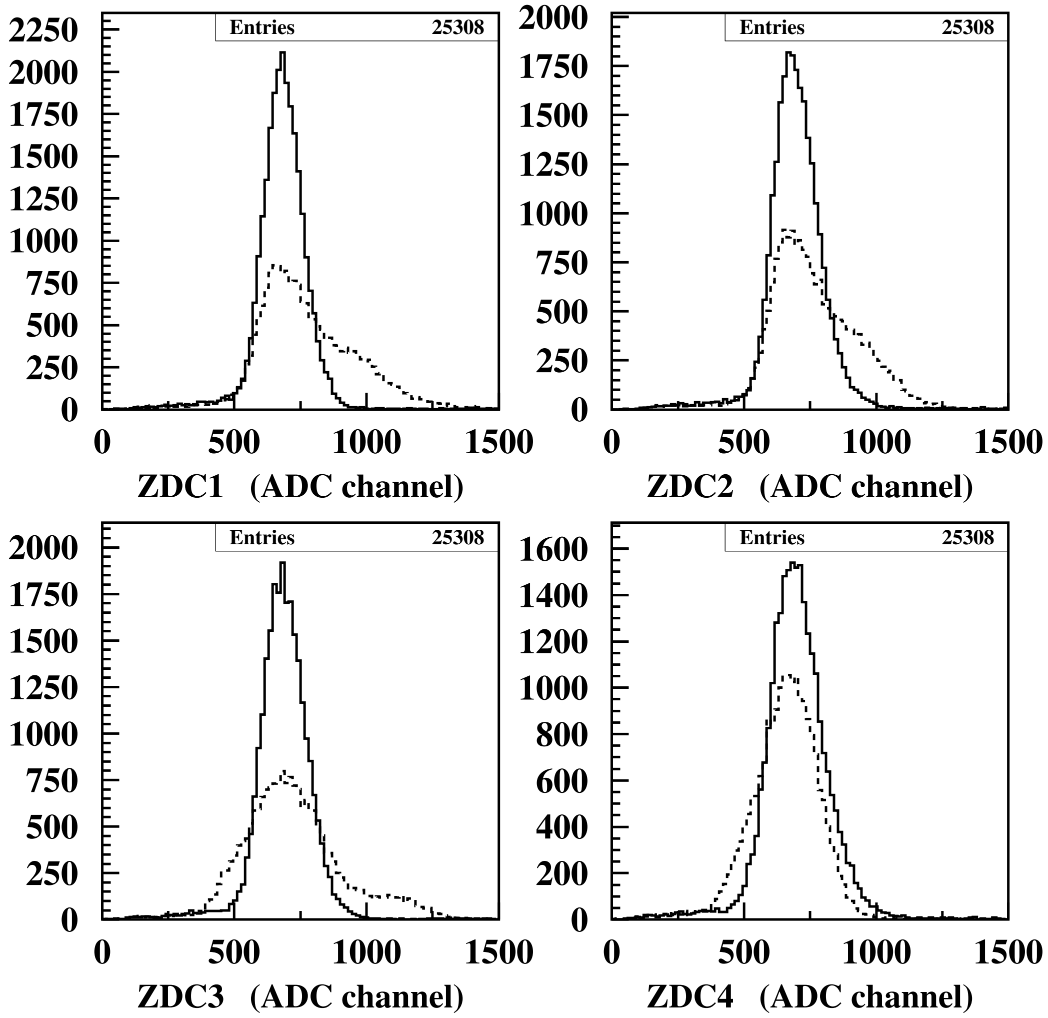

Figure 3.15: *Spectra (in ADC channel) produced by the four ZDC towers in run 9152 (dotted line) and in run 9301 (continuous line), after the calibration (MB trigger).*

gaussian fit to the calibrated spectra) is plotted as a function of the run number. The signal losses, due to the high radiation effects, have been completely recovered and the responses of the four towers have been equalized.

Fig. 3.14 shows the behaviour of the Pb peak resolution $\frac{\sigma_E}{E}$, after the calibration, as a function of time. The Pb peak resolution is worse in the initial runs (from 9107 to 9261) in comparison with the following runs of the data taking period. As the mean value of the Pb peak remains constant as a function of time, as we can see in Fig. 3.13, the resolution increase in the first runs must be attributed to a wider σ

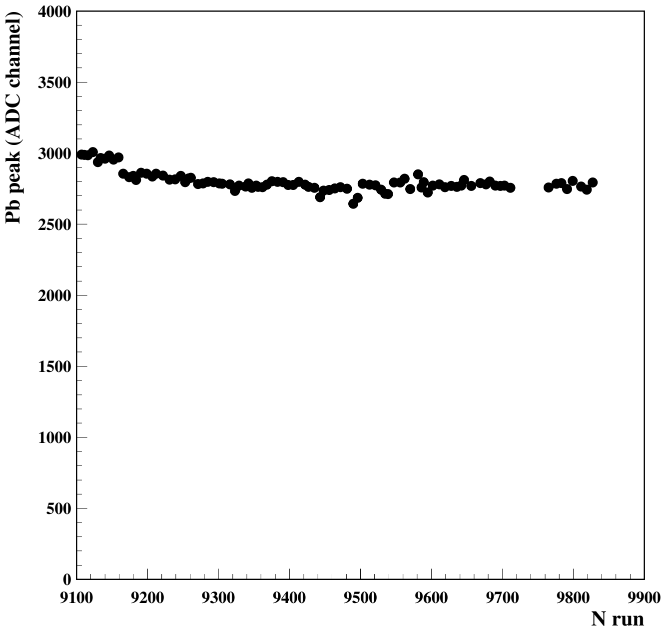

Figure 3.16: *Global Pb peak position, after the calibration, as a function of the run number.*

of the ZDC spectrum.

In Fig. 3.15 we can see the ZDC spectrum in the four towers for one initial run (run 9152) and for one of the following runs (run 9301), after the calibration. The comparison between the two spectra shows that the four tower signals have been well calibrated because their mean values are similar. Nevertheless the signal width decreases from the beginning runs (until run 9250) to the following ones. In the initial runs the ZDC spectrum of each tower is not gaussian and has a long "tail" on the right.

This fact has repercussions on the shape and position of the global ZDC signal. The signal coming from the four towers of the calorimeter has been summed up and the global peak position has been evaluated from the gaussian fit to the resulting spectrum. Therefore the global peak position has been plotted as a function of time (Fig. 3.16). In the first runs, until run 9250, the Pb signal is peaked at greater values with respect of following runs. The total ZDC spectrum turns out to be shifted toward higher values in run 9152, if compared with run 9301 (Fig. 3.17).

In order to solve this problem, due to the different shape of the ZDC signal at the beginning of the data taking period, I have introduced a multiplying factor in Eq. 3.6. It takes into account the difference between the Pb peak position in the initial runs and in the following ones.

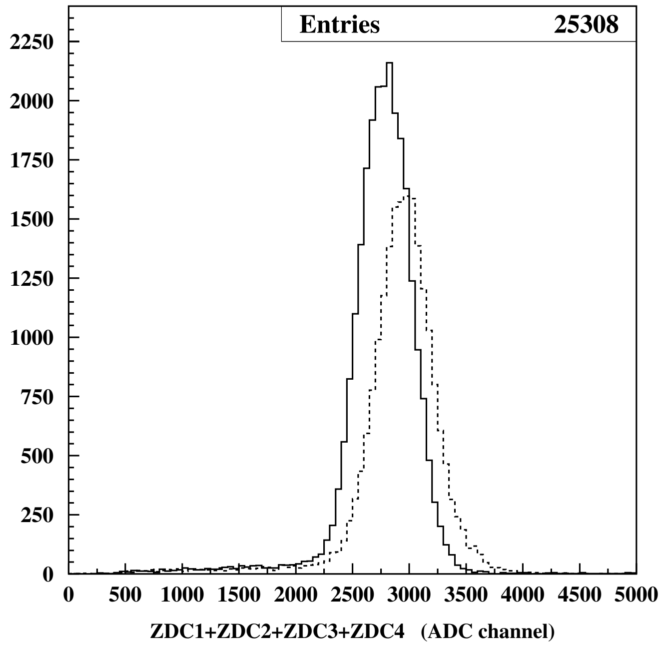

Figure 3.17: *Global Pb peak position in run 9152 (dotted line) and in run 9301 (continuous line), after the calibration.*

Eq. 3.6 becomes, only for initial runs (9107–9250):

$$ZDC_{correct}(i) = \frac{ZDC(i)}{ZDC^{gen}_{fit}(i)} * ZDC^{par}(1) * FACT(i) \tag{3.7}$$

with

$$FACT(i) = \frac{ZDC_{rif}}{ZDC^{gen}_{fit}(i)} \quad \text{i = 9107; 9250} \tag{3.8}$$

ZDC_{rif} is the mean Pb peak position in the runs from 9250 to the end of data taking; $ZDC^{gen}_{fit}(i)$ is the ZDC value deduced from the fit to the Pb peak for each tower in the initial runs.

Obviously, after this correction for initial runs, the Pb peak position is not constant, as a function of time, for the four ZDC towers separately, as shown in Fig. 3.18, but the ZDC global signal is now perfectly calibrated (Fig. 3.19).

The Pb peak position of the global ZDC spectrum obtained by the sum of the four tower signals is reported in Fig. 3.19 as a function of the run number. The trend is fitted as a straight line and can be approximated by a constant equal to the channel 2762. The ratio between the energy carried out by a Pb ion which has not interacted in the target and has deposited all its energy (158 GeV/nucleon $*$

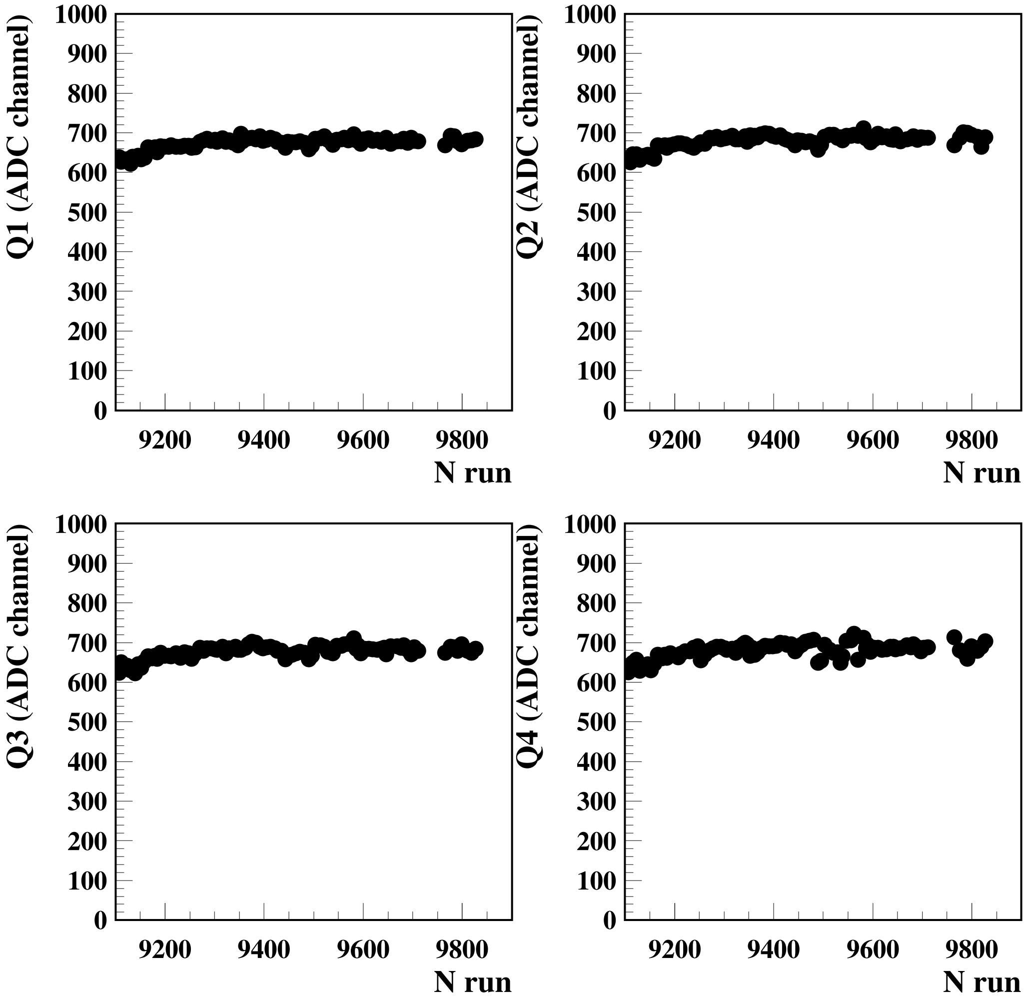

Figure 3.18: *Pb peak position (in ADC channel) in the four towers, after the calibration and the correction for initial runs, as a function of the run number.*

208 nucleons = 32864 GeV) in the calorimeter, and channel 2762 gives the factor for converting the signal expressed in ADC channels into GeV of energy.

The final E_{ZDC} spectrum in MB trigger, obtained summing all the runs considered for the calibration procedure, is shown in Fig. 3.20. The mean resolution of the Pb peak is about 8%.

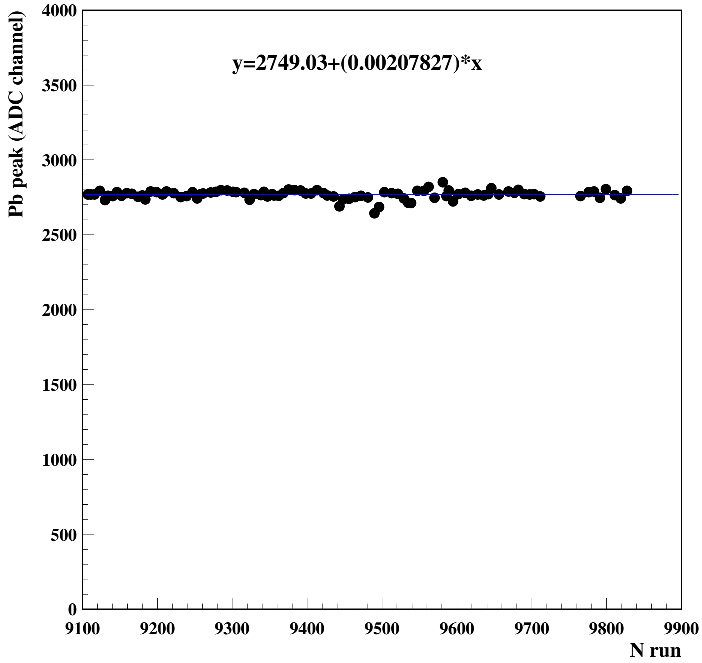

Figure 3.19: *Global Pb peak position, after the calibration and the correction for initial runs, as a function of the run number (linear fit superimposed).*

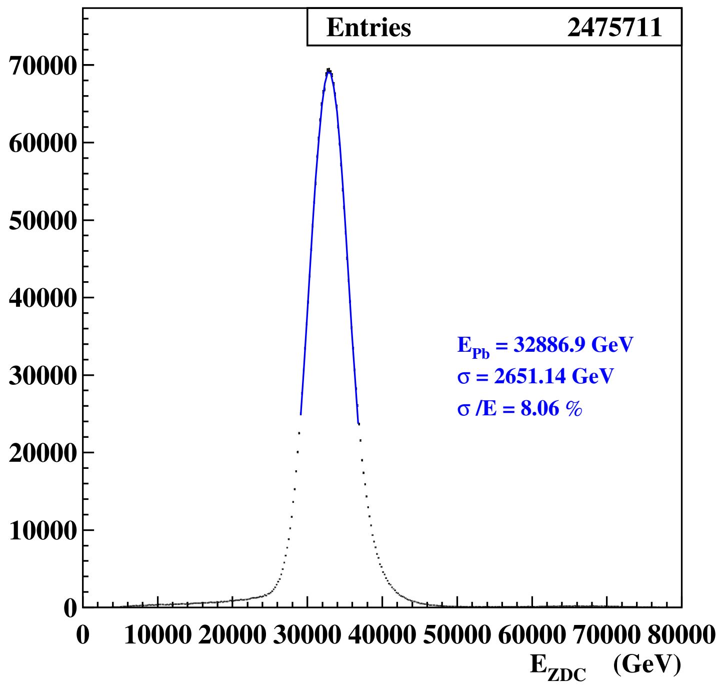

Figure 3.20: *Pb peak summed on a large sample of runs, after the calibration and the correction for initial runs (gaussian fit superimposed).*

3.4.3 Radiation damage

The 2000 data taking period has lasted 6 weeks, with an average beam intensity $I \simeq 6 \div 7 \cdot 10^7$ Pb ions/burst (burst of 5 seconds) and for a total number of $6 \cdot 10^{12}$ Pb ions incident on the target in the whole period.

The dose released in the ZDC can be evaluated considering the fact that the beam and the projectile fragments impinge only on the central region of the ZDC front face, due to the small size of the beam spot (of the order of few mm^2). Therefore we evaluate the dose deposited in the central region of the calorimeter (the most exposed to radiation damage), which is much larger than the average dose absorbed by all the detector. Monte Carlo simulations based on the GEANT code [8] allow to estimate the dose deposited in the four fibres closest to the beam axis, at a depth corresponding to the maximum development of the shower (between 1 and 2 λ_I). At the end of the 2000 run, a dose of about 5.5 Grad was released in the ZDC.

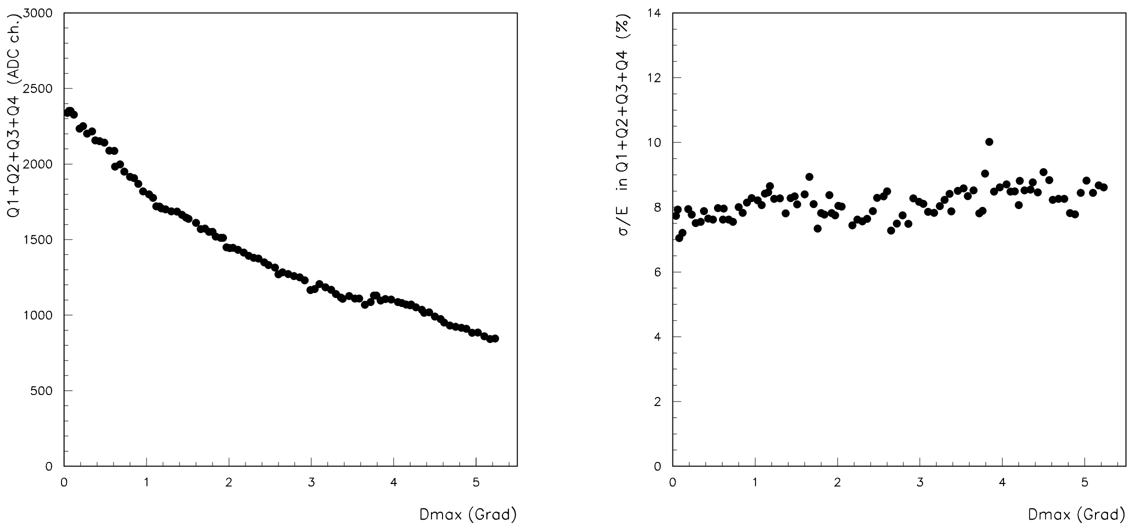

Figure 3.21: *a) Position of the Pb peak in the ZDC spectrum and b) energy resolution as a function of the dose D_{max} absorbed by the central (and most exposed to the radiation damage) region of the detector during the 2000 data taking.*

As already mentioned, the position of the ADC peak corresponding to the non–interacting Pb ions has been continuously checked during the data taking period. To recover the signal losses due to the radiation damage, the high voltages of the ZDC PMs have been increased twice to bring the ZDC response back to the value it had at the beginning of the run. In Fig. 3.21a the position of the Pb peak is plotted as a function of the dose D_{max} deposited in the central region of the calorimeter. Since we want to study the ZDC signal loss, in this plot the data has been corrected for the change in gain of the PMs. The response of each PM after the HV change has been brought back to its value before the HV change. Fig. 3.21a shows that the ZDC response decreases as a function of the delivered dose: at the end of the data acquisition period the light output was about 60% lower than at the beginning of the run.

In Fig. 3.21b the ZDC energy resolution $\sigma(E)/E$ is plotted as a function of D_{max}. The resolution gets worse with the increasing of the dose received during the run period: after a first worsening from 8% to 9%, the resolution remains nearly stable for the rest of the period.

3.4.4 Beam pile–up correction

In the 2000 NA50 run a thin target has been used, in order to reduce the reinteractions of the projectile fragments in the target. To collect a good statistics sample of events in six weeks of data taking, a high intensity beam has been adopted ($I \simeq 6 \div 7 \cdot 10^7$ Pb ions/burst). At such an intensity, pile–up problems rise, due to the fact that the detectors can not distinguish the signals of two ions arriving too much close in time. In particular for the ZDC, the acquisition gate is 12 ns wide, while the signal has a short duration of about 10 ns, but it has a long tail, which can superimpose with a following signal. Therefore two ions can produce pile–up effects if they arrive into the ZDC at a temporal distance lower than about 16 ns.

We can define two kinds of pile–up problems that affect our measurements:

- beam pile–up, if two Pb ions, which have not interacted inside the target, arrive into the ZDC with $\Delta t \leq 16\ ns$;
- interaction pile–up, if one or both these two Pb ions have interacted in the target and enter the ZDC with $\Delta t \leq 16\ ns$, summing up and giving a single signal.

In this section I will report the corrections performed to recover the events with problems of beam pile–up. To establish if there is beam pile–up or not, I have considered the information provided by the BH, whose TDCs give the arrival time of a Pb ion in one of its quartz blades, within a given interval (90 ns), appropriately timed with respect to the ion that has triggered the apparatus. If two ions hit two different BH blades in a time window of 34 ns, we define a new flag NIZDC=2. If only one Pb ion is detected in the same time by the BH, the value of this flag is 1.

Empty target runs

First I have considered "empty target" runs, where the target has been removed from the beam line. In such a case, all the pile–up events are due to beam pile–up problems and not to interactions within the target.

The ZDC signal, after the pedestal subtraction and the calibration of the detector, is plotted in Fig. 3.22 as a function of Δt, the difference between the arrival times

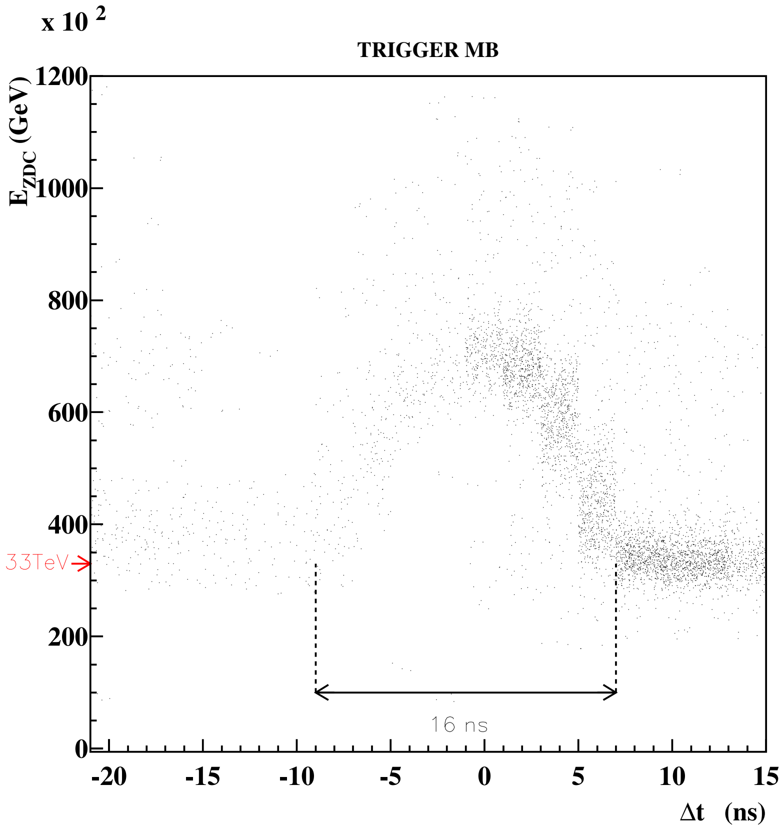

Figure 3.22: *Energy deposited in the ZDC as a function of the time difference between the arrivals of two Pb ions in a 34 ns BH TDC window, before beam pile–up correction. Two "Empty target" runs (9429 and 9430 summed) in MB ZDC trigger are considered and NIZDC=2 is required.*

of two ions in the BH, within a 34 ns TDC window. I have requested NIZDC=2 and selected only events acquired with the MB ZDC trigger.

Asking for two ions seen by the BH TDCs in a 34 ns window does not mean that these two particles necessarily cause pile–up in the zero–degree calorimeter. If their time distance is less than about 16 ns, they produce a ZDC pile–upped signal (see the "bump" of the correlation in Fig. 3.22) peaked at about 33 $TeV * 2 = 66\ TeV$, which corresponds to the entire energy of two incoming Pb ions. Otherwise, if they arrive separated in time by more than 16 ns, no pile–up problems affect the ZDC, which has the time to detect separately the two Pb signals. The corresponding signal in the ZDC is 158 GeV/nucleon $*$ 208 nucleons $\simeq$ 33 TeV, laying on the line at 33 TeV.

A correction on the pile–upped events has been performed in order to recover them. The Δt scale has been divided into 18 intervals, in which the Pb peak position of the ZDC spectrum has been considered. The found values have been interpolated

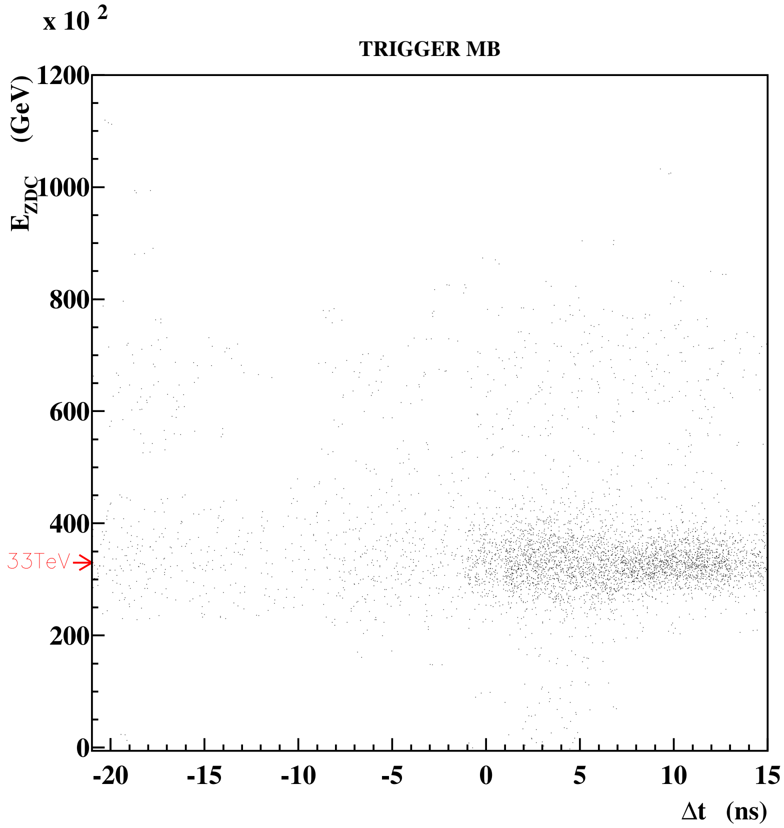

Figure 3.23: *Energy deposited in the ZDC as a function of the time difference between the arrival of two Pb ions in a 34 ns BH TDC window, after beam pile–up correction. Two "Empty target" runs (9429 and 9430 summed) in MB ZDC trigger are considered. NIZDC=2 is required.*

in each Δt interval, using an interpolating polynomial of third degree.

Therefore, for each event, the ZDC signal, corrected for beam pile–up, is:

$$E_{ZDCcorrect}(i) = E_{ZDC}(i) - DEV(i) \tag{3.9}$$

where $E_{ZDC}(i)$ is the energy value, after calibration, for the event i, and $DEV(i)$ is the deviation from 33 TeV of the interpolated function calculated for that event.

After the correction, the signal of the E_{ZDC} is constant (= 33 TeV) as a function of Δt (Fig.3.23).

In Fig. 3.24 the ZDC spectra before and after the beam pile–up correction are compared for two "empty target" runs considered in MB ZDC trigger. The request NIZDC=2 is made in both cases.

In Fig. 3.24a two peaks are visible: the first one is due to a single Pb ion entering the 12 ns gate, the second one, which is twice the first one, can be attributed to beam pile–up events.

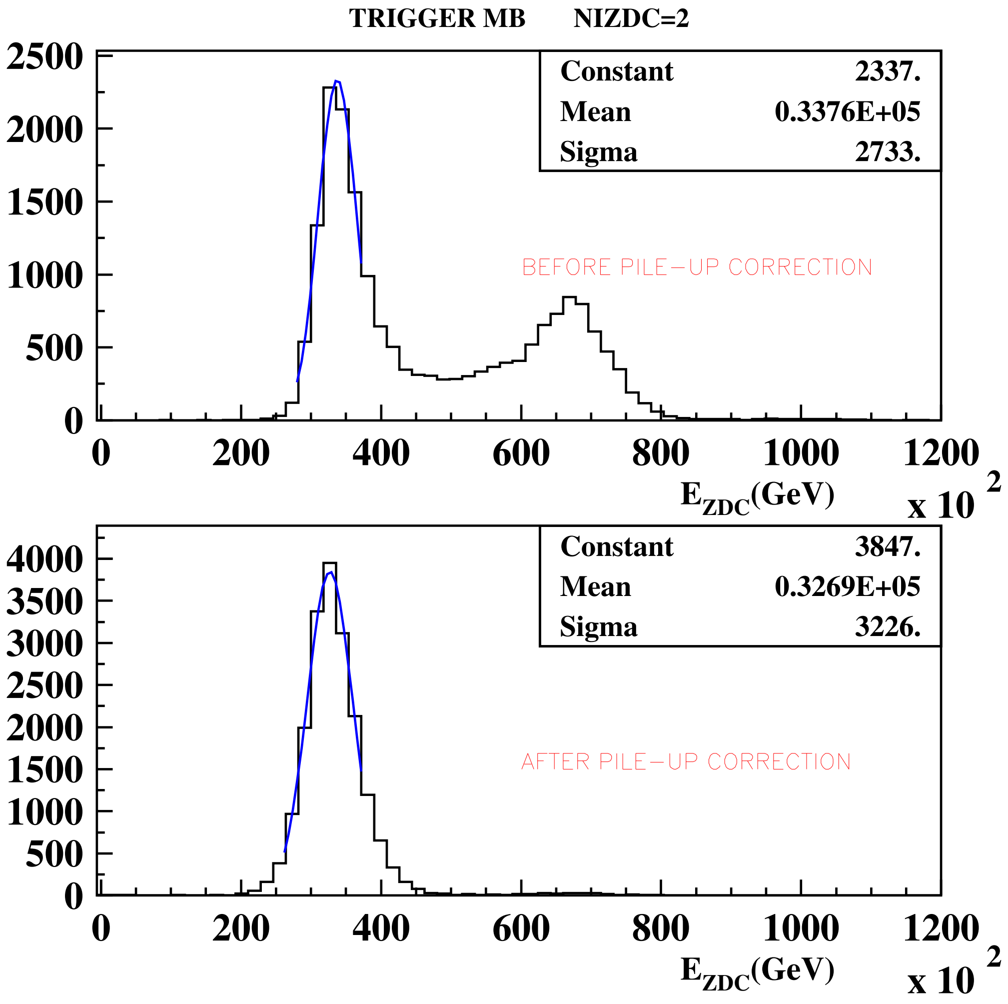

Figure 3.24: *ZDC spectrum in MB ZDC trigger before (a) and after (b) beam pile–up corrections for "empty target" runs (9429 and 9430 summed) and with NIZDC=2.*

After the correction (Fig. 3.24b), the beam pile–up events have been almost completely recovered and moved into the peak of the single not pile–upped Pb ions. In conclusion, for empty target runs, this procedure for correcting the beam pile–up gives satisfactory results.

Runs with target

In "empty target" runs no target is present on the beam line, so all the pile–up events can be attributed only to beam and not to interaction pile–up problems. Nevertheless, what interests us, is to apply the beam pile–up correction to standard NA50 runs, where the beam hits the target. In such a situation it is possible that

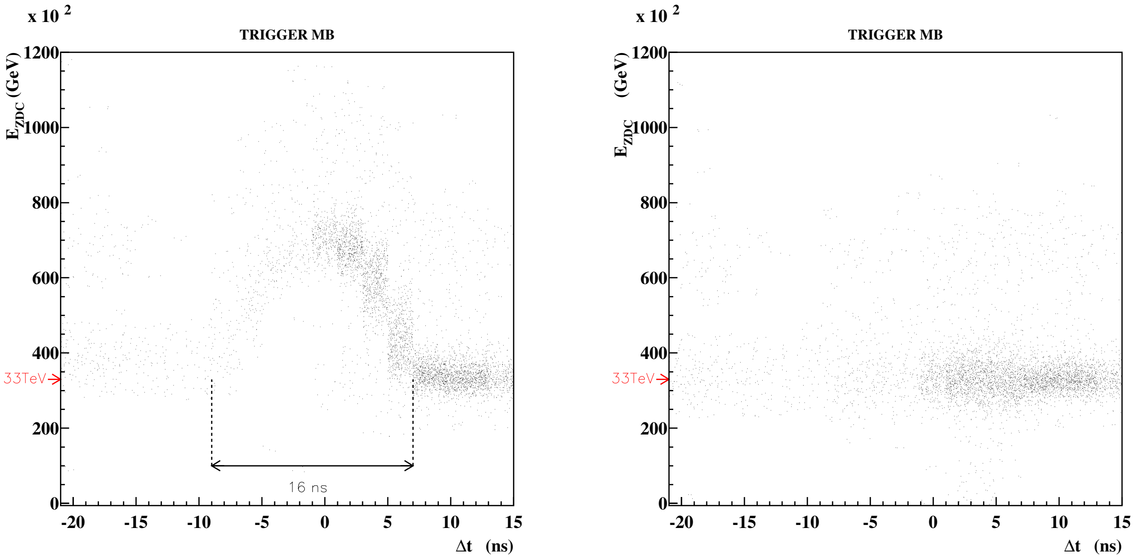

Figure 3.25: *Energy deposited in the ZDC as a function of the time difference between the arrival of two Pb ions in a 34 ns BH TDC window, before a) and after b) beam pile–up correction for run 9435 in MB ZDC trigger. NIZDC=2 and NICALO=1 are required.*

two ions reach the ZDC at a time distance lower than about 16 ns, after having interacted in the target region (interaction pile–up).

Therefore I have considered some runs (at the beginning, in the center and at the end of the data taking period) where the 4 mm thick target is present.

The beam pile–up correction, previously fixed with "empty target" runs, where only beam pile–up problems can affect the measurement, is now applied to the runs with target.

In Fig. 3.25 the correlation between the ZDC energy and Δt is plotted, before and after the correction, in MB ZDC trigger for the run 9435 ($I \simeq 6.81 \cdot 10^7$ Pb ions/burst). Only events with NIZDC=2 are selected.

This correction is able to correct only beam pile–up events, where no interactions have taken place inside the target. Therefore, to avoid applying the correction to interaction pile–up events, they have been excluded in Fig. 3.25, by requiring only one interacting ion in a $\sim$ 30 ns time window of the EMC (NICALO=1). This selection uses information provided by the electromagnetic calorimeter, which detects only events corresponding to ions that have interacted in the target (see Section 4.3.4).

The correlation E_{ZDC} versus Δt plotted in Fig. 3.25a is similar to the one observed in Fig. 3.22: the events relative to two not pile–upped Pb ions lie on the line at 33 TeV, while the "bump" at about 66 TeV is due to two Pb ions that arrive in the BH separated in time by less than 16 ns and therefore produce beam pile–up

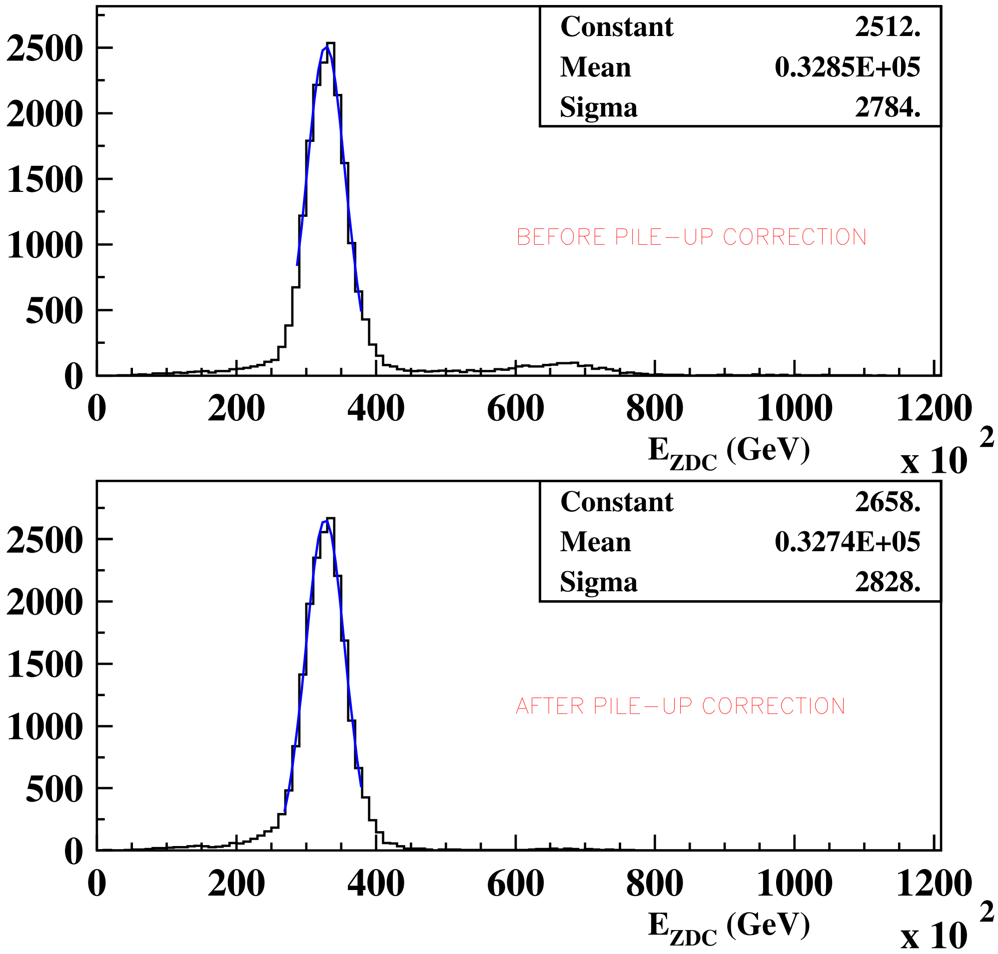

Figure 3.26: *ZDC spectrum in MB ZDC trigger before (a) and after (b) beam pile–up corrections for run 9435, with NICALO=1.*

problems in the ZDC.

In Fig. 3.26 the ZDC spectrum before and after the correction, fixed for "empty target" runs and applied to run 9435, is plotted in MB ZDC trigger, requiring NICALO=1. The beam pile–up events (second peak in Fig. 3.26a) have been completely recovered and put into the single Pb peak, which, for effect of this correction, becomes a little bit larger (Fig. 3.26b).

Let us now consider events in dimuon trigger. This trigger selects dimuons, that is couples of $\mu^+\mu^-$ produced during the interaction of the Pb beam within the target. This implies that a dimuon trigger fires only if an interaction has occured inside the target.

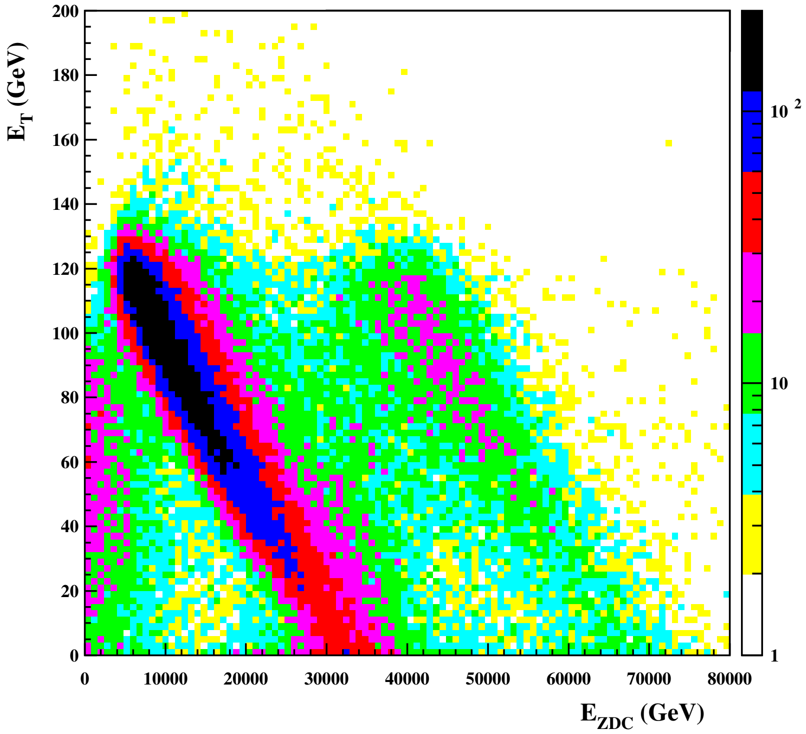

Figure 3.27: *Correlation E_T versus E_{ZDC} in dimuon trigger (NICALO=1). Note that the z scale is logarithmic.*

The correlation E_T versus E_{ZDC} is plotted in Fig. 3.27, by selecting dimuon trigger events and by requiring NICALO=1. A first more pronounced "banana" correlation is clearly visible: lower E_T values correspond to greater amounts of energy in the ZDC (peripheral collisions); in central collisions few energy is released in the ZDC while many particles reach the EM calorimeter. The E_{ZDC} maximum value corresponds to the peak of those Pb ions that have not interacted in the target and therefore depose all their energy in the ZDC ($E_{ZDC} \sim 33\,TeV$). Close to this first "banana" correlation there is a second one, shifted to greater E_{ZDC} values. It is due to pile–up events caused by two ions that have interacted in the target (zone at higher E_T values) or by two not interacting Pb ions (E_{ZDC} peak at 66 TeV).

The aim of the correction is to correct pile–up events so that the second "banana" correlation disappears.

As for the "empty target" runs, I have plotted the correlation E_{ZDC} versus Δt (Fig. 3.28a) and I have corrected pile–up events by using the coefficients deduced from "empty target" runs. The structure of the correlation is larger than that already observed in Fig. 3.22 and Fig. 3.25a. This is due to the fact that the dimuon trigger selects only events where an interaction inside the target has produced a

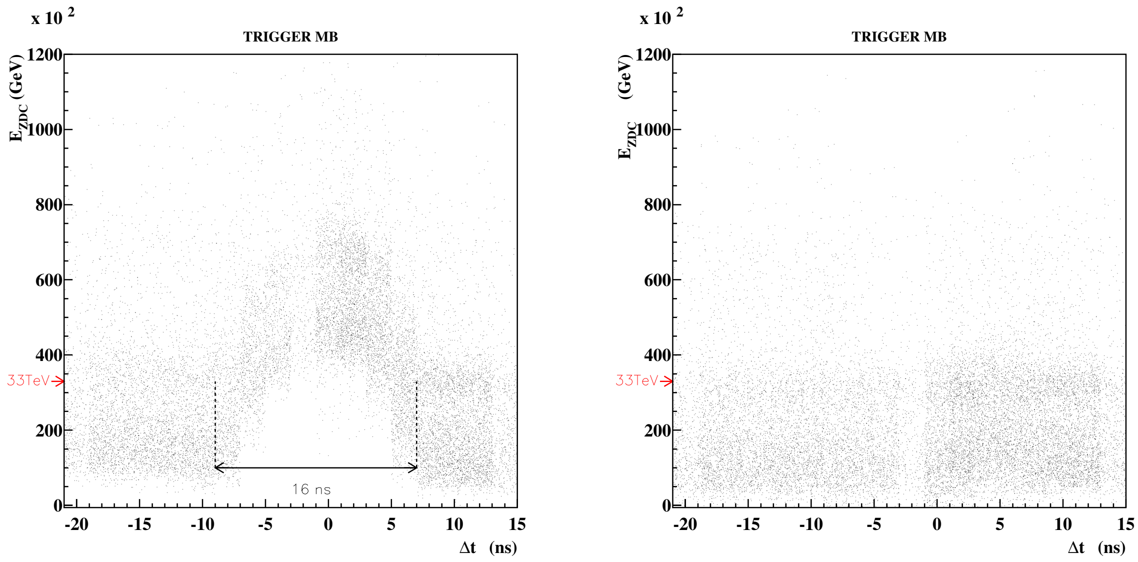

Figure 3.28: *Energy deposited in the ZDC as a function of the time difference between the arrival of two Pb ions in a 34 ns BH TDC window, before a) and after b) beam pile–up correction for run 9435 in dimuon trigger. NIZDC=2 and NICALO=1 are required.*

$\mu^+\mu^-$ pair. Therefore the energy detected in the ZDC is no longer centered at 33 TeV (or 66 TeV in case of two pile–upped Pb ions), but ranges from 0 to about 40 TeV (or from about 40 TeV to 80 TeV for pile–up events).

After the pile–up correction, the correlation in Fig. 3.28b is flat, but maintains the E_{ZDC} spread observed in Fig. 3.28a.

In dimuon trigger the request NICALO=1 is even more important than in MB trigger, because the dimuon events have a probability to be affected by interaction pile–up problems greater than the MB events (which are mainly due to ions that have not interacted in the target).

The correlation E_T versus E_{ZDC} in dimuon trigger after the pile–up correction is plotted in Fig. 3.29 (NICALO=1 is requested). The second and less pronounced banana visible in Fig. 3.27 and due to pile–up events has almost completely disappeared. The events in this second banana have been moved to the first correlation banana and thus almost totally recovered.

In Fig. 3.30 the E_{ZDC} spectrum before and after the pile–up correction is shown for dimuon events (NICALO=1 is required). Again the applied correction has allowed to recover almost all the events with pile–up problems.

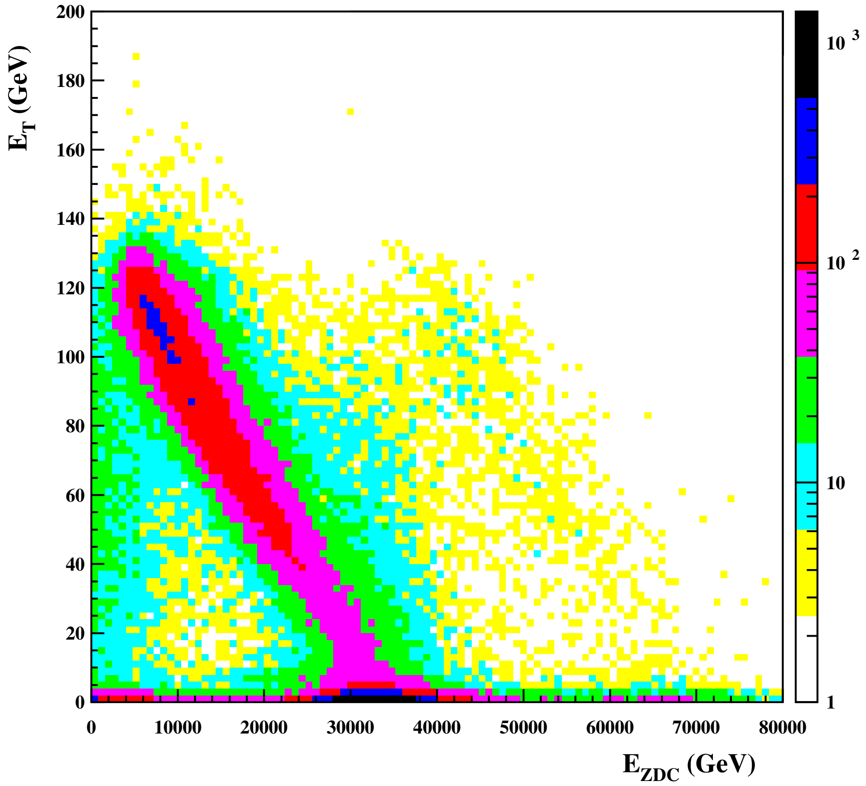

Figure 3.29: *Correlation E_T versus E_{ZDC} in dimuon trigger (NICALO=1), after the pile–up correction. Note that the z scale is logarithmic.*

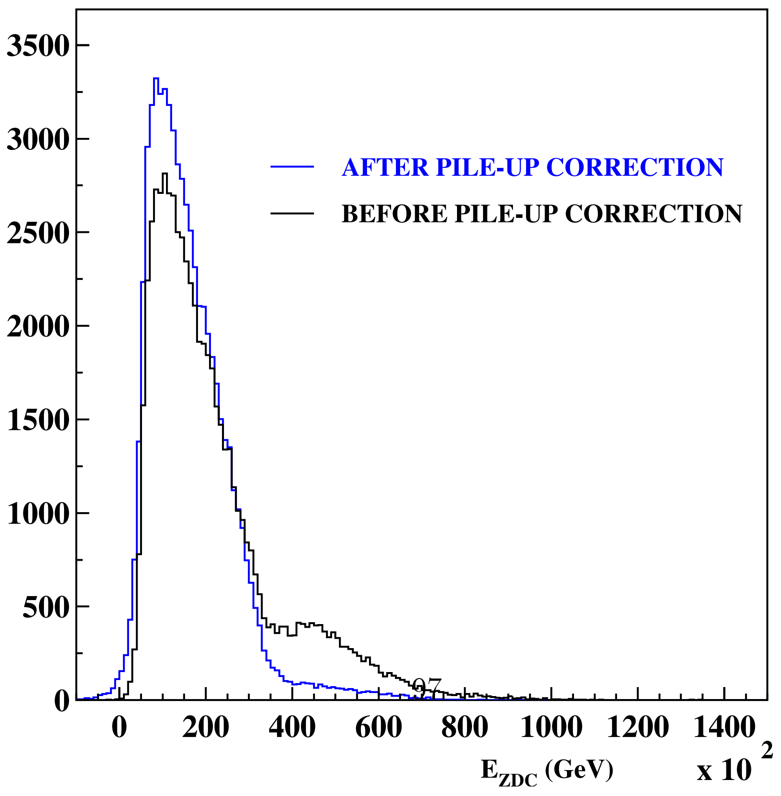

Figure 3.30: *ZDC spectrum in dimuon trigger before (a) and after (b) beam pile–up correction for run 9435, with NICALO=1.*

To have an idea of the percentage of pile–up events that affects the E_{ZDC} spectrum in dimuon and MB trigger, I will try to estimate the probability to have a pile–up event in a 16 ns time window (if two events arrive separated in time more than 16 ns, they can be detected separately by the ZDC and they do not produce pile–up problems, as seen before).

When a trigger is considered as a good one for the experiment, a 12 ns reading gate of the ADC's is opened. We do not have pile–up problems if no other ion arrives during the whole gate (actually a 16 ns window is considered, to take the signal tail into account). If we assume that the repartition of ions follows the Poisson law, the probability of having no other ion in the $\Delta t \sim 16\ ns$ interval is given by

$$P(0) = e^{-\overline{n}} \tag{3.10}$$

where $\overline{n}$ is the mean number of ions in the Δt interval, which can be evaluated by $\overline{n} = \Delta t \cdot I/B$ ($I \simeq 6 \div 7 \cdot 10^7$ Pb ions/burst is the beam intensity per burst and $B = 5\ s$ is the effective spill).

The probability of having pile–up, i.e. one or more other events in the Δt interval, is thus

$$1 - P(0) = 1 - e^{-\overline{n}} \tag{3.11}$$

which is of the order of 19%.

The hypothesis that the events are distributed according to a Poisson law is justified for the MB triggers, since they start every time a signal greater than a minimum threshold is released in the ZDC. This assumption has been demonstrated to be valid also for dimuon events [9], since the probability of having a dimuon trigger is very small if compared to the number of incident ions. But for the dimuon triggers we are not authorized to consider the gate window randomly opened. We have to take into account the fact that the probability $P(n)$ of detecting n ions in the Δt time window, opened by a previous ion, is conditioned by the "trigger", which requires that at least one incident ion has produced a dimuon. In this case $P(n)$ can be estimated by [9, 10]

$$P(n) = \frac{e^{-\overline{n}} \cdot \overline{n}^n}{n!\ (1 - e^{-\overline{n}})} \tag{3.12}$$

where $\overline{n}$ can be evaluated in the same way as for Eq. 3.10. The pile–up probability for dimuon events, estimated in the working condition of the NA50 experiment is about 10%.

3.5 ZDC energy measurement

As already discussed in Section 2.6, in the 2000 data taking the NA50 experiment disposed of three kinds of trigger: a dimuon trigger (which selects dimuon events), a Minimum Bias (MB) trigger that fires every time at least a small amount of energy is released in the ZDC (a threshold of about 50 mV is imposed) and a MB trigger, based on the information provided by one of the 16 baldes of the BH when the incoming Pb ions pass through it.

A typical spectrum of the ZDC, collected at a beam intensity of the order of $6-7\cdot 10^7$ Pb ions/burst with the two MB triggers, is shown in Fig. 3.31.

The clearly visible peak corresponds to the signal produced in the calorimeter by the Pb ions that have not interacted in the target (they release an energy of about 208 nucleons$*$158 GeV/nucleon $= 33$ TeV). The events that populate the region of the spectrum on the left of the Pb peak are due to interactions of the Pb projectiles in the target.

The events where a small amount of energy is deposited in the ZDC (corresponding to central collisions) are less frequent than those where the energy detected by the ZDC is larger (peripheral collisions). In particular, the energy released in the ZDC in very central collisions is never zero, but has a minimum at 2–3 TeV.

The same characteristics are observable in the E_{ZDC} spectrum collected with the dimuon trigger, which is the main trigger of the experiment (Fig. 3.32).

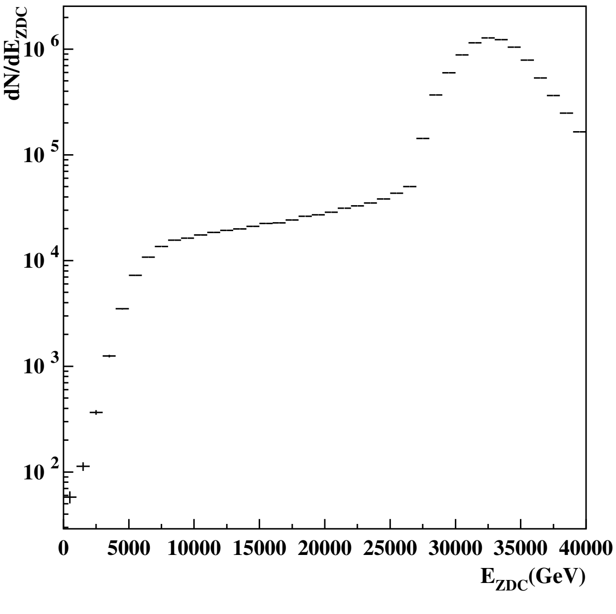

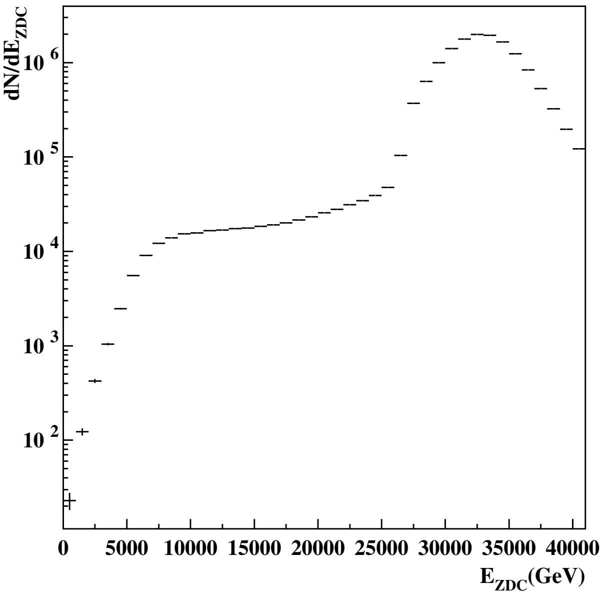

Figure 3.31: *Zero–degree energy spectrum in the minimum bias triggers: MB BH (left) and BH ZDC (right) trigger.*

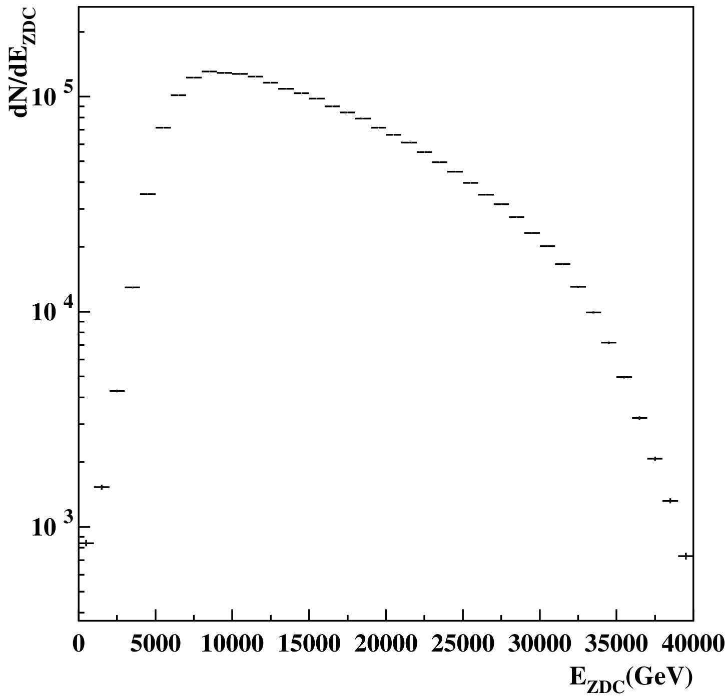

Figure 3.32: *Zero–degree energy spectrum in the dimuon trigger.*

The low–energy region of the E_{ZDC} spectrum is similar with the three triggers: a "knee" at about $E_{ZDC} \sim 6 - 7\,TeV$ and very few events at E_{ZDC} smaller than 2–3 TeV.

This confirms that even in the most central collisions a residual energy of 2–3 TeV is emitted at zero degree, giving the ZDC signal a dynamic range of about 10 (from 3 to 33 TeV) and allowing to discriminate it to provide an unbiased sample of events.

It has been observed that the MB ZDC trigger in some runs of the 2000 data taking period has problems of stabilization and of stability in time. This problems are limited to a part of the whole sample of events and do not affect all the operations of pedestal subtraction, calibration and pile–up corrections previously performed with the MB ZDC trigger. Nevertheless, it has been decided to use the trigger provided by the BH as a minimum bias trigger for the data analysis.

In the standard analysis method described in Chapter 5, the numbers of J/ψ and Drell–Yan events are extracted from the invariant mass spectrum of the opposite–sign muon pairs in dimuon trigger and the MB sample of events is only useful to choose the E_T cut to apply to the data. This cut on the transverse energy detected by the EMC is needed to get rid of the non–interacting Pb ions and to investigate only the events due to interactions in the target. For a detailed description of the adopted procedure see Chapter 4 and Section 5.6.1.

Bibliography

[1] M.C.Abreu et al. (NA50 coll.), Phys. Lett. B 521 (2001) 195.

[2] R.Arnaldi et al., Nucl. Instr. and Meth. in Phys. Res. A 411 (1998) 1.

[3] P.Gorodetzky et al., Nucl. Instr. and Meth. A 361 (1995) 161.

[4] G.Anzivino et al., Nucl. Instr. and Meth. A 357 (1995) 380.

[5] E. Chiavassa et al., Nucl. Instr. and. Meth. A 367 (1995) 267.

[6] T.C.Awes et al., Nucl. Instr. and Meth. A 311 (1992) 130.

[7] J.M. Dieulot et al., Nucl. Instr. and Meth. A 314 (1992) 185.

[8] R. Brun et al. GEANT, CERN Program Library, W5013, version 3.14.

[9] A.Sinquin, PhD Thesis, Université de Paris Sud, July 1988.

[10] L.Luquin, PhD Thesis, Université de Clermont Ferrand, July 1995.

Chapter 4

Event reconstruction and selection

4.1 Introduction

During the data taking period the raw data are stored on magnetic supports (Raw Data Tapes) by the acquisition program. These magnetic tapes contain, for each event, information related to all the detectors in the NA50 experimental apparatus, such as the ADC counts of the EMC and the ZDC, the wires hit in the proportional chambers, the signals from the scintillator blades of the hodoscopes, information from the "control" detectors (BH, BHI, BHI new, AH), etc. The raw data tapes are read by the experiment reconstruction program, called DIMUREC [1], which allows to estimate all the physical quantities necessary for the data analysis.

Depending on the trigger type (see section 2.6), different reconstruction algorithms and selection criteria are applied to the data. For dimuons events, DIMUREC reconstructs the dimuon tracks and calculates all the dimuon physical variables that will be useful for the final analysis and that are recorded on μDSTs (micro Data Summary Tapes).

Minimum bias events are collected simultaneously with the dimuon events, but are prescaled by a factor that brings their rate down to 10% of the total number of events recorded on tape. The muon track reconstruction is not performed for the MB events and only the information from different detectors is stored on μDSTs to be used during the analysis.

In this chapter I will describe the selections applied to the reconstructed muon pairs in order to obtain a clean data sample to be analysed. The data reduction criteria performed on the minimum bias events are also discussed.

4.2 Dimuon track reconstruction

The reconstruction of a dimuon event requires the identification of two single muon tracks with common origin in the target region, according to a trigger signal from the hodoscopes. This is realized thanks to 8 multiwire proportional chambers (from PC1 to PC8 in Fig 4.1).

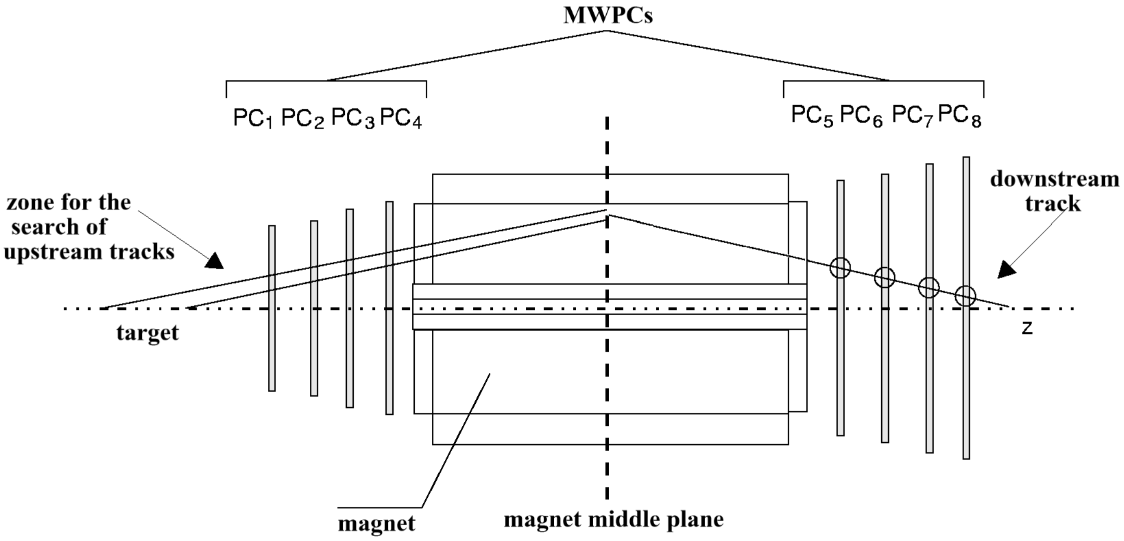

Figure 4.1: *Reconstruction of the muon tracks upstream and downstream the magnet.*

The reconstruction program selects the starting region for the track reconstruction from the patterns of the hodoscope scintillators that have given the dimuon trigger and begins to consider the MWPCs downstream the magnet. In these chambers the number of hit wires is lower because low transverse momentum muons are deviated by the magnet outside the spectrometer acceptance. For a given wire plane, the hit wires of the first (PC5) and the last (PC8) chambers define a road. Then it is verified that also the intermediate chambers (PC6 and PC7) have registered the muon passage. The four points must be aligned to define a track (see Fig 4.1).

The same procedure is adopted to search the tracks in the three projections corresponding to the (u,v,w) coordinates (see Fig 2.11). The association of the three projections defines a tube whose diameter (roadwidth) depends on the chamber resolution. The track is considered as reconstructed if at least three of the "downstream" chambers measure a point belonging to that tube.

The so–obtained downstream track is then extrapolated to the middle plane of the magnet to define a zone pointing toward the target, for the search of upstream tracks (Fig 4.1).

The procedure for the upstream track determination is the same adopted for the downstream ones, but the studied region is now reduced to the tracks compatible with the search zone previously defined. The downstream and upstream segments, in order to be associated to the same muon track, have to satisfy criteria concerning the distance between their impact points on the magnet middle plane (which must be less than 3 cm) and the difference between their azimuthal angles ($\Delta\Phi < 0.25$ rad) [2]. Two single muon tracks form a dimuon event if they have a common origin in the target [3].

For each dimuon event, the kinematic variables of the muons (the dimuon invariant mass $M_{\mu^+\mu^-}$, the transverse momentum p_t, the polar angle θ and the azimuthal angle ϕ in the Collins–Soper reference frame [4]) and the interaction vertex are computed and recorded on μDSTs.

The efficiency of the reconstruction program is of the order of 90%.

4.3 Dimuon event selection

Once the dimuon tracks are reconstructed, "general" criteria are applied to select a as cleaner as possible sample of events for the final analysis [3].

4.3.1 Run selection

The raw data are recorded on tape in samples of events, called runs. During the 2000 data taking period a total of 791 runs was collected, each of them corresponding to about 360000 events and to a data acquisition time of $\approx 1 - 1.5$ hours .

The first step of the data selection consists of the rejection of the runs during which the experimental apparatus did not satisfy all the criteria for a good working. We eliminate all the runs characterized by bad beam quality (big beam intensity fluctuations, bad beam alignment, too high intensity), by hardware problems or anomalies in one or more detectors, by a bad working of the acquisition system, etc.

4.3.2 Geometrical cuts

After the reconstruction of the dimuons tracks, further selections can be applied on the crossing point of the muons inside the experimental apparatus. Their purpose is to reduce the number of fake tracks due to reconstruction errors or to coincidences with background events. The quality of the reconstructed tracks is therefore refined.

Fiducial cut

This cut is based on geometrical criteria of the apparatus and selects only muons passing through the active volume of the tracking chambers. All the tracks crossing the iron part of the magnet are rejected, because they are affected by multiple scattering and they deteriorate the mass resolution of the spectrometer.

Image cut

It rejects those events where at least one of the two muons would not have been accepted if it had the opposite charge at the entrance of the magnet. The algorithm relative to this cut changes the charge sign of each muon and performs a fast simulation of the obtained track. If this track is lost from the sample of the accepted tracks, that dimuon event is stricken out.

This procedure is equivalent to change the sign of the magnetic field, letting the particle charge unchanged and guarantees that the spectrometer acceptance is independent of the electric charge of the detected muons.

Moreover this cut is necessary to correctly estimate the combinatorial background from the $\mu^+\mu^+$ and $\mu^-\mu^-$ muon pairs (see Section 5.3).

To reduce the possible inefficiencies of this cut, during the data taking period the sign of the magnetic field has been periodically reversed (every 15–20 runs).

P$*$DTarg cut

This cut allows to refine the sample of the reconstructed tracks, by rejecting the tracks not pointing to the target, which would be reconstructed with wrong values of the kinematic variables [5, 6]. The used selection criterion is based on the calculation of the distance from the beam axis of the intersection point between the reconstructed muon track and the target middle plane

$$Dtarg = \sqrt{D_x^2 + D_y^2} \tag{4.1}$$

where D_x and D_y are the coordinates on the x and y axes (perpendicular to the beam axis) of the track origin point in the target. Usually the estimated Dtarg values are much greater than the beam radius. Therefore a cut on the Dtarg variable allows to eliminate muon tracks not originated in the target region but somewhere downstream or upstream the target. In fact, a track produced upstream in the beam line or downstream in the hadron absorber, or a dimuon coming from the association of two muons produced by π or/and K disintegrations obviously have a very large Dtarg value.

Moreover, a big Dtarg can be due to the multiple scattering inside the target or the absorber, which depends on the muon transverse momentum, according to

$$Dtarg \propto \frac{1}{p} \tag{4.2}$$

A direct cut on Dtarg will affect muons in different ways, depending on their momenta. In order to select which tracks have to be rejected, it is thus preferable to apply the selection cut on the P$*$DTarg variable, which is independent of p.

If the beam is centred on the beam axis, the distributions of $P_x * D_x$ and $P_y * D_y$ are assumed to be gaussian, centred on zero and with width σ_x and σ_y. Otherwise the mean values $\mu_x = < D_x >$ and $\mu_y = < D_y >$ must be evaluated. The coefficients μ_i and σ ($\sigma_x = \sigma_y \equiv \sigma$ for symmetry reasons) are estimated for different intervals of the muon transverse momentum, in order to take into account possible p dependencies not completely solved by the P∗DTarg factorization.

We can define the variable

$$cut = \left(\frac{P * (D_x - \mu_x)}{\sigma_x}\right)^2 + \left(\frac{P * (D_y - \mu_y)}{\sigma_y}\right)^2 \tag{4.3}$$

which is distributed as a χ^2 with two degrees of freedom [1]. The probability to have $\chi^2 \geq\ cut$ for each track is defined by:

$$Prob\,(cut) \equiv Prob\,(P * Dtarg) \equiv \int_{cut}^{+\infty} f(\chi^2)\,d\chi^2 \tag{4.4}$$

If the experimental distribution of good tracks is gaussian, the χ^2 probability distribution must be flat. A typical $Prob(\chi^2)$ distribution is reported in Fig. 4.2 for opposite–sign muons with invariant mass $M_{\mu^+\mu^-} > 3\ GeV/c^2$ and both for convergent and divergent tracks. The peak at low $Prob(\chi^2)$ values corresponds to high P∗DTarg values, i.e. to events coming from strongly scattered tracks or from tracks not originated in the target. We decide to keep only the tracks corresponding to $Prob(\chi^2) \geq a$, where a is the value above which the distribution is flat. This cut eliminates an a% of muon tracks and an a^2 % of dimuons.

For the 2000 experimental data a 2% P∗DTarg cut is enough to ensure a flat $Prob(\chi^2)$ distribution.

The P∗DTarg parameters have been tuned for high mass dimuons ($M_{\mu^+\mu^-} > 3\ GeV/c^2$), since in this mass region the combinatorial background (which has a not flat $Prob(\chi^2)$ distribution) is negligible. The parameter values found with this procedure can then be used for any mass region, since the P∗DTarg distribution for signal muons does not depend on the dimuon mass.

The study of the P∗DTarg cut effects on the $J/\psi/DY$ ratio will be performed and reported in Section 5.6.3.

4.3.3 Kinematic cuts

The DIMUREC reconstruction program, for each accepted muon track, estimates the relative kinematic variables:

- the dimuon invariant mass $M_{\mu^+\mu^-}$

[1] This is not statistically correct because a priori the condition $\mu_x = < D_x >$ does not imply that $< P_x * (D_x - \mu_x) >= 0$. Practically this problem can be neglected because P and D_x or D_y are not correlated.

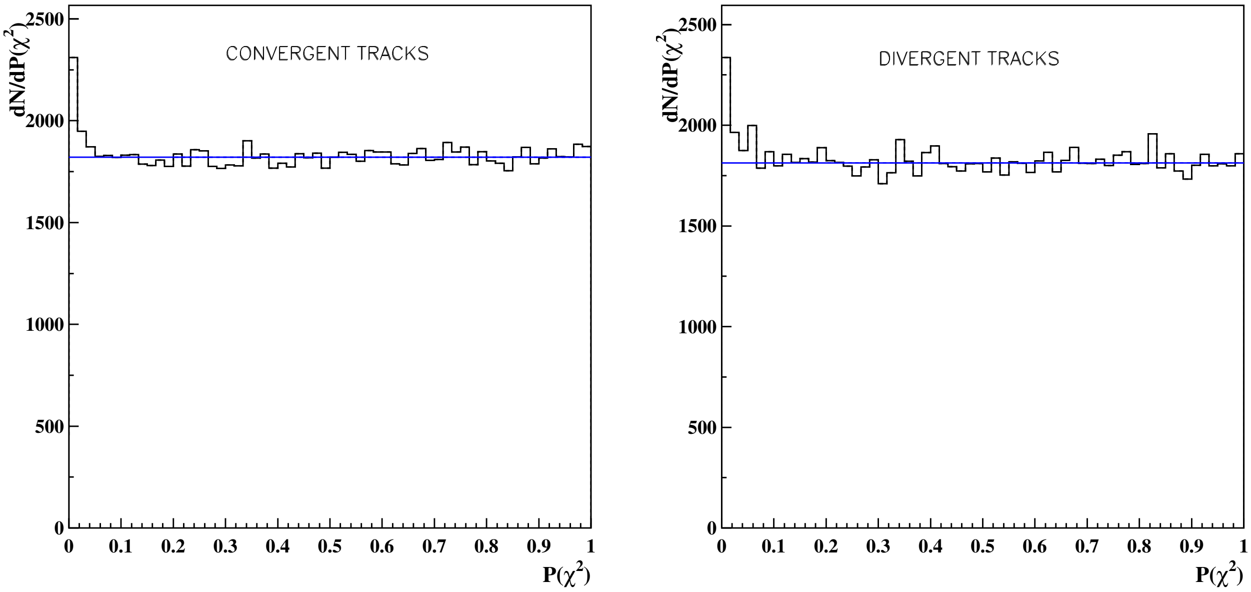

Figure 4.2: *$Prob(\chi^2)$ distribution for 2000 Pb–Pb data, for $M_{\mu^+\mu^-} > 3$ GeV/c^2.*

- the rapidity y, defined as
$$y = \frac{1}{2}\, ln\, \frac{E + p_z}{E - p_z} \tag{4.5}$$
where p_z is the component of the muon momentum along the beam axis and E is its energy. The rapidity depends on the reference frame and it can be evaluated in the centre of mass frame as:
$$y^* = y_{LAB} - y_{CM} \tag{4.6}$$
where y_{LAB} refers to the laboratory system and y_{CM} is the rapidity of the centre of mass in the laboratory frame. For Pb–Pb collisions at 158 GeV/c per nucleon, the target rapidity in the laboratory frame is around $y \sim 0$, while the projectile rapidity is $y \sim 5.8$. The rapidity of the centre of mass is thus $y_{CM} \sim 2.9$.

- the transverse momentum p_T

- the polar and azimuthal angles in the Collins–Soper reference frame (θ_{CS} and ϕ_{CS}) [4]. If $\overrightarrow{P_p}$ and $\overrightarrow{P_t}$ are the transverse momenta respectively of the projectile and of the target nucleus in the dimuon centre of mass, and $\overrightarrow{P_\mu}$ is the μ^+ momentum, the CS reference frame is defined as follows: the z axis is the bisector of $\overrightarrow{P_p}$ and $-\overrightarrow{P_t}$, while the y axis is parallel to $\overrightarrow{P_p} \times \overrightarrow{P_t}$. Therefore θ_{CS}

is the polar angle between $\hat{z}$ and $\overrightarrow{P_\mu}$ and ϕ_{CS} is the azimuthal angle between $\hat{y}$ and $\hat{z} \times \overrightarrow{P_\mu}$.

In order to eliminate dimuons coming from regions where the spectrometer acceptance is very small, some selection cuts are applied on these kinematic variables. This selection involves only the y and θ_{CS} variables

$$0 < y^* < 1 \qquad -0.5 < cos\theta_{CS} < 0.5 \tag{4.7}$$

since the acceptance is nearly constant all over the p_T and the ϕ_{CS} range.

Fig. 4.3 shows the invariant mass spectrum, the y^*, p_T and $cos\theta_{CS}$ distributions of the reconstructed events for the 2000 data. The effect of the kinematic cuts is reported on the y^* and $cos\theta_{CS}$ variables. The kinematic cuts and a 2% P∗DTarg cut have been applied to the invariant mass spectrum for opposite sign muons. In such a spectrum two regions can be distinguished:

- the intermediate mass region ($1.5 < M_{\mu^+\mu^-} < 2.5\ GeV/c^2$), which is between the Φ and J/ψ peaks and includes the Drell–Yan process and the semileptonic decays of the charmed mesons, plus the contribution from uncorrelated decays of π and K pairs;

- the high mass region (approximately from 2.5 GeV/c^2), where the J/ψ and ψ' resonances are visible on the Drell–Yan continuum.

The J/ψ peak is very pronounced, since the spectrometer apparatus has been designed in order to have the maximum acceptance and the best mass resolution in the high mass region. The peak of the ψ' decay is barely visible after the J/ψ, since the statistics is much lower than for the J/ψ.

As it is shown in Fig. 4.3, the dimuon rapidity in the center of mass system covers the range $0 < y^* < 1$, which corresponds to $2.9 < y_{LAB} < 3.9$ in the laboratory frame. This is a direct consequence of the limitations imposed by the spectrometer acceptance, which can explain the $cos(\theta_{CS})$ distribution as well. Actually the muon spectrometer selects dimuons with a $cos(\theta_{CS})$ distribution peaked around zero, which corresponds to muons produced orthogonally to the beam axis in the center of mass frame. High values of $|cos(\theta_{CS})|$ are not accepted because are linked to muons with very low momentum that have stopped in the hadron absorber.

4.3.4 Other cuts

Besides the run selection and the cuts for the quality of the dimuon track reconstruction, other parameters are introduced to guarantee the event quality. These parameters are evaluated on the basis of information provided by different detectors of the experimental apparatus.

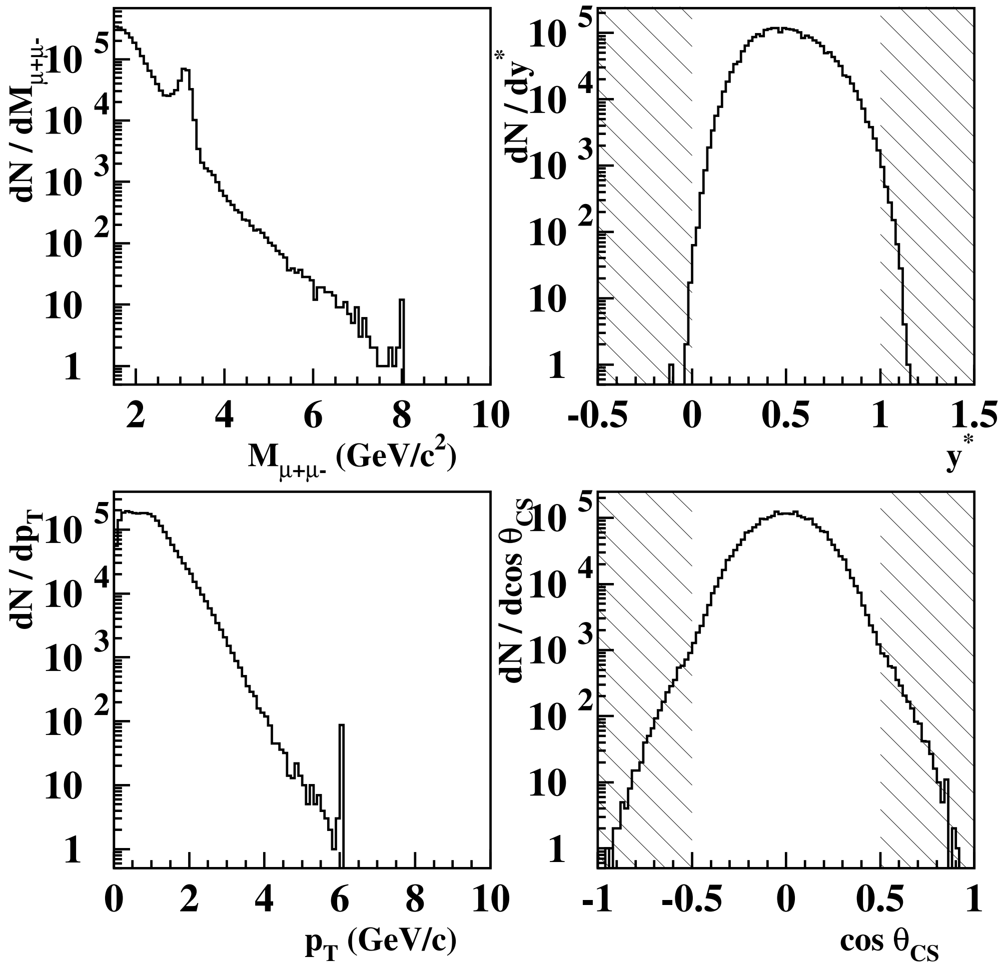

Figure 4.3: *Invariant mass spectrum $M_{\mu^+\mu^-}$, rapidity y^* (in the centre of mass system), transverse momentum p_T and $cos\theta_{CS}$ distributions of the reconstructed events for the 2000 Pb–Pb data. The shaded areas correspond to the applied kinematic cuts. A 2% P∗DTarg cut and the kinematic cuts have been applied to the $M_{\mu^+\mu^-}$ spectrum.*

Pile–up rejection

A second incident Pb ion that arrives in the 20 ns analysis window of the EMC photomultipliers and that interacts in the target, can introduce a bias in the transverse energy measurement of this detector. This is what we call an "interaction" pile–up event and it must be rejected for the final analysis. The procedure followed to cut these events is based on the analysis of the EMC signal shape [7]. Actually, when only one Pb ion interacts inside the target and produces a dimuon trigger, the amplitude of the signal received by the EMC varies with the produced energy, but its shape and time position are always the same. An interaction brought about by a second ion results in a similar shape signal, hence the shape and time position of the signal coming from the superimposition of these two interactions is aleatory. The analysis of the signal shape allows to identify and reject pile–up events. The flag NICALO=1 guarantees that no interaction pile–up event has been detected by the EMC in a time window of about 25 ns. The percentage of events rejected by this cut is about 27% of the total events, after that the kinematic, the image, the fiducial and a 2% P∗DTarg cuts have been applied to the dimuon sample.

An other algorithm is elaborated to identify and recover beam pile–up events. It is based on information provided by the ZDC and by the BH, as described in details in Section. 3.4.4. If two ions hit two different BH blades in a time window of 34 ns, a new NIZDC flag is defined equal to 2, otherwise its value is 1.

An event with NIZDC=2 does not necessary suffer from pile–up problems in the ZDC, since only if 2 Pb ions arrive separated in time by less than 16 ns, the ZDC is not able to detect them separately. Therefore, thanks to the unified information of the ZDC and of the BH, if an event with NIZDC=2 has produced a pile–upped signal in the ZDC (i.e. it has released an energy double with respect to the one of a single non–interacting Pb ion), a correction is applied to recover it, if not it is let unvaried.

The flag NIZDC=1 selects about 62% of the total sample of dimuon events, while the less strict requirement NIZDC=1 or 2, which includes also those pile–up events recovered by using the ZDC information, increases the statistics of about 26%.

An other cut to reduce the risk of pile–up is realized by requiring only one incident ion detected by the BH within the 20 ns gate opened by the trigger [6]. This condition rejects 36% of the total events and is redundant if used together with NICALO=1 and NIZDC=1 or 2. Thus it has been decided to release the NIBHAD=1 requirement in the 2000 data analysis.

Rejection of parasitic interactions

The purpose of the “interaction” detectors, the BHI and the BHI new, is to check that no incident ion has interacted in the BH, causing a pollution of the beam and producing fragments that can interact in the target region [6, 8]. Joint information from the BHI and the BHI new allows to estimate the flag NPARAS which, if equal to 0, cuts parasitic interactions in the BH (about 24% of the total dimuon events).

Beam halo rejection

The request NOHALO=0 selects only dimuon tracks passing through the hole of the “anti–halo” detectors, granting the exclusion of fragments coming from projectile interactions upstream the target or from incident ions distant more than 1.5 mm from the beam axis.

For the 2000 data analysis, this cut is not adopted because it has been observed that the "anti–halo" detectors see also particles that are produced during the interaction inside the target and that travel backward from the target region. Therefore, requiring NOHALO=0 would cut good interactions too, in particularly in case of central collisions.

Target recognition algorithm

The target identification algorithm is based on the signal detected by the two quartz blades located off the beam axis, on the right and the left sides of the target. In 1995 and 1996 each subtarget had two quartz blades, one on the right and one on the left (see Section 2.3). These detectors measure a fraction of the particles produced in the interaction inside the target and allow to identify the subtarget involved by the primary interaction of the projectile [2, 9].

The target identification was very important in 1995 and 1996 where 7 subtargets were used, but it was useful in 1998 and 2000 too, because it rejects events not originated in the used single target.

The efficiency of this identification strongly decreases for peripheral collisions where very few secondary particles are produced. In such a collision the very small signal released in the quartz blades is indistinguishable from that of δ rays generated by the non interacting ions crossing the target. This produces an efficiency loss of the target identification. Therefore a new selection method has been developed to reject off–target events and to recover the target identification efficiency for peripheral events [10]. This new method is based on the correlation between E_T and E_{ZDC}, as described in the following, and has been used instead of the standard target recognition algorithm.

Cut on the E_T–E_{ZDC} correlation

Event by event, if only one interaction has taken place in the target, the transverse energy E_T (proportional to the number of participant nucleons N_{part}) detected by the EMC must be correlated with the energy E_{ZDC} (proportional to the number of projectile spectator nucleons) released in the ZDC.

The correlation between E_T and E_{ZDC} for the 2000 data is reported in Fig. 4.4, after the application of all the cleaning cuts described before. Most of the events lie inside the correlation band defined by the two lines superimposed on the plot, which correspond to a 3σ distance from the average correlation. The events out of this band are attributed to off–target interactions or to residual pile–up and must be neglected in view of the data analysis.

The effect on the final $J/\psi/DY$ results of the choice of a different cut on the E_T–E_{ZDC} correlation is taken into account in Section 5.6.2.

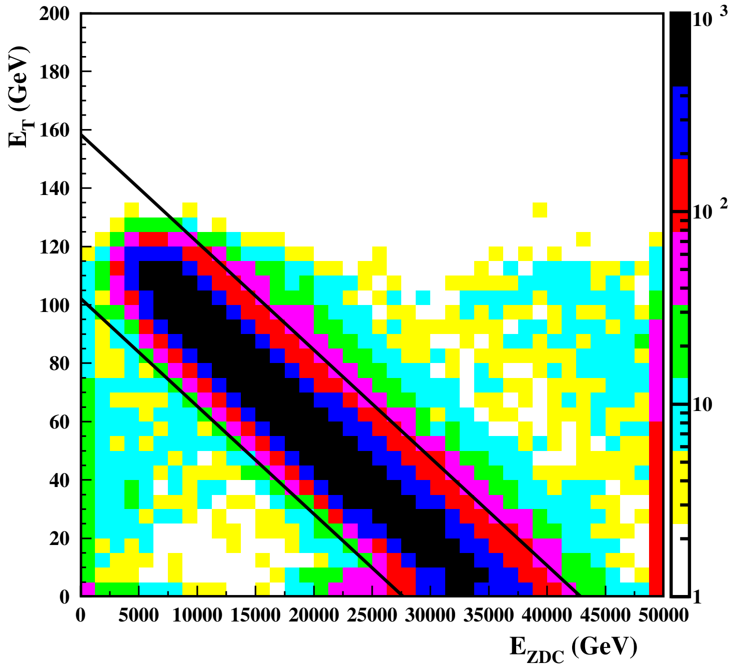

Figure 4.4: *Correlation between the neutral transverse energy E_T and the very forward hadronic energy E_{ZDC}. All the selection cuts previously described have been applied. Note that the z scale is logarithmic.*

Vertex reconstruction with the MD

Since 1998, an independent technique of target identification based on the MD information, has been studied, with the aim of improving the target reconstruction efficiency for peripheral events and of eliminating the Pb–air contamination [11]. The algorithm developed for the 2000 data performs a calculation of the likelihood of a given hypothesis on the interaction vertex position:

- hypothesis 0: the Pb ion has interacted before the target region
- hypothesis 4: the Pb ion has interacted inside the Pb target
- hypothesis 7: the Pb ion has interacted after the target region

A map of the MD strips is built in correspondence with each hypothesis. Then the number N_{poss} of possible coincidences between the two MD planes (i.e. the number of firing strips on MD1 with at least one corresponding good strip on MD2) is counted. The ratio between the effective number of detected tracks that have crossed MD1 and MD2 and N_{poss} gives a statistical estimator, with different values according to the four hypotheses.

The flag NOCIMD is defined as equal to 0, 4, 7, 8 if the larger value for the estimator is given by the case of hypothesis 0, 4, 7 or by none of them. The selection NOCIMD=4 is a valid alternative to the standard target identification based on the quartz blades signal, since it is more efficient for peripheral events, granting a better rejection of Pb–air interaction events. Nevertheless it reduces a lot the statistics for the most peripheral E_{ZDC} bins. Therefore, in the 2000 data analysis reported in this thesis, this selection has not been considered, while it has been adopted in the analyses that use E_T as a centrality estimator (Section 5.7).

In table 4.1 all the selection cuts used to clean the dimuon trigger sample are summed up. All the percentages of events rejected by the different cuts refer to the dimuon sample after the application of the kinematic, image, fiducial cuts and a 2% P$*$DTarg cut.

A cut on the neutral transverse energy, $E_T > 3 GeV$, is applied to reject events due to incident Pb ions that have not interacted inside the target. Since the centrality information provided by the EM and the zero–degree calorimeters is anti–correlated (Fig. 4.4), the requirement of at least a small amount of energy detected by the EMC ensures that an interaction has taken place. In Section 5.6.1 I will discuss the choice of this E_T cut.

For the cuts used in the 1996 and 1998 analyses see [12].

Selection type			% of rejected events
pile–up rejection	NICALO	1	27%
	NIZDC	1	38%
		1 or 2 (alternatively)	12%
	NIBHAD	1 (not selected)	36%
parasitic interaction rejection	NPARAS	0	24%
beam halo rejection	NOHALO	0 (not selected)	22%
target identification	NOCIMD	4 (not selected)	6%
$E_T - E_{ZDC}$ correlation		111.5790-0.003693*E_{ZDC} $< E_T <$ 149.0272-0.003693*E_{ZDC}	34%
non-interacting Pb	E_T cut	$E_T > 3\,GeV$	1.4%

Table 4.1: Selection cuts applied to the dimuon trigger sample of events, after the kinematic, the image, the fiducal and a 2% P$*$DTarg cut.

4.3.5 MB event selection

Besides the usual dimuon trigger already used by NA38, in each burst of the beam there is a prescaled fraction of “Minimum Bias” (MB) triggers. In the 2000 data taking two MB triggers were available, as discussed in Section 2.6. The event selection procedure adopted for the MB events is less strict than that used for dimuon events. A MB trigger fires whenever a minimum energy is released in the ZDC (MB ZDC trigger) or in the BH (MB BH trigger). Therefore no dimuon track reconstruction is performed for such events and, as a consequence, no geometrical and kinematic cut is applied.

The same cuts reported in Table 4.1 and referred to dimuon events, are applied to the MB sample (Table 4.2).

In Fig. 4.5 the E_T–E_{ZDC} correlation is shown in trigger MB after all the selection cuts. The correlation is much more contaminated by off–target interactions than the dimuon trigger one, since no dimuon reconstruction and vertex identification is applied to the MB events.

The same “diagonal” cut chosen for dimuon events is now applied, by selecting the events inside the two lines in Fig. 4.5, corresponding to a 3σ distance from the average correlation.

Selection type			% of rejected events
pile–up rejection	NICALO	1	47%
	NIZDC	1	40%
		1 or 2 (alternatively)	11%
	NIBHAD	1 (not selected)	28%
parasitic interaction rejection	NPARAS	0	9%
beam halo rejection	NOHALO	0 (not selected)	4%
target identification	NOCIMD	4 (not selected)	89%
$E_T - E_{ZDC}$ correlation		111.5790-0.003693*E_{ZDC} $< E_T <$ 149.0272-0.003693*E_{ZDC}	18%
non-interacting Pb	E_T cut	$E_T > 3\,GeV$	77%

Table 4.2: Selection cuts applied to the minimum bias (BH) trigger sample of events.

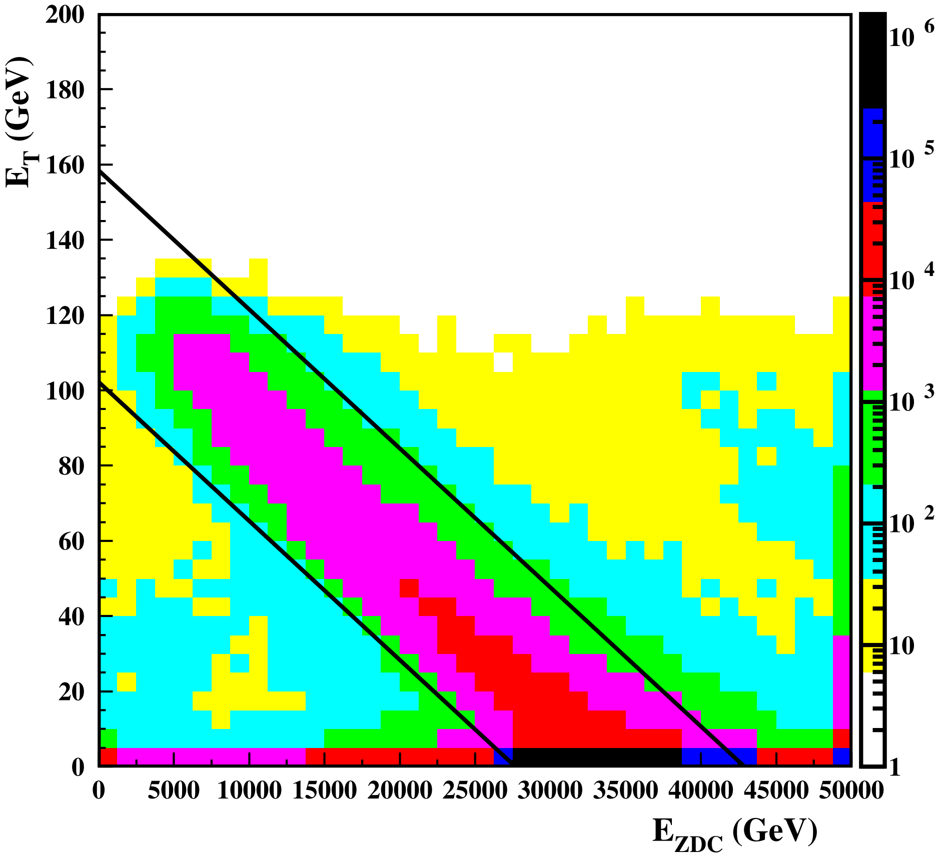

Figure 4.5: *Correlation between the neutral transverse energy E_T and the very forward hadronic energy E_{ZDC} in MB BH trigger. All the selection cuts previously described have been applied. Note that the z scale is logarithmic.*

Bibliography

[1] DIMUREC USER GUIDE 2.00/02 (1997).

[2] F.Bellaiche, PhD Thesis, Université de Lyon, 1997.

[3] M.C. Abreu et al. (NA50 Collaboration), Phys. Lett. B410 (1997) 327.

[4] J.C. Collins and D.E. Soper, Phys. Rev. D16 (1977) 2219.

[5] P.Cortese, PhD Thesis, Universitá di Torino, 2000.

[6] L.Villatte, PhD Thesis, Université de Paris 7, 2001.

[7] L.Luquin, PhD Thesis, Université de Clermont Ferrand, 1995.

[8] L.Villatte, PhD Thesis, Université de Paris 6, 1997.

[9] F.Bellaiche et al., Nucl. Instr. and Methods in Phys. Research A398 (1997) 180.

[10] M.C. Abreu et al. (NA50 Collaboration), Phys. Lett. B450 (1999) 456.

[11] F.Prino, PhD Thesis, Universitá di Torino, 2001.

[12] R.Arnaldi, PhD Thesis, Universitá di Torino, 2000.

Chapter 5

The Standard analysis

5.1 Introduction

As already said, the study of the J/ψ production is referred to the Drell–Yan mechanism, which produces muon pairs in the same invariant mass region as the J/ψ and which is not sensitive to the medium (deconfined or not) where it is generated. The choice of studying ratios, instead of absolute cross–sections, is dictated by the advantage to become free from systematic errors that are equal for the two samples of events, such as detector inefficiencies and flux uncertainties.

In the so–called "standard" analysis, the J/ψ and Drell–Yan cross–sections are extracted from the fit to the dimuon invariant mass spectrum. The whole sample of muon pairs is divided into subsamples, according to the centrality of that dimuon event (estimated by E_{ZDC}, E_T or N_{ch}). In particular, for the analysis reported in this thesis, E_{ZDC} is chosen as a centrality estimator.

In each E_{ZDC} bin a fit to the mass spectrum is performed, taking into account all the processes contributing to the spectrum in the region $M_{\mu^+\mu^-} \geq 2.9\ GeV/c^2$: the J/ψ and ψ' resonance decays, the Drell–Yan continuum, the semi–leptonic decays of D and $\overline{D}$ mesons and the combinatorial background of uncorrelated muons produced by K and π decays. Each process is simulated thanks to Monte–Carlo techniques, then the produced events are reconstructed by means of the same reconstruction program used for the experimental data and the obtained mass spectra are fitted with analytical functions. This method allows to get a sample of simulated events that undergo reconstruction rules and selection cuts identical to those of the experimental sample. Moreover it takes the resolution and the acceptance of the experimental apparatus into account.

Finally the shapes obtained for the different contributions, analytically parametrized, are introduced into the fit to the invariant mass spectrum, in order to extract the contribution to the signal of the different physical processes. Hence the ratio of the extracted J/ψ and Drell–Yan numbers is studied as a function of the collision centrality.

In this chapter I will describe the different steps of this analysis technique and I will show the final results. Then the consequence of systematic effects on the $\sigma_{J/\psi}/\sigma_{DY}$ will be discussed. In conclusion, the results of the NA50 data taking in the year 2000 will be compared to the previous results of the experiment and to the results of the analysis of the same data, performed as a function of E_T.

5.2 Monte Carlo simulation of physical sources

The shapes of the J/ψ, ψ', Drell–Yan and open charm contributions to the dimuon invariant mass spectrum are determined by a Monte–Carlo procedure that generates muon pairs and simulates the acceptance and the smearing effects of the experimental apparatus. The differential distributions of the four processes are generated by dedicated programs, such as DIMUJET [1] and PYTHIA [2], which include the theoretical knowledge about the production mechanisms of these processes.

These simulated events are tracked through the experimental setup and reconstructed with the same reconstruction program used for the data: DIMUREC [3]. Thus the simulated dimuon events are treated in the same way as the experimental ones. Also the same selection criteria are applied: the kinematic cuts

$$0 < y^* < 1 \qquad -0.5 < cos\theta_{CS} < 0.5 \tag{5.1}$$

(to select only the region where the acceptance of the muon spectrometer is significantly different from zero), the image and the fiducial cuts and a 2% P$*$DTarg cut.

The simulated events are generated on a phase space region larger than the acceptance of the spectrometer, in order to take properly into account the smearing effects of the apparatus. Thus the kinematic cuts are required to define the nominal acceptance of the spectrometer.

A 2% P$*$DTarg cut has been applied to the simulated distributions, as for the experimental data (see Section 4.3.2), but the coefficients for the calculation of the P$*$DTarg distributions have been re–tuned on the simulations. Actually, it has been observed that the Monte–Carlo simulations are not able to reproduce exactly the width of the P$*$DTarg distributions, which is very sensitive to the multiple scattering in the absorber and which is then overestimated by about 8%. Moreover, applying to the simulated distributions the P$*$DTarg cut coefficients tuned on the experimental data can produce a bias on the determination of their line shapes and can lead to an underestimation of the acceptances. For these reasons, I have tuned the coefficients of the P$*$DTarg distributions separately for the data and the simulations. In particular, I have re–calculated these coefficients for the J/ψ simulated distributions, following the standard procedure used for the data, and then I have applied them to the other simulated spectra (ψ', DY and open charm).

Once the reconstructed differential distributions have been obtained for the different processes contributing to the $\mu^+\mu^-$ invariant mass spectrum, they are fitted with ad–hoc functions. The same analytical functions are then used in the fit of the experimental mass spectrum, where the normalization factors of the different contributions are left as free parameters (see Section 5.4).

5.2.1 The Drell–Yan

As mentioned in Chapter 1, the Drell–Yan is the electromagnetic annihilation of a quark and an antiquark of the same flavour, which leads to the production of a lepton pair.

The Drell–Yan production cross–section is directly connected to the structure functions of the projectile and target nucleons. The generation of the Drell–Yan is based on a Monte–Carlo code (DIMUJET) that uses the GRV–LO (functions n. 4, 1992, $\Lambda_{QCD} = 200$ MeV, $Q^2_{min} = 0.25\, GeV^2$, $m_c = 1.5\, GeV/c^2$ [4]) parametrization of the structure functions. This choice of the Parton Distribution Functions (PDFs) is the same one previously adopted in the published analyses as a function of E_{ZDC} [6].

Since it has been observed that the numerical values of the $\sigma_{J/\psi}/\sigma_{DY}$ ratios are sensitive to the parametrization adopted for the PDFs, alternatively a second set of parton structure functions was used, the MRS A set (functions n. 43 in the PDFLIB package, $Q^2_{min} = 0.625\, GeV^2$ [5]). The systematic effects due to the PDF choice will be studied in Section 5.6.7.

The mass and rapidity differential distribution for the Drell–Yan process simulated at leading order is:

$$M^3 \frac{d^2\sigma}{dM\,dy^*} = \frac{8\pi\alpha^2}{9}\tau \sum_i e_i^2 \left[f_1^i(\sqrt{\tau}e^{y^*})\bar{f}_2^i(\sqrt{\tau}e^{-y^*}) + \bar{f}_1^i(\sqrt{\tau}e^{y^*})f_2^i(\sqrt{\tau}e^{-y^*}) \right] \quad (5.2)$$

where α is the fine structure constant, M is the invariant mass of the dilepton pair, $\tau = \sqrt{s}$ and y^* are respectively the dilepton energy and rapidity in the center of mass frame, e_i is the electric charge of the quark with flavour i, f_1^i and f_2^i are the parton distribution functions.

The p_T differential distribution has been generated as a Bessel function of the transverse mass m_T:

$$\frac{d\sigma}{dp_T} \propto p_T m_T K_1 \left(\frac{m_T}{T}\right) \quad (5.3)$$

where K_1 is the first order modified Bessel function.

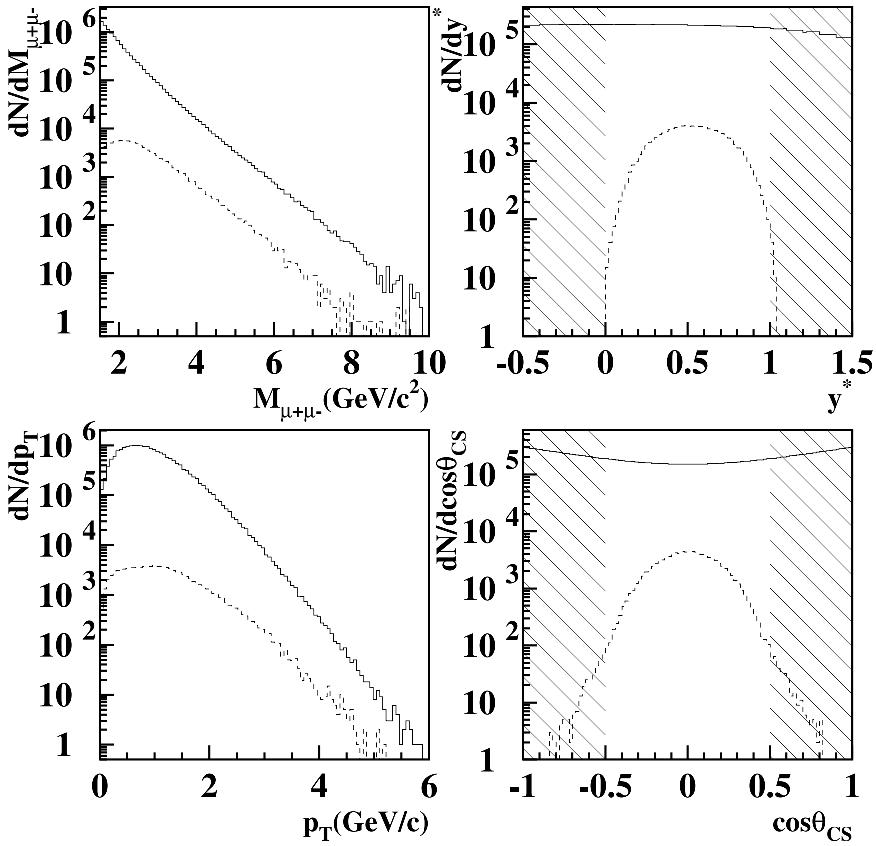

Figure 5.1: *DY generated (continuous line) and reconstructed (dotted line) mass, rapidity, p_T and $cos\theta_{CS}$ distributions for the Pb-Pb set-up. The shaded areas correspond to the applied kinematic cuts. This simulation uses the GRV–LO structure functions for the projectile and target nucleons.*

For the $cos\theta_{CS}$ distribution I have used the experimental angular distribution

$$\frac{d\sigma}{dcos\theta_{CS}} \propto 1 + \lambda cos^2\theta_{CS} \tag{5.4}$$

where $\lambda = 1$ has been measured by the NA10 experiment [7].

The ϕ_{CS} distribution has been assumed to be flat on the whole interval $[0, 2\pi]$.

The mass, center of mass rapidity, p_T and $cos\theta_{CS}$ distributions of the generated (continuous line) and reconstructed (dotted line) events are plotted in Fig. 5.1 and 5.2, respectively for the GRV–LO and the MRS 43 sets of parton structure functions. The effect of the kinematic cuts is also shown in the same pictures.

In Fig. 5.3 I have compared the invariant mass spectrum obtained using the two different set of PDFs. The two spectra are normalized in the mass region

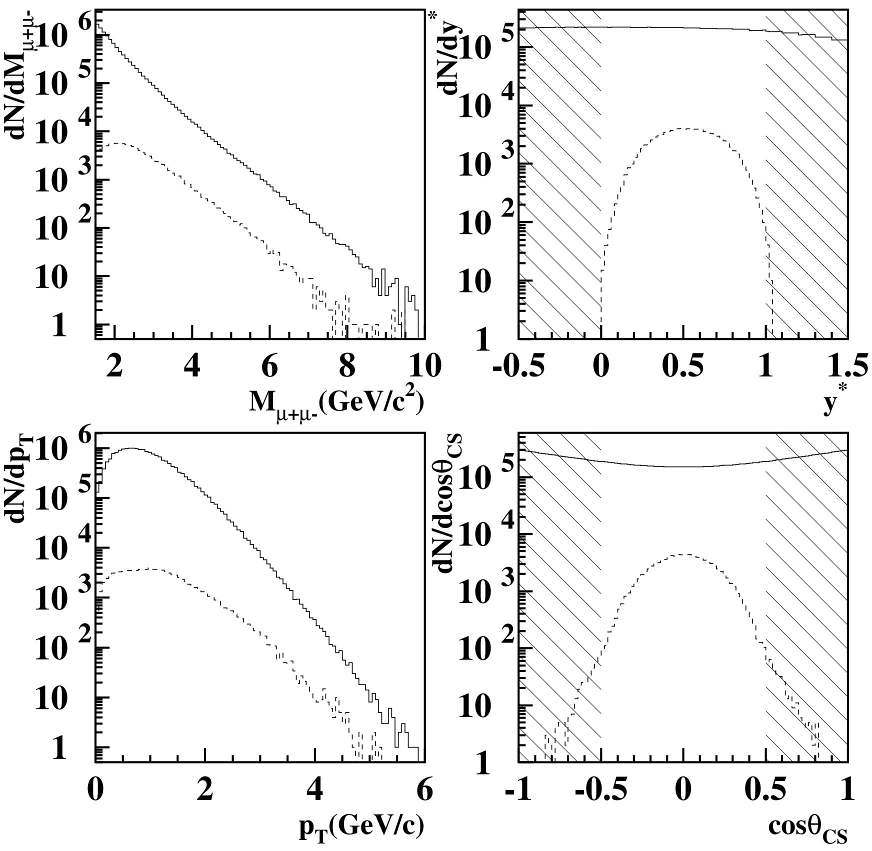

Figure 5.2: *DY generated (continuous line) and reconstructed (dotted line) mass, rapidity, p_T and $cos\theta_{CS}$ distributions for the Pb-Pb set-up. The shaded areas correspond to the applied kinematic cuts. This simulation uses the MRS 43 structure functions for the projectile and target nucleons.*

$M_{\mu^+\mu^-} \geq 4.2\, GeV/c^2$, which is the region of the dimuon invariant mass spectrum where only the Drell–Yan mechanism contributes and where the normalization of the Drell–Yan is fixed (see Section 5.4). Different PDFs give slightly different shapes for the Drell–Yan mass distribution, in particular in the region of the J/ψ and ψ' resonances, $2.9 < M_{\mu^+\mu^-} < 4.5\, GeV/c^2$, that we use to report the Drell–Yan cross–sections. For a description of the consequences of these differences on the $\sigma_{J/\psi}/\sigma_{DY}$ results see Section 5.6.7.

The DY reconstructed mass spectrum has been fitted with the following ad–hoc function:

$$\frac{dN}{dM} = p_1 * \left\{ exp\,(-p_2 * M) - p_3\, exp[-(M - p_4)^2] \right\} \tag{5.5}$$

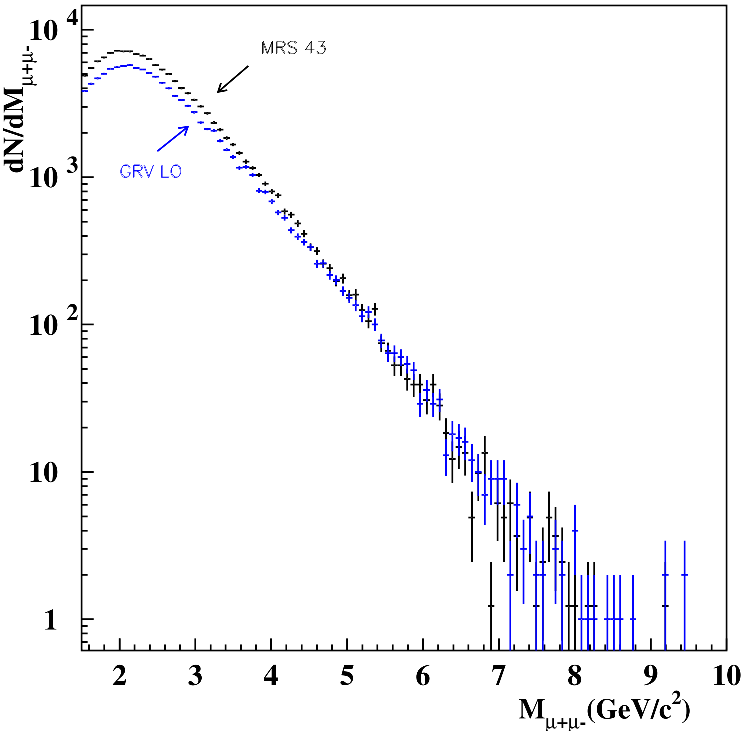

Figure 5.3: *Comparison of the Drell–Yan invariant mass spectra, obtained using the MRS 43 (black) and GRV–LO (blue) sets of parton distribution functions. The two spectra are normalized in the region $M_{\mu^+\mu^-} \geq 4.2\,GeV/c^2$.*

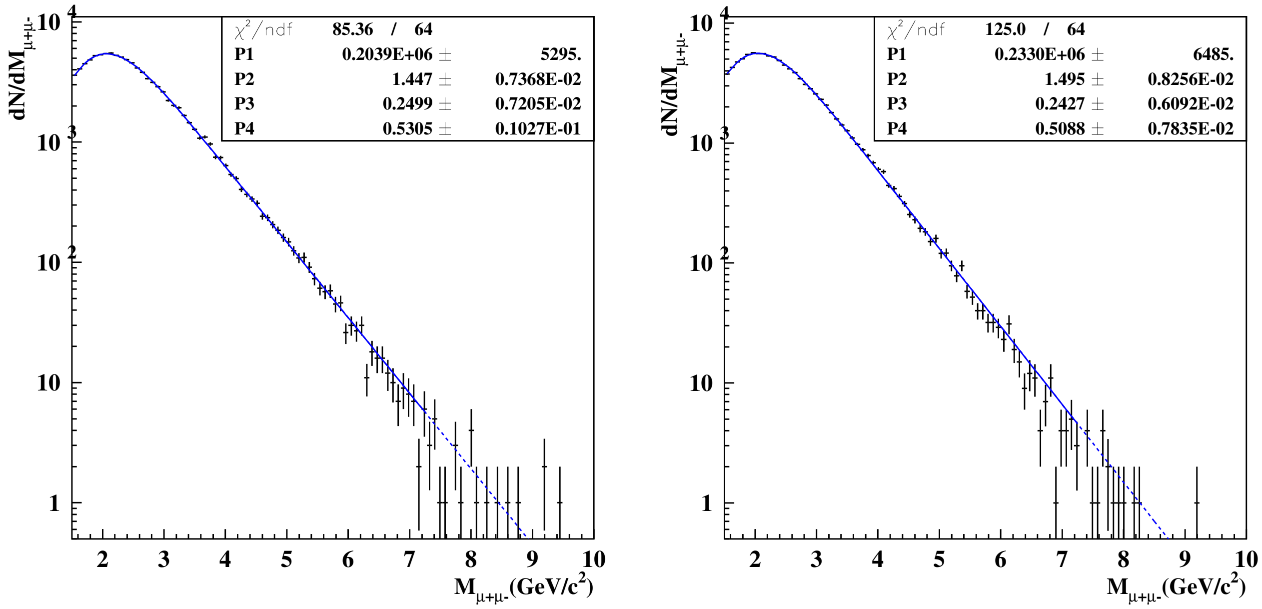

Figure 5.4: *Fit to the Drell–Yan spectra simulated with the GRV–LO (left) and MRS 43 (right) set of PDFs (with a 2% P∗DTarg cut).*

	P∗DTarg cut (%)	p_2	p_3	p_4
DY (GRV–LO)	0%	1.439 ± 0.007	0.245 ± 0.006	0.547 ± 0.008
DY (MRS 43)	0%	1.488 ± 0.008	0.239 ± 0.006	0.525 ± 0.007
DY (GRV–LO)	2%	1.447 ± 0.007	0.250 ± 0.007	0.530 ± 0.010
DY (MRS 43)	2%	1.495 ± 0.008	0.243 ± 0.006	0.509 ± 0.008
DY (GRV–LO)	6%	1.453 ± 0.008	0.251 ± 0.007	0.524 ± 0.011
DY (MRS 43)	6%	1.495 ± 0.007	0.247 ± 0.007	0.499 ± 0.011
DY (GRV–LO)	10%	1.453 ± 0.004	0.255 ± 0.007	0.514 ± 0.011
DY (MRS 43)	10%	1.495 ± 0.009	0.251 ± 0.008	0.490 ± 0.011
DY (GRV–LO)	18%	1.460 ± 0.010	0.254 ± 0.009	0.512 ± 0.012
DY (MRS 43)	18%	1.495 ± 0.010	0.253 ± 0.009	0.485 ± 0.012

Table 5.1: *Values of the parameters obtained by the fit to the Drell-Yan spectrum simulated using the GRV–LO and the MRS 43 parton distribution functions. Different P∗DTarg cut levels are considered.*

The results of the fit are shown in Fig. 5.4 for a P∗DTarg cut of 2%. The values of the fit parameters are listed in Tab. 5.1 for different P∗DTarg cut levels, both for the GRV–LO and the MRS 43 sets of PDFs. The normalization parameter p_1 is the only parameter that will be left free in the fit to the experimental $\mu^+\mu^-$ mass spectrum, in order to extract the size of the DY contribution. Therefore it has not been reported in the table.

5.2.2 The J/ψ and ψ' resonances

The J/ψ and ψ' are vector resonances with masses $M_{J/\psi} = 3.097\ GeV/c^2$ and $M_{\psi'} = 3.686\ GeV/c^2$ and full widths of 87 and 300 KeV [8]. The mass distributions for these two particles have been generated as Dirac distributions, centered on their nominal mass $M_{J/\psi}$ and $M_{\psi'}$:

$$\left(\frac{dN}{dM}\right)_\psi = \delta(M - M_h) \qquad \text{where } \psi = (J/\psi, \psi') \tag{5.6}$$

The rapidity distribution dN/dy^* of the dimuons coming from the disintegration of the charmonium resonances has been parametrized as a gaussian centered on $\mu_{y^*} = 0$ and with $\sigma_{y^*} = 0.6$, according to the empirical distribution of the rapidity differential cross–section [9].

The same p_T distribution already used for the Drell–Yan generation has been used for the charmonium states.

The choice of a uniform distribution $dN/dcos\theta_{CS}$ is justified by the fact that the J/ψ $(n = 1, l = 0)$ and the ψ' $(n = 2, l = 0)$ have orbital angular momentum $l = 0$ in the dilepton center of mass.

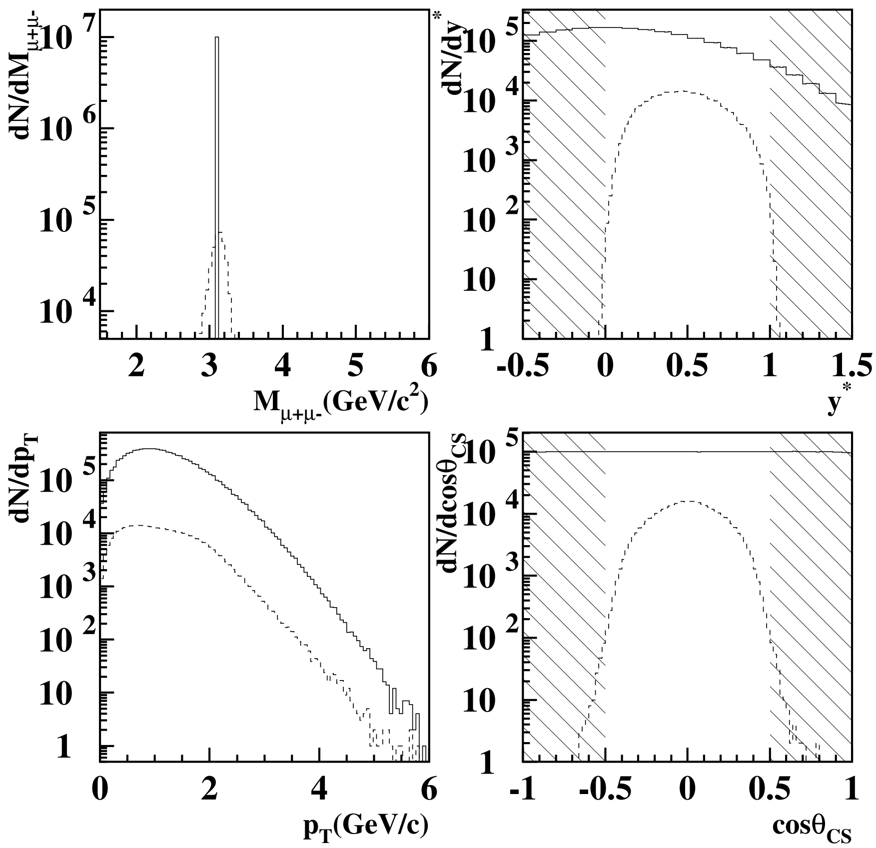

Figure 5.5: *J/ψ generated (continuous line) and reconstructed (dotted line) mass, rapidity, p_T and $cos\theta_{CS}$ distributions for the Pb-Pb set-up. The shaded areas correspond to the applied kinematic cuts.*

The invariance for rotations around the z axis implies a flat $dN/d\phi_{CS}$ distribution.

In Fig. 5.5 and 5.6 the J/ψ and ψ' generated and reconstructed mass, rapidity, p_T and $cos\theta_{CS}$ are shown. The effects of the kinematic cuts are also reported (shaded areas).

The reconstructed invariant mass spectrum of the J/ψ and ψ' resonances has a very peculiar shape. In order to reproduce its shape in a satisfactory way, the following procedure has been adopted. The ψ ($\psi = J/\psi, \psi'$) spectrum is divided into three regions: left region ($M < M_1$), central region ($M_1 \leq M \leq M_2$) and right region ($M > M_2$). In the central region the ψ is considered Gaussian, while in the other regions the tails are conveniently modified.

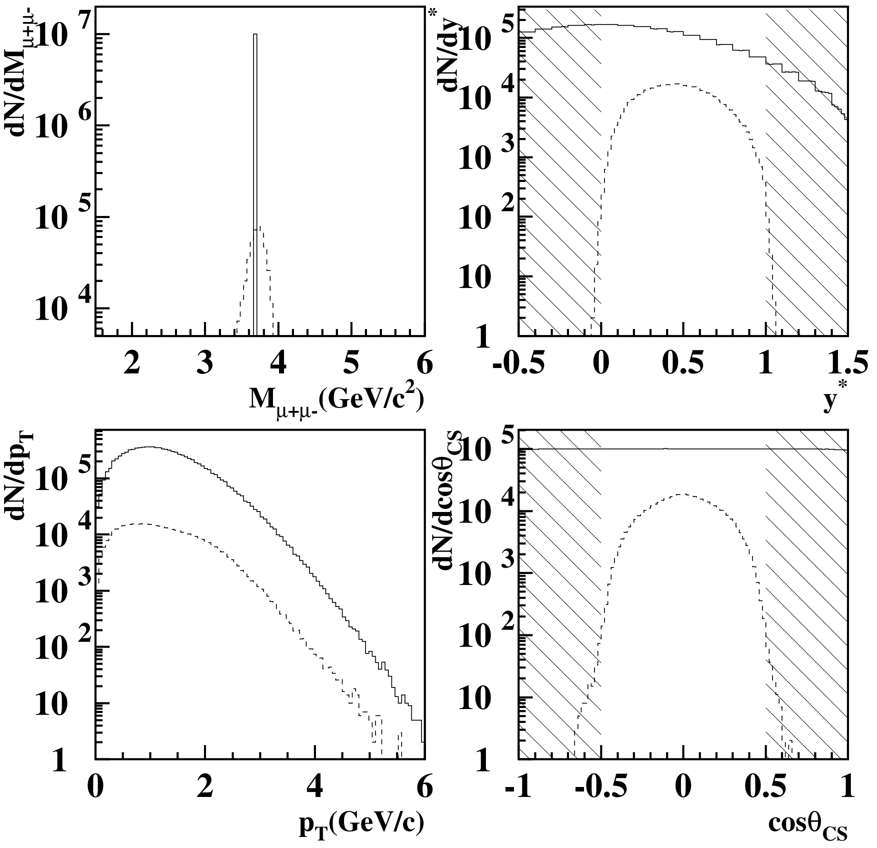

Figure 5.6: *ψ' generated (continuous line) and reconstructed (dotted line) mass, rapidity, p_T and $cos\theta_{CS}$ distributions for the Pb-Pb set-up. The shaded areas correspond to the applied kinematic cuts.*

Thus the J/ψ and ψ' spectra are described by the "pseudo–gaussian" function:

$$\frac{dN}{dM} = p_1 * exp\left[-0.5 * \left\{\frac{(M - p_2)}{\sigma}\right\}^2\right] \tag{5.7}$$

where p_1 is the normalization factor, M is the ψ mass expressed in GeV, p_2 estimates the mass of the resonance, as the mean value of the Gaussian distribution, and σ is the width of the distribution, which describes the full width of the resonance. The value of σ depends on M. In the central region σ has a fixed value which is estimated by a third free parameter p_3, while outside this region it is parametrized according to two different formulas, a "multiplicative" and an "additive" parametrization.

- the "multiplicative" parametrization is the so–called "standard" parametrization historically used by the NA50 Collaboration [10]:

$$\sigma = \begin{cases} p_3 & M_1 \leq M \leq M_2 \\ p_3 * \left\{1 + [p_4 * (M_1 - M)]^{p_5 - p_6 * (M_1 - M)}\right\} & M < M_1 \\ p_3 * \left\{1 + [p_7 * (M - M_2)]^{p_8 - p_9 * (M - M_1)}\right\} & M > M_2 \end{cases}$$

- the "additive" parametrization has been introduced by the NA50 Collaboration ("Ruben" parametrization) instead of the "standard" one to better reproduce the tails of the J/ψ and ψ' mass distributions:

$$\sigma = \begin{cases} p_3 & M_1 \leq M \leq M_2 \\ p_3 + p_4 * (M_1 - M)^{p_5 - p_6 * \sqrt{M_1 - M}} & M < M_1 \\ p_3 + p_7 * (M - M_2)^{p_8 - p_9 * \sqrt{M - M_1}} & M > M_2 \end{cases}$$

M_1 and M_2 in both cases are defined by

$$\begin{cases} M_1 = p_2 * p_{10} \\ M_2 = p_2 * p_{11} \end{cases}$$

The effect of the chosen parametrization on the final $\sigma_{J/\psi}/\sigma_{DY}$ ratio will be investigated in Section 5.6.

The same functions have been used to describe the J/ψ and the ψ' . In Fig. 5.7 and 5.8 the reconstructed mass spectra of the J/ψ and ψ' are fitted with the two different parametrizations. The resulting parameters are listed in Table 5.2 and 5.3 for the J/ψ and in Table 5.4 and 5.5 for the ψ' (for different P∗DTarg cut levels). The normalization parameter p_1 is not reported, since it will be treated as free parameter in the fit to the dimuon invariant mass spectrum (see Section 5.4).

The additive parametrization allows to better fit the shape of the charmonium mass spectra, as demonstrated by the lower χ^2 obtained in this fit, in comparison with the multiplicative parametrization. In particular, the tails of the distributions are better taken into account.

5.2.3 The open charm

The generation of the Monte–Carlo open charm has been performed by using the PYTHIA event generator [2], since it has been demonstrated that it well reproduces the differential distributions of the D and $\overline{D}$ mesons produced in proton and pion induced reactions [11].

The shape of the charm differential distributions depends on the used charm mass value, on the intrinsic transverse momentum k_T given to the incoming partons and on the chosen set of PDFs.

The value $m_c = 1.5\, GeV/c^2$ has been used for the charm mass in the simulations presented in this work. It has been verified that the difference between the Monte–Carlo mass distributions generated with different values of m_c are negligible in the high mass region where we are working [12].

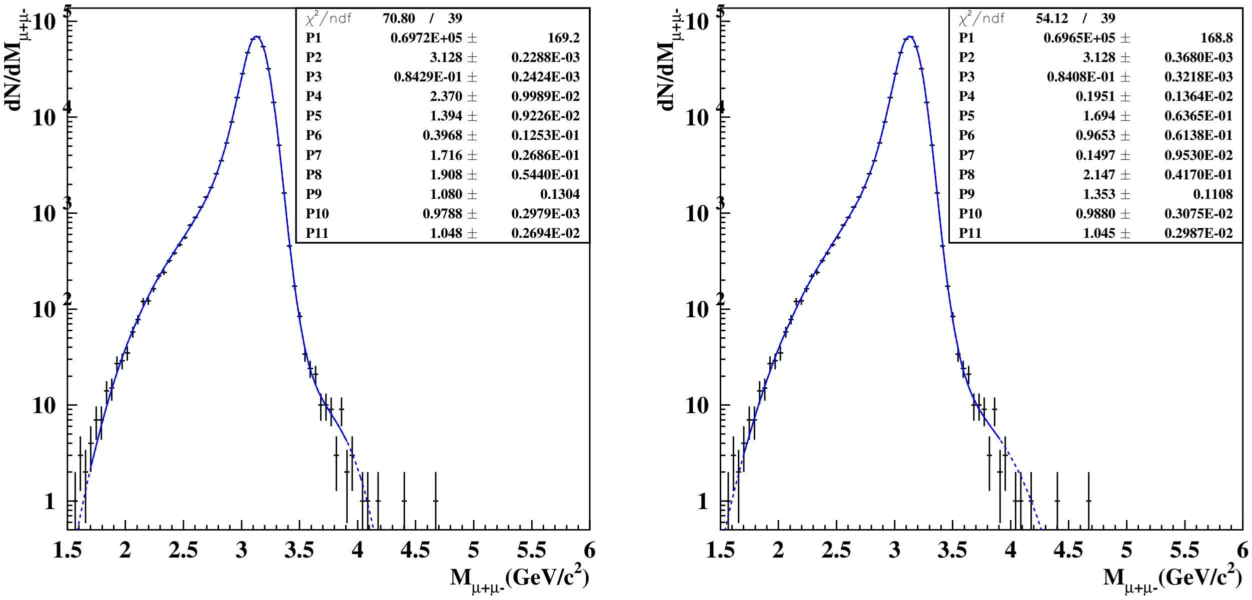

Figure 5.7: *Fit to the J/ψ reconstructed mass spectrum, by using the multiplicative (left) and the additive (right) parametrizations. A 2% P∗DTarg cut is imposed.*

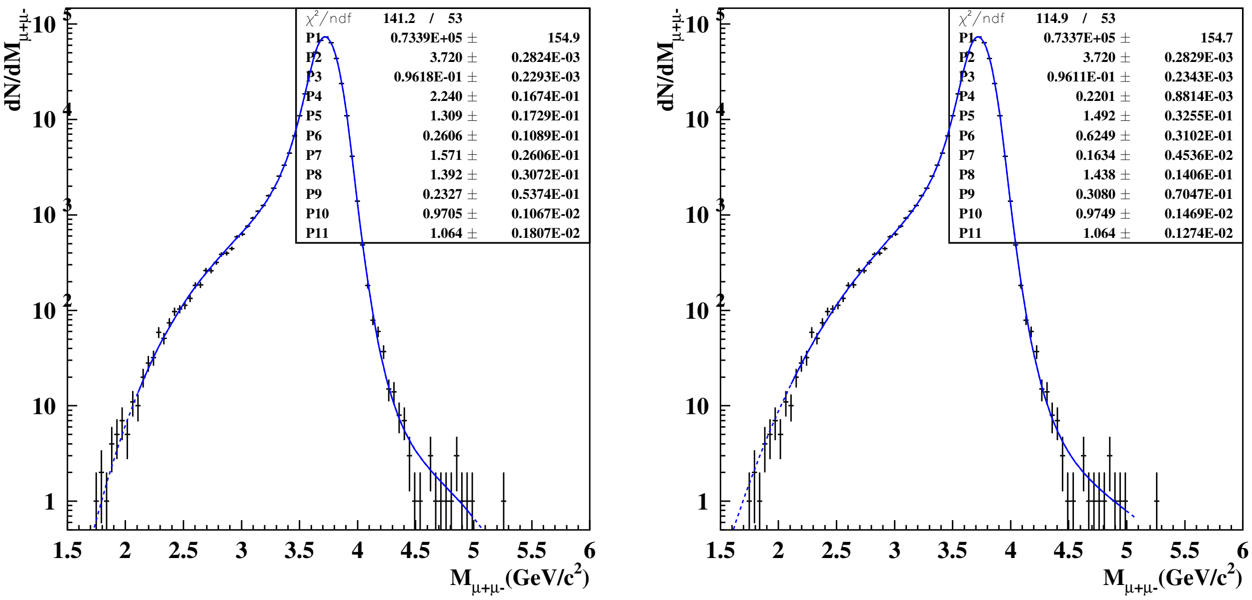

Figure 5.8: *Fit to the ψ' reconstructed mass spectrum, by using the multiplicative (left) and the additive (right) parametrizations. A 2% P∗DTarg cut is imposed.*

	P∗DTarg 0%	P∗DTarg 2%	P∗DTarg 6%	P∗DTarg 10%	P∗DTarg 18%
p_2	3.1280 ± 0.0002	3.1280 ± 0.0002	3.1270 ± 0.0003	3.1270 ± 0.0003	3.1270 ± 0.0003
p_3	0.0845 ± 0.0002	0.0843 ± 0.0002	0.0841 ± 0.0002	0.0839 ± 0.0002	0.0835 ± 0.0003
p_4	2.34 ± 0.01	2.37 ± 0.01	2.37 ± 0.01	2.38 ± 0.01	2.38 ± 0.01
p_5	1.41 ± 0.01	1.39 ± 0.01	1.40 ± 0.01	1.40 ± 0.01	1.41 ± 0.01
p_6	0.41 ± 0.01	0.40 ± 0.01	0.39 ± 0.01	0.40 ± 0.01	0.39 ± 0.01
p_7	1.69 ± 0.05	1.72 ± 0.03	1.70 ± 0.05	1.69 ± 0.05	1.66 ± 0.06
p_8	2.02 ± 0.14	1.91 ± 0.05	2.01 ± 0.15	2.05 ± 0.17	2.04 ± 0.16
p_9	1.49 ± 0.35	1.08 ± 0.13	1.27 ± 0.39	1.30 ± 0.43	1.30 ± 0.45
p_{10}	0.9796 ± 0.0006	0.9788 ± 0.0003	0.9793 ± 0.0007	0.9794 ± 0.0007	0.9806 ± 0.0006
p_{11}	1.046 ± 0.004	1.048 ± 0.003	1.046 ± 0.004	1.045 ± 0.005	1.043 ± 0.005

Table 5.2: *Values of the parameters of the Monte Carlo J/ψ fitting functions, with the multiplicative parametrization. Different P∗DTarg cut levels are considered.*

	P∗DTarg 0%	P∗DTarg 2%	P∗DTarg 6%	P∗DTarg 10%	P∗DTarg 18%
p_2	3.1290 ± 0.0004	3.1280 ± 0.0004	3.1280 ± 0.0004	3.1280 ± 0.0004	3.1280 ± 0.0004
p_3	0.0843 ± 0.0003	0.0841 ± 0.0003	0.0840 ± 0.0003	0.0836 ± 0.0003	0.0833 ± 0.0004
p_4	0.194 ± 0.001	0.195 ± 0.001	0.196 ± 0.001	0.196 ± 0.001	0.197 ± 0.002
p_5	1.70 ± 0.06	1.69 ± 0.06	1.67 ± 0.06	1.72 ± 0.05	1.69 ± 0.07
p_6	0.98 ± 0.06	0.96 ± 0.06	0.94 ± 0.05	0.99 ± 0.05	0.95 ± 0.07
p_7	0.147 ± 0.007	0.150 ± 0.009	0.154 ± 0.009	0.137 ± 0.014	0.141 ± 0.009
p_8	2.12 ± 0.07	2.15 ± 0.04	2.17 ± 0.04	2.48 ± 0.24	2.39 ± 0.13
p_9	1.42 ± 0.08	1.35 ± 0.11	1.35 ± 0.10	1.90 ± 0.46	1.70 ± 0.17
p_{10}	0.988 ± 0.003	0.988 ± 0.003	0.987 ± 0.003	0.990 ± 0.002	0.989 ± 0.004
p_{11}	1.046 ± 0.003	1.045 ± 0.003	1.045 ± 0.003	1.038 ± 0.005	1.039 ± 0.004

Table 5.3: *Values of the parameters of the Monte Carlo J/ψ fitting functions, with the additive parametrization. Different P∗DTarg cut levels are considered.*

	P∗DTarg 0%	P∗DTarg 2%	P∗DTarg 6%	P∗DTarg 10%	P∗DTarg 18%
p_2	3.7200 ± 0.0003	3.7200 ± 0.0003	3.7190 ± 0.0003	3.7190 ± 0.0003	3.7190 ± 0.0003
p_3	0.0965 ± 0.0002	0.0962 ± 0.0002	0.0959 ± 0.0002	0.0957 ± 0.0002	0.0953 ± 0.0002
p_4	2.22 ± 0.02	2.24 ± 0.02	2.24 ± 0.02	2.25 ± 0.01	2.25 ± 0.01
p_5	1.31 ± 0.02	1.31 ± 0.02	1.31 ± 0.02	1.32 ± 0.01	1.33 ± 0.01
p_6	0.26 ± 0.01	0.26 ± 0.01	0.26 ± 0.01	0.27 ± 0.01	0.28 ± 0.01
p_7	1.60 ± 0.02	1.57 ± 0.03	1.54 ± 0.02	1.55 ± 0.02	1.54 ± 0.02
p_8	1.43 ± 0.04	1.39 ± 0.03	1.44 ± 0.04	1.42 ± 0.02	1.43 ± 0.02
p_9	0.25 ± 0.06	0.23 ± 0.05	0.24 ± 0.08	0.18 ± 0.04	0.13 ± 0.05
p_{10}	0.971 ± 0.001	0.971 ± 0.001	0.971 ± 0.001	0.971 ± 0.001	0.972 ± 0.001
p_{11}	1.063 ± 0.001	1.064 ± 0.002	1.062 ± 0.002	1.062 ± 0.001	1.061 ± 0.001

Table 5.4: *Values of the parameters of the Monte Carlo ψ' fitting functions, with the multiplicative parametrization. Different P∗DTarg cut levels are considered.*

	P∗DTarg 0%	P∗DTarg 2%	P∗DTarg 6%	P∗DTarg 10%	P∗DTarg 18%
p_2	3.7210 ± 0.0003	3.7200 ± 0.0003	3.7200 ± 0.0003	3.7190 ± 0.0003	3.7200 ± 0.0003
p_3	0.0962 ± 0.0003	0.0961 ± 0.0002	0.0956 ± 0.0003	0.0955 ± 0.0003	0.0945 ± 0.0003
p_4	0.22 ± 0.01	0.22 ± 0.01	0.22 ± 0.01	0.22 ± 0.01	0.22 ± 0.01
p_5	1.51 ± 0.03	1.49 ± 0.03	1.51 ± 0.03	1.50 ± 0.03	1.59 ± 0.03
p_6	0.63 ± 0.03	0.62 ± 0.03	0.64 ± 0.03	0.64 ± 0.03	0.71 ± 0.03
p_7	0.165 ± 0.004	0.163 ± 0.004	0.157 ± 0.006	0.162 ± 0.005	0.150 ± 0.004
p_8	1.61 ± 0.04	1.44 ± 0.01	1.63 ± 0.12	1.52 ± 0.02	2.16 ± 0.20
p_9	0.50 ± 0.09	0.31 ± 0.07	0.52 ± 0.19	0.36 ± 0.09	1.02 ± 0.25
p_{10}	0.976 ± 0.001	0.975 ± 0.001	0.976 ± 0.001	0.976 ± 0.001	0.980 ± 0.001
p_{11}	1.058 ± 0.001	1.064 ± 0.002	1.057 ± 0.003	1.061 ± 0.001	1.041 ± 0.004

Table 5.5: *Values of the parameters of the Monte Carlo ψ' fitting functions, with the additive parametrization. Different P∗DTarg cut levels are considered.*

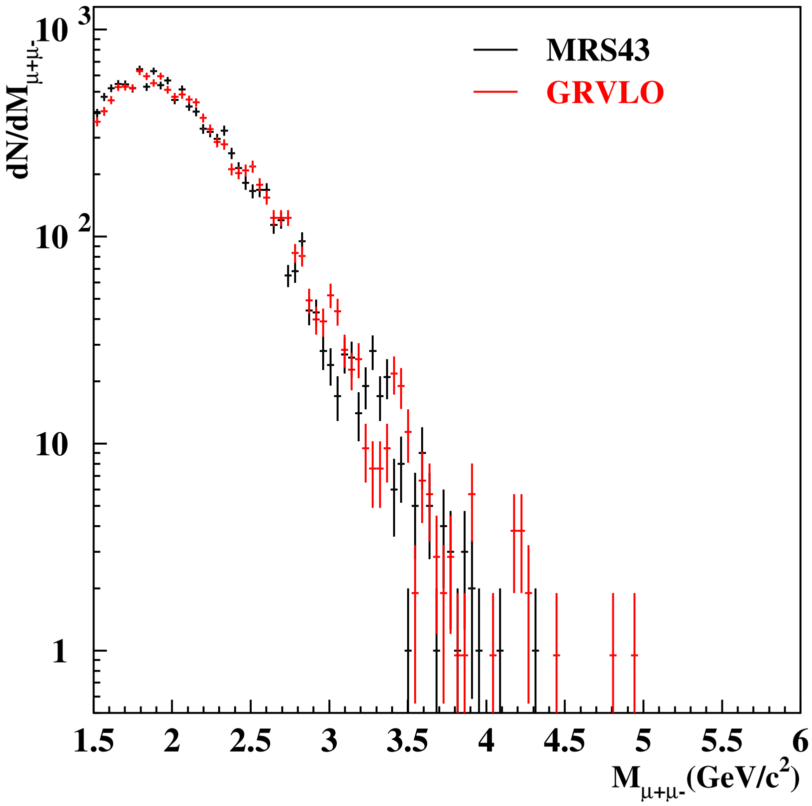

Figure 5.9: *Open charm reconstructed mass spectrum, generated by using MRS 43 or GRV–LO as parton distribution functions. A P∗DTarg cut of 2% has been imposed and the kinematic, image and fiducial cuts have been applied.*

The transverse momentum of the generated charmed mesons originates from the intrinsic transverse momentum k_T given to the colliding partons inside hadrons. This transverse momentum distribution has been simulated with PYTHIA as a Gaussian distribution of width $\sigma_{k_T} = 0.8\,GeV/c$. This value has been previously tuned on the experimental p_T distributions by the NA38/NA50 experiment [9]. Moreover, the study with different σ_{k_T} values has demonstrated that the open charm mass distribution is not sensitive to the chosen value in the HMR, where we fit the dimuon invariant mass spectrum [12].

The possibility of a dependence of the open charm generation on the chosen PDF set has been taken into account. The open charm simulation has been performed in both cases and the effect on $\sigma_{J/\psi}/\sigma_{DY}$ has been studied in Section 5.6.7. Since the processes of hadro–production of open charm are based essentially on gluon fusion, the distributions are independent of the choice of the nucleon structure functions, as shown in Fig. 5.9.

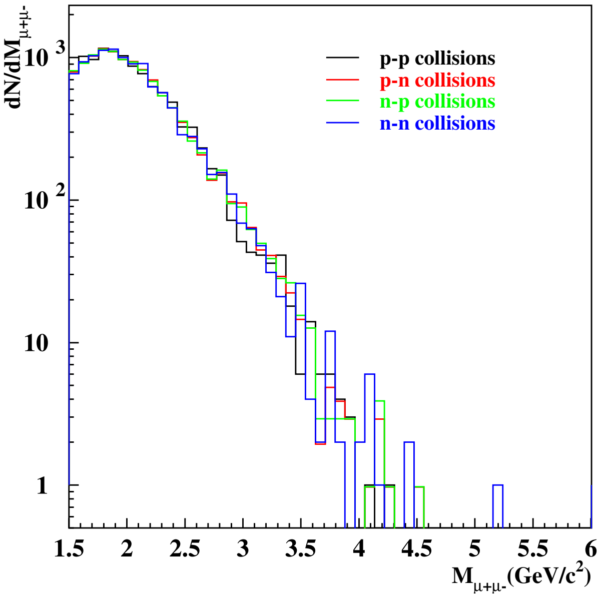

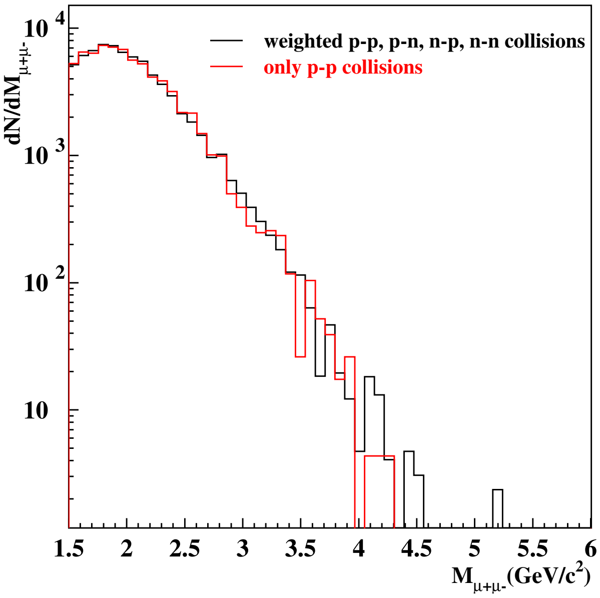

Figure 5.10: *Open charm reconstructed mass spectrum for p–p, p–n, n–p and n–n collisions (left) and comparison (right) between the spectrum obtained with p–p collisions and with the full simulation (taking account all the processes, opportunely weighed). The MRS 43 set of PDFs has been adopted and the kinematic, image and fiducial cuts and a 2% P∗DTarg cut have been applied to the spectra.*

The open charm generation is very long, in terms of CPU time, since the generated muons are in general outside the phase space defined by the kinematic domain studied by the muon spectrometer. For this reason the simulations have been performed only in case of p–p interactions and then it has been verified that the shape of the open charm mass distribution does not change if all the processes (p–p, p–n, n–p, n–n, opportunely weighed) are considered.

In Fig. 5.10 (left) I have compared the open charm mass spectra obtained simulating p–p, p–n, n–p and n–n collisions. Moreover, in Fig. 5.10 (right) the open charm shape that refers only to p–p collisions has been compared to the one obtained by means of the full simulation of the p–p, p–n, n–p and n–n processes, weighed considering the cross–section for each process as proportional to the number of colliding nucleons. Since no significant difference is visible between the two spectra, for the calculations reported in the following, only the p–p simulation has been performed, in order to speed up the generation of the open charm events. In Section 5.6.6 I will demonstrate that the effect of this choice on the $\sigma_{J/\psi}/\sigma_{DY}$ ratios is negligible.

In Fig. 5.11 the generated (continuous line) and reconstructed (dotted line) mass, rapidity, p_T and $cos\theta_{CS}$ differential distributions of open charm dimuons are plotted for the NA50 Pb-Pb setup. The effect of the applied kinematic cuts is also reported.

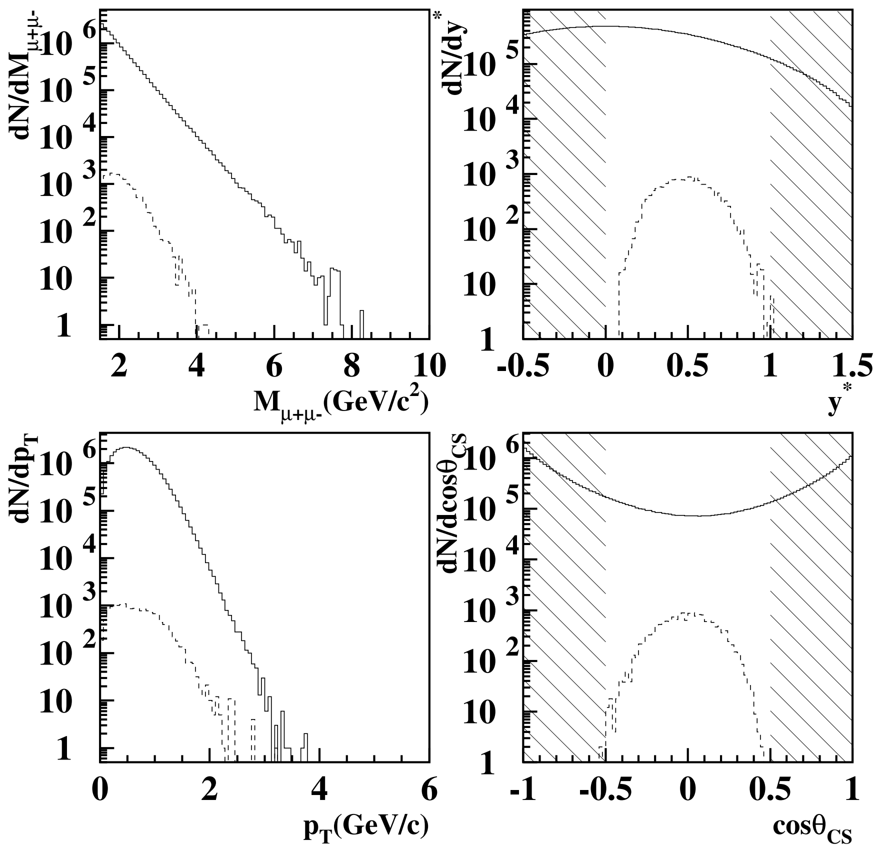

Figure 5.11: *Open charm generated (continuous line) and reconstructed (dotted line) mass, rapidity, p_T and $cos\theta_{CS}$ distributions for the Pb-Pb set-up. The shaded areas correspond to the applied kinematic cuts.*

The Monte–Carlo mass differential distribution of open charm dimuons has been fitted with the following function:

$$\frac{dN}{dM} = p_1 * exp\left[-0.5\left(\frac{M-p_2}{\sigma}\right)^2\right] \tag{5.8}$$

where

$$\sigma = \begin{cases} p_3 & M < p_5 \\ p_3 * \{1 + [p_4 * (M - p_5)]\} & M > p_5 \end{cases}$$

Table 5.6 lists the values of the parameters given by the fit to the open charm spectra, simulated both with the MRS 43 and the GRV–LO set of parton structure functions. Different P∗DTarg cuts have been applied on the reconstructed mass

MRS 43

	P∗DTarg 0%	P∗DTarg 2%	P∗DTarg 6%	P∗DTarg 10%	P∗DTarg 18%
p_2	1.815 ± 0.006	1.809 ± 0.006	1.804 ± 0.007	1.807 ± 0.007	1.803 ± 0.008
p_3	0.31 ± 0.03	0.31 ± 0.03	0.31 ± 0.03	0.31 ± 0.03	0.31 ± 0.03
p_4	0.36 ± 0.03	0.36 ± 0.03	0.37 ± 0.03	0.38 ± 0.03	0.34 ± 0.03
p_5	1.2 ± 0.3	1.2 ± 0.3	1.2 ± 0.3	1.2 ± 0.3	1.1 ± 0.1

GRV LO

	P∗DTarg 0%	P∗DTarg 2%	P∗DTarg 6%	P∗DTarg 10%	P∗DTarg 18%
p_2	1.834 ± 0.006	1.831 ± 0.006	1.831 ± 0.006	1.827 ± 0.007	1.818 ± 0.008
p_3	0.30 ± 0.03	0.30 ± 0.03	0.30 ± 0.02	0.30 ± 0.03	0.31 ± 0.04
p_4	0.42 ± 0.04	0.42 ± 0.04	0.43 ± 0.02	0.42 ± 0.04	0.37 ± 0.03
p_5	1.4 ± 0.3	1.4 ± 0.3	1.4 ± 0.1	1.4 ± 0.3	1.2 ± 0.1

Table 5.6: *Values of the parameters of the Monte Carlo $D\bar{D}$ fitting functions, for different P∗DTarg cut levels and both for the MRS 43 and the GRV LO sets of PDFs.*

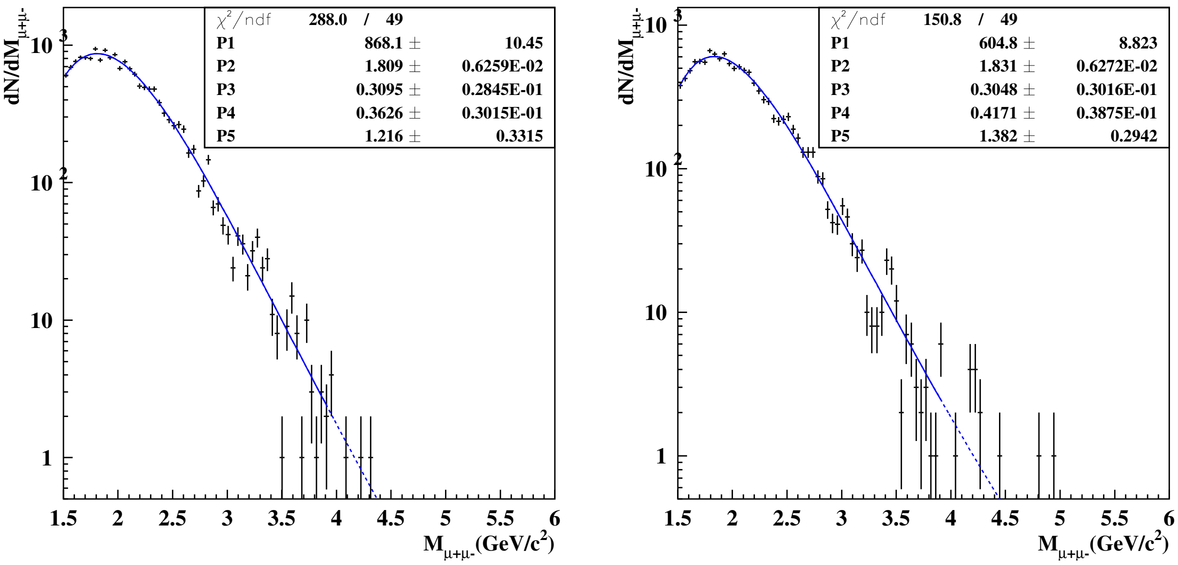

Figure 5.12: *Fit to the open charm reconstructed mass spectrum, generated by using MRS 43 (left) or GRV–LO (right) as parton distribution functions. A 2% P∗DTarg cut has been imposed.*

spectra. In particular, in Fig. 5.12 the fit to the open charm mass distribution with 2% P∗DTarg cut is shown, both for MRS 43 and GRV–LO.

Despite the slight difference between the fit parameters, in Section 5.6.6 I will prove that the final $\sigma_{J/\psi}/\sigma_{DY}$ results do not depend on the set of PDFs chosen for the open charm generation.

5.2.4 Acceptances

The simulation of the passage of the dimuon tracks inside the spectrometer allows to calculate the acceptances for the different processes that contribute to the dimuon invariant mass spectrum. The acceptance must be evaluated in the experimentally sensitive region, that is

$$0 < y^* < 1 \qquad -0.5 < cos\theta_{CS} < 0.5$$

and in the mass region related to the specific physical process.

The dimuon events have been generated in a kinematic window larger than that corresponding to the experimental sensitivity, in order to take into account the experimental resolution of the apparatus. This way we have properly considered the smearing effect of the apparatus: some events generated inside the acceptance region can be seen, once reconstructed, outside it (or vice versa), because of the finite resolution on the various physical variables.

The acceptance of the apparatus for a given process in a certain kinematic window can be defined as the ratio between the numbers of Monte–Carlo reconstructed and generated events in that window:

$$A = \frac{\int_{M_1}^{M_2} \frac{dN_{rec}}{dM}\, dM}{\int_{M_1}^{M_2} \frac{dN_{gen}}{dM}\, dM} \tag{5.9}$$

where M is the mass of the dimuon pair, (M_1, M_2) is the mass interval where the acceptance is calculated for the considered process. The kinematic, image and fiducial cuts must be applied to both distributions.

Table 5.7 lists the acceptances for all the physical processes previously discussed. The calculation of the acceptances for the J/ψ and ψ' resonances considers the whole mass distribution, while for the Drell–Yan and the open charm mechanisms only the regions $2.9 \leq M_{\mu^+\mu^-} \leq 4.5\, GeV/c^2$ and $M_{\mu^+\mu^-} \geq 1.5\, GeV/c^2$ are respectively taken into account.

The values of the acceptance for the different processes depend on the imposed P∗DTarg cut. In particular, they decrease with the increase of the P∗DTarg cut level, because more events are rejected and not included in the spectrometer acceptance. What is important is that, at a given P∗DTarg cut level, the ratios between the acceptances of different processes remain constant. For example, I have reported in the table the $A_{DY}/A_{J/\psi}$ ratios, which are necessary to estimate the ratio of the experimental cross–sections $\sigma_{J/\psi}/\sigma_{DY}$. The fact that the $A_{DY}/A_{J/\psi}$ is independent of the chosen P∗DTarg cut guarantees that no bias is introduced on the results by the particular choice of the P∗DTarg cut level.

The ratio of the DY and J/ψ acceptances, calculated using GRV LO or MRS 43 for the Drell–Yan simulation, differs by less than 1%. The effect of the PDF choice on the $J/\psi/DY$ results will be investigated in Section 5.6.7.

	$A_{J/\psi}(\%)$	$A_{\psi'}(\%)$	$A_{DY}(\%)$	$A_{D\overline{D}}(\%)$	$A_{DY}/A_{J/\Psi}$
no P$*$DTarg, MRS43	13.49	16.10	14.61	1.76	1.083
no P$*$DTarg, GRVLO			14.68	1.79	1.088
P$*$DTarg 2%, MRS43	12.69	15.03	13.69	1.69	1.079
P$*$DTarg 2%, GRVLO			13.82	1.73	1.089
P$*$DTarg 6%, MRS43	11.61	13.70	12.51	1.58	1.078
P$*$DTarg 6%, GRVLO			12.66	1.62	1.090
P$*$DTarg 10%, MRS43	10.62	12.52	11.44	1.45	1.077
P$*$DTarg 10%, GRVLO			11.55	1.49	1.087
P$*$DTarg 18%, MRS43	8.81	10.37	9.52	1.22	1.080
P$*$DTarg 18%, GRVLO			9.56	1.25	1.085

Table 5.7: *Values of the acceptances (in %) for the different processes contributing to the dimuon invariant mass spectrum, calculated after having applied the kinematic, image, fiducial cuts and different P$*$DTarg cuts on the data. The DY and $D\overline{D}$ contributions have been generated both with MRS 43 and GRV–LO as PDFs.*

5.3 The combinatorial background

The pairs of muons $\mu^+\mu^-$ with opposite–sign, measured by the NA50 experiment, are contaminated by the fortuitous muons coming from uncorrelated decays of K and π mesons

$$\pi^+ \to \mu^+\nu \quad \text{and} \quad \pi^- \to \mu^-\overline{\nu} \tag{5.10}$$

$$K^+ \to \mu^+\nu \quad \text{and} \quad K^- \to \mu^-\overline{\nu} \tag{5.11}$$

These processes generate both opposite–sign and like–sign (LS) dimuons. For instance, it can happen that one of the two opposite–sign muons comes from the decay of a $D\overline{D}$ meson, while the other comes from a pion or a kaon decay. In this case both opposite and like–sign events will be produced and this is considered as a source of background. In order to have access to a clean opposite–sign dimuon signal, we must estimate this background contribution and subtract it from the dimuon spectra. For this reason, the NA50 experiment acquires both the $\mu^+\mu^-$ pairs and the $\mu^+\mu^+$ and $\mu^-\mu^-$ ones. The like–sign sample is used to estimate the combinatorial background, since it is exclusively due to the background, unlike the opposite–sign spectrum that is the superimposition of signal dimuons and a certain amount of background.

This background estimation method is based on the fact that the like–sign muons are not correlated and their production follows the Poisson law [12]. Let consider a set of N_0 dimuon events. If each interaction produces N^+ positive mesons and N^- negative ones, with the associated P(N^+) and P(N^-) muon decay probabilities, the number of produced positive like–sign dimuons $\mu^+\mu^+$ is:

$$N^{++} = N_0 \int A^{++}\, P(N^+)\, \frac{N^+(N^+-1)}{2}\, dN^+ = \frac{N_0}{2}\left(< N^{+2} > - < N^+ >\right) A^{++} \tag{5.12}$$

where A^{++} is the acceptance for positive LS dimuons.

Analogously, the number of produced negative like–sign dimuons $\mu^-\mu^-$ is:

$$N^{--} = N_0 \int A^{--}\, P(N^-)\, \frac{N^-(N^--1)}{2}\, dN^- = \frac{N_0}{2}\left(< N^{-2} > - < N^- >\right) A^{--} \tag{5.13}$$

where A^{--} is the acceptance for negative LS dimuons.

If the numbers N^+ and N^- of produced positive and negative mesons are uncorrelated, the number of opposite–sign dimuons $\mu^+\mu^-$ resulting from the combination of their decay products can be expressed as:

$$N^{+-} = N_0 \int A^{+-} P(N^+)\, P(N^-)\, N^+N^-\, dN^+\, dN^- = N_0 < N^+ >< N^- > A^{+-} \tag{5.14}$$

where A^{+-} is the acceptance for opposite–sign dimuons.

Since the meson multiplicity follows the Poisson law, this implies that

$$< N >=< N^2 > - < N >^2 \tag{5.15}$$

and therefore Eq. 5.14 can be re–written as:

$$N^{+-} = 2\sqrt{N^{++}N^{--}} * \frac{A^{+-}}{\sqrt{A^{++}A^{--}}} \tag{5.16}$$

The application of the image cut guarantees that the muon spectrometer acceptance for positive and negative muons is the same, that is $A^{++} = A^{--} = A^{+-}$. Therefore Eq. 5.16 becomes:

$$N^{+-} = 2\sqrt{N^{++}N^{--}} \tag{5.17}$$

Furthermore, during the data taking period, the sign of the magnetic field has been periodically reversed, in order to have an equal sample of events with both the magnetic field polarities. This way we can recover possible image cut inefficiencies, which can bring to an acceptance asymmetry. The combinatorial background can thus be approximated by:

$$N^{+-} = 2\left(\sqrt{N^{++}_{(+)}N^{--}_{(+)}} + \sqrt{N^{++}_{(-)}N^{--}_{(-)}}\right) \tag{5.18}$$

where the bottom index between the parentheses indicates the sign of the magnetic field.

Eq. 5.18 is strictly valid only if the meson production is completely charge uncorrelated. In a real physical situation this hypothesis is not valid, since in each interaction the positive and the negative charged mesons are constrained by the total charge conservation law. Nevertheless, Eq. 5.18 can be adopted in case of high multiplicity of produced particles, such as in Pb–Pb collisions, where the charge correlation is smeared out. Otherwise, it must be multiplied by a factor R_{bck}, which accounts for charge correlation effects and which is expected to be equal to 1 in nucleus–nucleus collisions and larger than 1 when the multiplicity is lower (as in p–A collisions) [13]. In the analysis reported in this thesis the R_{bck} factor is always assumed to be equal to 1.

5.4 Fit to the invariant mass spectrum

As already explained, the dimuon invariant mass spectrum is the sum of different contributions. Once the combinatorial background is estimated from simple statistical arguments (see the previous section), the normalizations of the other physical contributions, extracted from the fit to the Monte–Carlo simulated spectra, are adjusted on the experimental mass spectra through a fit procedure. This fit to the $M_{\mu^+\mu^-}$ spectrum is performed in 4 steps.

1. Fit to the combinatorial background in the region $2 - 4\,GeV/c^2$, according to the following expression:

$$\frac{dN}{dM} = p_1 * exp\left[-0.5 * \left(\frac{M - p_2}{\sigma}\right)^2\right] \tag{5.19}$$

   where

$$\sigma = \begin{cases} p_3 & M < p_5 \\ p_3 * \{1 + [p_4 * (M - p_5)]\} & M > p_5 \end{cases}$$

   In this step the normalization factor $p_1 = N_{bck}$ for the background contribution is fixed for the following steps.

2. Fit in the mass region above $2.9\,GeV/c^2$ with:

$$\frac{dN}{dM} = N_{bck}\frac{dN_{bck}}{dM} + N_{J/\psi}\frac{dN_{J/\psi}}{dM} + N_{\psi'}\frac{dN_{\psi'}}{dM} + N_{DY}\frac{dN_{DY}}{dM} \tag{5.20}$$

   where the J/ψ , ψ' and Drell–Yan normalization factors, $N_{J/\psi}, N_{\psi'}, N_{DY}$, are left as free parameters, while their shapes are fixed by the Monte–Carlo simulations.

   The Monte–Carlo simulations slightly underestimate the resolution on the invariant mass of muon pairs and therefore do not exactly reproduce the shape of the invariant mass spectrum of the reconstructed events. While this effect is almost negligible for the components of the spectrum that have a smooth shape (Drell–Yan and open charm), for the resonances the simulated line shapes are narrower than the experimental ones. For this reason, the mass and the width of the J/ψ ($M_{J/\psi}$ and $\sigma_{J/\psi}$) are also considered as free parameters.

Moreover, the ψ' mass and width are related to those of the J/ψ through the values expected from the Monte–Carlo simulations:

$$M_{\psi'}^{data} = M_{J/\psi}^{data} + (M_{\psi'}^{MC} - M_{J/\psi}^{MC}) \tag{5.21}$$

$$\sigma_{\psi'}^{data} = \sigma_{J/\psi}^{data} \frac{\sigma_{\psi'}^{MC}}{\sigma_{J/\psi}^{MC}} \tag{5.22}$$

3. Fit between $2.2 - 2.6\, GeV/c^2$ to evaluate the $D\overline{D}$ contribution, with:

$$\frac{dN}{dM} = N_{bck}\frac{dN_{bck}}{dM} + N_{J/\psi}\frac{dN_{J/\psi}}{dM} + N_{D\overline{D}}\frac{dN_{D\overline{D}}}{dM} + N_{DY}\frac{dN_{DY}}{dM} \tag{5.23}$$

where the background, the Drell–Yan and the J/ψ contributions are fixed to the values found in the previous steps of the fit. The only free parameter is the normalization of the $D\overline{D}$, while its shape is given by the MC simulations. $N_{D\overline{D}}$ is thus determined in this step of the fit.

The four step fitting method has been adopted to fix accurately the open charm contribution. Actually, it has been observed, in the analysis of the intermediate mass region [13, 14], that between the ϕ and the J/ψ masses the $D\overline{D}$ contribution includes also an excess, explained as an abnormally enhanced open charm production in nucleus–nucleus collisions, with respect to the linear extrapolation of p–A sources. The followed fit procedure allows to adapt the $D\overline{D}$ and the excess contribution to the high mass spectrum, reducing the systematic error from this source on the $J/\psi/DY$ ratio.

4. Final fit to the $M_{\mu^+\mu^-}$ spectrum from $2.9\, GeV/c^2$ with:

$$\frac{dN}{dM} = N_{bck}\frac{dN_{bck}}{dM} + N_{J/\psi}\frac{dN_{J/\psi}}{dM} + N_{D\overline{D}}\frac{dN_{D\overline{D}}}{dM} + N_{DY}\frac{dN_{DY}}{dM} + N_{\psi'}\frac{dN_{\psi'}}{dM} \tag{5.24}$$

where $N_{DY}, N_{J/\psi}, N_{\psi'}, M_{J/\psi}, \sigma_{J/\psi}$ are considered as free parameters, while the background and the open charm contributions are fixed respectively by step 1 and 3. Again the ψ' mass and width are related to those of the J/ψ by means of the expressions 5.21 and 5.22.

This procedure makes use of the maximum likelihood method and is applied to the dimuon invariant mass spectrum corresponding to eight different bins of the forward

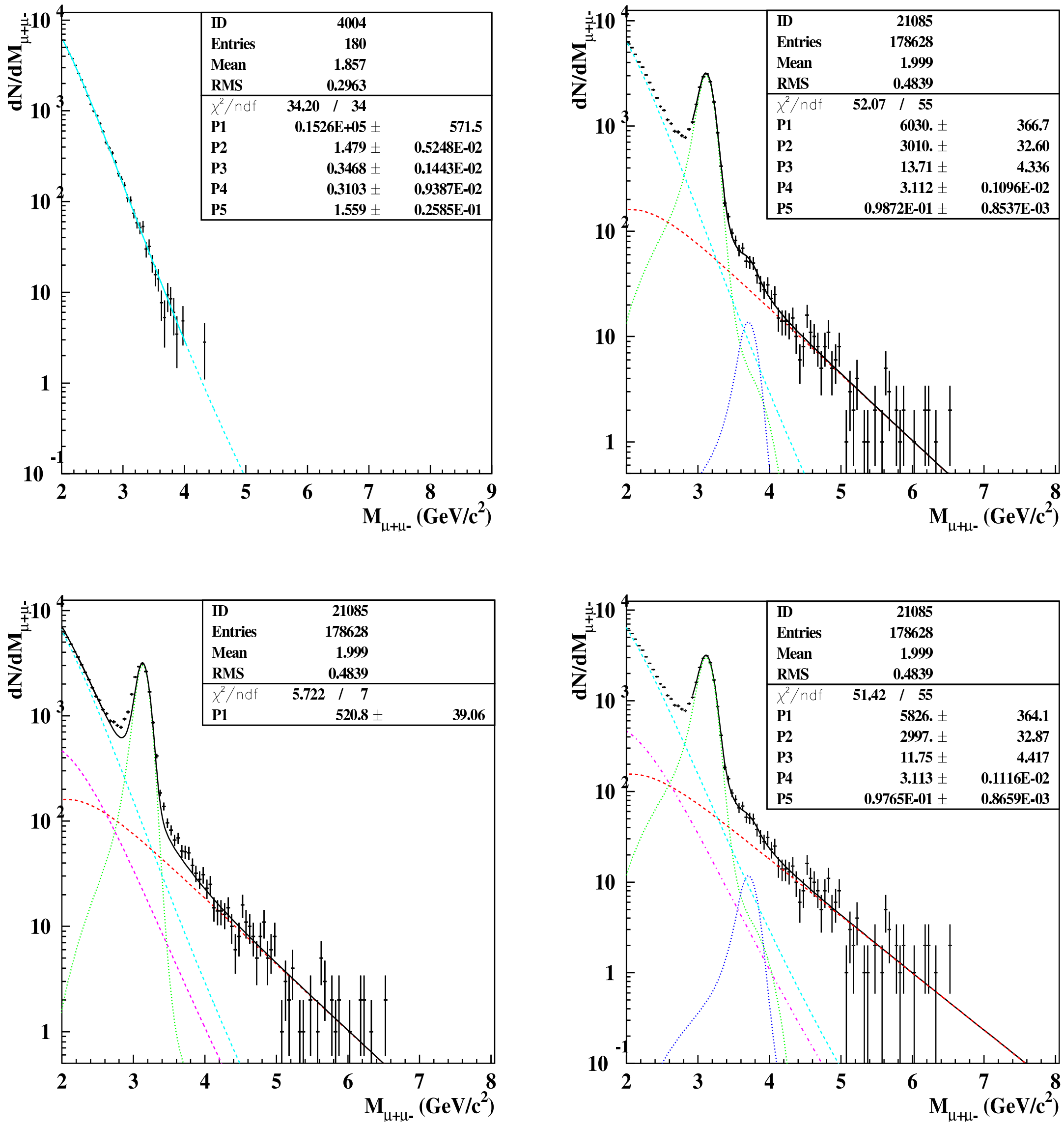

Figure 5.13: *Four steps of the fit to the invariant mass spectrum.*

energy measured by the ZDC. An example of such a fit in four steps is reported in Fig. 5.13 for an intermediate centrality E_{ZDC} bin. In Fig. 5.14 a zoom of the fourth step of the fit is sketched: the different contributions to the dimuon invariant mass spectrum are clearly visible.

As said before, the MC simulations are not able to reproduce exactly the shapes of the J/ψ and ψ' . Actually the values of the J/ψ and ψ' widths obtained by the fit to the simulated spectra are of the order of $\sigma_{J/\psi} \sim 84\,MeV$ and $\sigma_{\psi'} \sim 96\,MeV$ (see Fig. 5.7 and 5.8). By contrast, the fit to the experimental dimuon invariant mass spectrum gives $\sigma_{J/\psi} \sim 98\,MeV$ (in the case reported in Fig. 5.14 $p_5 = 0.09765\,GeV$

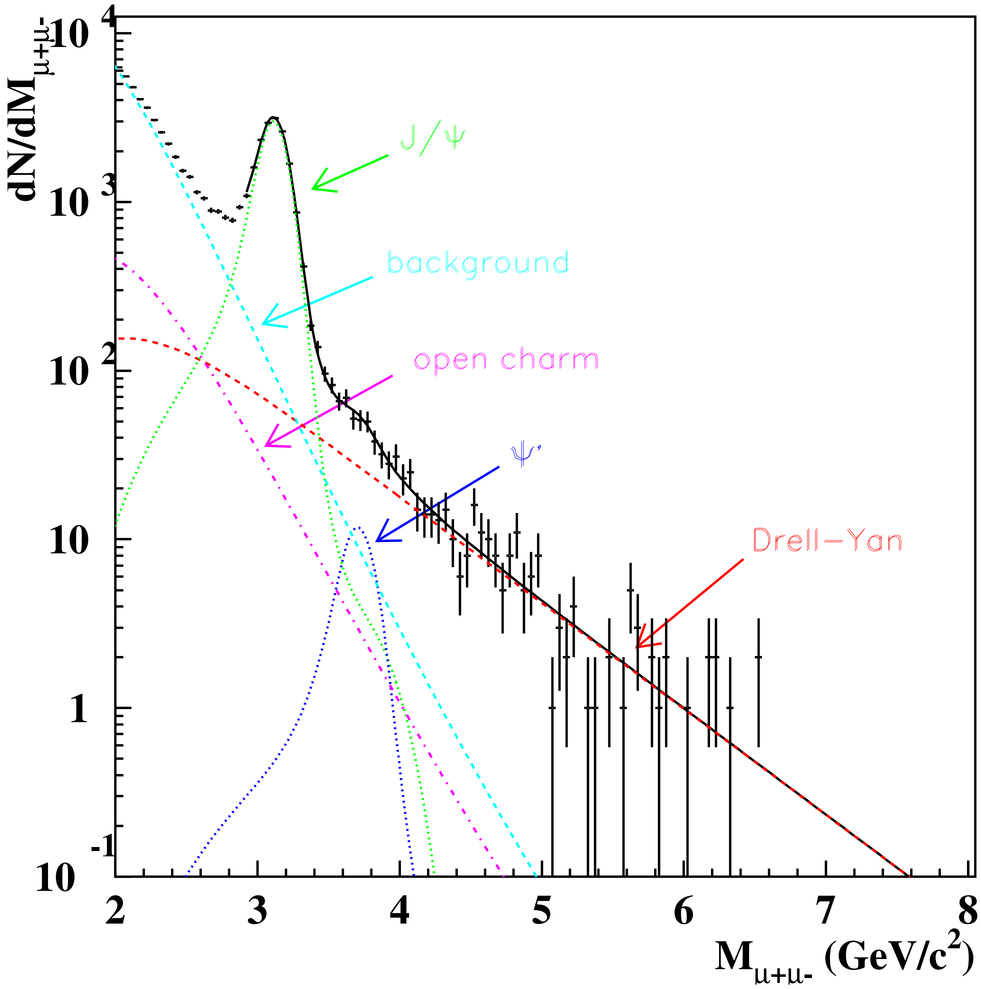

Figure 5.14: *Latest step of the four step fitting procedure applied to the opposite–sign muon pair invariant mass spectrum for Pb-Pb collisions.*

in the last step of the fit) and $\sigma_{\psi'} \sim 115\, MeV$ (linked to $\sigma_{J/\psi}$ through Eq. 5.22). The values of the resonance masses provided by the MC simulations are $M_{J/\psi} \sim 3128\, MeV$ and $M_{\psi'} \sim 3720\, MeV$, while the fit to the data gives $M_{J/\psi} \sim 3113\, MeV$ and, as a consequence, $M_{\psi'} \sim 3705\, MeV$.

The stability of the fitting procedure will be checked in Section 5.6.4, by considering alternative fit method and verifying that the results are always consistent.

5.5 Results

As already said, the standard analysis takes the Drell–Yan events as a reference for the study of the J/ψ production in Pb–Pb collisions. Actually it has been experimentally proved that the Drell–Yan behaves as a hard process (i.e. the cross–section for the Drell–Yan pair production in proton–nucleus and nucleus–nucleus interactions is proportional to the number of effective nucleon–nucleon collisions),

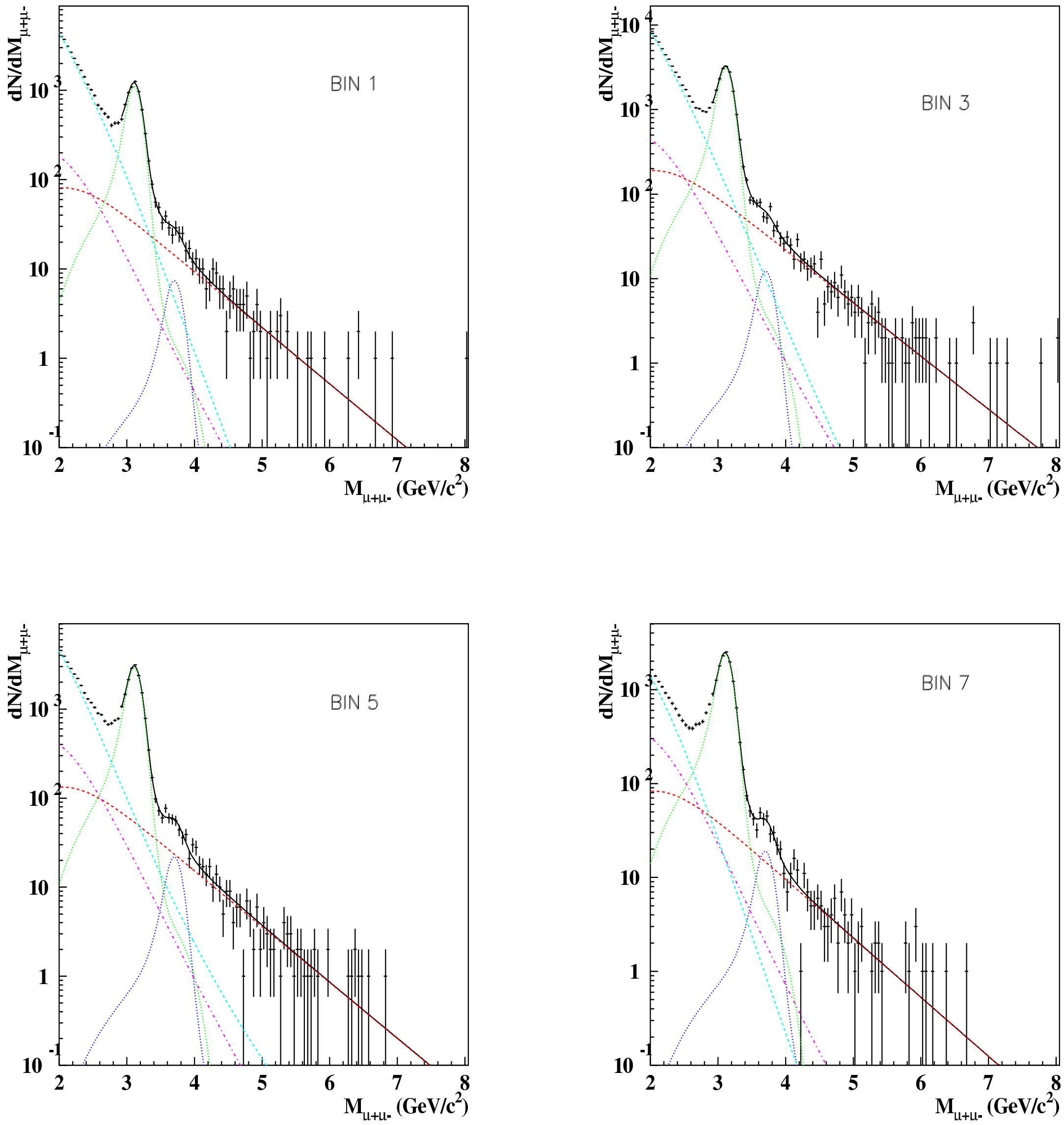

Figure 5.15: *Latest step of the four step fitting procedure applied to the dimuon invariant mass spectrum in four different E_{ZDC} bins. BIN 1 corresponds to a very central collision, while BIN 7 to a peripheral one.*

N. bin	ΔE_{ZDC} (GeV)	$< E_{ZDC} >$ (GeV)	$N_{J/\psi}$ ($M \geq 1.5$)	N_{DY} ($2.9 \leq M \leq 4.5$)	$J/\psi/DY$	χ^2
1	0-7000	5670	6404 ± 167	559 ± 47	12.5 ± 1.1	0.7
2	7000-11000	9047	16574 ± 264	1214 ± 71	14.9 ± 0.9	0.9
3	11000-15000	12980	17564 ± 272	1308 ± 74	14.6 ± 0.9	1.2
4	15000-19000	17000	17468 ± 266	1071 ± 67	17.7 ± 1.1	0.9
5	19000-23000	20980	16728 ± 252	918 ± 62	19.8 ± 1.4	1.1
6	23000-27000	24980	16254 ± 246	796 ± 56	22.2 ± 1.6	1.0
7	27000-31000	28910	14702 ± 235	573 ± 49	27.9 ± 2.4	1.6
8	31000-36000	32980	9745 ± 183	367 ± 37	28.9 ± 2.9	1.5

Table 5.8: *Final $J/\psi/DY$ values for each bin, together with the corresponding E_{ZDC} range, the mean E_{ZDC} value, the number of J/ψ and DY events and the χ^2 of the fit. The mass range for J/ψ and DY events is given in GeV/c^2. The error on the number of J/ψ and DY and on their ratio is also given.*

but does not suffer from the deconfinement of the medium where it is produced. Therefore it represents a good reference to establish if the J/ψ yield is suppressed or not, i.e. if nuclear matter has deconfined or not.

Since we want to study the J/ψ suppression pattern as a function of the collision centrality, estimated by the forward energy measured by the ZDC, the sample of events is divided into 8 subsamples, according to the E_{ZDC} value. Apart from the first (most central) and the last (most peripheral) bins, the other bins range over 4 TeV of E_{ZDC} and have nearly the same statistics of events.

The fitting procedure described above is repeated for each E_{ZDC} bin. The comparison between the fits to the invariant mass spectrum in different centrality bins is shown in Fig 5.15.

The contribution of non-J/ψ signal events under the J/ψ peak is roughly 14%. It is mainly due to Drell–Yan events (about 5%) and to the combinatorial background (about 8%), as the $D\overline{D}$ contribution is expected to be, at mass of 3 GeV/c^2, one order of magnitude lower.

For each E_{ZDC} bin, the number of events that originate from the J/ψ decays and from the Drell–Yan mechanism is deduced from the fit to the invariant mass spectrum. The Drell–Yan events are obtained in the mass range $2.9 \leq M_{\mu\mu} \leq 4.5\,GeV/c^2$, while the total number of J/ψs in the spectrum is considered. The ratio $N_{J/\psi}/N_{DY}$, corrected for the acceptances, gives directly the ratio of the J/ψ and DY cross–sections, multiplied by the branching ratio of the J/ψ in two muons.

$$\frac{B_{\mu\mu}\sigma_{J/\psi}}{\sigma_{DY}} = \frac{N_{J/\psi}}{A_{J/\psi}}\frac{A_{DY}}{N_{DY}} \tag{5.25}$$

In the following I often refer to $B_{\mu\mu}\sigma_{J/\psi}/\sigma_{DY}$ as simply $J/\psi/DY$. In table 5.8

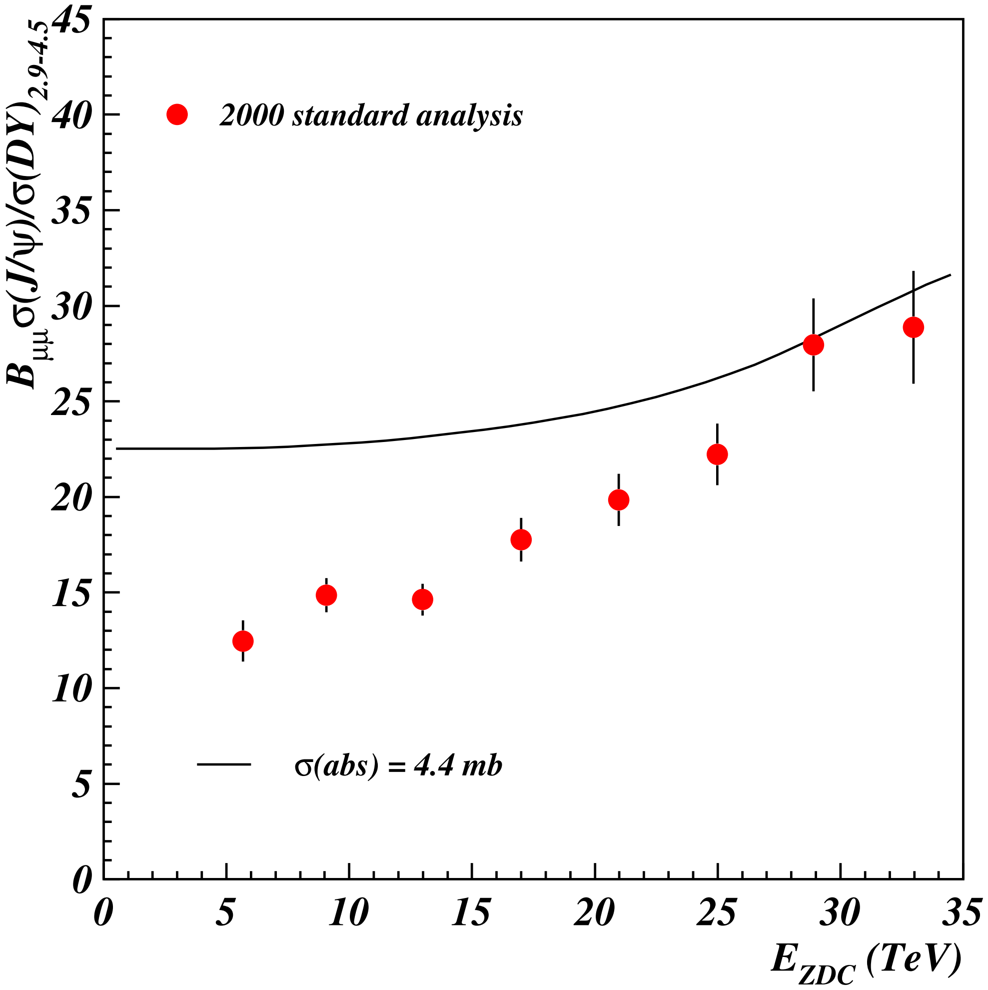

Figure 5.16: $\sigma_{J/\psi}/\sigma_{DY}$ *standard analysis results as a function of* E_{ZDC}*. The GRV–LO set of PDFs and the "multiplicative" charmonium parametrization have been used.*

the numbers of J/ψ and Drell–Yan events obtained from the fit are reported for each E_{ZDC} bin (whose mean value is $< E_{ZDC} >$). In the same table the ratios $J/\psi/DY$ and the χ^2 of the fit are also listed. The quoted errors on the $J/\psi/DY$ ratios are purely statistical. The systematic errors are negligible since performing the ratio of two measured quantities allows to cancel the uncertainties connected to the luminosity evaluation and/or the efficiency calculations, which are the same for the numerator and denominator terms. Unfortunately, using the ratio $J/\psi/DY$ we introduce larger statistical errors because of the small statistics of the DY sample of events.

Fig. 5.16 displays the $\sigma_{J/\psi}/\sigma_{DY}$ ratios as a function of E_{ZDC}, obtained with the standard analysis method. The GRV–LO set of parton distribution functions has been used in the simulation of the Drell–Yan contribution and the "multiplicative" parametrization has been adopted to fit the charmonium line shapes. In sections 5.6.7 and 5.6.8 the effects of changing the PDFs and the charmonium parametrization will be taken into account.

The solid line visible in Fig. 5.16 represents the "ordinary" nuclear absorption of the $c\bar{c}$ pair with a cross–section of 4.4 mb, evaluated b means of collisions ranging from p–p, p–A up to S–U, as explained in Section 1.8.1.

The J/ψ production yield in peripheral collisions (high amount of energy released in the ZDC) follows the pattern of the normal nuclear absorption. A departure from this behaviour is observed at $E_{ZDC} \sim 27\,TeV$ and no saturation is present at low E_{ZDC} values, corresponding to the most central collisions.

5.6 Study of systematic effects

In order to check the stability of the standard analysis results, various controls have been performed, as discussed in the following sections.

5.6.1 Amplitude of the E_T cut

As anticipated in chapter 4, a threshold on the neutral transverse energy E_T is imposed to eliminate the Pb ions that have not interacted inside the target. In the E_T–E_{ZDC} correlation (reported in Fig. 4.4) this means a sharp cut in the E_T variable, while it corresponds to a broaden selection in E_{ZDC}.

The procedure followed to correctly select the E_T cut is based on the Glauber formalism [15]. This model provides a quantitative geometrical description of the nucleus–nucleus collisions, treated as a superposition of nucleon–nucleon collisions. The experimental E_{ZDC} spectrum can be described in the frame of the Glauber model and, since this theoretical model accounts only for the interacting Pb ions, the correct E_T cut can be determined as the cut that allows to reject all the non-interacting Pb ions and to obtain a good agreement between the experimental E_{ZDC} spectrum and the Glauber model predictions.

In Fig. 5.17 the E_{ZDC} spectrum is plotted for MB events, without applying any E_T cut (the peak of the non-interacting Pb ions is clearly visible at around 32864 GeV) and for different E_T cuts. These cuts affect the E_{ZDC} spectrum from about 27000 GeV.

According to the Glauber model, the E_{ZDC} spectrum in nucleus–nucleus collisions can be described as (see [6]):

$$\left(\frac{dN}{dE_{ZDC}}\right)^{th}_{MB} \propto \int P_{AB}(E_{ZDC}, b)\,[1 - P(0,b)]\, b\, db \tag{5.26}$$

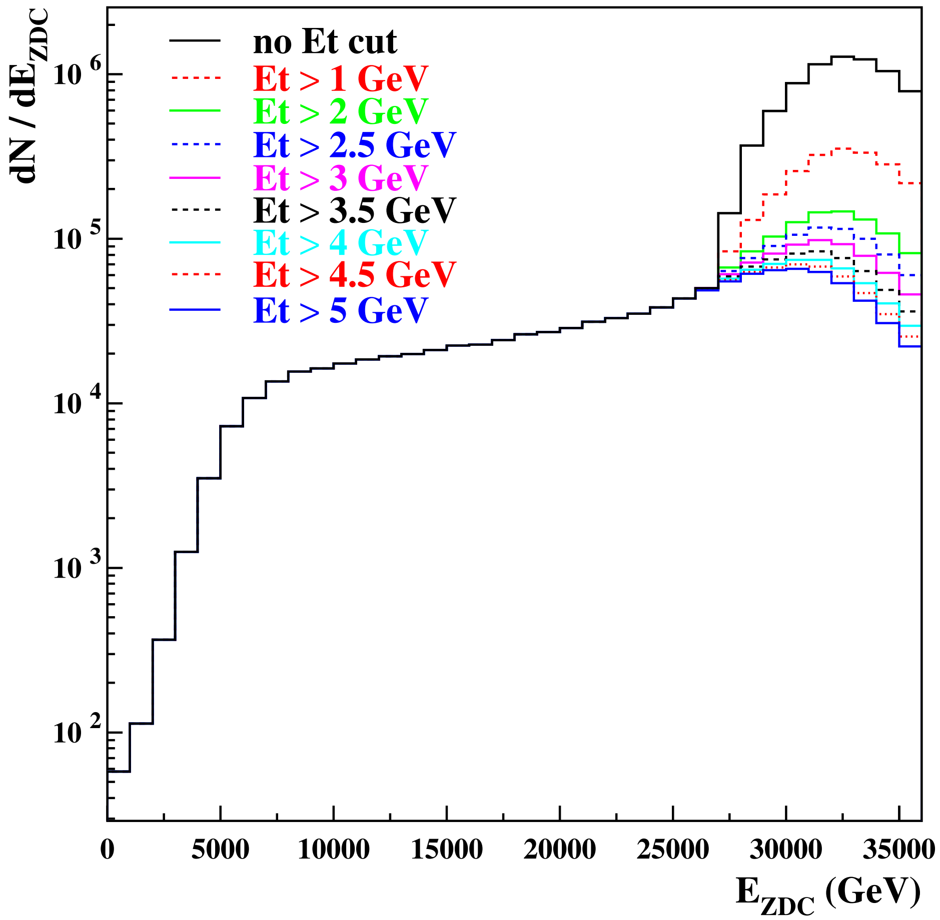

Figure 5.17: *Experimental E_{ZDC} spectrum without E_T cut and when different E_T cuts are applied, in MB BH trigger.*

where $P(0, b)$ represents the probability that no nucleon–nucleon interaction occurs at a given impact parameter b and $P_{AB}(E_{ZDC}, b)$ is the probability of having a given E_{ZDC} value for a collision at impact parameter b. This latter probability is assumed to have a gaussian distribution around the mean value $< E_{ZDC}(b) >$ which, for a Pb-Pb collision at 158 AGeV/c, can be expressed as a function of the number of spectator (N_s) and participant (N_p) nucleons reaching the ZDC:

$$< E_{ZDC}(b) >= 158 \times N_s(b) + \alpha N_p(b) \tag{5.27}$$

where αN_p is the energy released in the ZDC by participants and secondary particles. The α factor depends on the detector, and essentially on the rapidity range where the produced secondaries are measured. The link between participants (or spectators) and b is obtained in the frame of the Glauber model [15].

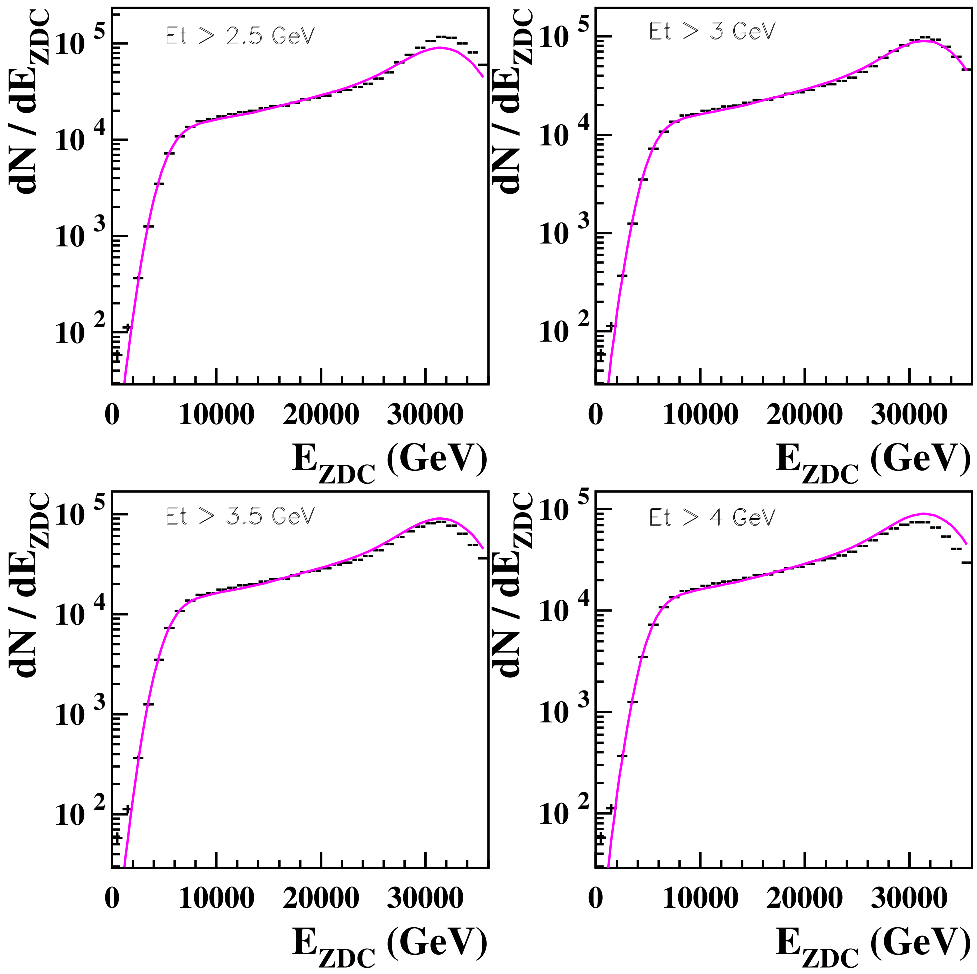

Figure 5.18: *Comparison between the theoretical minimum bias distribution obtained in the frame of the Glauber model (continuous line) and the experimental spectra with different E_T cuts.*

The width $\sigma_{E_{ZDC}}(b)$ of the gaussian is enlarged both by the detector experimental resolution and by the physical fluctuations ($\sigma_{physics}$) on the number of involved participants and can be expressed by the quadratic sum:

$$\sigma_{E_{ZDC}}(b) = (\beta \cdot \sqrt{E_{ZDC}(b)} + \gamma \cdot E_{ZDC}(b)) \oplus \delta \oplus \sigma_{physics}(b) \tag{5.28}$$

where the δ term takes into accounts the smearing of the signal due to the pedestal width and to calibration uncertainties. The β and the γ coefficients are related to the resolution of the detector and their values have been fixed with measurements done with low intensity proton and ion beams ($\beta = 3.39\,GeV^{1/2}$ and $\gamma = 0.062$) [16],

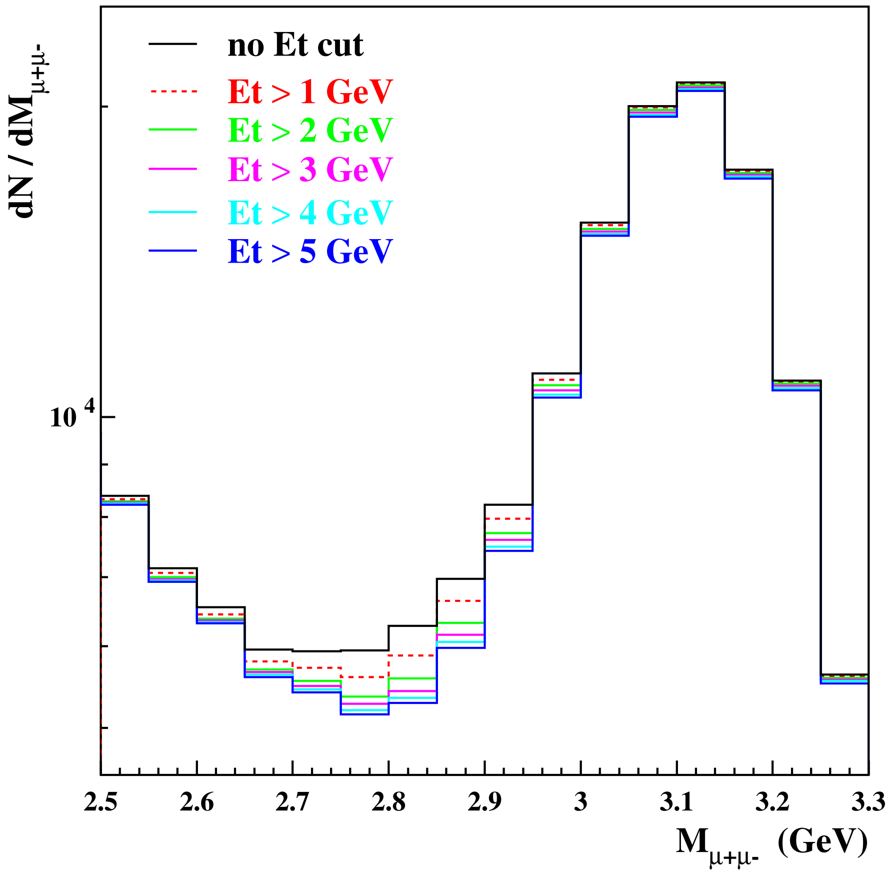

Figure 5.19: *Experimental $M_{\mu^+\mu^-}$ spectrum without E_T cut and when different E_T cuts are performed. All the cleaning cuts and a 2% P*DTarg cut are applied.*

while the other parameters included in the $< E_{ZDC}(b) >$ and $\sigma_{E_{ZDC}}(b)$ expressions are estimated adjusting the theoretical distribution on the experimental minimum bias spectrum.

In this approach, the theoretical minimum bias distribution is minimized on the experimental data up to 22 TeV, i.e. up to a region which is not yet biased by the effect of the E_T cut. The parameters resulting from the fit are:

$$\alpha = 7.93\, GeV \quad \text{and} \quad \delta = 1170\, GeV$$

Then the fit is extrapolated up to 35 TeV and compared to the experimental E_{ZDC} spectrum cleaned with different E_T cuts (Fig. 5.18). From the figure it emerges that the best value of the E_T cut is $E_T > 3\ GeV$, since it allows to reproduce the experimental E_{ZDC} spectrum by means of the Glauber fit extrapolation.

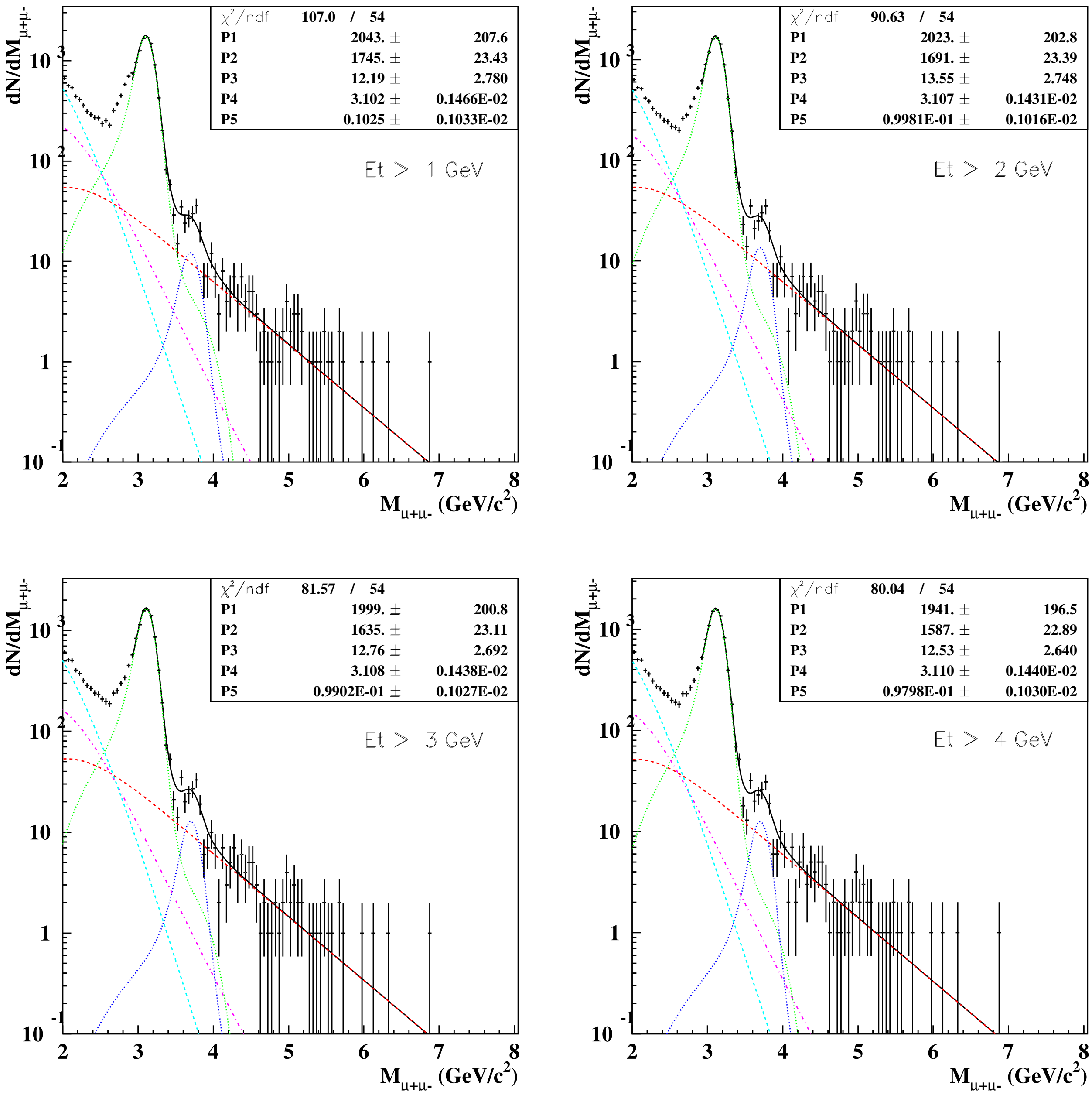

Figure 5.20: *Results of the fourth step of the fit to the invariant mass spectrum with different E_T cuts.*

If a higher ($E_T \geq 3.5$ GeV, $E_T \geq 4$ GeV) cut is imposed, too many events are rejected, while asking $E_T \leq 2.5$ GeV leaves still some lead ions in the spectrum.

The choice of the E_T cut amplitude is a very crucial point in the data selection, since it has consequences on the dimuon invariant mass spectrum in the J/ψ region

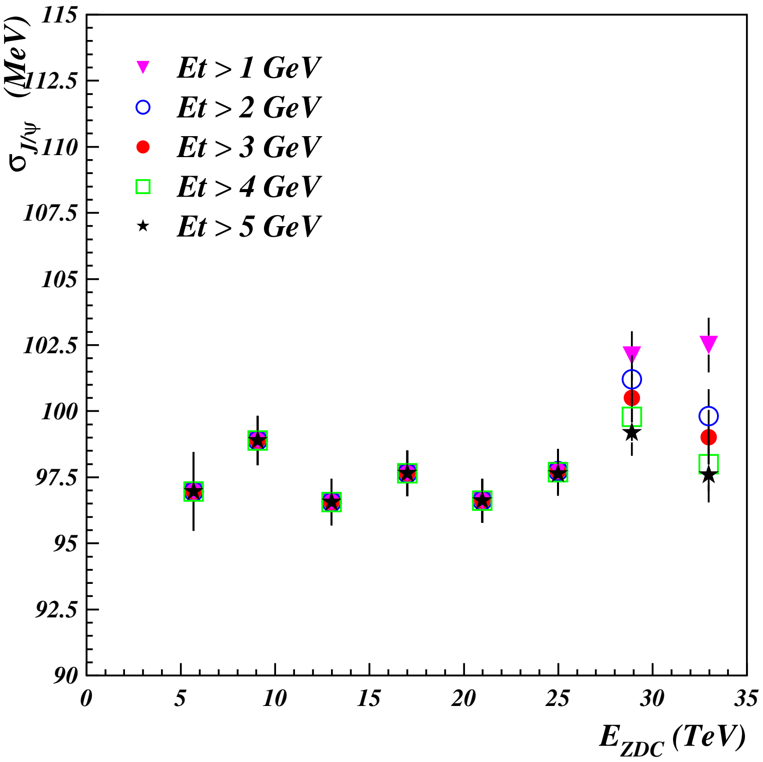

Figure 5.21: *$\sigma_{J/\psi}$ resulting from the fit to the experimental mass spectrum for different E_T cut amplitudes. The $\sigma_{J/\psi}$ values are plotted as a function of centrality E_{ZDC} bins.*

and, therefore, on the final $\sigma_{J/\psi}/\sigma_{DY}$ results. Actually, the E_T cut affects the dimuon invariant mass spectrum in the J/ψ region in a different way, according to the amplitude of the cut itself, as it can be seen in Fig. 5.19. In this picture the mass spectrum around the J/ψ resonance is plotted for different E_T cuts.

In particular, we can notice that the effect of the $E_T > 3$ GeV cut is compatible with the one imposed by stricter E_T cuts, while lower cuts reject fewer events in the mass spectrum. Hence the $E_T > 3$ GeV cut seems to be the minimum threshold that guarantees a sufficient cleanliness of the mass spectrum.

The fact that a very low E_T cut does not guarantee that the dimuon mass spectrum is properly cleaned, can be observed in Fig. 5.20, where the fourth step of the fit to the invariant mass spectra is reported for different E_T cuts. If a low E_T cut is applied, the J/ψ peak turns out to be affected by bad events (on the left of the peak), which disappear when the amplitude of the E_T is increased. This fact is pointed out by the enlargement of the J/ψ peak, if a low E_T cut is adopted (see the p_5 parameter of the fit in Fig 5.20 a and b).

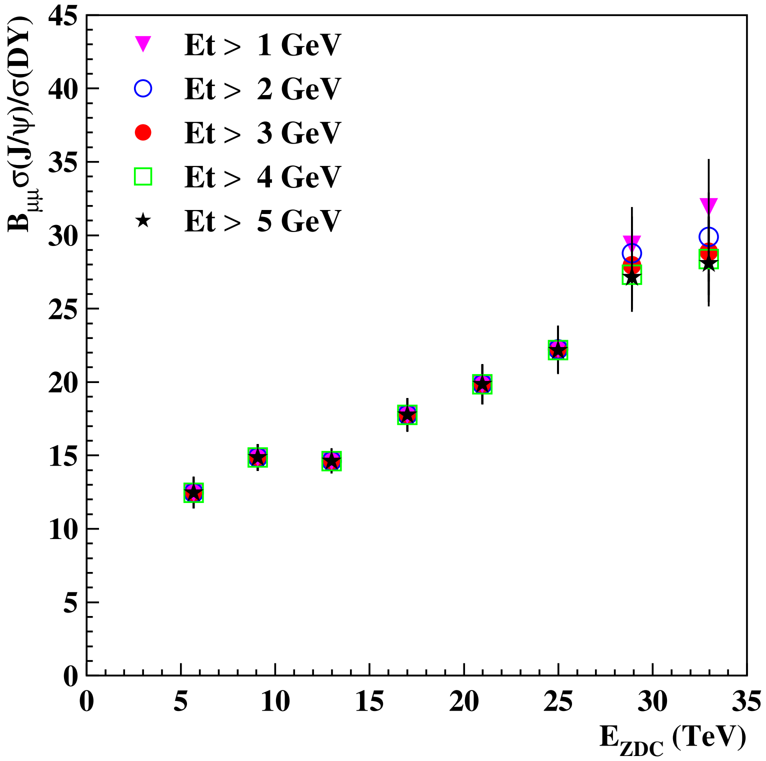

Figure 5.22: *$\sigma_{J/\psi}/\sigma_{DY}$ ratio as a function of E_{ZDC} when different E_T cuts are applied to the experimental data.*

In Fig. 5.21 the behaviour of $\sigma_{J/\psi}$ (given by the fit to the invariant mass spectrum) is plotted as a function of E_{ZDC}. For central or middle–centrality events no difference is introduced by the different E_T cuts, since they affect only the most peripheral events, where the contribution of the non-interacting Pb ions is concentrated. With a low E_T cut, the $\sigma_{J/\psi}$ value in the peripheral E_{ZDC} bins is larger than in more central bins, because of the pollution of the J/ψ peak by non–interacting Pb ion events. A $E_T > 3$ GeV cut is a compromise between the need to clean as much as possible the event sample and the need not to lose too much statistics.

Finally, in Fig. 5.22, the effect of different E_T cuts on the $\sigma_{J/\psi}/\sigma_{DY}$ ratio has been studied. For low E_T cuts, where the J/ψ peak is enlarged, the resulting $J/\psi/DY$ ratio are larger than for high E_T cuts. The amplitude chosen for the E_T selection ($E_T > 3$ GeV) gives results fully compatible with higher cuts (which allow to better clean the dimuon spectrum, but which have the drawback to empoverish the data sample).

In conclusions, however the level of the E_T cut is determined, by comparing the E_{ZDC} experimental spectrum to the Glauber model predictions or by checking that the dimuon mass spectrum has been properly cleaned, the best value for this cuts is $E_T > 3$ GeV. Such a cut leads to $\sigma_{J/\psi}/\sigma_{DY}$ results compatible with those obtained with higher and more selective cuts.

5.6.2 Effects of the selection cuts

In this section the effects on the $J/\psi/DY$ ratio, due to different choices of some selection and cleaning cuts, will be studied. The standard analysis procedure has been repeated changing one cut at a time and keeping the other ones unvaried.

As discussed in Chapter 4, the correlation between the energy measured by the electromagnetic calorimeter and the forward energy detected by the zero–degree calorimeter is a useful tool to clean the data sample and to reject events that have not originated in the target.

In Fig. 5.23 the correlation between E_T and E_{ZDC} is reported. Event by event, E_T is proportional to the number of target and projectile nucleons that have taken part

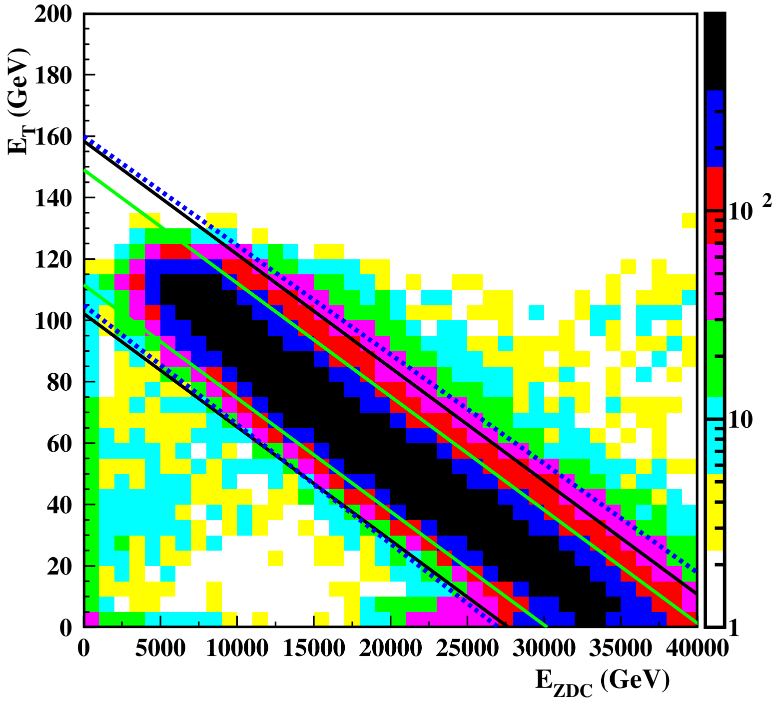

Figure 5.23: *Correlation between E_T and E_{ZDC}, after the application of all the selection cuts described in Chapter 4, except for the diagonal cut. The superimposed lines represent: 3σ (black continuous lines), 2σ (green continuous lines) and "level" (blue dotted lines) diagonal cuts. Note that the z scale is logarithmic.*

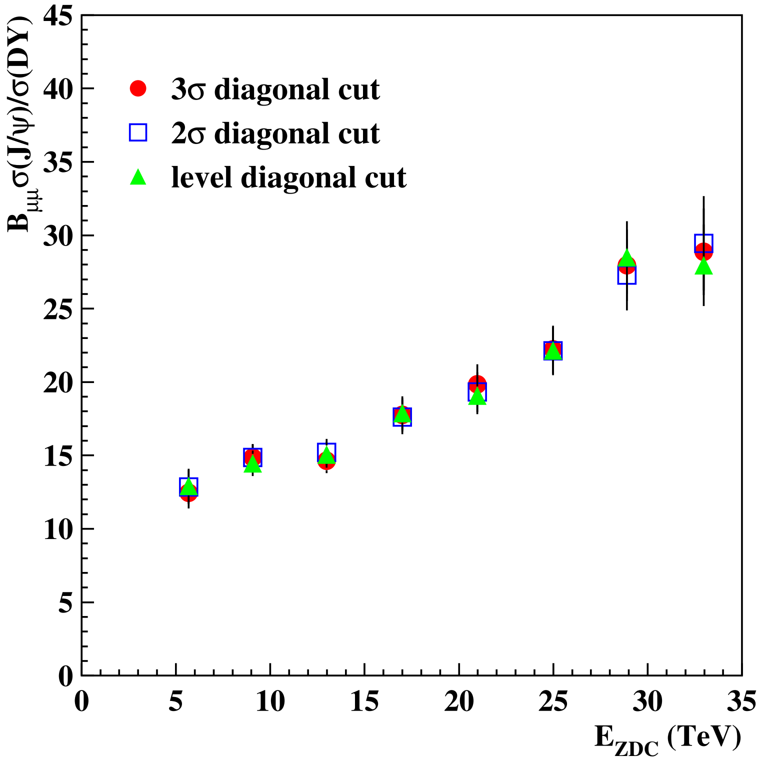

Figure 5.24: *$\sigma_{J/\psi}/\sigma_{DY}$ ratio as a function of E_{ZDC} when different $P{*}DTarg$ cuts are applied to the experimental data.*

to the interaction. E_{ZDC} is directly connected to the number of projectile nucleons that have not interacted in the target. The information of the two detectors is strictly correlated, as it can be seen in the figure, and can be used to eliminate events that lie outside the correlation, attributed to off-target interactions or to pile–up problems.

In the standard analysis reported in the previous sections all the events at a distance greater then 3σ from the average correlation (black continuous lines superimposed to Fig. 5.23) have been neglected in the data analysis.

In the following, the same standard analysis already described in Section 5.5 will be repeated with two alternative diagonal cuts: a cut defined by the green lines plotted in Fig. 5.23 at a distance of 2σ from the average correlation; a cut that takes into account the asymmetry of the correlation and that has been fixed on the fuchsia level of the correlation contour plot (blue dotted lines superimposed to Fig. 5.23).

In Fig. 5.24 the $\sigma_{J/\psi}/\sigma_{DY}$ results obtained with the standard analysis method are compared for the different diagonal selections. The results of the three analyses are compatible, as it is better visible by performing the ratios between the $\sigma_{J/\psi}/\sigma_{DY}$

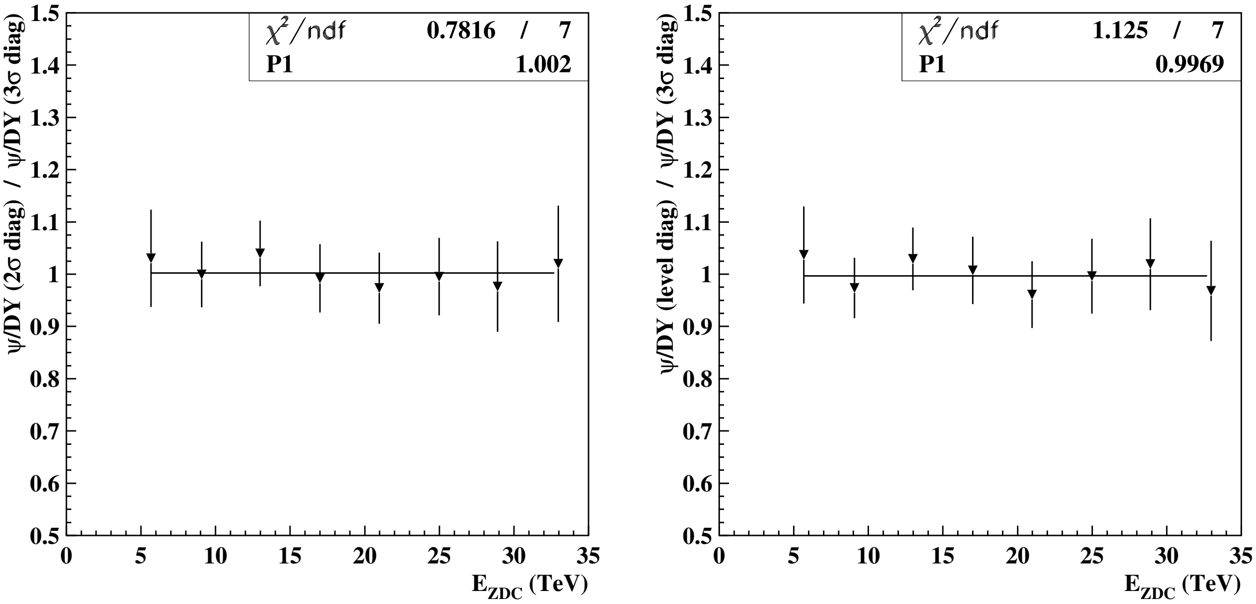

Figure 5.25: *Ratio between the $\sigma_{J/\psi}/\sigma_{DY}$ results obtained as a function of E_{ZDC} with the 2σ and the 3σ diagonal cuts (left) and with the "level" and the 3σ diagonal cuts (right). The constant fit is superimposed.*

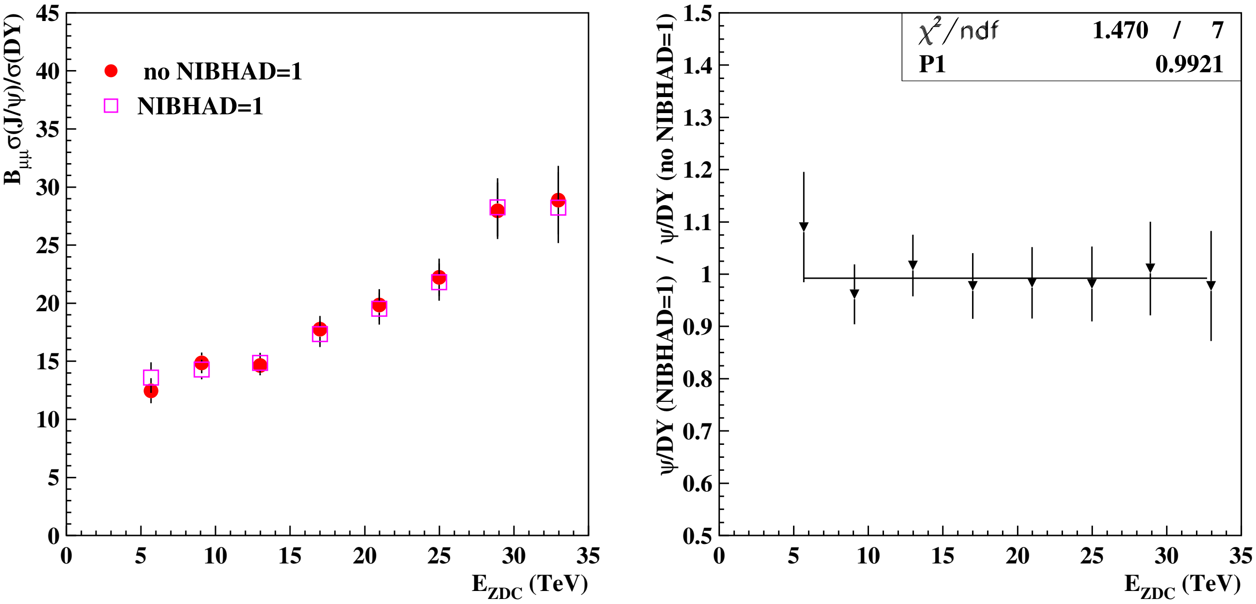

Figure 5.26: *Left: comparison between the $\sigma_{J/\psi}/\sigma_{DY}$ ratios evaluated with or without the NIBHAD=1 request. Right: ratio between the $\sigma_{J/\psi}/\sigma_{DY}$ results obtained as a function of E_{ZDC} with and without the NIBHAD=1 selection. The constant fit is superimposed.*

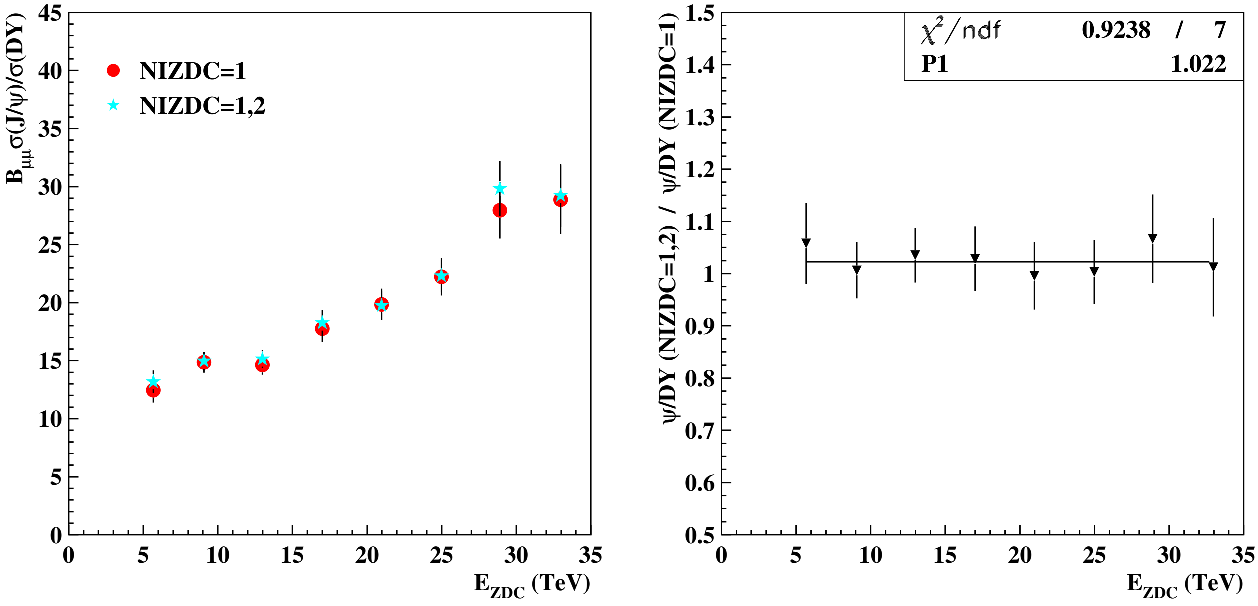

Figure 5.27: *Left: comparison between the $\sigma_{J/\psi}/\sigma_{DY}$ ratios obtained with NIZDC=1 or NIZDC=1 or 2 as a function of E_{ZDC}. Right: ratio between the $\sigma_{J/\psi}/\sigma_{DY}$ results with NIZDC=1 or 2 and with NIZDC=1. The constant fit is superimposed.*

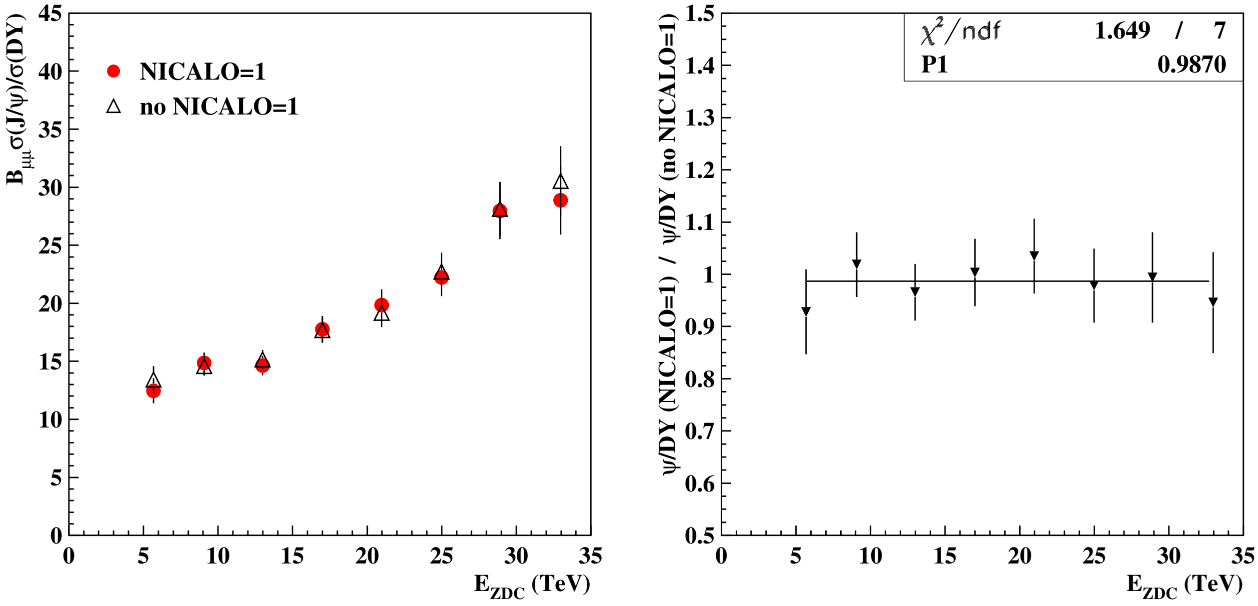

Figure 5.28: *Left: comparison between the $\sigma_{J/\psi}/\sigma_{DY}$ ratios obtained as a function of E_{ZDC} with or without NICALO=1. Right: ratio between the $\sigma_{J/\psi}/\sigma_{DY}$ results with and without NICALO=1. The constant fit is superimposed.*

values with the different diagonal cuts (Fig. 5.25).

The NIBHAD=1 selection corresponds to the request of only one incident ion detected by the BH within the 20 ns analysis window of the acquisition. This cut is redundant if used together with NICALO=1 and NIZDC=1 and I have decided not to use it in the 2000 data analysis. I want now to check if this choice does not influence the final $J/\psi/DY$ results. In Fig. 5.26 the comparison and the ratio between the standard analysis results obtained without selecting the NIBHAD flag (Section 5.5) and the $J/\psi/DY$ ratios re–evaluated by requiring NIBHAD=1 are plotted as a function of E_{ZDC}. The differences are lower than 1%.

The flag NIZDC selects, if equal to 1, only events not affected by beam pile–up problems and, if equal to 1 or 2, includes also those pile–upped events recovered with the correction method described in Section 3.4.4.

Up to now, the standard analysis has been performed with the stricter NIZDC selection, but is now repeated with the larger NIZDC=1 or 2 requirement. In Fig. 5.27 (left) the $\sigma_{J/\psi}/\sigma_{DY}$ results obtained in the two cases are compared, showing that the differences are negligible. The ratio between the two analyses, plotted as a function of E_{ZDC} in Fig. 5.27 (right), allows to check that the differences (of about 2%) are independent of the collision centrality.

The effect of releasing the requirement NICALO=1 is analysed in Fig. 5.28 (left), where the $J/\psi/DY$ ratios, evaluated as a function of E_{ZDC} with and without selecting the flag NICALO=1 (all the other selection and cleaning cuts are present), are plotted. The ratio between the two sets of results shows a slightly dependence (but the systematic effect is always smaller than the statistical error bars) on the centrality of the collision. The rejection of pile–up events, performed by means of the EMC information, seems therefore necessary to have a clean sample of events to be analysed.

5.6.3 Level of the P∗DTARG cut

As introduced in section 4.3.2, the so–called P∗DTarg cut has been elaborated in order to reject dimuon tracks not originated in the target or dimuons that have suffered from multiple scattering inside the target or the absorber.

For the 2000 Pb–Pb data, which is the subject of this thesis, a 2% P∗DTarg cut level has been used. Actually, this cut is enough to ensure that the Prob(P∗DTarg) distribution is flat and to cut bad events, which accumulate at low Prob(P∗DTarg) values (see Fig. 4.2).

This choice is corroborated by the observation of the P∗DTarg cut effects on the dimuon invariant mass spectra. In Fig. 5.29 the mass spectra for different P∗DTarg cuts are superimposed. The higher the P∗DTarg cut level is the more events are

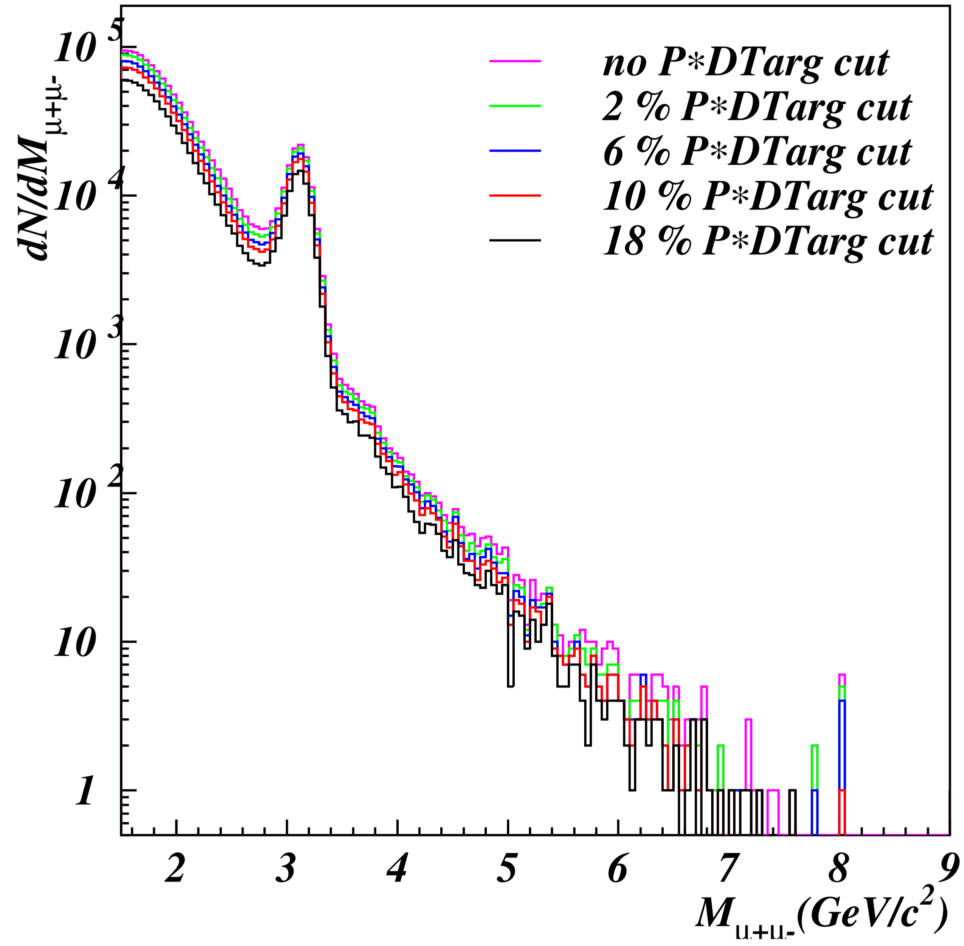

Figure 5.29: *Dimuon invariant mass spectra for different P∗DTarg cuts.*

rejected.

It is important to verify that the different P∗DTarg cuts affect the invariant mass spectrum in the same way. Otherwise, the ratio between J/ψ and Drell–Yan events can depend on the choice of the P∗DTarg cut level. For this purpose in Fig. 5.30 I have plotted the ratios between the mass spectra obtained applying different P∗DTarg cuts. The ratio $M_{\mu^+\mu^-}$ (2% P∗DTarg cut) / $M_{\mu^+\mu^-}$ (no P∗DTarg cut) shows that the effect of the 2% P∗DTarg cut is particularly visible in the region immediately below the J/ψ resonance, i.e. in the region between 2 and 3 GeV. Hence the P∗DTarg cut acts in different way on the different regions of the $M_{\mu^+\mu^-}$ spectrum. The constant fit to the ratio demonstrates that about 8% of the events are in average cut by a 2% P∗DTarg cut.

If the ratio between the invariant mass spectra with different P∗DTarg cut levels

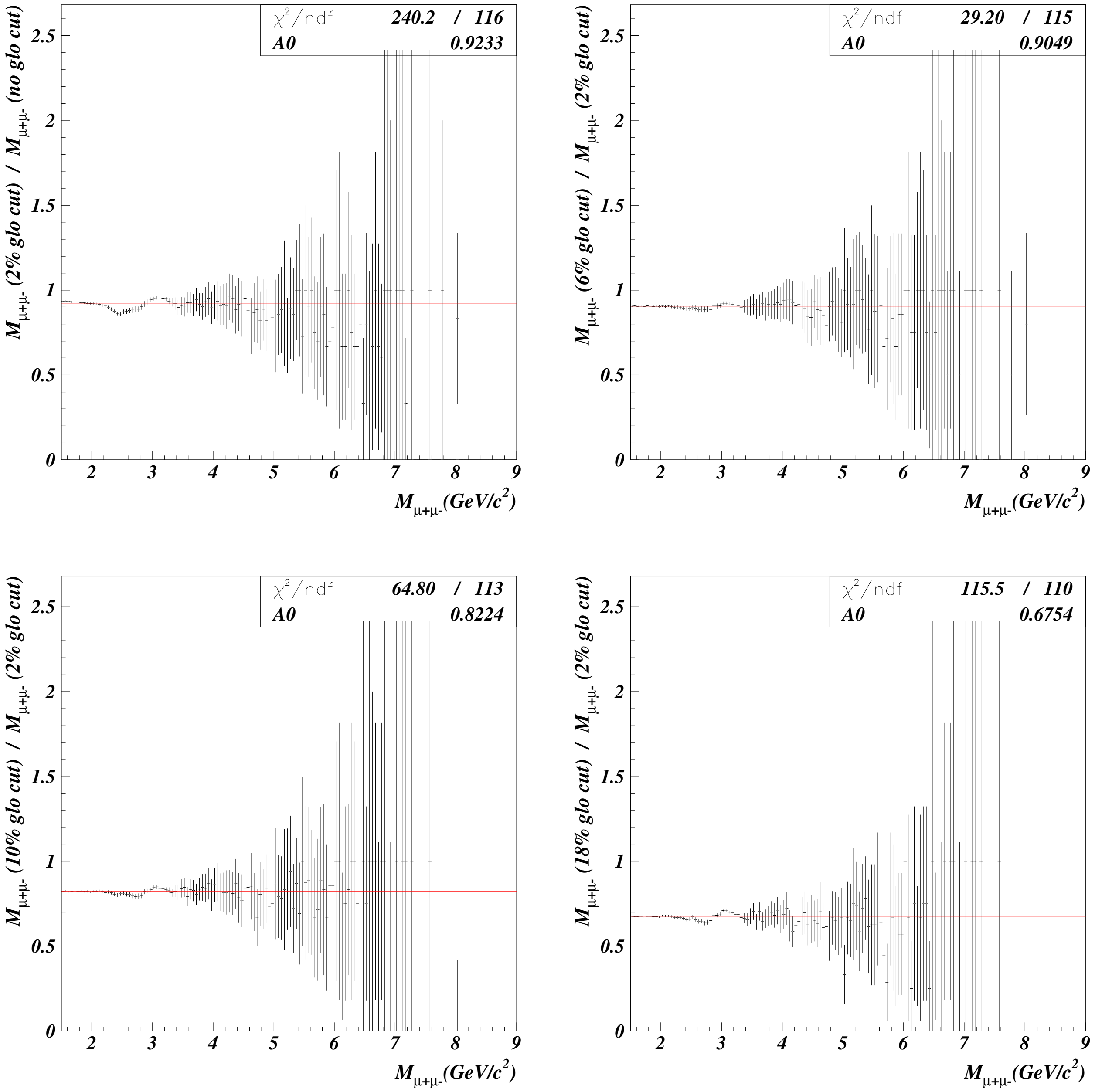

Figure 5.30: *Ratios between the invariant mass spectra obtained with a) 2% P∗DTarg cut and no P∗DTarg cut, b) 6% and 2% P∗DTarg cuts, c) 10% and 2% P∗DTarg cuts and d) 18% and 2% P∗DTarg cuts. A constant fit is superimposed.*

exhibits a flat behaviour, this proves that the different cuts behave in the same way. In Fig. 5.30 *b*, *c* and *d* the ratios $M_{\mu^+\mu^-}$(6% P∗DTarg cut)/$M_{\mu^+\mu^-}$(2% P∗DTarg cut), $M_{\mu^+\mu^-}$(10% P∗DTarg cut)/$M_{\mu^+\mu^-}$(2% P∗DTarg cut) and $M_{\mu^+\mu^-}$(18% P∗DTarg

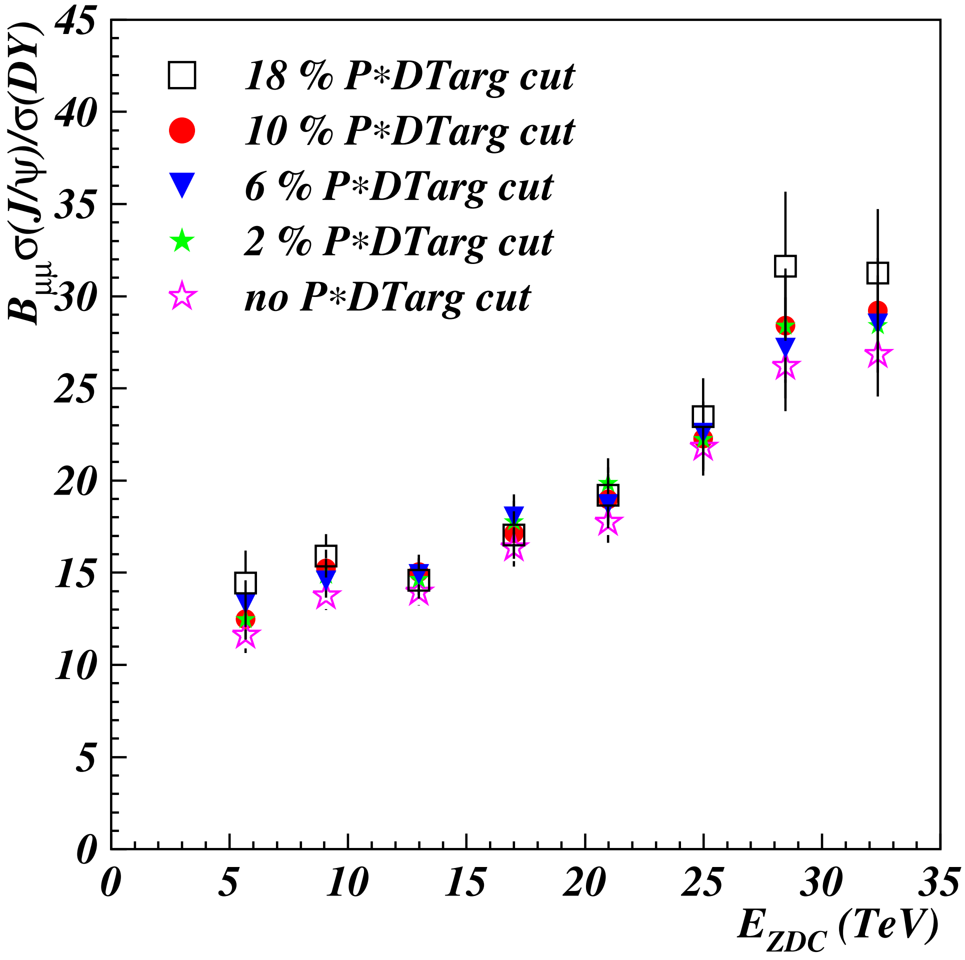

Figure 5.31: $\sigma_{J/\psi}/\sigma_{DY}$ *standard analysis results as a function of* E_{ZDC} *for different* $P{*}DTarg$ *cut levels. The GRV–LO set of PDFs and the "multiplicative" charmonium parametrization have been used.*

cut)/ $M_{\mu^+\mu^-}$(2% P$*$DTarg cut) are plotted. From these figures we can conclude that the 2%, 6% and 10% P$*$DTarg cuts have the same effects over the whole mass spectrum, even if they cut different percentages of events.

The ratio between the mass spectra with 18% and 2% P$*$DTarg cuts is nearly constant, apart from a deviation from the flat behaviour of the order of 5% in the region around the J/ψ resonance. Therefore the 18% P$*$DTarg cut does not act on the whole mass spectrum in the same way as lower cuts.

Between 2%, 6% and 10% P$*$DTarg cuts, we have chosen the minimum cut (2%) that allows to clean the data sample without loosing too much statistics of events.

The results of the standard analysis shown in Section 5.5 have been obtained

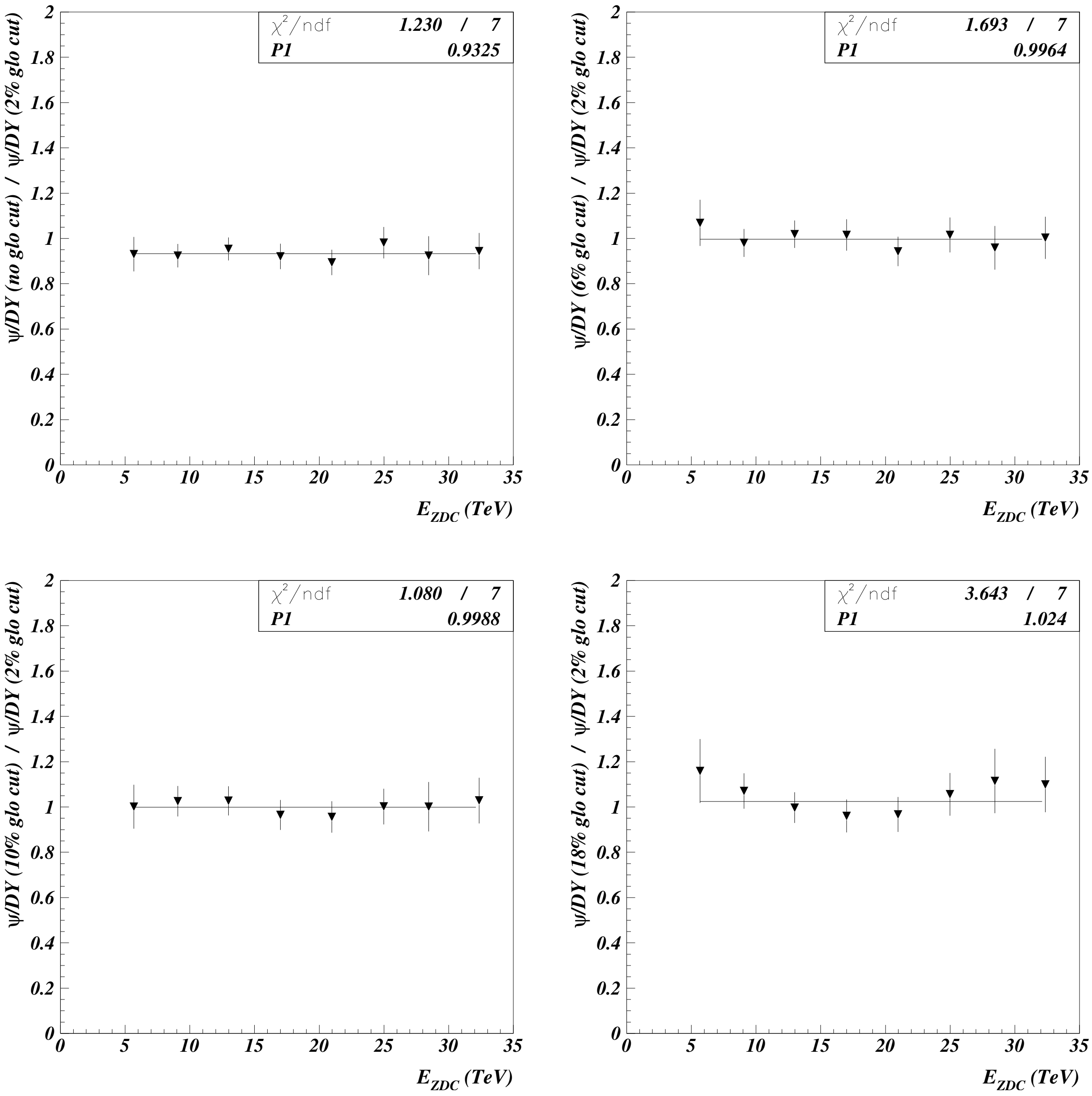

Figure 5.32: *Ratios between the $\sigma_{J/\psi}/\sigma_{DY}$ results obtained as a function of E_{ZDC} with a) no P∗DTarg cut and 2% P∗DTarg cut, b) 6% and 2% P∗DTarg cuts, c) 10% and 2% P∗DTarg cuts, d) 18% and 2% P∗DTarg cuts. A constant fit is superimposed.*

with this selection cut. To check the stability of the analysis, as a function of the chosen P∗DTarg cut, other P∗DTarg cuts have been considered and the full analysis has been re–performed. All the other selection and cleaning cuts and the analysis procedure are the same already adopted for the results plotted in Fig. 5.16, since in this section I want only to look for the effects of the different P$*$DTarg cuts.

The experimental results have been analyzed with 6%, 10%, 18% and without P$*$DTarg cuts, even if in the latest two cases the invariant mass spectrum can be not properly cleaned. In Fig. 5.31 the results of these analyses are compared to those obtained with the reference 2% P$*$DTarg cut. All the $\sigma_{J/\psi}/\sigma_{DY}$ values refer to the GRV LO set of PDFs for the Drell–Yan simulation and to the "multiplicative" parametrization for the charmonium states.

The analyses with 2%, 6% and 10% give compatible results, as it is better visible performing the ratios between the different results (Fig. 5.32 *b* and *c*). Actually, the ratios $\sigma_{J/\psi}/\sigma_{DY}$ (6% P$*$DTarg cut)/$\sigma_{J/\psi}/\sigma_{DY}$ (2% P$*$DTarg cut) and $\sigma_{J/\psi}/\sigma_{DY}$ (10% P$*$DTarg cut)/$\sigma_{J/\psi}/\sigma_{DY}$ (2% P$*$DTarg cut) are flat and nearly equal to 1, indicating that there are no differences, as a function of E_{ZDC}, between the different analyses.

The results of the standard analysis performed without applying a P$*$DTarg cut are lower than the previous ones of about 7%, even if this systematic effect is lower than the statistical error bars. This percentage is equal for all the E_{ZDC} bins, i.e. it does not depend on the centrality of the collision.

We have already seen that a 18% P$*$DTarg cut affects the invariant mass spectrum in a different way with respect to lower cuts. This introduces a bias on the $J/\psi/DY$ ratios, which turn out to be higher than those obtained with a 2%, 6% or 10% P$*$DTarg cut. This discrepancy is different according to the E_{ZDC} bin.

In conclusion, the $J/\psi/DY$ results have been proved to be independent of the P$*$DTarg cut level, provided that this level is chosen in order to properly clean the data, without introducing biases.

5.6.4 Different fitting procedure

To check the stability of the standard analysis results, alternative fitting procedures, different from the method described in Section 5.4, have been adopted.

A first approach can consists in fixing the J/ψ width, which, in all the fits performed up to now to the dimuon invariant mass spectrum, has always been considered as a free parameter. As already shown in Fig. 5.21, the fit with the $\sigma_{J/\psi}$ as a free parameter gives values of $\sigma_{J/\psi}$ ranging from 97 to 100 MeV (if an $E_T > 3\,GeV$ cut is considered). The mean value on all the E_{ZDC} bins is 98.5 MeV.

The $\sigma_{J/\psi}$ is now fixed in the fourth step of the fit procedure to this mean value, while $\sigma_{J/\psi}$ is still considered as a free parameter in the second step of the fit.

The evaluated $\sigma_{J/\psi}/\sigma_{DY}$ ratios are then compared to those previously obtained with the free $\sigma_{J/\psi}$ fit (Fig. 5.33). The two fit procedures give compatible results (within 1–2%, as it is visible performing the ratio of the two sets of results), except for the most peripheral collisions. In particular, fixing $\sigma_{J/\psi} = 98.5\,MeV$ in the latest but one E_{ZDC} bin (whose $\sigma_{J/\psi}$, given by the free $\sigma_{J/\psi}$ fit, was about 100 MeV, higher than in the other bins), produces a reduction of the number of J/ψ events

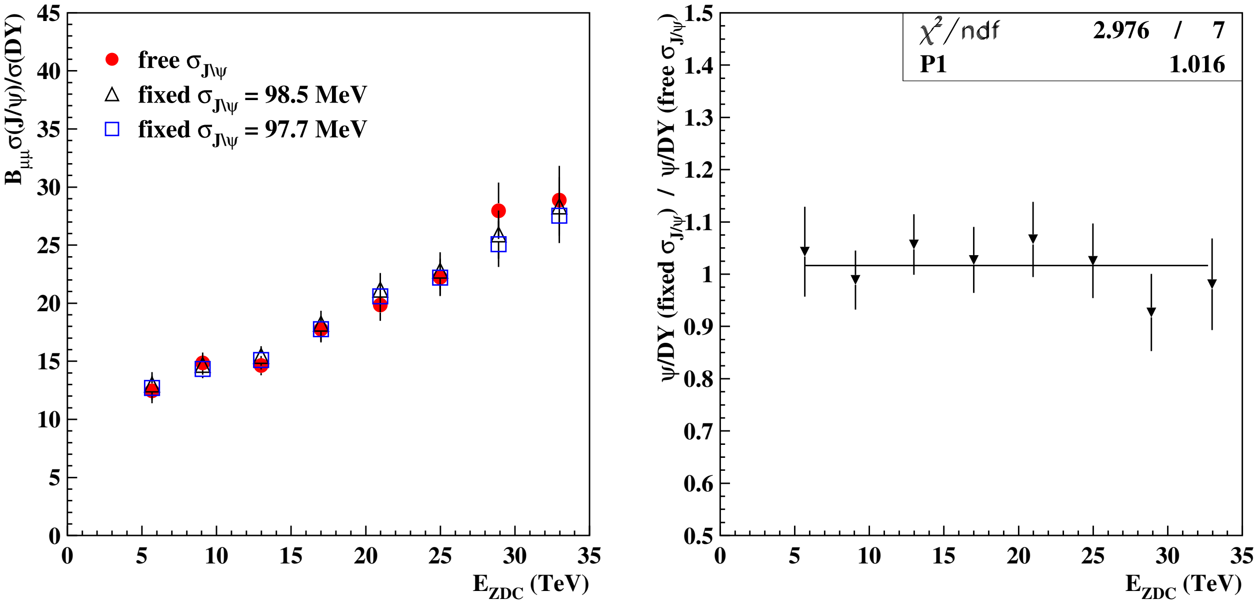

Figure 5.33: *Left: comparison between the $\sigma_{J/\psi}/\sigma_{DY}$ ratios obtained, as a function of E_{ZDC}, in the fit with the $\sigma_{J/\psi}$ free, fixed to 98.5 GeV or to 97.7 MeV (a 2% P∗DTarg cut is applied). Right: ratio between the $\sigma_{J/\psi}/\sigma_{DY}$ results given by the fit with $\sigma_{jp} = 98.5$ GeV or as a free parameter. The constant fit is superimposed.*

and, consequently, a decreasing of the final $J/\psi/DY$ ratio.

The reason of the $\sigma_{J/\psi}$ enlargement in the most peripheral collisions could be attributed to residual off-target events, whose interaction vertex is not correctly identified.

In any case, the systematic effect linked to the fit procedures is smaller than the statistical error bars, also in the most peripheral centrality bins.

An other method to fix the $\sigma_{J/\psi}$ value can be adopted. It is based on the fit to the invariant mass spectrum in a single E_{ZDC} bin, including all the E_{ZDC} values up to 20 TeV (where the $\sigma_{J/\psi}$ behaviour was more stable, as observed in Fig. 5.21). The advantage of this alternative procedure is that, in a single large E_{ZDC} bin, the available statistics allows a good fit of the different contributions to the $\mu^+\mu^-$ mass spectrum (in particular of the Drell–Yan). The found $\sigma_{J/\psi}$ value is 97.7 MeV, which is comparable to the mean value of the J/ψ widths obtained considering the $\sigma_{J/\psi}$ as a free parameter of the fit. As a consequence, the $J/\psi/DY$ results will be fully consistent with both methods of fixing the $\sigma_{J/\psi}$ (Fig. 5.33).

In conclusion, the $\sigma_{J/\psi}/\sigma_{DY}$ values provided by the standard analysis method are independent of the fact that $\sigma_{J/\psi}$ is fixed or not in the fit to the $\mu^+\mu^-$ invariant mass spectrum. All the results, obtained considering the $\sigma_{J/\psi}$ as a free fit parameter or fixing it in different ways, are fully compatible, except for a slight difference, always

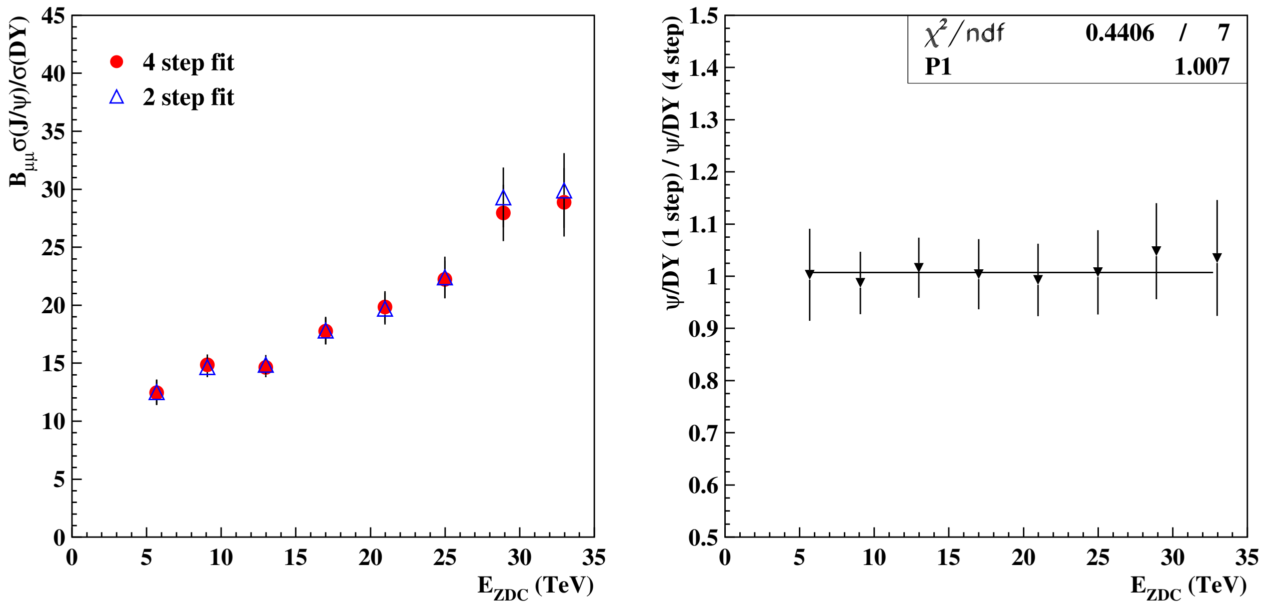

Figure 5.34: *Left: comparison between the $\sigma_{J/\psi}/\sigma_{DY}$ ratios obtained, as a function of E_{ZDC}, by the 4–step and the 2–step procedures (2% P∗DTarg cut). Right: ratio between the $\sigma_{J/\psi}/\sigma_{DY}$ results given by the two fit methods. The constant fit is superimposed.*

negligible compared to the statistical error bars, visible in the most peripheral E_{ZDC} bins.

I have then checked that the $\sigma_{J/\psi}/\sigma_{DY}$ results are independent of the number of steps of the fit procedure applied to the dimuon mass spectrum in order to reproduce the different contributing mechanisms. In particular, the four step fitting method adopted up to now, was chosen to accurately fix the open charm contribution.

We limit now the fit to two steps: the first step to evaluate the combinatorial background contribution, the second one, from 2.2 GeV/c^2, with

$$\frac{dN}{dM} = N_{bck}\frac{dN_{bck}}{dM} + N_{J/\psi}\frac{dN_{J/\psi}}{dM} + N_{D\overline{D}}\frac{dN_{D\overline{D}}}{dM} + N_{DY}\frac{dN_{DY}}{dM} + N_{\psi'}\frac{dN_{\psi'}}{dM} \tag{5.29}$$

where $N_{J/\psi}, N_{D\overline{D}}, N_{DY}, N_{\psi'}, M_{J/\psi}, \sigma_{J/\psi}$ are considered as free parameters, while the background contribution is fixed by the first step . The ψ' mass and width are related to those of the J/ψ by means of the expressions 5.21 and 5.22.

No significant difference can be observed between the $J/\psi/DY$ results given by the two–step or the four–step fit procedures (see Fig. 5.34). Both results refer to the charmonium multiplicative parametrization, the GRV LO set of PDFs and a 2% P∗DTarg cuts.

Moreover, the $J/\psi/DY$ results do not depend on the starting point of the second step of the fit (initially fixed to 2.2 GeV/c^2), provided that it is not higher than 2.9GeV/c^2, otherwise it becomes difficult to reproduce the open charm contribution. Passing from 2 GeV/c^2 to 2.8 GeV/c^2, the $\sigma_{J/\psi}/\sigma_{DY}$ values vary by less than 2%, difference that maintains within the error bars (which increase raising the fit limit, due to the increasing difficulty in fixing the $D\overline{D}$ contribution).

5.6.5 Empty target subtraction

For the data collected in the year 2000 and analyzed here, a vacuum system has been designed for the target, including also the region between the target and the BeO preabsorber, in order to reduce the contamination from Pb–air interactions. Actually, a Pb ion that interacts with the air around the target, loses a small fraction of its energy and is registered by the apparatus as a peripheral event.

The improved experimental conditions and cleaning cuts have allowed to have a clean data sample to analyze, as it can be seen in Fig. 5.35 and 5.36. In the first picture, the dimuon invariant mass spectrum is plotted at low E_T (left) and

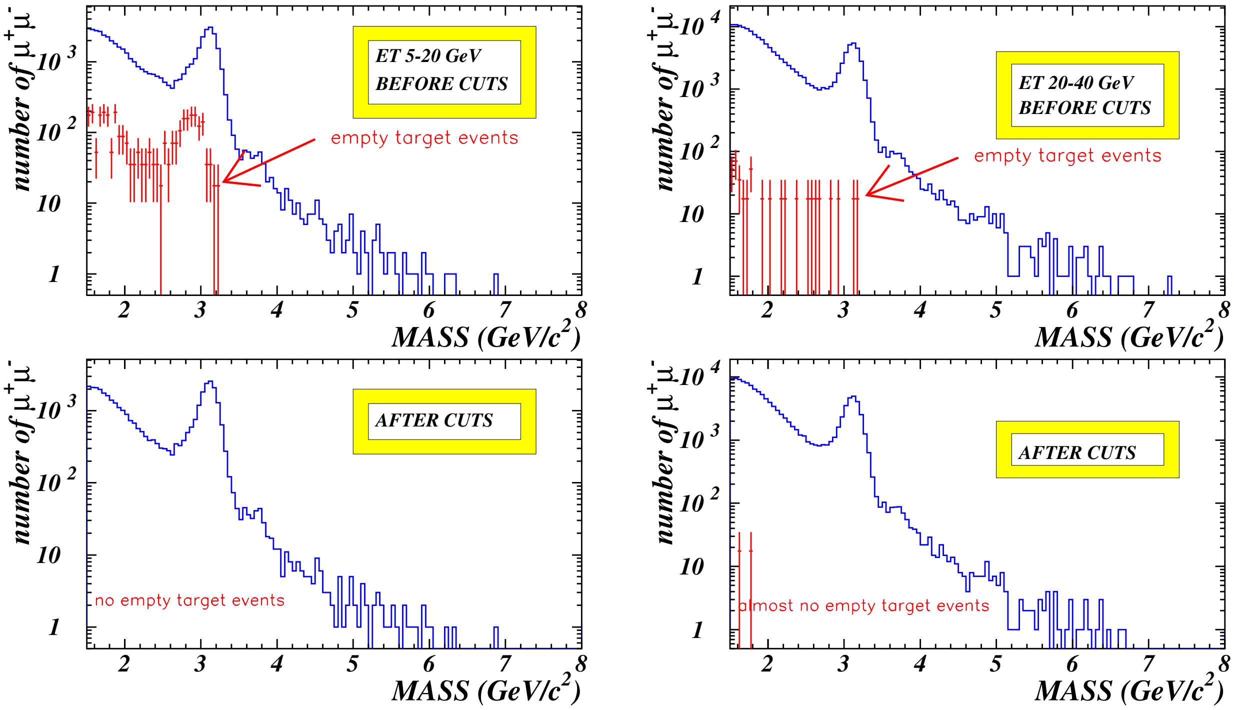

Figure 5.35: *Dimuon invariant mass distribution for low E_T (left) and at intermediate and high E_T values (right). The empty target mass spectrum is also superimposed (in red).*

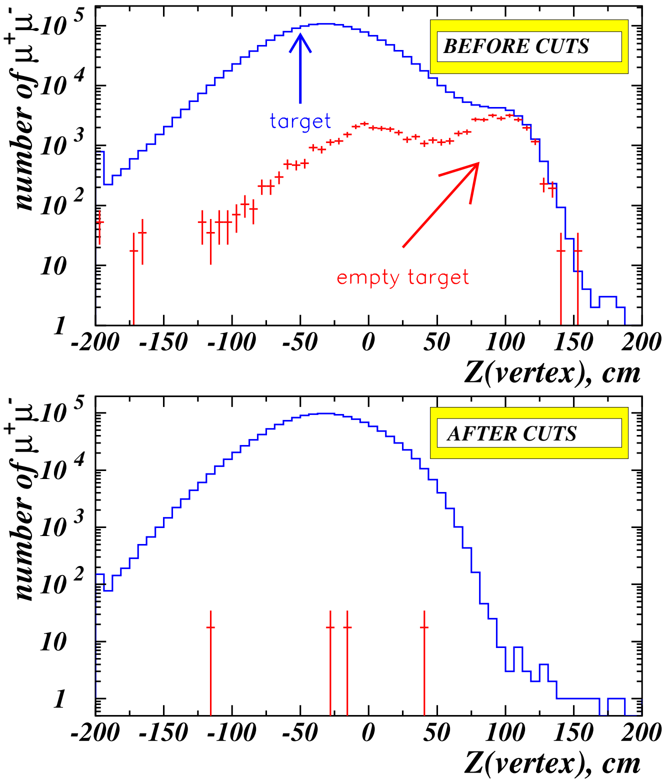

Figure 5.36: *Distribution of the interaction vertex for opposite–sign muons, before (top) and after (bottom) the cleaning and selection cuts. The red histograms refer to the empty target contribution.*

at intermediate and high E_T (right), before and after applying the selection and cleaning cuts. The mass spectra obtained in *empty target* runs (special runs where the target was removed from the beam line) are also reported. In such runs, a negligible contribution from Pb–air interactions is expected, since the target has been put under vacuum, but "out of target" events (muons originated after the target, e.g. in the BeO preabsorber or in the ZDC) can be present.

As visible in Fig. 5.35, the contamination of *empty target* events is bigger at low E_T values, which correspond to peripheral Pb–Pb collisions. However this contribution is almost completely removed by applying the cuts.

For more central collisions (higher E_T values), the contamination of events originated outside the target region is already low without cuts and is almost fully eliminated if the cuts are imposed.

The reconstruction program calculates the impact points of the reconstructed tracks in a plane perpendicular to the beam axis. In Fig. 5.36 the distribution of the z coordinate of the reconstructed interaction vertex is reported for opposite–

sign muons, before and after the application of the cleaning cuts. The position of the target corresponds to $Z_{vertex} = -47\ cm$. The *empty target* contributions are superimposed to the figure. The contamination due to out of target events is clearly visible at high Z_{vertex} values, i.e. in the region after the target. With the application of the selection and cleaning cuts, almost all the dimuons not coming from the target are rejected.

From the previous observations, we can conclude that the standard analysis results, reported in Section 5.5, should not be influenced from the fact that we have not performed the *empty target* subtraction, since the adopted cleaning and selection cuts allow to almost completely get rid of this contribution. An estimation of the entity of such a contribution gives a value of about 2.4%, limited to the E_{ZDC} region between 26 and 36 TeV.

5.6.6 Open charm simulations

The generation of the Monte–Carlo open charm contribution has been performed by means of the PYTHIA event generator [2], with the MRS 43 set of parton distri-

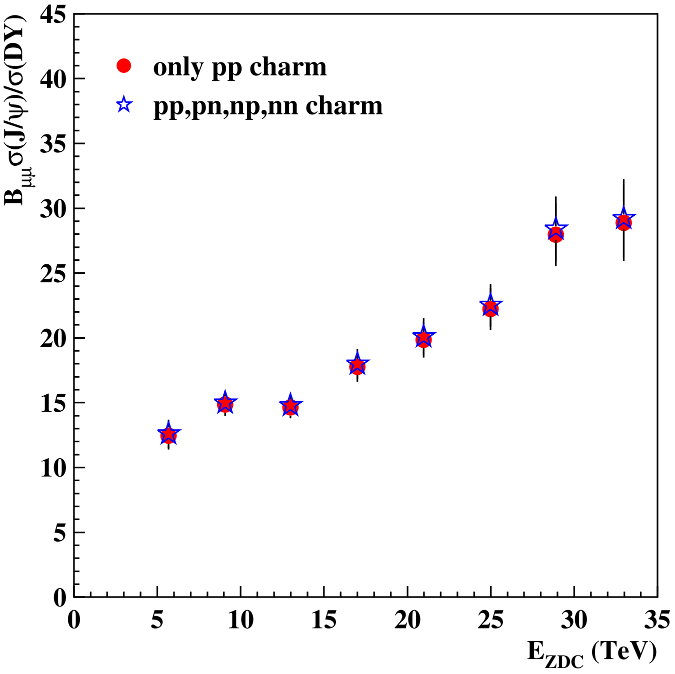

Figure 5.37: *Comparison between the $\sigma_{J/\psi}/\sigma_{DY}$ results obtained using the simulation of pp, pn, np and nn collisions or only pp collisions for the open charm contribution. The GRV LO set of PDFs has been used for the Drell-Yan, the MRS 43 set for the $D\overline{D}$. In both cases the multiplicative charmonium parametrization has been adopted.*

bution functions. The generation of $D\overline{D}$ events takes long time, since the generated muon pairs are generally outside the kinematic domain of the muon spectrometer. For this reason, although all the p–p, p–n, n–p, n–n interactions might be taken into account to correctly simulate the open charm mechanism, it has been chosen to limit to p–p interactions.

As already shown in Fig. 5.10 (right), the open charm shape that refers only to p–p collisions is comparable to the one obtained by means of the full simulation of the p–p, p–n, n–p and n–n processes, weighed considering the cross–section for each process proportional to the number of colliding nucleons.

The $\sigma_{J/\psi}/\sigma_{DY}$ results obtained in the two cases are reported in Fig. 5.37 as a function of E_{ZDC}. They confirm that no influence on the final results is due to the approximation done.

5.6.7 Different sets of PDFs

The $\sigma_{J/\psi}/\sigma_{DY}$ results reported in Section 5.5 were evaluated by means of the standard analysis method, using the GRV 92 LO set of parton distribution functions for the Drell–Yan mechanism simulation [4]. This PDF set has been used by the NA50 Collaboration in the first published analyses, while for the latest data analyses the

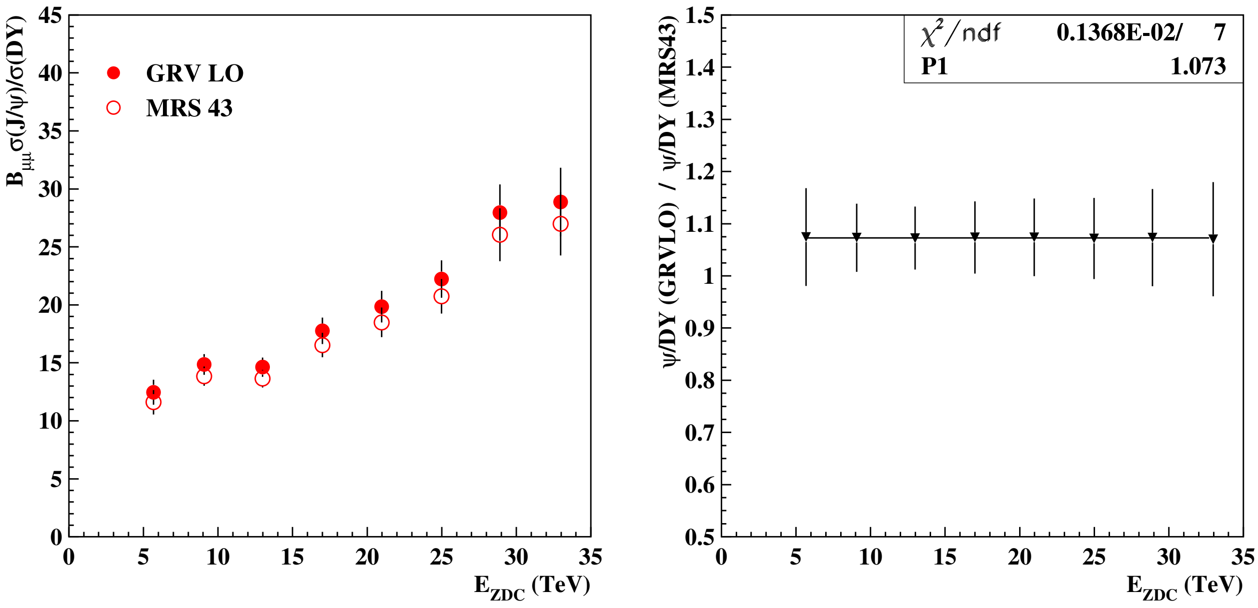

Figure 5.38: *Left: comparison between the $J/\psi/DY$ values obtained using GRV LO and MRS 43 as sets of PDFs. In both cases the multiplicative charmonium parametrization has been adopted. Right: ratio between the $\sigma_{J/\psi}/\sigma_{DY}$ values relative to GRV LO and MRS 43.*

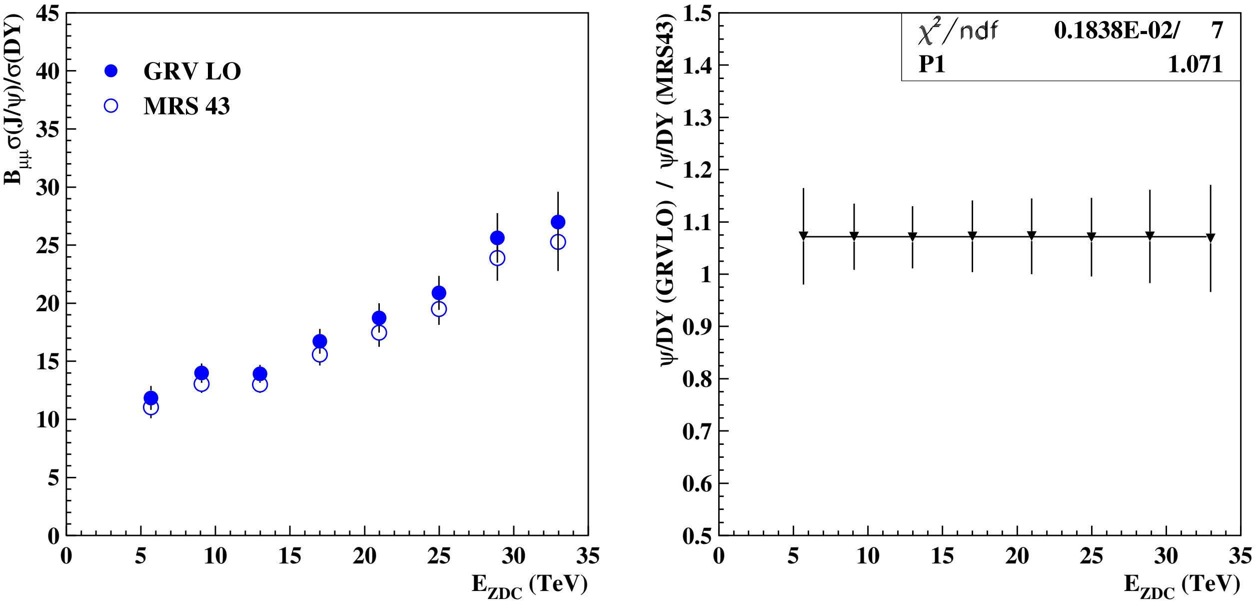

Figure 5.39: *Left: comparison between the $J/\psi/DY$ values obtained using GRV LO and MRS 43 as sets of PDFs. In both cases the additive charmonium parametrization has been adopted. Right: ratio between the $\sigma_{J/\psi}/\sigma_{DY}$ values relative to GRV LO and MRS 43.*

more recent MRS A (LQ) set [5] has been adopted, since it takes into account the $\bar{u}/\bar{d}$ asymmetry as measured by the NA51 experiment [17].

To compare the 2000 Pb–Pb data analysis results, as a function of E_{ZDC}, to the analyses of the 1996 and 1998 data [6], I have decided to make use of the same set of PDFs (GRV LO) and to check then the effect of a different choice.

In Section 5.2.1 I have already considered both the GRV LO and MRS 43 sets for the Drell–Yan simulation and also the acceptance calculation reported in Table 5.7 has taken into account both sets of PDFs.

The results, reported in Fig. 5.38 and in Fig. 5.39, respectively for the multiplicative and the additive parametrizations of the charmonium shapes, show the same J/ψ suppression pattern as a function of E_{ZDC}, although the numerical values differ of about 7%. The figures refer to a 2% P∗DTarg cut applied to the experimental data and to the simulations, but the same conclusions on the GRV LO–MRS 43 differences are drawn with a 6% or a 10% P∗DTarg cut.

As already seen in Section 5.2.1, the ratio of the DY and J/ψ acceptances, calculated using GRV LO or MRS 43 for the Drell–Yan simulation, differs by less than 1%. In particular, the $A_{DY}/A_{J/\Psi}$ values corresponding to the Drell–Yan simulated by means of MRS 43 are always lower than those obtained by means of GRV LO.

Moreover the two different sets provide slightly different shapes for the Drell–Yan

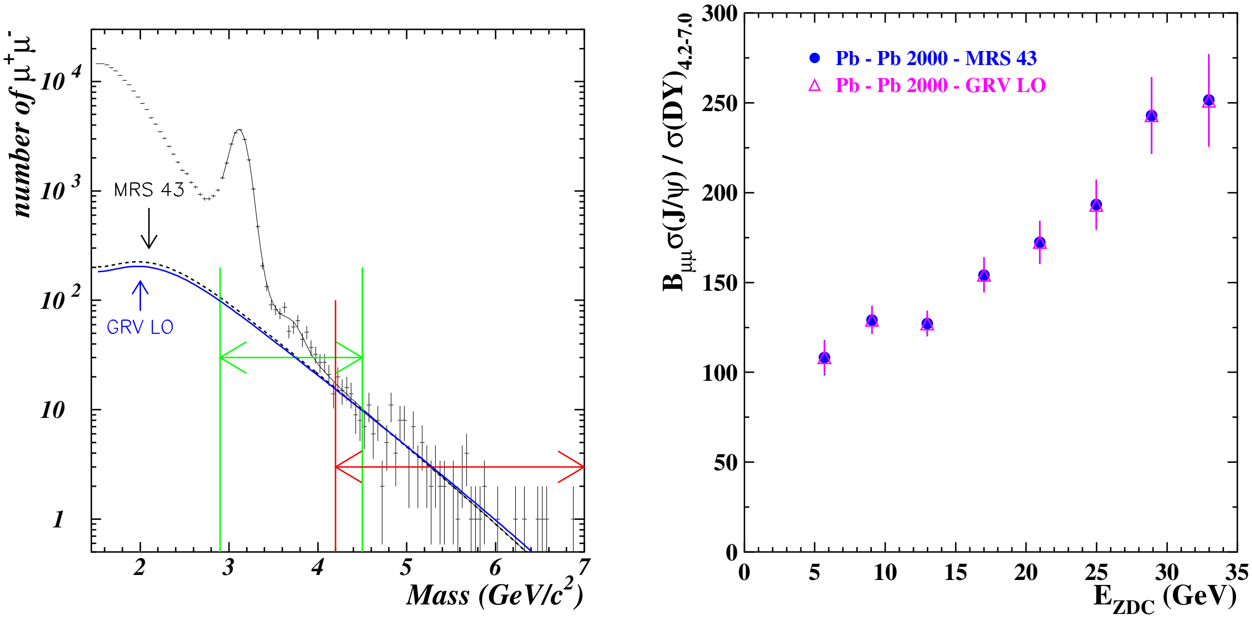

Figure 5.40: *Left: comparison of the fits to the Drell–Yan components of the dimuon invariant mass spectrum obtained using GRV LO and MRS 43. Right:* $J/\psi/DY(4.2-7.0)$ *ratios as a function of* E_{ZDC}*, with GRV LO and MRS 43 as PDFs (multiplicative charmonium parametrization).*

mass distribution, as shown in Fig. 5.3 or in Fig. 5.40 (left), where the two spectra are normalized in the region $M_{\mu^+\mu^-} \geq 4.2\, GeV/c^2$. This is the region where only the Drell–Yan mechanism contributes and, therefore, where the normalization of the Drell–Yan is fixed during the 4 step fit (see Section 5.4). From these pictures it results that the Drell–Yan mass spectrum generated by means of MRS 43 is higher than that obtained with GRV LO in the region around the J/ψ resonance peak. As a consequence, fixed the normalization of the Drell–Yan spectrum in the region above the resonances, we get different extrapolations into the mass interval $2.9 \leq M_{\mu^+\mu^-} \leq 4.5\, GeV/c^2$, which we use to report the Drell–Yan cross–sections, as a reference for the J/ψ cross–sections.

This explains the observed discrepancy (of the order of 7%) between the $J/\psi/DY$ cross–sections, if the MRS 43 or the GRV LO PDF set is used.

To overcome this problem, concerning only the normalization of the $\sigma_{J/\psi}/\sigma_{DY}$ results, a new Drell–Yan reference has been defined in the higher mass region $4.2 \leq M_{\mu^+\mu^-} \leq 7.0\, GeV/c^2$ (see Fig. 5.40 left). In the same figure (on the right) the new cross–section ratios, namely $\sigma_{J/\psi}/\sigma_{DY}(4.2-7.0)$, have been plotted as a function of E_{ZDC}. These ratios have been corrected for the acceptances, where A_{DY} now is evaluated in the mass region $4.2 \leq M_{\mu^+\mu^-} \leq 7.0\, GeV/c^2$ (see Table 5.9). The two analyses, performed with the GRV LO and MRS 43 set of PDFs, practically

	$A_{J/\psi}(\%)$	A_{DY}(4.2-7.0)(%)	$A_{DY}(4.2-7.0)/A_{J/\Psi}$
no P∗DTarg, MRS43	13.49	18.69	1.385
no P∗DTarg, GRVLO		18.94	1.404
P∗DTarg 2%, MRS43	12.69	17.30	1.363
P∗DTarg 2%, GRVLO		17.64	1.390
P∗DTarg 6%, MRS43	11.61	15.78	1.359
P∗DTarg 6%, GRVLO		15.96	1.375
P∗DTarg 10%, MRS43	10.62	14.43	1.359
P∗DTarg 10%, GRVLO		14.58	1.373
P∗DTarg 18%, MRS43	8.81	11.94	1.355
P∗DTarg 18%, GRVLO		11.92	1.353

Table 5.9: *Values of the acceptances (in %) for the J/ψ and for the Drell–Yan processes, calculated after having applied the kinematic, image, fiducial cuts and different P∗DTarg cuts on the data. The DY contribution has been generated both with MRS 43 and GRV–LO as PDFs, and its acceptance is estimated in the region* $4.2 \leq M_{\mu^+\mu^-} \leq 7.0\, GeV/c^2$.

coincide, using the new Drell–Yan reference. Of course, the conclusions on the J/ψ suppression pattern, discussed in Section 5.5, remain valid, since only the scale of the cross–section ratio has changed.

The small statistics in the region used to fix the Drell–Yan normalization reflects in a larger uncertainty on the Drell–Yan for this method and, therefore, in larger error bars for the $J/\psi/DY$ ratio.

This procedure has allowed to verify that the two different sets of PDFs give compatible results if the Drell–Yan reference is established in the high mass region where the two simulated Drell–Yan shapes coincide, and to confirm that an identical J/ψ suppression pattern is observed whatever PDF set is used and whatever region is chosen to provide the Drell–Yan reference.

Moreover, the possibility of a dependence of the open charm generation on the chosen PDF set has been taken into account. Since the processes of hadro–production of open charm are based essentially on gluon fusion, we expect that the distributions are independent of the choice of the nucleon structure functions.

The open charm simulation has been performed in Section 5.2.3 with both the PDF sets, and the reconstructed spectra, shown in Fig. 5.12, were compatible. Therefore, the final $\sigma_{J/\psi}/\sigma_{DY}$ results do not depend on the set of PDFs chosen for the $D\overline{D}$ simulation, as it is proved by the comparison reported in Fig. 5.41. For all the results the standard parametrization was adopted to fit the charmonium mass spectum, while the GRV LO parton distribution functions have been used to simulate the Drell–Yan mechanism. A 2% P∗DTarg cut has been imposed on the data.

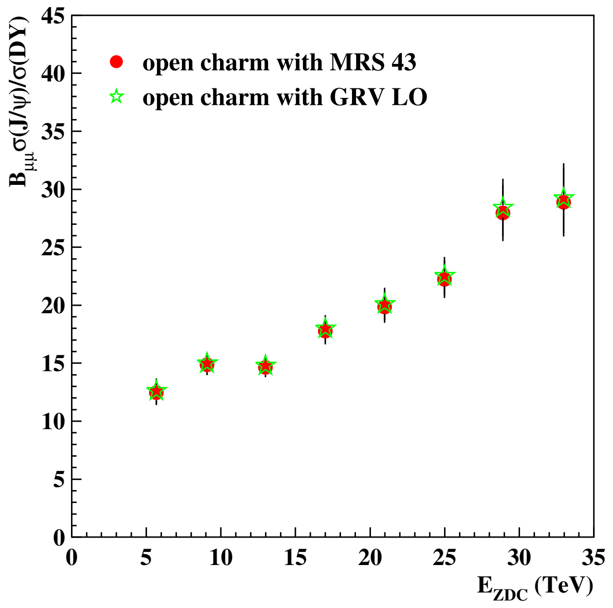

Figure 5.41: *Comparison between the $\sigma_{J/\psi}/\sigma_{DY}$ results obtained using the GRV LO and MRS 43 sets of PDFs for the open charm simulation. In both cases the multiplicative charmonium parametrization has been adopted and a 2% P∗DTarg cut has been imposed.*

5.6.8 Parametrization of the charmonium shape

In Section 5.5 the standard analysis has been performed by using the so– called "multiplicative" parametrization for the charmonium line shapes, which is the standard parametrization historically used by the NA50 Collaboration.

An alternative charmonium description ("additive" parametrization) has been recently elaborated, in order to better reproduce the tails of the J/ψ and ψ' mass distributions.

In this section I want to investigate a possible dependence of the $J/\psi/DY$ results on the chosen parametrization. The same analysis procedure adopted for the results shown in Section 5.5 has been followed, except for the charmonium line shape parametrization.

The results of the fit to the simulated J/ψ and ψ' mass spectra have been already reported in Table 5.3 and 5.5. Comparing these tables to Table 5.2 and 5.4 we can notice that the p_3 parameter, which indicates the width of the resonance, is always lower with the additive parametrization than with the multiplicative one. This produce a lowering of the $J/\psi/DY$ ratio, if the same Drell–Yan reference is used at the denominator, as it is visible in Fig. 5.42 (left), where the results obtained with the two different charmonium parametrizations are compared. In both cases the

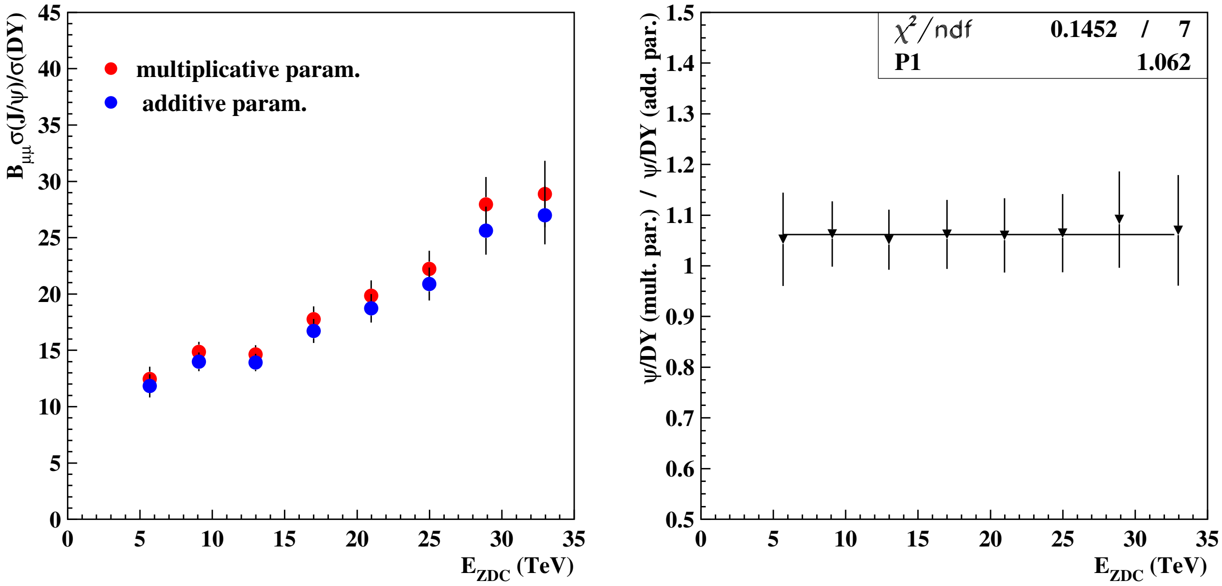

Figure 5.42: *On the left: comparison between the $\sigma_{J/\psi}/\sigma_{DY}$ results as a function of E_{ZDC} obtained using the "multiplicative" and the "additive" charmonium parametrizations. The GRV–LO set of PDFs has been adopted and a 2% P∗DTarg cut has been imposed. On the right: ratios (as a function of E_{ZDC}) between the $\sigma_{J/\psi}/\sigma_{DY}$ results relative to the "multiplicative" and the "additive" parametrizations.*

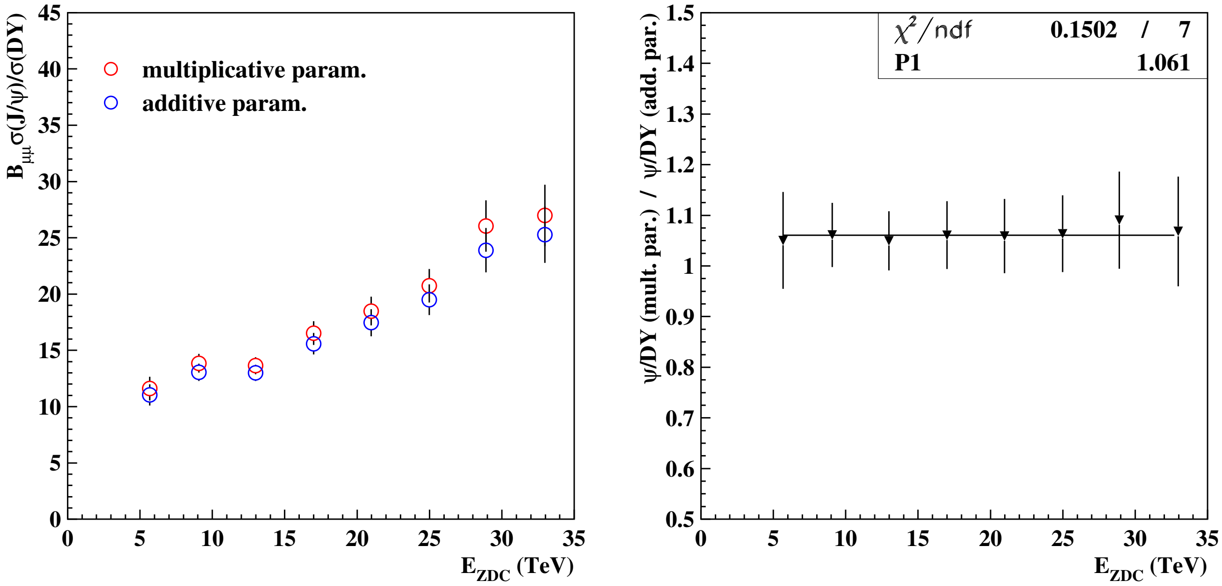

Figure 5.43: *On the left: comparison between the $\sigma_{J/\psi}/\sigma_{DY}$ results as a function of E_{ZDC} obtained using the "multiplicative" and the "additive" charmonium parametrizations. The MRS 43 set of PDFs has been adopted and a 2% P∗DTarg cut has been imposed. On the right: ratios (as a function of E_{ZDC}) between the $\sigma_{J/\psi}/\sigma_{DY}$ results relative to the "multiplicative" and the "additive" parametrizations.*

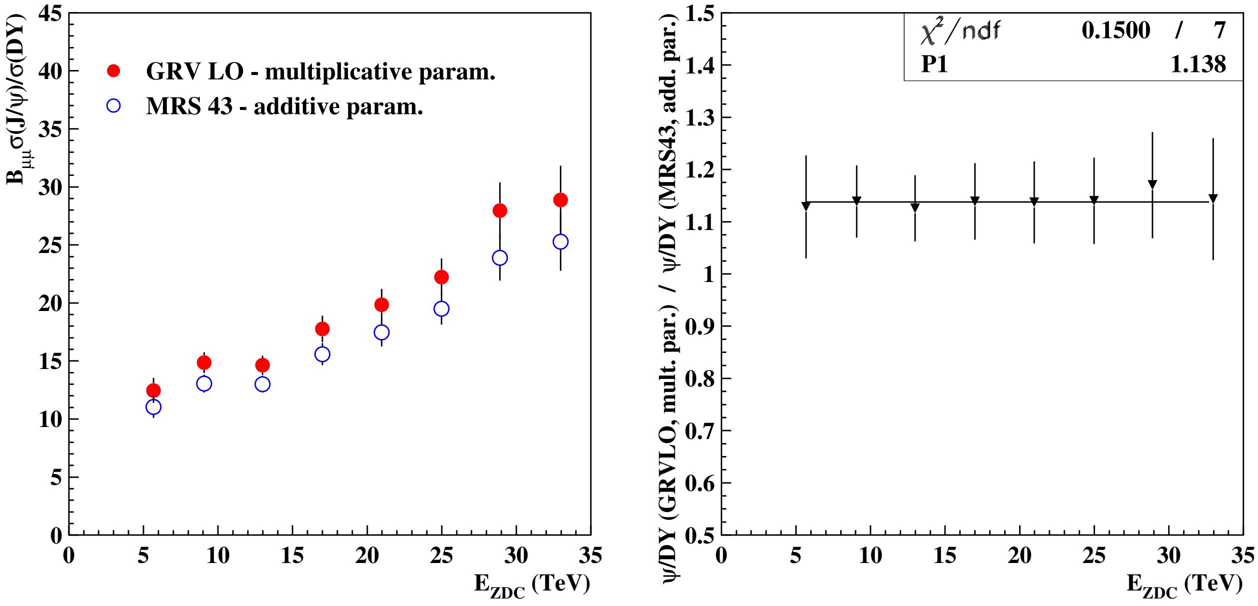

Figure 5.44: *On the left: comparison between the $\sigma_{J/\psi}/\sigma_{DY}$ results as a function of E_{ZDC} obtained using respectively the "multiplicative" parametrization and GRV–LO and the "additive" parametrization and MRS 43. A 2% P∗DTarg cut has been imposed. On the right: ratios (as a function of E_{ZDC}) between the two sets of $\sigma_{J/\psi}/\sigma_{DY}$ results.*

GRV LO structure functions have been used to simulate the Drell–Yan contribution. All the results refer to a 2% P∗DTarg cut.

The $\sigma_{J/\psi}/\sigma_{DY}$ values relative to the additive parametrization are about 6% lower than those obtained by means of the multiplicative parametrization, as it is evident in Fig. 5.42 (right), where the ratio $\sigma_{J/\psi}/\sigma_{DY}$ (multiplicative par.)/ $\sigma_{J/\psi}/\sigma_{DY}$ (additive par.) is performed. This ratio is plotted as a function of E_{ZDC} to check that the rescaling factor between the results given by the two parametrizations does not depend on the centrality of the collision. The oscillations with respect to a flat behaviour are within the error bars and can therefore be neglected.

Analogous conclusions can be drawn if the MRS 43 set of PDFs is used to simulate the Drell–Yan mechanism (Fig. 5.43).

In conclusion, the choice of the additive charmonium parametrization, which reproduce the charmonium line shapes better than the multiplicative one, affect only the normalization of the $J/\psi/DY$ results, but not the observed J/ψ suppression pattern. In order to directly compare the 2000 standard analysis results, as a function of E_{ZDC}, to the published ones [6], the same multiplicative parametrization used in the past has been adopted, but I could also have used the additive one and rescaled the results of a 6% constant factor to perform the comparison with the previous NA50 results.

Finally, in Fig. 5.44 the global effect of the charmonium parametrization and of the Drell–Yan PDFs is considered. The $\sigma_{J/\psi}/\sigma_{DY}$ ratios obtained with the multiplicative parametrization and GRV–LO (this is the situation of the published E_{ZDC} results [6]) and with the additive parametrization and MRS 43 (these are more accurate solutions, because they allow respectively to better reproduce the tails of the charmonium mass distributions and to take into account the $\bar{u}/\bar{d}$ asymmetry in the Drell–Yan simulation) are plotted as a function of E_{ZDC}. The ratio between the two sets of results indicates a difference constant with centrality and of the order of 14%.

5.7 Comparison with the E_T analysis

The NA50 experiment makes use of three detectors to measure the centrality of the Pb–Pb collisions: a zero–degree calorimeter, an electromagnetic calorimeter and a multiplicity detector (see Chapter 2). In particular, the EMC detects the neutral transverse energy of the interaction, while the ZDC gives a measure of the forward residual energy of the projectile spectator fragments. Each of these quantities is

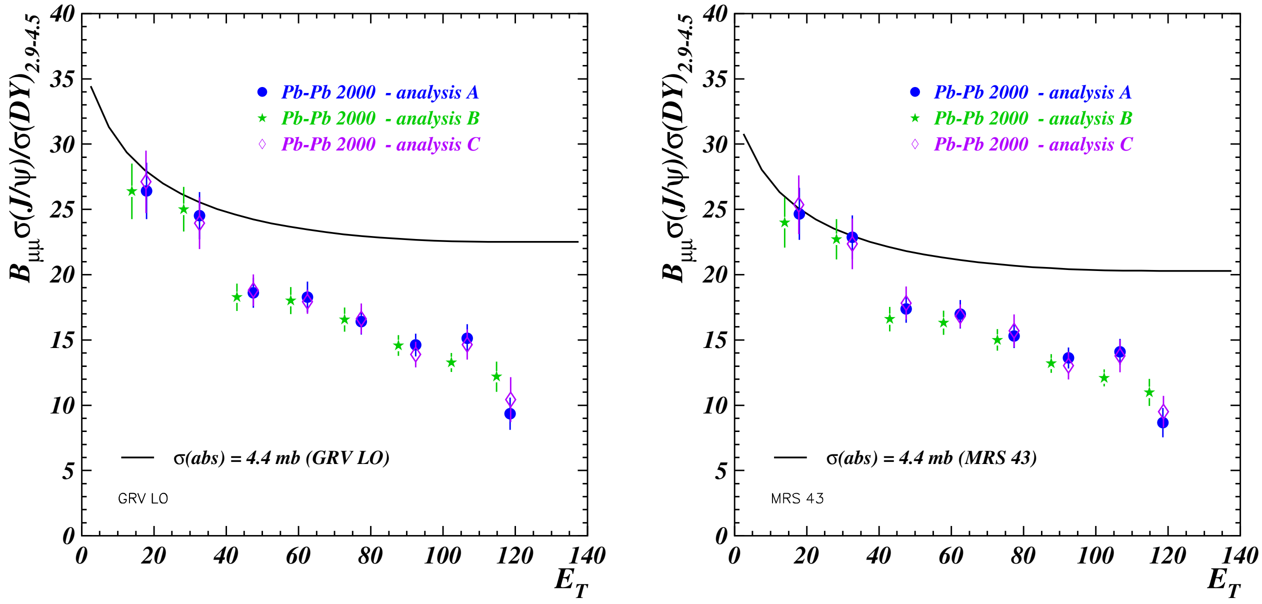

Figure 5.45: *$\sigma_{J/\psi}/\sigma_{DY}$ results obtained as a function of E_T using the GRV–LO (left) and the MRS 43 (right) set of PDFs, with the multiplicative charmonium parametrization and a 2% P∗DTarg cut. Also the normal absorption curves refer to GRV–LO (left) and MRS 43 (right).*

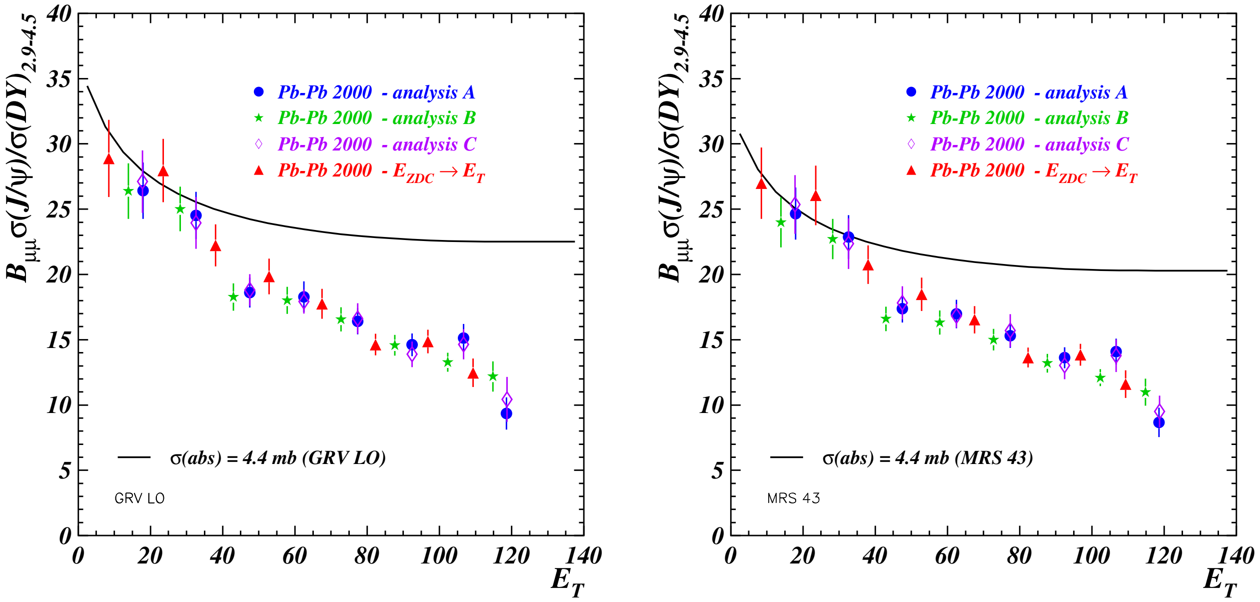

Figure 5.46: *Comparison between the $\sigma_{J/\psi}/\sigma_{DY}$ results obtained as a function of E_T and as a function of E_{ZDC} (converted to E_T), using the GRV–LO (left) and the MRS 43 (right) set of PDFs, with the multiplicative charmonium parametrization and a 2% P∗DTarg cut. Also the normal absorption curves refer to GRV–LO (left) and MRS 43 (right).*

related to the impact parameter of the collision. Actually, the number of interacting nucleons grows with centrality and, hence, also E_T increases, being proportional to the number of participant nucleons. On the opposite, the number of projectile fragments reaching the ZDC decrease with the collision centrality, and so does the forward energy E_{ZDC}.

Up to now, I have considered E_{ZDC} as a centrality estimator and I have studied the J/ψ suppression as a function of this variable. The same analysis can be repeated as a function of E_T.

For this purpose, three independent analyses of the 2000 Pb–Pb data have been performed in different laboratories collaborating to the NA50 experiment, using slightly different criteria of data selection and analysis methods [18]. I have called them analysis A, B and C and I have plotted their results in Fig. 5.45, both for GRV LO and MRS 43 as parton structure functions. The "multiplicative" charmonium parametrization has been used and a 2% P∗DTarg cut has been imposed on the experimental data. From Fig. 5.45 it emerges that all the analyses give consistent results within few %.

As already observed in the analysis performed as a function of E_{ZDC} (Section 5.6.7), the change of the PDF set affects only the normalization of the results, in the same

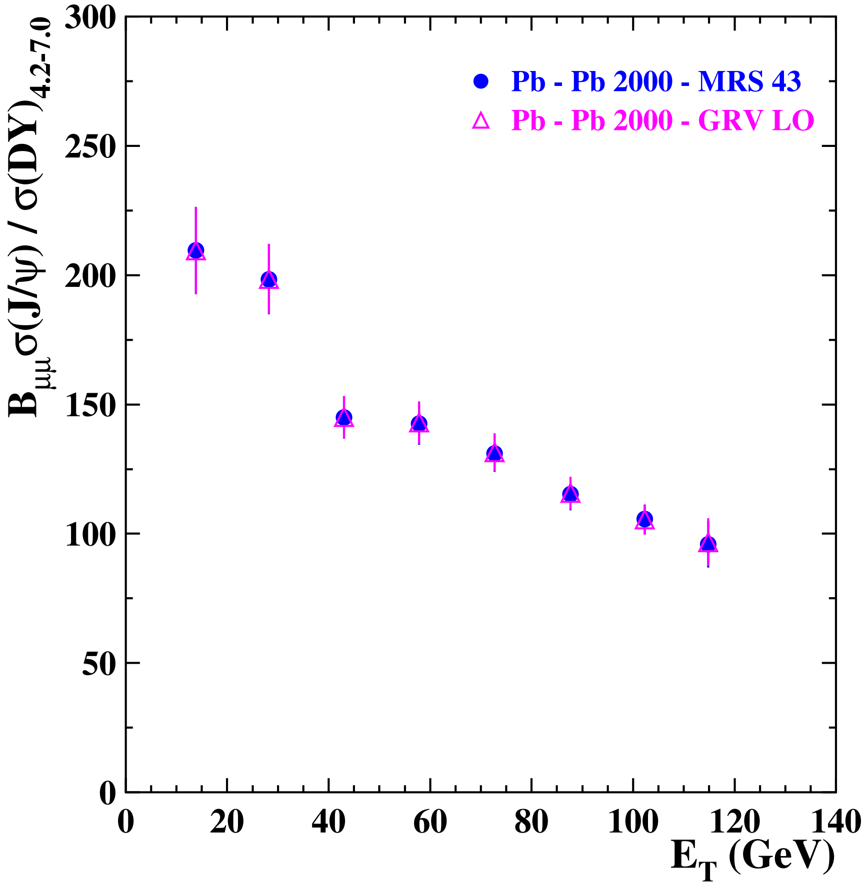

Figure 5.47: *$J/\psi/DY(4.2-7.0)$ ratios as a function of E_T, with GRV LO and MRS 43 as PDFs (multiplicative charmonium parametrization).*

way for all the centrality bins.

The continuous black line corresponds to a J/ψ normal nuclear absorption cross–section of $4.4 \pm 0.5\, mb$, obtained from the latest NA50 p–A results [19] and from previous p–p, p–d, p–A and S–U results from the NA38, NA51 and NA50 experiments [17, 20, 21] (see Section 1.8.1). In Fig. 5.45 left the normal nuclear absorption curve has been evaluated by using the GRV LO set of PDFs, while in Fig. 5.45 right the MRS 43 set has been adopted. The absorption curve is thus compatible with the $J/\psi/DY$ results in both cases.

In all the analyses the J/ψ production yield in peripheral collisions (low E_T values, which correspond to high E_{ZDC} values) follows the normal absorption curve. A departure from this curve is visible at around $E_T \sim 40\, GeV$ and no saturation is reached at high E_T (central collisions). Therefore, the J/ψ suppression pattern observed in the analyses performed as a function of E_T has the same characteristics found if E_{ZDC} is used as centrality estimator.

The consistency of the analyses as a function of E_T and E_{ZDC} is clearly visible in Fig. 5.46, where the analysis as a function of E_{ZDC} has been converted into E_T by means of the correlation between E_T and E_{ZDC} reported in Fig. 4.4. The average correlation has been used to performed such a conversion. The so–converted E_{ZDC} analysis shows a fair agreement with the three E_T analyses, within the different resolutions of the two calorimeters as a function of centrality.

This compatibility between the E_T and E_{ZDC} analyses is observed both with the GRV–LO and the MRS 43 parton structure functions, which induce on the $J/\psi/DY$ results only a change in the normalization and not in the behaviour as a function of centrality.

For the sake of completeness, I have plotted in Fig. 5.47 the results of the E_T analyses performed using GRV LO and MRS 43 as PDFs for the Drell–Yan mechanism, which is evaluated in the mass region $4.2 \leq M_{\mu^+\mu^-} \leq 7.0\, GeV/c^2$. As for the E_{ZDC} analysis, the $\sigma_{J/\psi}/\sigma_{DY}$ ratio obtained with this new Drell–Yan reference are independent of the set of parton distribution functions used for the Drell–Yan simulations.

5.8 Comparison with published results

The results obtained, as a function of E_{ZDC}, with the standard analysis method for the 2000 Pb–Pb data are now compared to the previous NA50 results [6].

Fig. 5.48 shows the $J/\psi/DY$ ratios relative to the 1996, 1998 and 2000 data taking periods. All the data have been analyzed by means of the same procedure, using the multiplicative parametrization for the fit to the charmonium mass distributions and the GRV LO set of parton distribution functions for the Drell–Yan simulation.

The solid line corresponds to a J/ψ normal nuclear absorption cross–section of $4.4 \pm 0.5\, mb$, deduced from the latest NA50 p–A results [19] and from previous p–p, p–d, p–A and S–U results from the NA38, NA51 and NA50 experiments [17, 20, 21] (see Section 1.8.1). Also the normal absorption curve refers the to GRV–LO set of PDFs, since all the experimental data used to define it have been analysed using this set of parton structure functions.

There is, in general, a good agreement between the year 2000 data and the previous results, with the exception of the most peripheral point (highest E_{ZDC} value), probably due to the contamination from Pb–air interactions in the 1996 set. In fact, a Pb ion that interacts with the air around the target, loses a small fraction of its energy and is registered by the apparatus as a peripheral event.

This problem has been solved for the 2000 data taking by using a vacuum system for the target region. Therefore, the 2000 results allow to conclude more confidently that the most peripheral Pb–Pb points lie on the ordinary nuclear absorption curve, indicating that, in these collisions at high impact parameter ($b > 8.5\ fm$), the

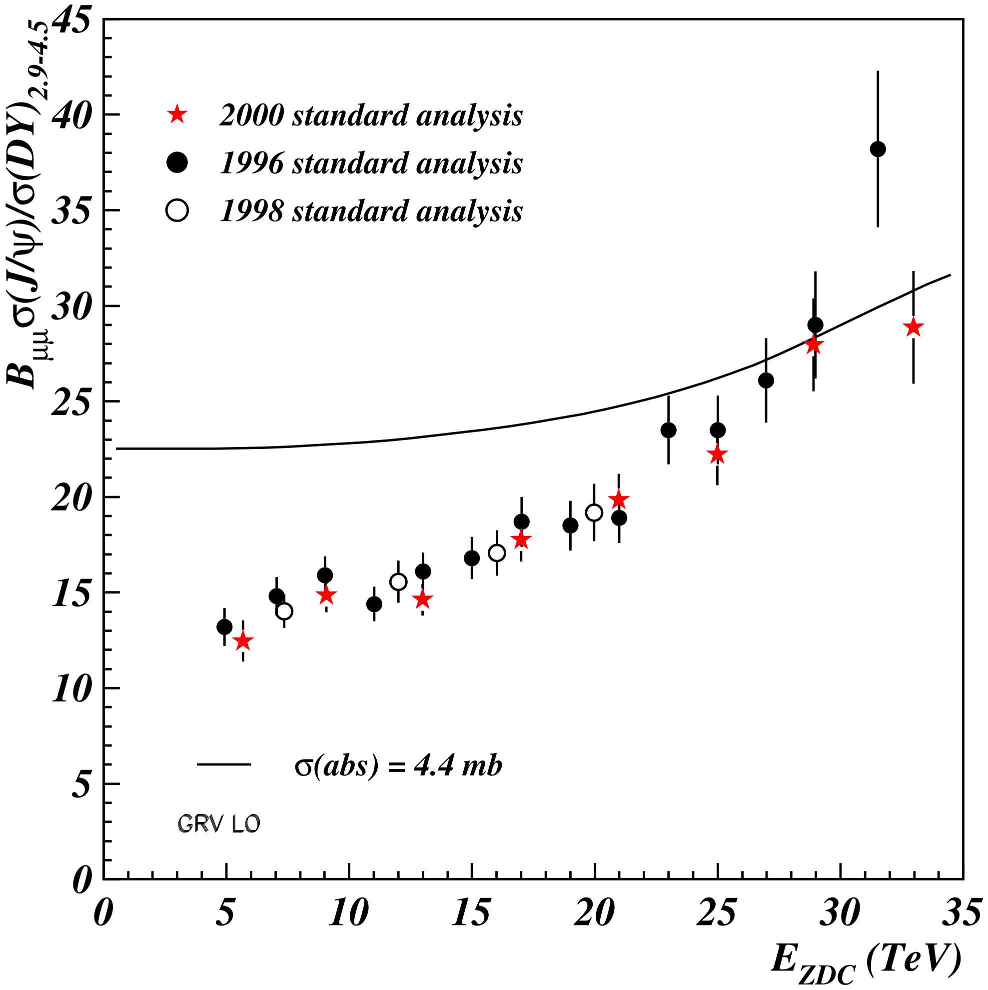

Figure 5.48: *Comparison between the $\sigma_{J/\psi}/\sigma_{DY}$ results, obtained as a function of E_{ZDC}, and the NA50 published results. The GRV–LO set of PDFs and the "multiplicative" charmonium parametrization have been used for all the analyses.*

conditions for the QGP phase transition have not yet been achieved.

In all the analyses reported in Fig. 5.48 the same J/ψ suppression pattern can be identified: a departure from the normal absorption curve is clearly visible at around $E_{ZDC} \sim 27\,TeV$ and a steady decrease is observed at low E_{ZDC} values, corresponding to the most central collisions.

In conclusion, the 2000 experimental data, collected with the purpose of investigating the most peripheral collisions and of providing a complete description of the J/ψ suppression, ranging from peripheral to central Pb–Pb collisions, have confirmed and extended the previous NA50 observations.

5.9 Conclusions

The main aim of this work was the analysis of the experimental data collected by the NA50 Collaboration at the end of the year 2000, in the frame of the J/ψ suppression study.

The suppression of the charmonium state production in ultra–relativistic nucleus–nucleus collisions is in fact considered as one of the most reliable signature of Quark–Gluon Plasma formation. Since the transition from ordinary hadronic matter to QGP can occur only if a high energy density is reached and since the energy density grows with the centrality of the collision, three centrality detectors are used by the NA50 experiment. In particular, in this thesis the J/ψ suppression pattern has been studied as a function of the energy measured by the NA50 zero–degree calorimeter, which provides a measure of the forward energy carried by the nucleons that have not interacted in the target.

The J/ψ mesons are identified in NA50 through their decays into opposite–sign muons. Since the probability of producing a resonance that decays in a muon pair is very low (the charmonium production cross–section is $\sigma_{J/\psi}$/nucleon $\sim 30\ nb$ and the branching ratio for the J/ψ in the $\mu^+\mu^-$ channel is $\sim$6%), a high beam intensity (about $1.3 \cdot 10^7$ Pb/s) has been used, in order to increase the number of nucleus–nucleus collisions per second.

Previous NA50 measurements have shown a decreasing pattern of the J/ψ production yield from peripheral to central Pb–Pb collisions, with a clear departure from the "ordinary" nuclear absorption curve, fixed by means of collisions ranging from p–p to central S–U collisions (NA38, NA51 and NA50 measurements).

The year 2000 data taking was performed to extend the previous knowledge about the suppression mechanism of the charmonium states to very peripheral Pb–Pb interactions. For this reason, a vacuum system has been designed for the target region, in order to reduce the contamination from Pb–air interactions, which produce a bias expecially on the peripheral events.

Moreover a thin target was used to reduce the probability to have reinteractions of the secondary particles produced in the collision, which can bias the results relative to the most central collisions.

The improved experimental conditions have allowed to refine the $\sigma_{J/\psi}/\sigma_{DY}$ results, which turn out to be fully compatible with the previous NA50 published results, except for the most peripheral points, which are now more confident thanks to the adopted target vacuum system.

The J/ψ suppression pattern observed in the past, as a function of E_{ZDC}, has been confirmed by the 2000 Pb–Pb results: the most peripheral $J/\psi/DY$ points lie on the "normal" nuclear absorption curve, determined by new more accurate and high statistics p-A data, together with previous p–p, p–d, p–A and S–U results from the NA38, NA51 and NA50 experiments. A departure from this curve is observed at around $E_{ZDC} \sim 27\,TeV$ and no saturation is reached at low E_{ZDC}

values, corresponding to the most central collisions.

The comparison between the analyses performed using the information of the electromagnetic calorimeter as centrality estimator and the results as a function of E_{ZDC} shows a full consistency of these two kinds of analysis, within the different resolutions of the two detectors as a function of centrality. The J/ψ suppression pattern observed in the analyses performed as a function of E_T has the same characteristics found if E_{ZDC} is used to estimate the centrality of the collision.

In order to check the stability of the year 2000 standard analysis results, various controls have been done to demonstrate the independence of the $J/\psi/DY$ values from the followed analysis procedure, from the selection and cleaning cuts applied to the data, from the parametrizations used to simulate the different processes that can produce opposite–sign muons in the same mass interval of the charmonium states, etc.

The apparent dependence on the set of parton distribution functions adopted in the simulation of the Drell–Yan mechanism, is solved if a new mass region is chosen to provide the Drell–Yan reference, with respect to which the J/ψ production yield is evaluated. In any case, the effect of the choice of different PDF sets does not influence the conclusions on the J/ψ suppression pattern, but affects only the normalization of the $J/\psi/DY$ ratio.

Also the parametrization used to reproduce the mass spectrum of the charmonium states acts on the scale of the cross–section ratio, but does not influence the behaviour of the $\sigma_{J/\psi}/\sigma_{DY}$ results as a function of E_{ZDC}.

In conclusion, the 2000 data taking, performed with the purpose of investigating the most peripheral collisions and of providing a complete description of the J/ψ suppression, ranging from peripheral to central Pb–Pb collisions, has allowed to confirm and extend the previous NA50 observations, showing a departure, at about $b \sim 8.5\ fm$, from the nuclear absorption reference, as expected in case of Quark Gluon plasma formation.

Bibliography

[1] DIMUJET USER GUIDE 2.00/02 (1997).

[2] T.Sjostrand, Pythia 5.7 and Jetset 7.4 (1993).

[3] DIMUREC USER GUIDE 2.00/02 (1997).

[4] PDFLIB 7.09, Users's Manual, CERN/PPE (1997).

[5] A.D.Martin et al., Phys. Lett. B 306 (1993) 145.

[6] M.C.Abreu et al. (NA50 coll.), Phys. Lett. B 521 (2001) 195.

[7] P.Bordalo et al., Phys. Lett. B 193 (1987) 368.

[8] Review of particle physics, Phys. Rev. D 66 (2002) 010001.

[9] A.Borhani, PhD thesis, April 1996, Ecole Politechnique, Paris.

[10] R.Arnaldi, PhD Thesis, Universitá di Torino, 2000.

[11] P.Braun–Munzinger et al., CERN–PPE/97–65 (1997) submitted to Z. Phys. C.

[12] C.Soave, PhD Thesis, December 1998, Universitá di Torino.

[13] M.C. Abreu et al. (NA50 coll.), European Physics Journal C14 (2000) 443.

[14] M.C.Abreu et al. (NA50 coll.), Nucl. Phys. A 610 (1996) 331c.

[15] R. J. Glauber, Lectures in Theoretical Physics, edited by W.E. Brittin and L.G. Dunham (Interscience, NY, 1959), Vol. 1, p 315.

[16] R.Arnaldi et al., Nucl. Instr. and Meth. in Phys. Res. A 411 (1998) 1.

[17] M.C.Abreu et al. (NA51 coll.), Phys. Lett. B 438 (1998) 35.

[18] M.C.Abreu et al. (NA50 coll.), Proceeding of Quark Matter 2002, Nantes, submitted to Nucl. Phys. A (2002)

[19] M.C.Abreu et al. (NA50 coll.), Proceeding of Quark Matter 2002, Nantes submitted to Nucl. Phys. A (2002)

[20] M.C.Abreu et al. (NA38 coll.), Phys. Lett. B 449 (1999) 128.

[21] M.C.Abreu et al. (NA38 coll.), Phys. Lett. B 466 (1999) 408.

Chapter 6

Fission

6.1 Introduction

As I have discussed in the previous chapters, the main aim of the NA50 experiment at the CERN SPS is the study of the J/ψ and ψ' suppression as a signal of Quark Gluon Plasma formation. In parallel with these studies, the NA50 Collaboration has investigated the fission of ^{208}Pb projectiles at 40 and 158 GeV/c per nucleon on different targets. For this purpose, a Cerenkov quartz detector was added to the standard NA50 set–up to measure the charge of the fragments emitted by the projectile after its interaction in the target.

In heavy–ion collisions at ultra–relativistic energies, fission can be due both to electromagnetic and nuclear processes. At large impact parameters (greater than the sum of the projectile and the target nuclear radii) only the long–range Coulomb force plays a role. The exchange of an energetic virtual photon may lead to the excitation of the Pb–projectile and to its subsequent decay in the fission channel. For smaller impact parameters the interaction is dominated by the strong nuclear force and the fissile projectile, after its de–excitation by nucleon emission, can undergo fission.

The fission of 158 AGeV/c ^{208}Pb–projectiles impinging on a 12 mm thick ^{nat}Pb target was already observed by NA50 in an experimental measurement performed in 1996 and published in [1]. Although the yield of the observed fission events was roughly consistent with the one expected in case of Coulomb fission, no firm conclusion on the fission mechanism could be drawn from this single data point.

More light on the contributions of the nuclear and the electromagnetic mechanisms to the fission cross–sections is expected to be shed by measurements on different target nuclei at different incident energies, since the dependence of the fission cross–section as a function of the incident energy and of the target nucleus mass (or charge) are different for the two mechanisms. For this reasons, in 1998 and 1999 other fission data of *Pb* projectiles has been collected respectively at 158 and 40 AGeV/c on different target nuclei: C, Al, Cu, Ag, Pb. This data is analyzed here and the results are reported in the following.

After a brief description of the experimental setup modifications with respect to the standard NA50 apparatus described in Chapter 2, I will discuss the fission mechanisms and, in particular, I will hint at the Weizsäcker–Williams model for the electromagnetic fission cross–section. The contributions to the fission arising from the nuclear and the electromagnetic fission mechanisms will be extracted from the measured cross–sections, according to a model–dependent analysis. The electromagnetic contributions will be then compared to the predictions of the Weizsäcker–Williams model [2].

6.2 Experimental apparatus

The first fission measurement has been performed by the NA50 Collaboration in 1996, in parallel to the main NA50 acquisition [1]. The experimental setup has been equipped with a Cerenkov Fragment Detector (FD) to provide information on the charge of the spectator fragments emitted by the projectiles after the interaction

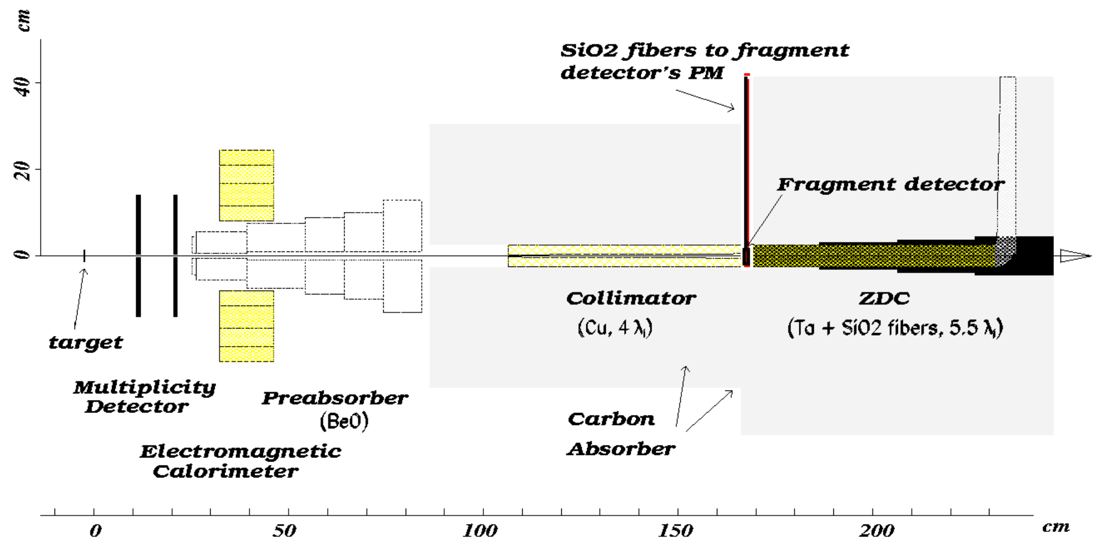

Figure 6.1: *NA50 experimental apparatus in the target and hadron absorber region, with the insertion of the fragment detector.*

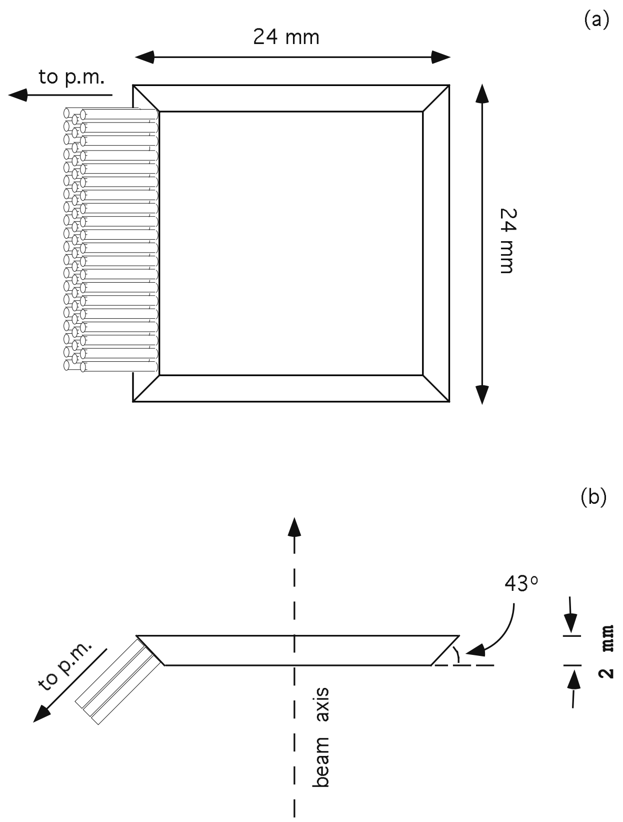

Figure 6.2: *Structure of the fragment detector. a) Front view (the beam enters into the drawing); b) top view. For the sake of a clear presentation only a sample of the quartz fibres is shown and the fibre diameter is not in scale with respect to the quartz blade.*

with the target nuclei.

Since the experimental conditions are optimized for the charmonium detection and not for the fission study, the FD has been designed to operate at the high beam intensity used by NA50 (10^7 Pb ions/sec). For this reason, the FD has to be radiation resistant (doses of several Grad are released during the NA50 data taking periods, as seen in Section 3.4.3) and to be able to produce fast signals in order to reduce pile–up problems.

Moreover, its dimensions are limited from the only place available for its insertion, inside the hadron absorber, on the beam trajectory and just in front of the ZDC (see Fig. 6.1).

The solution to all these requirements is a quartz Cerenkov detector whose structure is shown in Fig. 6.2. It consists of a blade made of SiO_2 suprasil, shaped as a truncated pyramid 2 mm thick ([1]). The trajectory of the beam and of the nuclear fragments is orthogonal to the pyramid bases (about 20×20 mm^2 in area). The

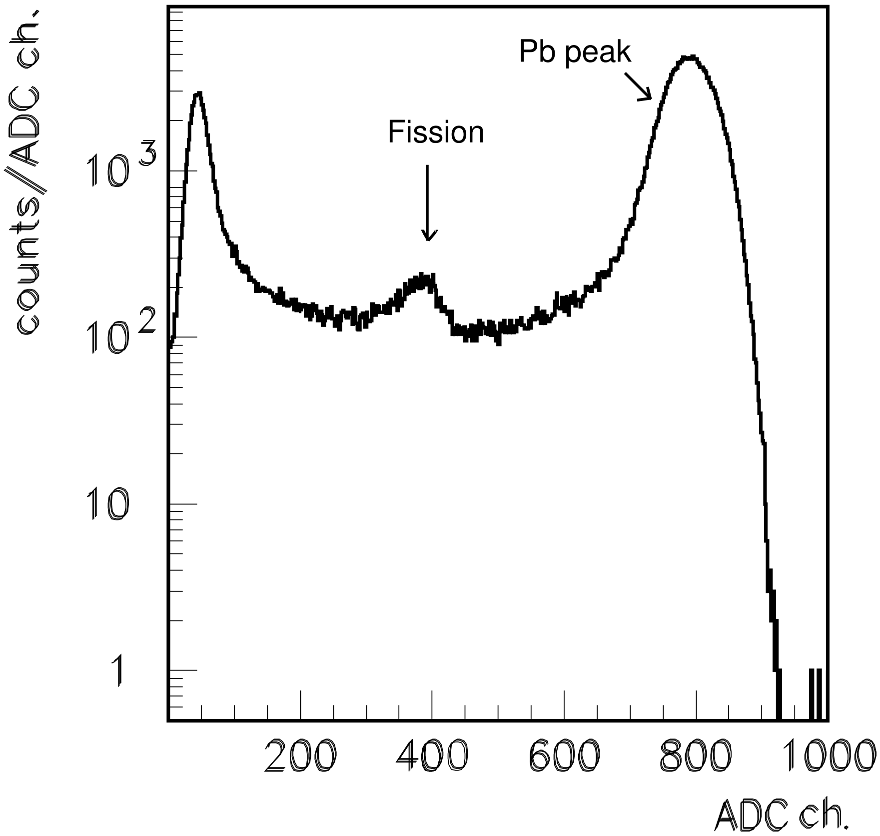

Figure 6.3: *Light output (ADC channels) measured in 1996 by the fragment detector in Pb–Pb collisions at 158 AGeV/c [1].*

Cerenkov light produced by the shower particles in the blade is totally reflected on both its bases and is collected in quartz optical fibres (about 80 cm long) up to the photomultiplier (*Philips XP2242*, 6 stages). The quartz fibres resist high radiations and allow to have fast signals to minimize pile–up.

The signal of the quartz blade photomultiplier is amplified, then sent to a linear gate module and finally integrated by an ADC. The information provided by the FD, together with that coming from the other detectors of the experiment, is read out and recorded by the general acquisition system.

The angular acceptance of the fragment detector is determined by the collimator (placed before the ZDC), which has an angular aperture of 3.3 mrad, corresponding to a 7 mm radius hole on the ZDC front face. A simulation of the fragment detector shows that inside this central region the response of the detector is constant within fluctuations of 1%, due to the dead space between the fibres.

The aperture of the collimator is large enough to ensure the detection of the projectile spectators, including the fission fragments, which are emitted at angles smaller than $1mrad$ with respect to the beam axis. Therefore, since the yield of the

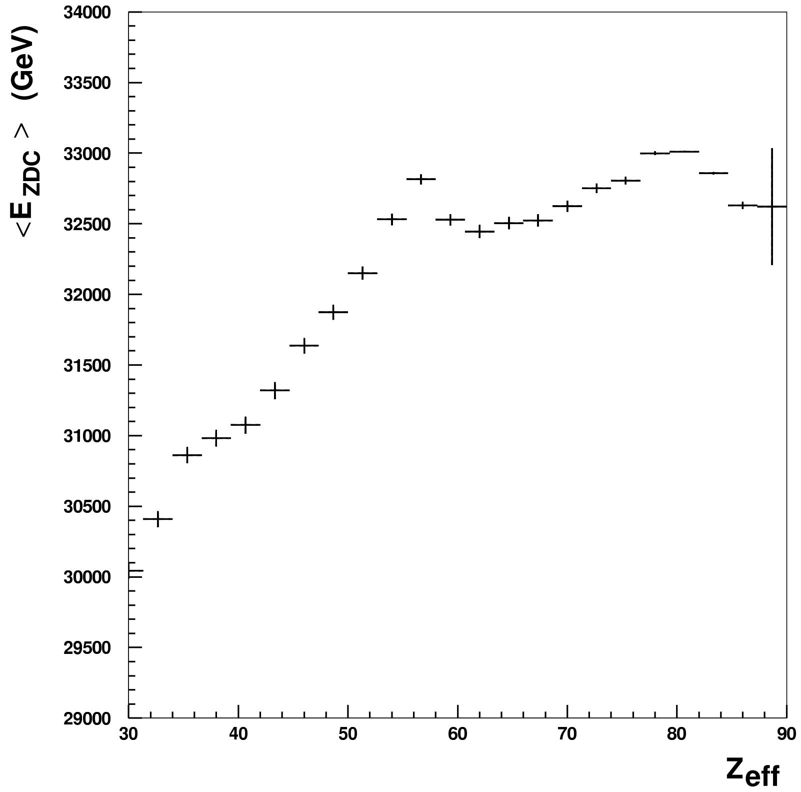

Figure 6.4: *Mean value of the ZDC energy ($\langle E_{ZDC}\rangle$) per bin of Z_{eff}, plotted as a function of Z_{eff}.*

Cerenkov light is proportional to the squared charge of the particle, the quantity measured by the FD is the sum of the squared charges of the fragments emitted in the decay of the projectile (ΣZ_i^2, where Z_i is the charge of the i-th fragment).

In Fig. 6.3 a typical ADC spectrum of the fragment detector is shown. This spectrum represents the first NA50 evidence of the fission mechanism, observed in 1996 in the interaction of a ^{208}Pb beam at 158 AGeV/c with a 12 mm thick Pb target [1]. In the figure a peak is visible at channel 800, corresponding to the incoming lead ions that have not interacted in the target. Indeed this peak is also populated by events where the incident Pb ions have lost one or more neutrons, mainly by electromagnetic interaction.

A second peak, centred at channel 400, has been interpreted as a signal of symmetric or quasi–symmetric binary Pb fission. In this case, in fact, a peak of the ADC spectrum is expected at $\Sigma(Z_i)^2 = 2(Z_{Pb}/2)^2 = (Z_{Pb})^2/2$, which is half the Pb peak.

The fission measurement performed in 1996 by the NA50 experiment has underlined the fact that fission occurs only in extremely peripheral collisions [1]. In Fig. 6.4 the mean value of the forward energy measured by the ZDC, $\langle E_{ZDC}\rangle$, is displayed as a function of the effective charge Z_{eff}, defined as $Z_{eff} = \sqrt{\Sigma Z_i^2}$ and normalized so that the value for the beam is $Z_{eff} = 82$. The peak of the non–interacting Pb ions corresponds to $\langle E_{ZDC} \rangle = 33\,TeV$.

The fission peak is visible in the region $50 \leq Z_{eff} \leq 62$. Outside this region, $\langle E_{ZDC} \rangle$ increases monotonically with Z_{eff}, suggesting that the continuum is mainly due to nuclear interactions , in which lighter fragments (smaller values of Z_{eff}) are more likely emitted at low impact parameters (smaller values of E_{ZDC}).

In Fig. 6.4 is also clearly visible the deviation from the continuum in correspondence of the fission events, represented by a sudden $\langle E_{ZDC} \rangle$ bump. This means that the continuum is due to collisions less peripheral than those leading to fission. Besides, the fission events reach a $\langle E_{ZDC} \rangle$ value very close to the one of the non–interacting Pb ions.

In conclusion, this first observation of the fission has provided an indication that fission is expected to occur in extremely peripheral collisions.

6.3 Run conditions

Although the apparatus used for the measurements reported in this chapter was basically the same as the one of the 1996 fission run and of the standard NA50 runs (see Chapter 2), the experimental conditions were quite different. In fact, while the 1996 fission data has been taken in parallel to the standard NA50 runs, (i.e. in conditions suitable for the charmonium suppression study), in 1998 and 1999 the fission mechanism was studied during two short and dedicated runs with thinner targets (1–4 mm) and at lower beam intensity (few times 10^5 Pb–ions per burst).

These experimental conditions allow to avoid pile–up corrections and to minimize the contributions to the fission due to projectiles different from ^{208}Pb, as lighter Pb isotopes and heavy nuclei produced mainly by EM dissociation of the beam in the target.

In table 6.1 the targets used in the 1998 and 1999 fission runs are summarized, together with their material characteristics.

The use of several targets of different material allows to study the dependence of the fission cross–section (both the electromagnetic and the nuclear contributions) on the target atomic number and to compare the results with the theoretical predictions.

In order to reduce the contamination of Pb–air interactions, a new target system under vacuum has been realized for the 1999 data taking, as described in Section 2.3. Unlike in the year 2000, where a tube extends the vacuum region up to the multiplicity detector, including the BeO preabsorber and thus reducing the distance that the incoming particles cover in air, the 1999 vacuum system includes only the target region.

The targets are mounted on a support that can rotate and be monitored on–line, allowing to change the target without directly access to the experimental apparatus.

Moreover, a different trigger strategy with respect to the 1996 run was adopted to speed up the data taking. In 1996, the data acquisition was enabled by the ZDC trigger, generated whenever an energy larger than a given threshold E_{th} is deposited in the ZDC. Since even in the most central collisions a residual energy $E_{min} \sim 2 \div 3\ TeV$ is emitted in the acceptance of the ZDC and since the threshold value was chosen in such a way that $E_{th} < E_{min}$, the ZDC trigger allows to collect an *unbiased* sample of events, ranging from the central collisions to the non–interacting Pb–ions.

In the analysis of the 1996 data, the fission cross–section was directly deduced from the *unbiased* light output distribution of the fragment detector, shown in Fig. 6.3, by computing the ratio between the number of events in the fission peak and the total number of events in the histogram (see [1] for more details). It is clear that this approach, based on the ZDC trigger only, imposes severe limitations on the statistics achievable for the fission events. In fact, even at low beam intensities, the acquisition system is saturated by the high rate of the non–interacting Pb projectiles which, as it can be seen in Fig. 6.3, dominate the sample of events collected with the ZDC trigger, while only a small fraction corresponds to fission events.

To increase the fission sample, in the 1998 and 1999 data takings, besides the ZDC trigger, a second one, called ZDC–VETOED trigger, was also used. This trigger is generated by requiring, in coincidence with a ZDC trigger, a signal from the fragment detector with amplitude smaller than the one of the non–interacting beam. This way, the Pb–ions that did not interact in the target are rejected, as it will be presented in Fig. 6.6, where the light output distributions recorded with this trigger on different targets are shown.

1998 - 158 AGeV/c

target	thickness	Z	A	density (g/cm^3)
C	4 mm	6	12.01	2.26
Al	3 mm	13	26.98	2.70
Cu	1 mm	29	63.55	8.96
Ag	1 mm	47	107.87	10.50
Pb	4 mm	82	207.19	11.35

1999 - 40 AGeV/c

target	thickness	Z	A	density (g/cm^3)
C	4 mm	6	12.01	2.26
Cu	3.2 mm	29	63.55	8.96
Ag	3 mm	47	107.87	10.50
Pb	3 mm	82	207.19	11.35

Table 6.1: *List of the main characteristics of the targets used during the 1998 and 1999 fission runs: material, thickness, atomic number, mass number and density.*

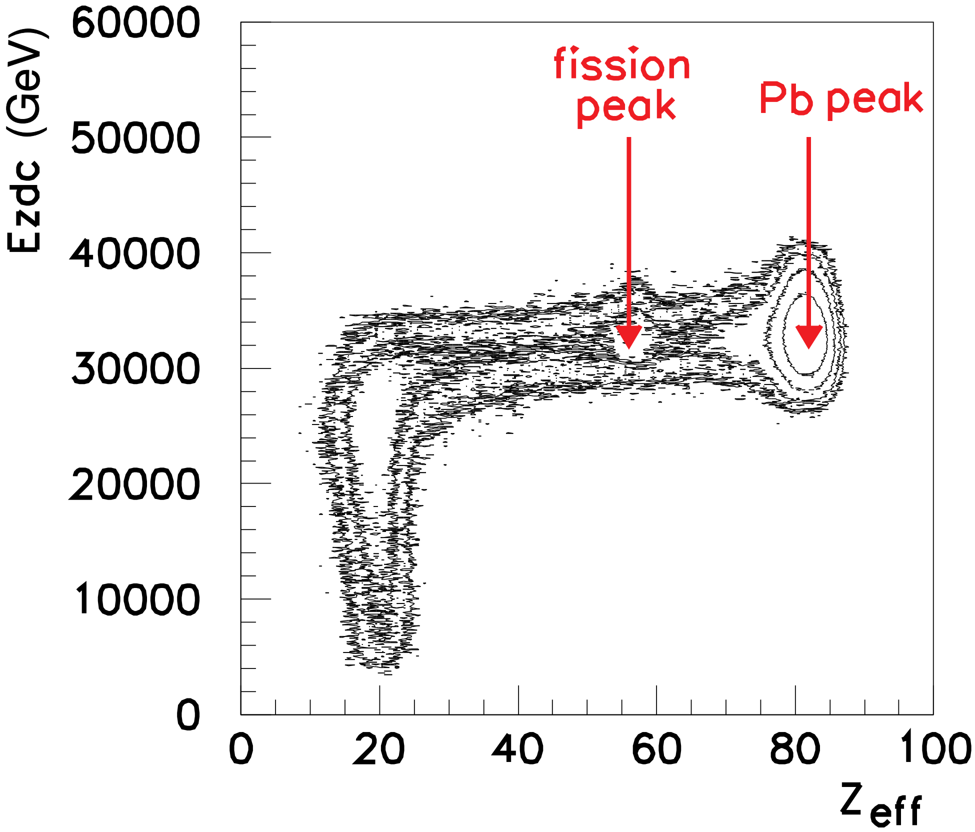

Figure 6.5: *Correlation between the energy measured by the ZDC and the Z_{eff} variable estimated from the fragment detector.*

It is important to underline that the fragment detector, rather than the ZDC, has been used to perform such a rejection. This is due to its better resolution for Pb–ions (4% for the fragment detector, 7% for the ZDC) and to the fact that, for extremely peripheral collisions, the quantity $Z_{eff} = \sqrt{\Sigma Z_i^2}$, measured by the fragment detector, is more sensitive to the impact parameter than the zero–degree energy measured by the ZDC (see [1]). This is clearly visible in Fig. 6.5, where the correlation between E_{ZDC} and Z_{eff} is shown. In the ZDC spectrum the signals corresponding to fission events and to non-interacting Pb ions are superimposed, since the fission fragments have nearly the same energy as the beam, while in the Z_{eff} scale the Pb peak and the fission peak are visibly separated. Therefore, with the fragment detector, it is easier than with the ZDC to choose a threshold value above which to cut the non–interacting Pb ions.

During the 1998 and 1999 fission measurements, which are the object of this chapter, about one million events were collected for each target.

6.4 Data analysis and experimental results

Fig. 6.6 shows the ADC spectra of the fragment detector in Pb–C and Pb–Pb interactions at 40 and 158 AGeV/c, obtained by means of the ZDC–VETOED trigger (where the statistics for fission events is higher and the non–interacting Pb peak is not visible).

All the spectra are subtracted of the pedestal contribution, according to a pro-

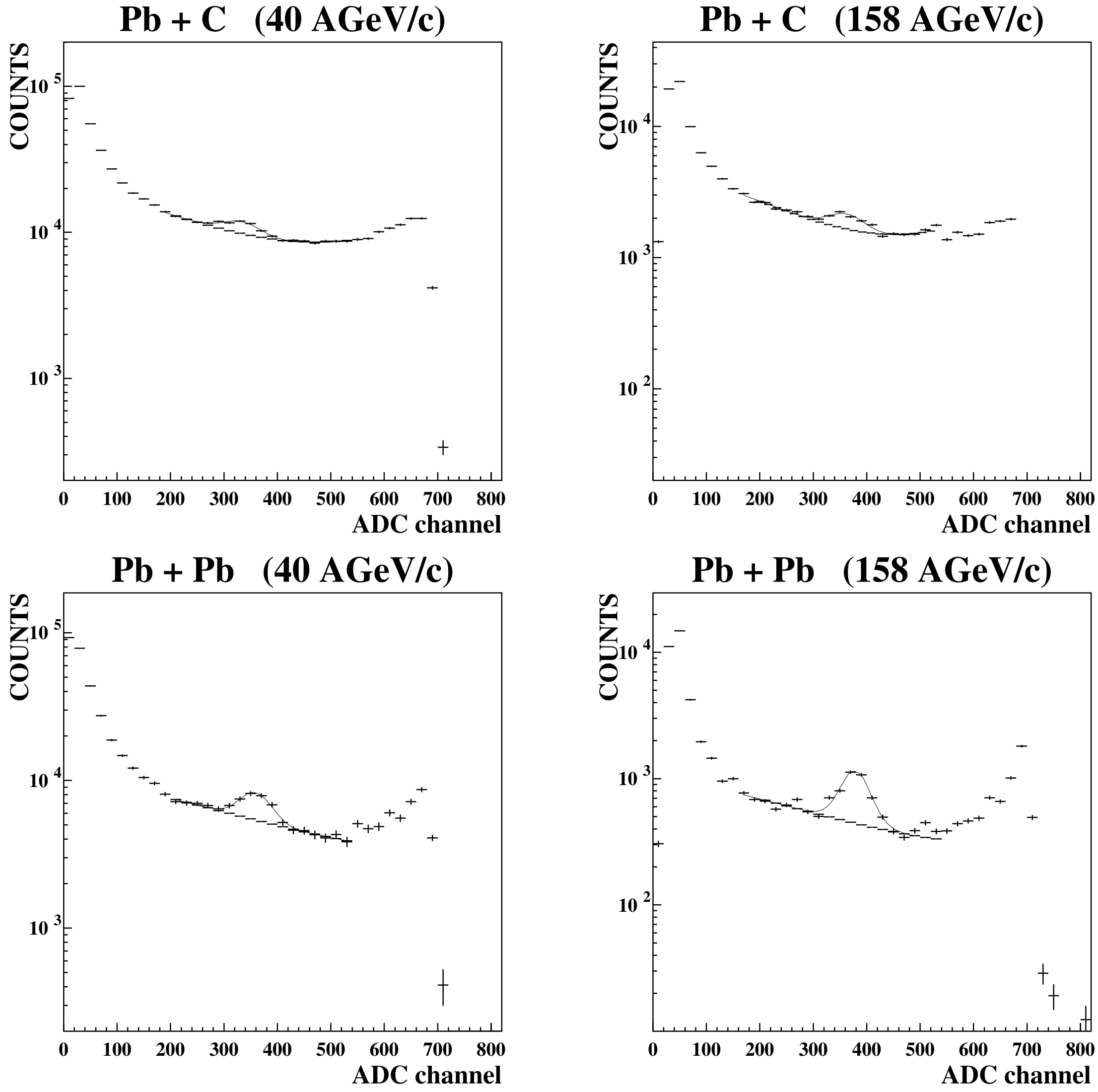

Figure 6.6: *Light output (ADC) measured by the fragment detector for the C (top) and the Pb target (bottom) at 40 (left) and 158 AGeV/c (right). The solid line is the fit to the fission peak, the dotted line is the fit to the continuum lying under the fission peak.*

158 AGeV/c			40 AGeV/c		
target	thickness	empty/full	target	thickness	empty/full
C	4 mm	63%	C	4 mm	58%
Al	3 mm	75%			
Cu	1 mm	84%	Cu	3.2 mm	62%
Ag	1 mm	85%	Ag	3 mm	66%
Pb	4 mm	65%	Pb	3 mm	74%

Table 6.2: *Ratio (in %) between the number of events in the empty target runs and in the correspondent runs with targets, for the different targets at 40 and 158 AGeV/c.*

cedure similar to the one described in Section 3.4.1. Moreover, the *empty target* contribution, i.e. the contribution from those fission events formed in the air before and after the target, has been evaluated in special *empty target* runs, with no target placed on the beam trajectory. The *empty target* contribution in the fission region of the spectrum ranges from about 60% to 85%, depending on the target thickness (Table 6.2). Also in 1999, when a vacuum system has been adopted for the target region, the *empty target* contribution is not negligible, since the lead ions still travel along 160 cm of air between the target and the fragment detector.

In order to extract from the ADC spectra of the fragment detector the number of fission events, the fission peak and the underlying continuum have been fitted simultaneously with a second order polynomial plus a variable width gaussian function:

$$y_{fit} = a_1 + a_2 \cdot x + a_3 \cdot x^2 + a_4 \cdot e^{-\frac{1}{2}(\frac{x-a_5}{\sigma})^2} \tag{6.1}$$

where

$$\sigma = a_6 + a_7 \left| \frac{x - a_5}{a_5} \right| \tag{6.2}$$

The polynomial provides an estimation of the background under the fission peak, while the gaussian fits the peak itself.

The variable width gaussian takes into account the asymmetry of the fission peak distribution, which is always more populated in correspondence of the ADC channels lower than the mean value. This tail indicates the presence of events where the sum of the two fragment charges is smaller than the charge of the ^{208}Pb projectiles. These events can be due to the fission of nuclei lighter than ^{208}Pb, or to fissions followed by the emission of light charged particles.

The results of the fit are superimposed to the spectra reported in Fig. 6.6: the solid line represents the gaussian fit to the fission peak, while the dotted line is the fit to the background lying under the fission peak.

The number of fission events n_f is then obtained by integrating the fission peak,

	$\sigma_f(mb)$ - 40 AGeV/c	σ_f (mb) - 158 AGeV/c
C	27.8 $\pm$ 2.6	30.0 $\pm$ 3.0
Al		56.0 $\pm$ 5.0
Cu	49.1 $\pm$ 5.0	77.0 $\pm$ 11.0
Ag	60.1 $\pm$ 5.3	129.0 $\pm$ 14.0
Pb	120.5 $\pm$ 9.5	332.0 $\pm$ 19.0

Table 6.3: *Experimental fission cross–section values at 40 and 158 AGeV/c.*

after background subtraction. The fission cross–section is thus calculated as

$$\sigma_f = \frac{K \cdot n_f}{N_p \cdot n_t} \tag{6.3}$$

where N_p is the number of incident lead ions, n_t is the number of target nuclei per cm^2 and K is the correction for fission fragment reinteraction and projectile absorption prior to the fission (see Section 6.6).

For the ZDC–VETOED runs, N_p has been evaluated by comparing the ADC spectra taken with the ZDC and the ZDC–VETOED triggers. The first spectrum has been integrated up to the ADC channel below the non–interacting lead ions peak (e.g. ADC channel 650), getting $n(zdc)$, and the second one (which does not contain the Pb peak) up to the same ADC channel, getting $n(zdc\ vetoed)$. From the ratio of the obtained values I have deduced N_p for the ZDC–VETOED runs as

$$N_p(zdc\ vetoed) = N_p(zdc) \cdot \frac{n(zdc\ vetoed)}{n(zdc)}$$

The numerical values obtained for the fission cross–sections are listed in Table 6.3 and plotted in Fig. 6.7 as a function of the target atomic number Z_t at 40 and 158 AGeV/c. The reported errors are purely statistical. An estimation of the systematic errors, mainly due to the uncertainty in the extrapolation of the continuum under the fission peak (since different fit procedures lead to slightly different results), gives about 10%.

For lighter targets there is no sensitive difference between the data at the two different energies; for heavier targets the fission cross–sections at 158 AGeV/c become more and more larger with Z_t than the ones at 40 AGeV/c. At both energies the fission cross–section increases with Z_t.

The Pb–Pb fission cross–section measured in this experiment at 158 AGeV/c is consistent with the one (about 340 mb) recently reported by the emulsion experiment EMU13 [3].

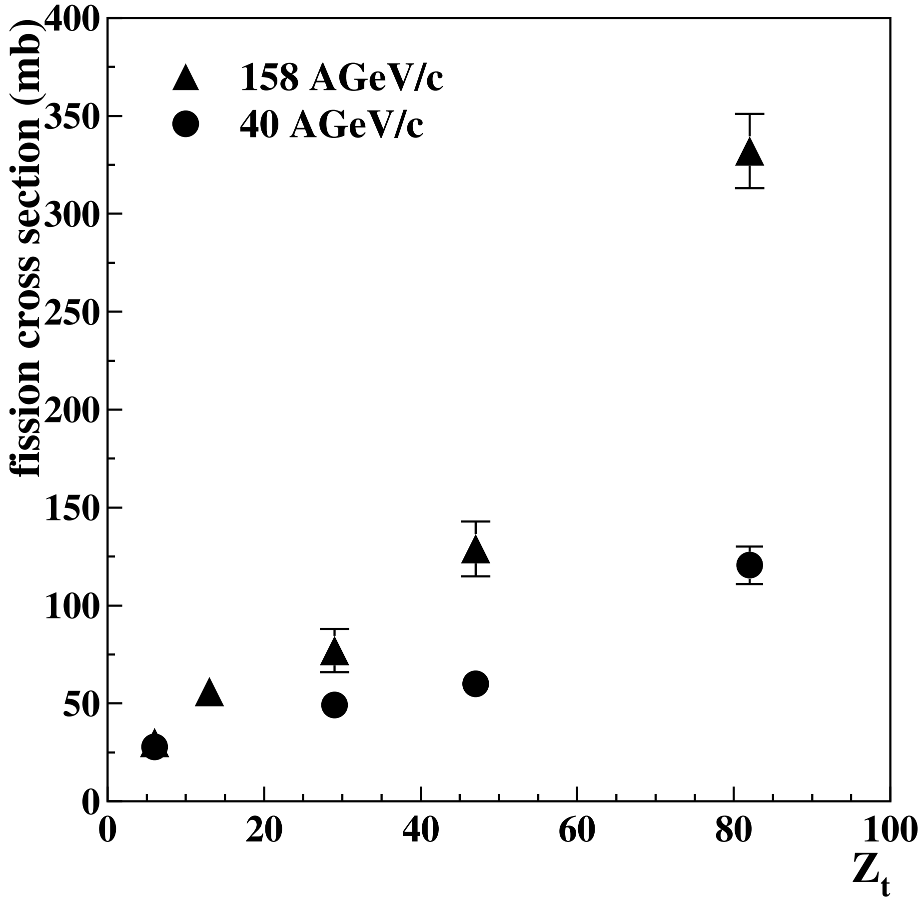

Figure 6.7: *Experimental fission cross–sections as a function of Z_t at 40 (full circles) and 158 AGeV/c (full triangles).*

6.5 Fission mechanism

In order to better understand the fission results, in this section I will deal with the mechanisms that are at the basis of the fission process in nucleus–nucleus interactions.

In heavy ion collisions fission can be induced both by nuclear and electromagnetic interactions. Therefore the total fission cross–section can be expressed as the sum of the contributions arising from these two mechanisms:

$$\sigma_f = \sigma^{C_f} + \sigma^{N_f}$$

This approximation can be justified by the short range of the nuclear force, which contributes only when the nuclei come into contact. At larger impact parameter (greater than the sum of the radii of the two colliding nuclei) the nuclear fission mechanism vanishes and the fission cross–section is assumed to be entirely due to the EM interaction. In reality, there is a small but finite region of b (close to the sum of the nuclear radii) where both processes can occur, but the magnitude of such interference has been estimated with an idealized form of the nucleon–nucleon interaction, and was found to be less than one percent of the total cross–section [4].

In order to disentangle these two contributions from the measured fission cross–sections, the different behaviour of σ^{C_f} and σ^{N_f} as a function of the target atomic (mass) number will be studied. For this purpose, the dependence of σ^{C_f} and σ^{N_f} respectively on Z_t and A_t will be estimated in Sec. 6.5.1 and Sec. 6.5.2. In Sec. 6.5.3 these dependences will be used to fit the experimental data and to extract the two contributions.

As already said in Section 6.2, the fission is expected to occur in extremely peripheral collisions.

6.5.1 Coulomb fission cross–section

The electromagnetic processes become dominant when two nuclei collide at impact parameters b larger than the cut–off impact parameter b_{min}, which is close to the sum of the nuclear radii.

In the frame of the Weizsäcker–Williams (WW) method ([2]), the EM interaction between two nuclei can be expressed in terms of the interaction of the projectile nucleus with a virtual photon emitted by the target nucleus, which may induce the fission of the projectile.

The Coulomb fission cross–section of the projectile nucleus is determined by the equivalent photon spectrum $N_t(\omega, b)$ of the target nucleus, multiplied by the projectile photofission cross–section $\sigma_p^{\gamma f}(\omega)$. For the computation of $\sigma_p^{C_f}$ we must integrate over all the virtual photon energies ω and the impact parameters b:

$$\sigma_p^{C_f} = \int_{b_{min}}^{+\infty} 2\pi b db \int N_t(\omega, b)\sigma_p^{\gamma f}(\omega) d\omega \tag{6.4}$$

The integral on the impact parameter ranges from $b = b_{min}$ to $b = +\infty$, where the b_{min} value depends on the considered process.

Benesh, Cook and Vary [4] proposed the following parametrization for b_{min}:

$$b_{min}^{BCV} = r_0(A_p^{\frac{1}{3}} + A_t^{\frac{1}{3}} - x(A_p^{-\frac{1}{3}} + A_t^{-\frac{1}{3}})) \tag{6.5}$$

where A_p and A_t are the mass numbers of the projectile and the target nuclei, r_0=1.34 fm and $x = 0.75$.

The expression for the equivalent photon distribution can be derived in the frame of the classical electromagnetism [5]. The WW method was extended by including higher multipolarities πl [6] in the equivalent photon spectrum. The resulting

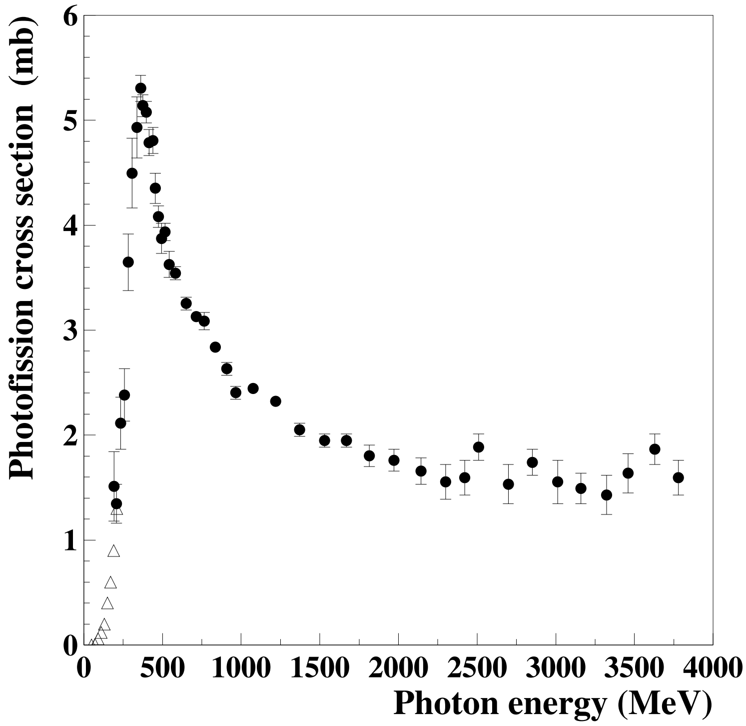

Figure 6.8: *Photofission cross–sections for ^{nat}Pb (from [8]) as a function of the incident photon energy. For photon energy values below 0.17 GeV ^{208}Pb data from [7] are used (open triangles).*

number of virtual photons, integrated over the impact parameter, is then given by:

$$n_t(\omega) = \int_{b_{min}}^{+\infty} 2\pi b N_t(\omega, b) db = \frac{2Z_t^2\alpha}{\pi\omega\beta^2}[\xi K_0(\xi)K_1(\xi) - \frac{\beta^2\xi^2}{2}(K_1^2(\xi) - K_0^2(\xi))] \quad (6.6)$$

where α is the fine structure constant, K_0 and K_1 are the modified Bessel functions of order zero and one, $\xi = \frac{\omega \cdot b_{min}}{\beta\gamma}$ (where γ is the Lorentz factor of the target nucleus in the rest frame of the projectile nucleus) and b_{min} is the cutoff impact parameter below which the nuclear processes take over and become dominant.

In conclusion, the Coulomb fission cross–section of the projectile nucleus given by Eq. 6.4 becomes:

$$\sigma_p^{C_f} = \int n_t(\omega)\sigma_p^{\gamma f}(\omega) d\omega \quad (6.7)$$

Eq. 6.6 and 6.7 reveal an important feature of the Coulomb fission mechanism: $\sigma_p^{C_f}$ approximately scales as Z_t^2, i.e. it strongly depends on the target atomic number.

To compute the Coulomb fission cross–section for ^{208}Pb–nucleus interactions at 158 and 40 AGeV/c, the photofission cross–section of ^{208}Pb should be used as input

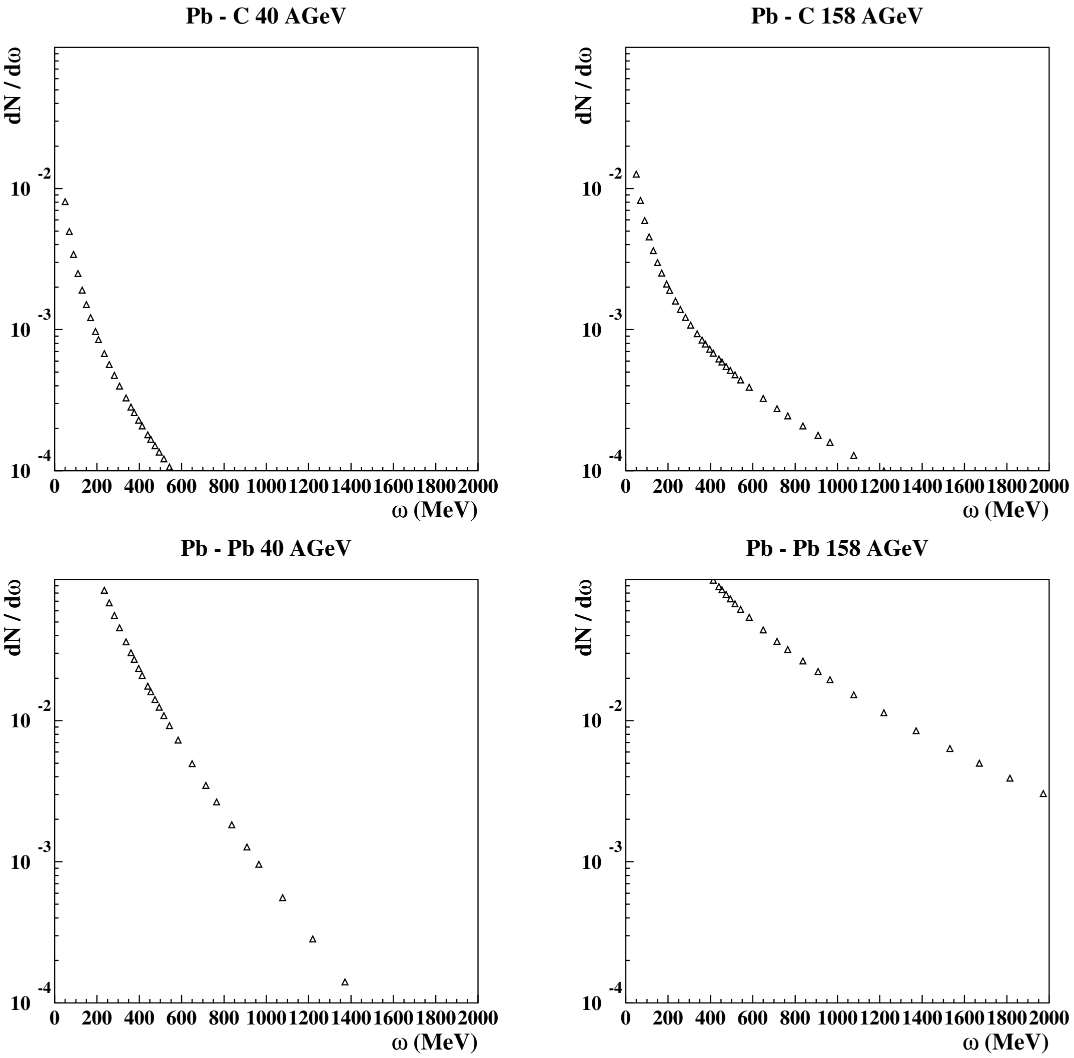

Figure 6.9: *Spectra of the virtual photons emitted by a C (top) and a Pb target (bottom) for incident Pb ions of 40 (left) and 158 AGeV/c (right).*

of Eq. 6.7. Indeed, due to the lack of photofission data for ^{208}Pb over the full energy range of the virtual photons emitted at SPS energies (from the ^{208}Pb fission threshold of 28 MeV up to about 2 GeV), the following strategy has been adopted. For photon energies below 0.17 GeV the photofission cross–section for ^{208}Pb was taken from [7], by unfolding electrofission cross–section data of ^{208}Pb. At higher energies the ^{nat}Pb photofission values recently measured at the Jefferson Laboratory in the energy interval ω=0.17–3.84 GeV [8] have been used. In Fig. 6.8 the photofission cross–sections from these sets of experimental data are reported.

The other ingredient needed to evaluate the ^{208}Pb Coulomb fission cross–section by means of Eq. 6.7 is the expression of the equivalent photon distribution $n_t(\omega)$ of

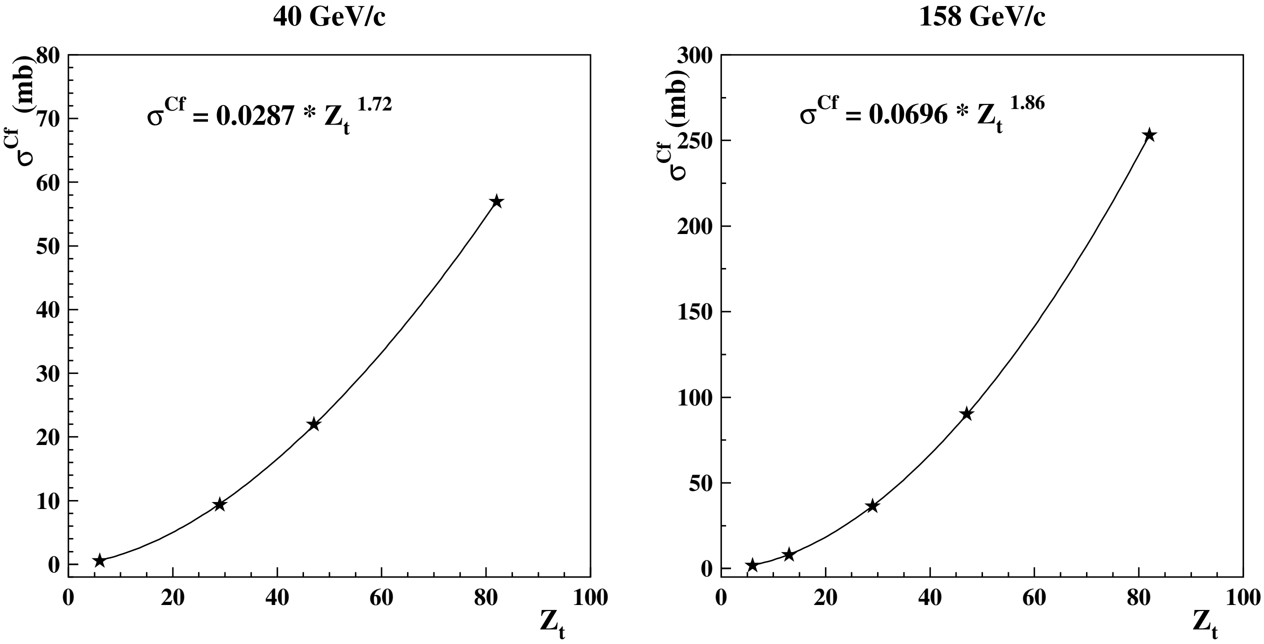

Figure 6.10: *Fit to the Coulomb fission cross–sections σ^{Cf}, plotted as a function of Z_t, with a dependence $\sigma^{Cf} = \sigma_1 Z_t^{\delta}$ for a Pb incident beam of 40 (left) and 158 AGeV/c (right).*

the target nucleus, provided by Eq. 6.6, where b_{min} is given by Eq. 6.5. In Fig. 6.9 a typical photon spectrum is shown for two different targets (carbon and lead) at 40 and 158 AGeV.

In order to determine the behaviour (i.e. the slope as a function of Z_t) of the σ^{Cf} values, the computed Coulomb fission cross–sections have been fitted as $\sigma^{Cf} = \sigma_1 Z_t^{\delta}$ (Fig. 6.10). The obtained values for δ are 1.72 and 1.86 respectively at 40 and 158 AGeV/c. It is worth to note that values of the δ parameter slightly smaller than two are due to the fact that the explicit Z_t^2 dependence of Eq. 6.6 is to some extent smoothed by the increase of the minimum impact parameter b_{min} with the target mass number (Eq. 6.5).

6.5.2 Nuclear fission cross–section

The nuclear contribution σ^{Nf} to the fission cross–section can be computed according to the geometrical scaling model proposed in [9] to interpret data of Uranium fission on several targets at 120 AMeV. As only the most peripheral collisions are expected to contribute, we can consider the region of impact parameter ranging from $b_{min} - \Delta b$ to b_{min}, which defines an annulus of width Δb, whose area gives the cross–section for nuclear fission

$$\sigma^{N_f} = 2\pi \cdot \Delta b \cdot (b_{min} - a - \frac{\Delta b}{2}) \tag{6.8}$$

where

$$a = \frac{Z_p Z_t e^2}{\mu \beta^2 \gamma}$$

corrects for the Rutherford bending of the trajectory [10].

In order to apply this geometrical model to the Pb fission, the fact that the fissility of Pb, unlike that of Uranium, is smaller than one must be taken into account. Therefore Eq. 6.8 has been multiplied for a correction factor f, which represents the probability for Pb to undergo fission, when a collision with impact parameter comprised between $b_{min} - \Delta b$ and b_{min} has occurred.

Moreover, at the beam energies used for the measurements reported here, the Rutherford correction term is negligible.

Therefore, in case of Pb fission at the SPS energies, Eq. 6.8 becomes

$$\sigma^{N_f} = 2\pi \cdot f \cdot b_{min} \cdot \Delta b \tag{6.9}$$

where the second order term in Δb has been neglected (for Uranium a Δb value of about 0.8 fm was found in [9]) and b_{min} can be computed according to Eq. 6.5. This means that, in contrast to the predicted Z_t^δ rise of σ^{C_f}, σ^{N_f} is expected to increase more slowly (as $A_t^{1/3} + A_p^{1/3}$).

6.5.3 Experimental result interpretation

In this section the experimental data are interpreted in the light of the previous considerations.

The comparison between the ADC spectra of the fragment detector relative to the C target (reported in Fig. 6.6) has shown that the fission peaks are similar at the two energies. This is an indication of the fact that the fission cross–section for carbon (and in general for light targets) is mainly nuclear and weakly dependent on the beam energy. By contrast, for heavier targets, such as Pb, the EM contribution prevails and the fission peak is more pronounced at 158 AGeV/c (by a factor 3) than at lower energy (Fig. 6.6 bottom).

Let us consider again the measured fission cross–sections shown in Fig. 6.7. As previously stated, the energy dependence of the fission cross–section is negligible for the carbon target and becomes more and more pronounced for higher values of Z_t. Such a behaviour suggests that for light targets the relevant fission mechanism is the nuclear one (which is expected to exhibit a weak dependence on the incident energy), while the EM contribution (which has a much stronger energy dependence) becomes dominant for heavy targets. This interpretation is consistent with the fact that, as discussed in Sec. 6.5.1 and 6.5.2, the EM contribution increases much faster than the nuclear one as a function of the target mass (or atomic) number.

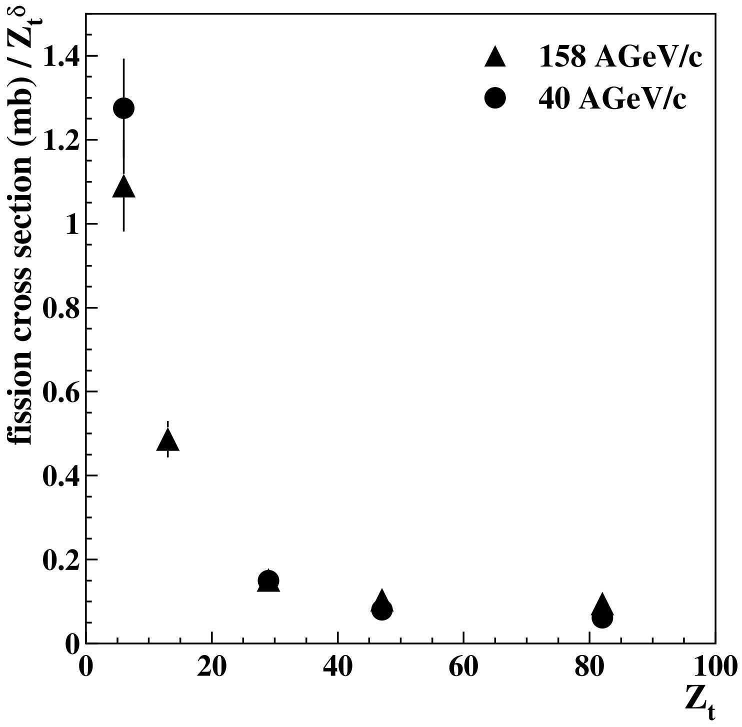

Figure 6.11: *Experimental fission cross–sections divided by Z_t^δ as a function of Z_t at 40 (full circles) and 158 AGeV/c (full triangles).*

Moreover, this is also confirmed by the behaviour of the fission cross–section divided by Z_t^δ (where $\delta = 1.72$ and $\delta = 1.86$ were determined respectively at 40 and 158 AGeV/c, as described in Sec. 6.5.1), plotted versus Z_t (Fig. 6.11). If fission was purely EM this ratio should be constant, since the Coulomb cross section is proportional to Z_t^δ. Indeed, the ratio is constant only for heavy targets and becomes larger for low values of Z_t, indicating that for light targets the EM mechanism alone cannot account for the measured cross–sections and the nuclear one plays a significant role.

In order to extract the nuclear and EM contributions from the experimental fission cross–sections, data have been fitted as the sum of a term proportional to Z_t^δ (EM contribution) and a nuclear term given by Eq. 6.9:

$$\sigma^f = \sigma^{C_f} + \sigma^{N_f} = c_1 \cdot Z_t^\delta + 2\pi c_2 \cdot b_{min} \tag{6.10}$$

where the δ exponent has been fixed as described in Sec. 6.5.1, while c_1 and c_2 are free parameters. In particular c_2 is equal to the product $\Delta b \cdot f$ (see Eq. 6.9) and its value given by the fit is 0.0411 ± 0.035 fm (0.0497 ± 0.040 fm) at 40 (158) AGeV/c. The errors are only statistical.

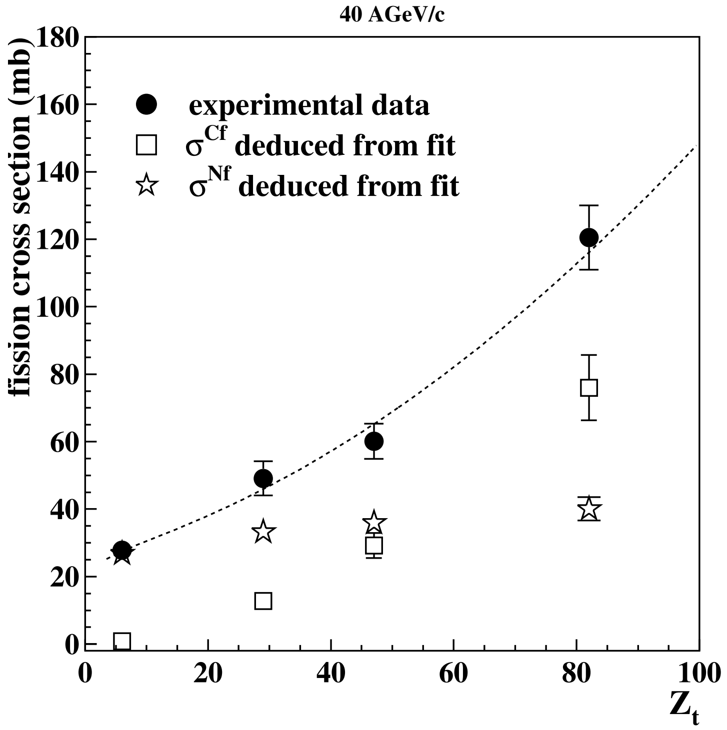

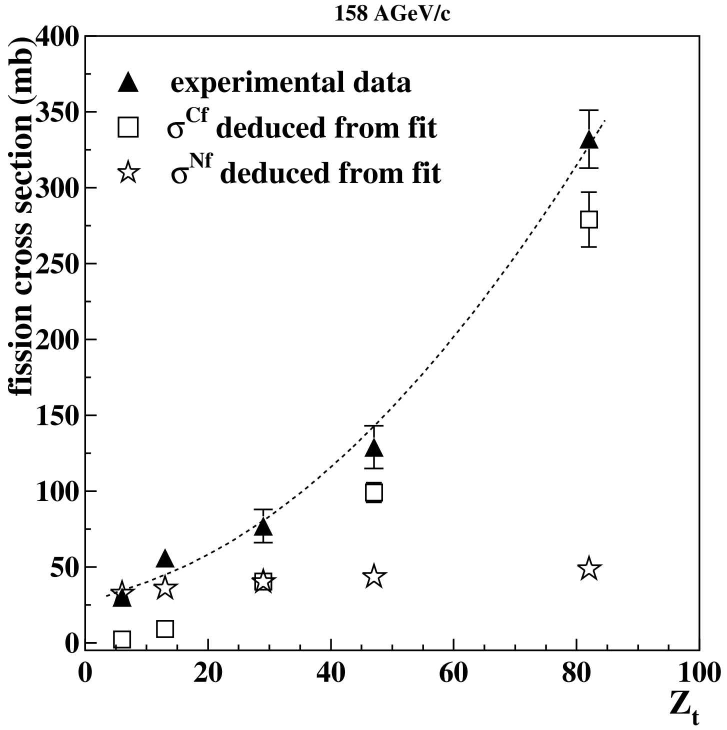

Figure 6.12: *Experimental fission cross–sections (full symbols) as a function of Z_t at 40 AGeV/c (top) and 158 AGeV/c (bottom). The dotted lines are the fit to the data according to Eq. 6.10. The σ^{C_f} (open squares) and σ^{N_f} (open stars) values deduced from the fit are also reported.*

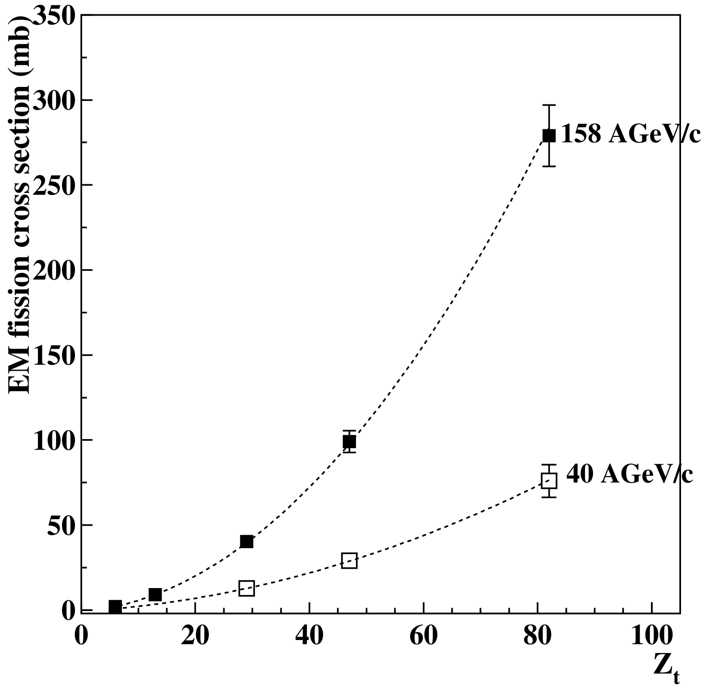

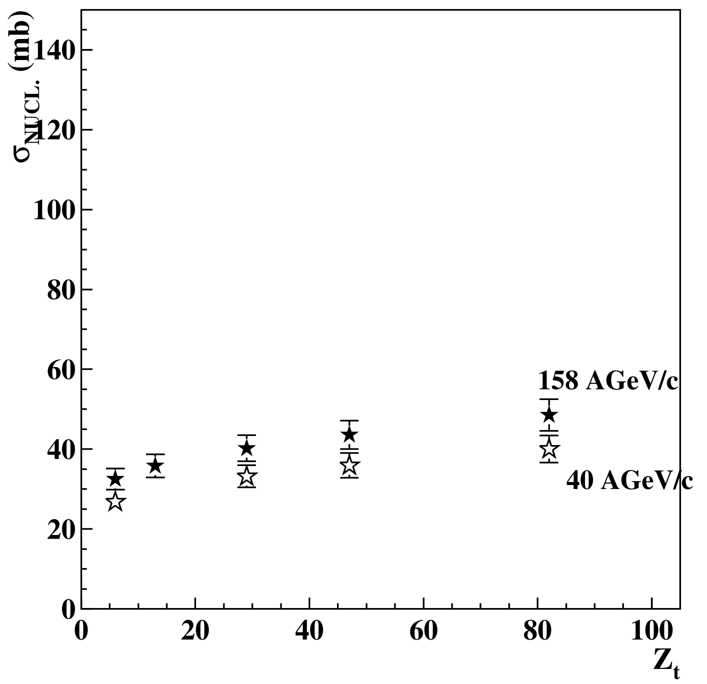

Figure 6.13: *On the top: E.M. fission cross–sections deduced from the fit to the experimental data as a function of Z_t at 40 AGeV/c (open squares) and 158 AGeV/c (full squares). On the bottom: nuclear contributions, deduced from the fit, plotted versus Z_t at 40 AGeV/c (open stars) and 158 AGeV/c (full stars).*

	40 AGeV/c		158 AGeV/c	
	$\sigma^{C_f}(mb)$	σ^{N_f} (mb)	σ^{C_f}(mb)	$\sigma^{N_f}(mb)$
C	0.8 ± 0.1	26.8 ± 2.3	2.1 ± 0.1	32.5 ± 2.6
Al			9.1 ± 0.6	35.8 ± 2.9
Cu	12.7 ± 1.6	33.2 ± 2.8	40.4 ± 2.6	40.2 ± 3.2
Ag	29.2 ± 3.7	35.9 ± 3.1	99.0 ± 6.4	43.5 ± 3.5
Pb	76.0 ± 9.6	40.0 ± 3.4	278.9 ±18.0	48.5 ± 3.9

Table 6.4: *EM and nuclear contributions to the fission cross–section, deduced from the fit to the experimental values, using two different δ exponents at 40 and 158 AGeV/c.*

For the sake of completeness, we note that, even if only the product $\Delta b \cdot f$ can be deduced from the fit, an indication about the value of the parameter f can be obtained by dividing c_2 by $\Delta b \simeq 0.8\ fm$, found for Uranium and reported in [9, 10]. This calculation gives $f \simeq 0.05 - 0.06$, a value of the same order of magnitude of the fissility, which is about $(8 \pm 1)\%$ for ^{nat}Pb [11].

The values of the c_1 parameters obtained from the fit are 0.0388 ± 0.0049 mb and 0.0768 ± 0.0049 mb respectively at 40 and 158 AGeV/c (only statistical errors are reported).

The EM (σ^{C_f}) and nuclear (σ^{N_f}) contributions to the fission cross–sections deduced from the fit to the experimental data are reported in Table 6.4 and displayed in Fig. 6.12 for incoming Pb beams of 40 and 158 AGeV/c. The errors are only statistical errors.

As expected, the nuclear term increases very weakly with the target mass, while the EM contribution, negligible for light targets, becomes dominant for heavier ones. Moreover, the EM term quickly increases as a function of energy, as shown in Fig. 6.13 (top), while the nuclear one weakly depends on the beam energy (Fig. 6.13 bottom).

Another way to extract the EM contributions from the fission cross–section is to subtract from the experimental fission cross–sections the nuclear contributions given by the geometrical model (second term of Eq. 6.10). The c_2 parameter is fixed by assuming that the fission cross–section for the Carbon target at 40 AGeV/c is only nuclear. This procedure leads to $c_2 = (0.0417 \pm 0.0039)\ fm$. The values of the nuclear contributions to the fission cross–section of the other projectiles can then be deduced, and the EM contributions are evaluated as the difference $\sigma^f - \sigma^{N_f}$. The obtained values for σ^{N_f} and σ^{C_f} are reported in Table 6.5.

In Fig. 6.14 the EM contributions to the fission cross–section, deduced from the fit to the experimental σ^f results and by assuming that the Pb–C fission cross–section at 40 AGeV/c only nuclear are compared. The results obtained with these two different methods are in good agreement.

	40 AGeV/c		158 AGeV/c	
	$\sigma^{C_f}(mb)$	σ^{N_f} (mb)	σ^{C_f}(mb)	$\sigma^{N_f}(mb)$
C	0.0 ± 0.0	27.8 ± 2.6	2.2 ± 3.9	27.8 ± 2.6
Al			25.4 ± 5.7	30.6 ± 2.8
Cu	14.7 ± 5.9	34.4 ± 3.2	42.6 ± 11.4	34.4 ± 3.2
Ag	22.8 ± 6.3	37.2 ± 3.4	91.7 ± 14.4	37.2 ± 3.4
Pb	79.0 ± 10.3	41.5 ± 3.8	290.5 ±19.4	41.5 ± 3.8

Table 6.5: *EM and nuclear contributions to the fission cross–section, evaluated assuming $\sigma^f(Pb-C)$ at 40 AGeV/c only nuclear.*

The figures also show the WW model predictions computed by means of Eq. 6.7 by using the $\sigma_A^{\gamma f}$ values from [8, 7], as described in Sec. 6.5.1. A satisfactory description of the extracted EM contributions is obtained at 158 AGeV/c and, for light targets, at 40 AGeV/c.

On the contrary, the WW predictions for Pb–Pb interactions at 40 AGeV/c are significantly below the value of the EM contributions to the fission cross–section. Since the EM contributions have been deduced from the experimental data assuming the nuclear term scaling of [9], the observed discrepancy suggests a faster increase of the nuclear contribution (as a function of the target mass) than the one assumed in Eq. 6.9 and 6.5. We note that this effect plays a minor role at 158 AGeV/c, since at this energy the fission cross–section is dominated by the EM contribution (see Fig. 6.12).

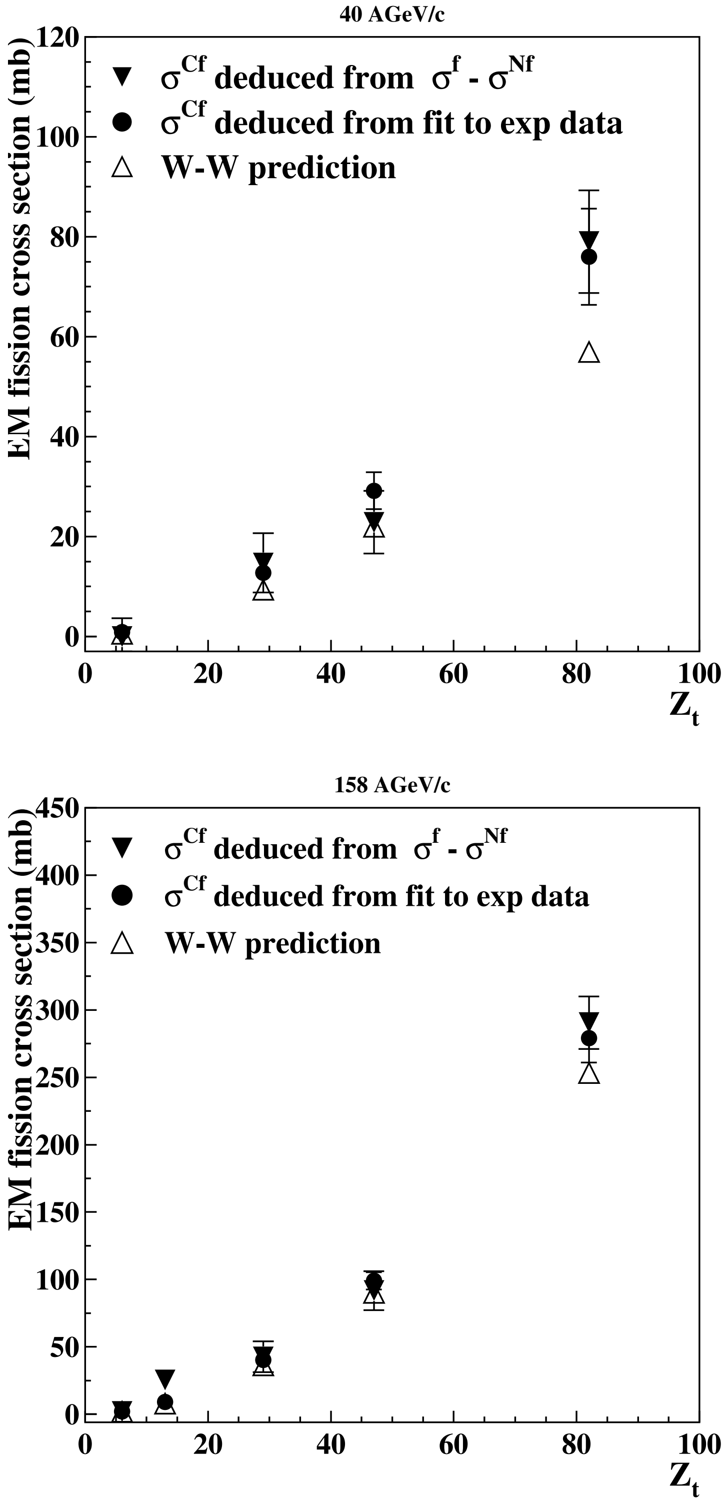

Figure 6.14: *EM contributions to the fission cross–section as a function of Z_t at 40 AGeV/c (top) and 158 AGeV/c (bottom): extracted from the fit to the data (full circles), extracted from data assuming that $\sigma_f(Pb-C)$ at 40 AGeV/c is only nuclear (full triangles), WW predictions (open triangles).*

6.6 Corrections

Two different corrections have been performed on the experimental data, to take into account the interactions of the fission fragments with the air after the target or the absorption within the target both of the projectile Pb ions prior to a potential fission and of the fission fragments. These corrections are included in the factor K of Eq. 6.3, which is the product of two terms $K_1 \times K_2$.

6.6.1 Correction for the absorption in air

The first correction accounts for the fission fragments, originated in the target, that subsequently interact in the 1.6 metres between the target and the quartz blade. These events, in fact, do not appear in the recordered fission peak.

This correction is performed with the following assumptions:

- the air chemical composition is: $Ar(1\%) + O_2(21\%) + N_2(78\%)$. The average mass number is then $\langle A \rangle \simeq 14.7$. The air is approximated to a single gas with mass number 14.7.
- the air density is $\rho_{air} = 1.29 \cdot 10^{-3}\ g/cm^3$
- a fission fragment has a mass approximately half the one of the Pb projectile ($A_p \simeq 100$), i.e. the fission is assumed to be symmetric

The probability for a fission fragment of interacting in the $l = 1.6$ metres of air after the target can be estimated as

$$P_{int} = 1 - e^{-\frac{l}{\lambda}} \tag{6.11}$$

where

$$\lambda = \frac{\langle A \rangle}{N_{AV} \cdot \rho_{air} \cdot \sigma_{int}} \tag{6.12}$$

is the mean free path of the fragment in air. The cross–section for the interaction of the fission fragments in air is assumed as dominated by the nuclear interaction, approximately evaluated by means of the Schukraft–Schmidt parametrization ([12]):

$$\sigma_{nucl} = \pi r_0^2 \cdot (A_p^{\frac{1}{3}} + A_t^{\frac{1}{3}} - \delta)^2 \tag{6.13}$$

with $r_0 = 1.35$ fm and $\delta = 1.1$. The value found for σ_{nucl} is about 2 barns, while the contribution from the EM dissociation cross–section σ_{EM}^{diss} is expected to be negligible for Pb fragment–air interactions.

Therefore the probability that both fission fragments do not interact is

$$P = (1 - P_{int})^2 = (1 - 0.017)^2 = 0.97 \tag{6.14}$$

To take into account the absorption in air of the fission fragments, I have thus multiplied all the experimental fission cross–sections by a factor $K_1 \simeq 1/0.97 \simeq 1.03$, so increasing their values of about 3%.

6.6.2 Correction for the absorption in the target

There is a not negligible probability that the projectile *Pb* ions are absorbed (for EM or nuclear interactions) before they can undergo fission. On the other hand, also the produced fission fragments can be absorbed in the target itself and not reach the quartz blade. All these events are lost and disappear from the fission peak, leading to a slight underestimation of the number of fission events.

If no interaction (like the ones just described) happens inside the target, the number of fission events should be

$$n_{f,0} \propto \sigma_f \cdot l \tag{6.15}$$

where l is the target thickness and σ_f is the fission cross–section.

In presence of interactions in the target, n_f becomes

$$n_f \propto \sigma_f \cdot \int_0^l P_1(x) \cdot P_2(x) dx \tag{6.16}$$

where $P_1(x)$ is the probability of finding a given projectile–like Pb at a depth x in the target, $P_2(x)$ is the probability that both the fission fragments, produced at a depth x in the target, manage to come out of the target without interacting.

From the ratio of (6.15) and (6.16) we deduce the corrective term K_2 for projectile absorption prior to fission and fragment reinteraction in the target.

The calculation of the correction has been done for all the targets, by considering

$$P_1(x) = e^{-\frac{x}{\lambda_1}} \quad \text{and} \quad P_2(x) = e^{-\frac{2(l-x)}{\lambda_2}}$$

where λ_1 and λ_1 are the mean free paths in the target respectively of an incident Pb ion and of a fission fragment.

The probability that both the projectile Pb ions and the fission fragments do not interact within the target has been then estimated as:

$$\frac{1}{l} \cdot \int_0^l e^{-\frac{x}{\lambda_1}} \cdot e^{-\frac{2(l-x)}{\lambda_2}} dx \tag{6.17}$$

The values of λ_i ($\lambda_i = A \,/\, (N_{AV}\, \rho\, \sigma^i_{nucl+EM})$ have been calculated by means of Eq. 6.13 for the nuclear cross–section and estimating the cross–sections for the EM dissociation of a Pb ion or of a fission fragment according to the WW method (see Section 6.5.1), by replacing in Eq. 6.7 the photofission cross–section with the photon absorption cross–section reported in [13].

For the computation of the EM term we have to consider that only high energy photons ($\omega \geq 40$ MeV) can produce the break up of a nucleus. In fact, at low intensity the EM dissociation is dominated by the excitation of the Giant Dipolar Resonance, which leads only to the emission of one or more neutrons and hence does not modify the quartz blade signal.

158 AGeV/c

target	thickness	λ_1 (cm)	λ_2 (cm)	P(x) (%)	K_2
C	4 mm	3.00	4.52	85	1.17
Al	3 mm	4.51	6.54	92	1.08
Cu	1 mm	2.21	3.20	94	1.06
Ag	1 mm	2.26	3.35	95	1.05
Pb	4 mm	2.26	3.52	82	1.22

40 AGeV

target	thickness	λ_1 (cm)	λ_2 (cm)	P(x) (%)	K_2
C	4 mm	3.04	4.51	85	1.17
Cu	3.2 mm	2.49	3.50	85	1.17
Ag	3 mm	2.84	3.97	88	1.14
Pb	3 mm	3.39	4.86	90	1.11

Table 6.6: *Values of λ_1, λ_2 and K_2 and probabilities that the projectile Pb ions and the fission fragments do not interact in the target for the different targets at 40 and 158 AGeV/c.*

Once $\sigma_{EM}(\omega > 40\,GeV)$ has been estimated for Pb–Pb collisions, it has been extrapolated to lighter targets by assuming a Z_t^2 scaling. The extrapolation for fragment–Pb interactions has been based on a $N_p Z_p / A_p$ scaling [14].

The so estimated K_2 values are listed in Table 6.6 for the different target nuclei and at the two Pb beam energies, together with the λ_1 and λ_2 values and the corresponding probabilities that the Pb projectiles and the fission fragments do not interact in the target. These probabilities range from 82% to 95% ($K_2 \simeq 1.05 - 1.22$), depending on the target. This correction has already been included in the experimental fission cross–section results reported in Table 6.3.

In the computation of K_2, we have not taken into account the possibility that an incident ^{208}Pb ion can lose one or more neutrons for EM interaction and produce other Pb isotopes, mainly ^{207}Pb or ^{206}Pb. Since also these isotopes could undergo fission and hence contribute to the fission cross–section, the probability of finding a Pb isotope at a depth x in the target should have been considered in the evaluation of $P_2(x)$. In Fig. 6.15 this probability is plotted as a function of the target thickness for the different Pb isotopes. Increasing the target thickness the contribution of Pb isotopes different from ^{208}Pb becomes more and more important, while it is negligible for thin targets.

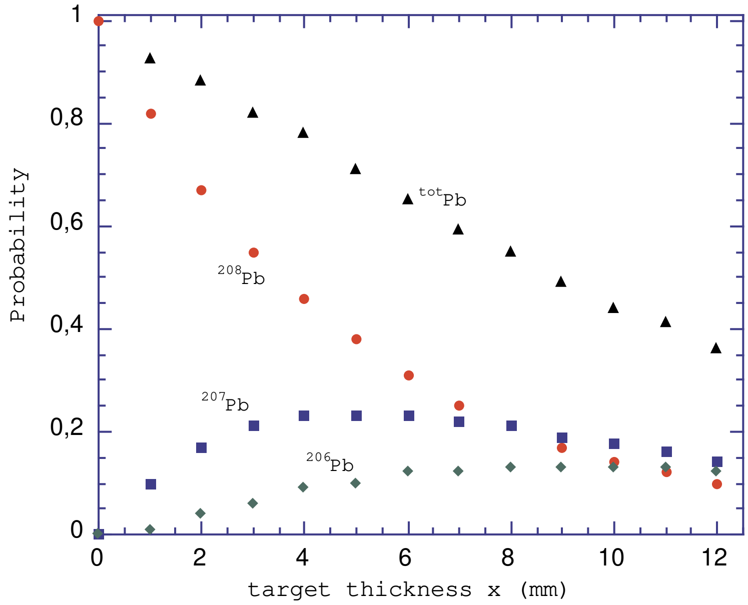

Figure 6.15: *Probability of finding a ^{206}Pb (diamonds). ^{207}Pb (squares) and ^{208}Pb (circles) as a function of the depth x in the target. The sum of these probabilities is also shown (triangles).*

6.7 Conclusions

The fission cross–sections of Pb projectiles in Pb-nucleus interactions have been measured at the CERN SPS by the NA50 experiment. In order to disentangle the electromagnetic and the nuclear contributions, measurements have been performed at two different energies (40 and 158 GeV/c per nucleon) and on different targets.

For this purpose a Cerenkov detector has been placed downstream the target to provide information on the charge of the spectator fragments emitted in the decay of the Pb projectile after its interaction in the target. A clear fission peak is visible in the ADC spectrum of the fragment detector. Information provided by the ZDC has allowed us to check that fission occurs in extremely peripheral collisions, compatible with E.M. fission or with fission induced by soft nuclear interactions involving very few participant nucleons.

Two procedures have been adopted to extract the EM and the nuclear contributions from the experimentally observed fission cross–sections. First, the fission cross–sections have been fitted as the sum of a term proportional to Z^δ (where δ is fixed by the WW model predictions) and a geometrical nuclear term. An alternative method assumes that the Pb–C fission cross–section is only nuclear and estimates the EM term by subtracting the nuclear one from the total fission cross–section. The results obtained with these two methods for the EM fission cross–section are fully consistent. The nuclear contributions to the fission cross–section are compatible with those found in emulsion experiments using a 10.6 AGeV gold beam at the Brookhaven AGS [15]. At such an incident energy the EM fission mechanism is expected to be negligible with respect to the nuclear one.

The E.M. contributions to the fission cross–section, deduced from the experimental values, have been compared to calculations performed using the Weizsäcker–Williams method. The comparison indicates a good agreement at 158 AGeV/c and, for light targets, at 40 AGeV/c. The discrepancy observed for heavier targets at 40 AGeV/c seems to indicate an underestimation of the nuclear contribution on heavy target nuclei.

Since experimental data of ^{208}Pb photofission were not available on the whole energy range of virtual photons radiated at SPS energies, we have used ^{nat}Pb measurements for the WW calculation of the EM contribution. A better evaluation of the W–W predictions could be performed when experimental data of ^{208}Pb photofission will be available.

At the LHC heavy ion collider, the EM processes will constitute the major beam loss mechanism. In particular, the EM dissociation cross–section for Pb–Pb interactions at LHC energies, which is expected to be of the order of 220 barn, will represent the main contribution to the total cross–section. Therefore, an accurate description of the EM interactions is necessary, in order to give a correct prediction of the beam lifetime for operations with heavy ions and to measure the beam luminosity.

Even if the fission contribution to the EM interactions is negligible at energies like the ones reached at the LHC collider, the fission studies are a useful tool to test the WW model, which will be then applied to all the EM processes.

Bibliography

[1] M.C.Abreu et al., Phys. Rev. *C 59*, 876 (1999).

[2] E.J.Williams et al., Proc. R. Soc. London, Ser. A *139*, 163 (1933); C.F. von Weizsäcker, Z.Phys. *88*, 612 (1934).

[3] M.L.Cherry et al., Acta Phys. Polonica *B 29* (1998).

[4] C.J.Benesh, B.C.Cook, J.P. Vary, Phys. Rev. C *40*, 1198 (1989).

[5] M.Vidovic, M.Grainer, C.Best and G.Soff, Phys. Rev. C *47*, 2308 (1993).

[6] C.A.Bertulani and G.Baur, Phys. Rep. *163*, 299 (1988).

[7] L.G.Moretto et al., Phys. Rev. *179*, 1176 (1969).

[8] C.Cetina et al., Phys. Rev. *C 65*, 044622 (2002).

[9] M.L.Justice et al., Phys. Rev. C *49*, 49 (1994).

[10] M.L.Justice, Ph.D thesis, University of California, Berkeley, 1991; Lawrence Berkeley Laboratory Report *LBL-31704*.

[11] C.Cetina et al., Phys. Rev. Lett. *84*, 5740 (2000).

[12] A.S.Goldhaber and H.H. Heckman, Ann. Rev. Nucl. Sci. *28*, 161 (1979).

[13] M.Vidovic, M.Grainer and G.Soff, Phys. Rev. C *48*, 2011 (1993).

[14] Berman and Fulz, Rev. of Modern Physics, *47,n.3*, 713 (1975)

[15] C.J. Waddington, Int. J. Mod. Phys. *E 2*, 739 (1993)